

# Cellular, Cytoskeletal, and Biophysical Mechanisms of Spiral Cleavage during *Platynereis dumerilii* Embryogenesis

DISSERTATION

Zur Erlangung des akademischen Grades  
**Doctor rerum naturalium**  
(Dr. rer. nat.)

vorgelegt  
der Fakultät Mathematik und Naturwissenschaften  
der Technischen Universität Dresden

von  
**Hsieh, Yu-Wen**  
Geboren 02.02.1988 in Taipei, Taiwan

Betreuer  
**Dr. Pavel Tomancak**

January 2020

Die Dissertation wurde in der Zeit von 07.2014 bis 07.2018 im Max Planck Institute für  
Molecular Cell Biology and Genetics angefertigt





# Abstract

Embryogenesis is one of the most delicate biological processes which requires precise control in various levels, including molecular distribution and gene expression, cellular orientation and specification, and tissue dynamics giving rise to proper morphology. The diverse animal morphology can be resulted from the difference during early embryonic cleavages. Spiral cleavage is a conserved embryonic patterning strategy used in the majority of the animal clade Spiralia. The specific cell positioning during cell division and quadrant-based clonal domain formation make the embryos with the blastomeres orientated in a spiral manner when viewing from the animal pole. Although spiral cleavage is conserved in many phyla, the detailed cellular, molecular and biophysical mechanisms for this left-right symmetry breaking event remain unclear.

Here I studied the early development of the prototypic annelid spiral-cleaver *Platynereis dumerilii*, which performs two unequal embryonic cleavages followed by the first dextral spiral cleavages, and compared the mechanisms to other spiralian or to other cleavage types. First, I described the morphology of each cell cycle from the zygote until 64-cell stage by imaging the fluorescently labeled fixed embryos. Second, with mRNA injection, whole-embryo live-imaging with Selective Plane Illumination Microscopy (SPIM), and *in silico* cell tracking, I monitored these cleavages in 4-D, constructed the early cell lineages, and revealed the subtle asynchrony of the four quartets. Third, together with the spindle inclination angle measurement, I discovered the leading role of the D macromere during *P. dumerilii* spiral cleavage. I also confirmed that the dextral micromere orientation is neither affected by the eggshell nor the presence of all the neighbor macromeres, suggesting that this cellular property may be achieved by cell autonomous molecular mechanisms.

In order to quantify the candidate cytoskeletal dynamics during spiral cleavage, I optimized the construction of the injected mRNAs and the injection protocol to achieve the highest translational level of the fluorescent protein within a given developmental time. Beside mRNA injection, I also established a protein expression and injection protocol for *P. dumerilii* protein injection in order to visualize the target gene as early as possible. Both techniques didn't dramatically influence embryogenesis and allow for quantification of the protein dynamics. With these strategies, I discovered and measured the chiral counter rotational flow of cortical actomyosin in each spiral

## Abstract

cleavage and revealed that it's present in the first two spiral cleavages, especially of the macromeres. The biophysical force generated by actomyosin contributes in the cell deformation and spindle inclination, resulting in proper dextral micromere positioning, during the first spiral cleavage, confirmed by the chemical treatment to the *P. dumerilii* embryos. The asymmetric actomyosin distribution, nuclei migration, and the change of the cell axes during cytokinesis in the macromeres also suggests that the macromeres may play critical roles to lead spiral cleavage.

This work is built on the knowledge of the spiral cleavage machinery and has extended it in multiple dimensions. The detailed phase-by-phase description of each cleavage increases the information of *P. dumerilii* embryogenesis. The established labeling and imaging techniques in this thesis are the important basis for investigation and comparisons of different spiralian development in the future. More broadly, the discovery of actomyosin dynamics shows conservation to the left-right symmetry breaking events of the animals which does not belong to Spiralia. These together bring insights to a global evolutionary speculation: a conserved mechanical force generation pathway, tuned by the upstream molecular signals, may be the key of the miscellaneous cleavage types, resulting in the astonishing variety of embryo patterning.

# Dedication

This thesis is dedicated to my dad, a *warship* rides the waves. And to my mom, an *anchor* stabilizes him with *whoever* on board.



# Acknowledgements

This singularity occurred at a meet up with Shang-Yun in Taiwan right after my “amazing” military services in 2013. A journey into the unknown world has started without any bit of regret since then.

This thesis cannot be done without the help of many, especially the 331N family in MPI-CBG with our perfect working environment. PAvel as a great mentor and supervisor always gives mind-exploding ideas which are the breakthrough of the project. Mette is definitely the best supervisor I’ve ever met. I couldn’t imagine how lucky I am to be able to have this opportunity to work on this project with her. She is not only patient and dedicated to science, but also knowing all the details regarding to her profession. Most importantly, she fills in all the gaps which were missing in this project smoothly. Thanks to Pavel and Michi for maintaining the lab and time to time the lovely baby worms. The Mighty Akanksha with the flying donkey, the Lord of voice, without your optimistic mind I couldn’t survive the cold winter. Bruno the giant, Hugo the Boss, your joining has made this project expanded exponentially, opening up so many new roads for the spiral dancing world. Of course also to all the other LoPaTs, here is for sure the warmest/wormy-ist place ever.

I want to thank my TAC committee, Stephan Grill and Jochen Rink. The annual TAC meetings were always like the light guiding me through darkness, correcting the path in the scientific soup. Both Grill and Rink lab members are also the best colleagues and friends. Especially to Lokesh, Teije, and Dora, you are amazing in cortex and beyond. Heino, James, Olga, and Hanh, I can’t stay in the worm room without you. That’s way too cold and the light cycle is way too routine.

The 3N in MPI-CBG is and always will be a magical place. No one could work properly without Angelika’s watch! But even so, what is crazy remains the way it is. Gaia, Gwen (you’re always part of Pigino lab to me), Mareike, Gonzalo, Petra, and Dennis, you neighbors make 3N so great, just need to keep that door behind the “CPU” a bit open. And to dear Sandy, you’re the most efficient person I’ve ever work with, plus don’t need to worry about any potential problems if you say you’ll handle it. There are many others making MPI-CBG a wonderful place to work and stay till late. Ania, Albert, and Miquel were nearly always there no matter it’s about

## *Acknowledgements*

imaging, jogging, or doing whatever crazy. Katja, Katja, Katja, the only glue sticking every soul as a whole, provides enough dose of dopamine to these poor labors. This optimized my performance and let this project moving forward like a rocket. The reception which keeps us safe during late stay and library for us to calm a bit are also the crucial gears that makes this institute perfectly functional.

The amazing facilities of MPI-CBG offer the best scientific services and advices for us. Jan, Britta, Sebastian, Bert, and Davide of our LMF, no microscopes could work so nicely without your daily maintenance and kind assistance for the users. Barbara and Aliona of the protein facility, I wouldn't have the protein for injection if you didn't help me to synthesize and purify them. Oscar, and Matt of the computer department, how could this institute remain running if you're not geeky and siliceous like you are? Misho and John of the genome engineering facility, no "Guide" of my RNAs would have happened without your help and they'd have got lost in the C(ho)AS. Thanks to Ian from scientific computing facility for analysis of the transcriptomic data which made me much faster to explore the target genes, and to Benoit and Robert for creating wonderful Fiji plugins solely for analyzing "wormy" spiral events. Last but not the least, the PhD office, Birgit and Brian, IMPRS-CellDevoSys is indeed the best and I've received all the care from you, sincerely.

Live in a foreign country is always not an easy job. I want to thank all the friends I've met in Dresden, Germany, and Europe. The volleyball team Pumpkins, TSV Prohlis, MoMix, and Shatterhand Radebeul let me continue what I need in my life, and even make leaps in progress. The Taiwanese community increased by 200% during this 5 years. I'm glad that people like what I offer and how I lead this group of lovely lads. And to all the friends I maybe haven't met in person in Europe. Internet is the connection and your existence makes me feel not alone. My friends in Taiwan form a bridge for me to know that I still hook with the humid sweet potato and the parasites over there.

To who I love, to who loves me. You made Ü.

# Author's Declaration (Deu.)

## Erklärung entsprechend §5.5 der Promotionsordnung

Hiermit versichere ich, dass ich die vorliegende Arbeit ohne unzulässige Hilfe Dritter und ohne Benutzung anderer als der angegebenen Hilfsmittel angefertigt habe; die aus fremden Quellen direkt oder indirekt übernommenen Gedanken sind als solche kenntlich gemacht. Die Arbeit wurde bisher weder im Inland noch im Ausland in gleicher oder ähnlicher Form einer anderen Prüfungsbehörde vorgelegt.

Die Dissertation wurde im Zeitraum vom 14.07.2014 bis 13-07-2018 verfasst und von Dr. Pavel Tomancak at the Max Planck Institute of Molecular Cell Biology and Genetics, Dresden betreut. Meine Person betreffend erkläre ich hiermit, dass keine fruheren erfolglosen Promotionsverfahren stattgefunden haben. Ich erkenne die Promotionsordnung der Fakultät für Mathematik und Naturwissenschaften, Technische Universität Dresden an.

SIGNED: ..... DATE: .....





# Author's Declaration (Eng.)

## Erklärung entsprechend §5.5 der Promotionsordnung

I herewith declare that I have produced this paper without the prohibited assistance of third parties and without making use of aids other than those specified; notions taken over directly or indirectly from other sources have been identified as such. This paper has not previously been presented in identical or similar form to any other German or foreign examination board.

The thesis work was conducted from 14.07.2014 to 13.07.2018 under the supervision of Dr. Pavel Tomancak at the Max Planck Institute of Molecular Cell Biology and Genetics, Dresden. I declare that I have not undertaken any previous unsuccessful doctorate proceedings. I declare that I recognize the doctorate regulations of the Fakultät für Mathematik und Naturwissenschaften of the Technische Universität Dresden.

SIGNED: ..... DATE: .....

# Contents

Abstract	i
Dedication	iii
Acknowledgements	v
Author’s Declaration (Deu.)	vii
Author’s Declaration (Eng.)	ix
Contents	x
List of Figures	xv
List of Tables	xvii
List of Equations	xvii
Abbreviations	xix
<b>I Introduction</b>	<b>1</b>
<b>1 Introduction</b>	<b>3</b>
1.1 Diverse cleavage types in metazoans . . . . .	3
1.1.1 Bilateral cleavage . . . . .	5
1.1.2 Radial cleavage . . . . .	6
1.1.3 Rotational cleavage . . . . .	6
1.1.4 Spiral cleavage . . . . .	7
1.2 Evo-Devo of spiral cleavage . . . . .	8
1.2.1 Evolutionary relationships of spiralian . . . . .	8
1.2.2 Rosetta stone of spiral cleavage . . . . .	10
1.2.3 Dorsal-ventral axis determination mechanisms . . . . .	10
1.2.4 Cellular mechanisms of the first spiral cleavage . . . . .	13

1.2.5	Spiral cleavage, a left-right symmetry breaking event . . . . .	14
1.2.6	Molecular mechanisms involved in spiralian development . . . . .	16
1.2.7	First spiral cleavage, key of spiral looking embryo . . . . .	21
1.3	<i>Platynereis dumerilii</i> : a model organism for studying spiral cleavage . .	22
1.3.1	Life cycle of <i>Platynereis dumerilii</i> . . . . .	24
1.3.2	Available research tools for <i>Platynereis dumerilii</i> studies . . . . .	28
1.4	Imaging methods for fluorescently labeled samples . . . . .	29
1.5	Cellular processes involved in cleavages . . . . .	35
1.5.1	Cell division machinery: Mitotic spindle and DNA . . . . .	35
1.5.2	Cell division machinery: Cell cortex . . . . .	37
1.5.3	Factors for cleavage plane determination . . . . .	43
1.5.4	Influence of division plane to cell stemness . . . . .	49
1.6	Objectives . . . . .	51
1.6.1	Develop the labeling techniques for studying early embryogenesis	52
1.6.2	Decipher the mechanisms of spiral cleavage . . . . .	52
<b>II</b>	<b>Results</b>	<b>55</b>
<b>2</b>	<b>Early development of <i>P. dumerilii</i></b>	<b>57</b>
2.1	Synchrony of the first six embryonic cleavages . . . . .	57
2.2	Orientation of the cytoskeletal elements . . . . .	60
2.2.1	The first two asymmetric embryonic cleavages . . . . .	61
2.2.2	The first spiral cleavage of <i>P. dumerilii</i> . . . . .	63
2.2.3	Spiral cleavages divide the embryo into clonal domains . . . . .	71
2.3	Live-imaging and lineage tracking of <i>P. dumerilii</i> spiral cleavages . . .	74
2.3.1	Clonal domain formation . . . . .	75
2.3.2	Variation of cell cycles during <i>P. dumerilii</i> early cleavages . . .	77
2.4	Cell autonomy of spiral cleavage and determinate development . . . . .	83
2.5	Early polarization of the <i>P. dumerilii</i> embryo . . . . .	89
2.6	Cellular and intracellular dynamics during spiral cleavages . . . . .	91
<b>3</b>	<b>live-imaging of cytoskeleton dynamics during early <i>P. dumerilii</i> spiral cleavage</b>	<b>97</b>
3.1	Chemical dyes fail to label microtubule or actomyosin for live-imaging .	98
3.2	Labeling of cytoskeleton by gene cloning and mRNA injection . . . . .	100
3.2.1	Microtubule . . . . .	100
3.2.2	Actin . . . . .	103
3.2.3	Non-muscle-myosin . . . . .	103
3.3	Sequence optimization increases fluorescent signal of the injected mRNA	105
3.4	Protein synthesis and injection for early labeling of actomyosin . . . . .	114

<b>4</b>	<b>Contribution of actomyosin to <i>P. dumerilii</i> spiral cleavage</b>	<b>119</b>
4.1	Actomyosin distribution analysis in early developing <i>P. dumerilii</i> embryos	120
4.1.1	Asymmetric actomyosin distribution during the first two embryonic cleavages . . . . .	120
4.1.2	Actomyosin labeling by Lifeact during spiral cleavage . . . . .	122
4.2	Actomyosin dynamics during cell division in micromeres and macromeres	125
4.2.1	Distribution of cortical actomyosin during cell division . . . . .	125
4.2.2	Cytosolic actomyosin accumulates at the nuclear envelope before cell division . . . . .	127
4.3	Quantitative analysis of actomyosin dynamics during the first spiral cleavage . . . . .	130
4.4	Mitotic spindle inclination during spiral cleavage . . . . .	135
4.5	Contribution of the cytoskeletal components to the first spiral cleavage	140
4.5.1	The chemical treatments targeting cytoskeletal elements . . . . .	140
4.5.2	Cell division axis is not affected upon microtubule depolymerization	143
4.5.3	Cortical actomyosin is essential for cell deformation and microtubule orientation . . . . .	144
4.5.4	Mitotic spindle angle in the absence of microtubules or cortical actomyosin . . . . .	148
<b>III</b>	<b>Discussion and Conclusions</b>	<b>151</b>
<b>5</b>	<b>Discussion</b>	<b>153</b>
5.1	Visualization of the protein dynamics at early spiralian embryogenesis .	154
5.1.1	Different microscopy approaches for live-imaging of spiral cleavage	155
5.1.2	Optimization of transient fluorescent labeling during spiral cleavage	156
5.2	The cellular processes before and during spiral cleavage . . . . .	162
5.2.1	The first two unequal embryonic cleavages result in four macromeres with different cell sizes and cell fates . . . . .	163
5.2.2	Early lineage tracking reveals symmetry breaking events . . . . .	165
5.2.3	Cellular mechanisms contributing to spiral cleavage . . . . .	168
5.2.4	Body handedness formation and potential physical force triggering spiral cleavage . . . . .	172
5.3	Molecular basis and mechanical force generation of spiralian development	175
5.3.1	Cell fate determination and mechanogenetics of spiralian . . . . .	175
5.3.2	Evolutionary conserved mechanism during left-right symmetry breaking by active cortical actomyosin counter rotation . . . . .	179
5.3.3	Cellular and molecular differences between micromeres and macromeres . . . . .	184

5.3.4	Evolutionary speculations on the effects of cytoskeletal machineries to embryonic patterning . . . . .	187
<b>6</b>	<b>Conclusions, open questions, and future directions</b>	<b>191</b>
6.1	Summary and conclusions . . . . .	191
6.2	Open questions and future directions . . . . .	197
<b>IV</b>	<b>Materials and Methods</b>	<b>203</b>
<b>7</b>	<b>Materials and Methods</b>	<b>205</b>
7.1	Culture . . . . .	205
7.1.1	<i>P. dumerilii</i> animal culturing . . . . .	205
7.1.2	<i>Tetraselmis</i> sp. algae culturing . . . . .	207
7.1.3	Moon cycle and feeding . . . . .	208
7.2	Equipment . . . . .	209
7.3	Reagents and solutions . . . . .	210
7.3.1	Seawater for <i>P. dumerilii</i> culture . . . . .	210
7.3.2	Calcium magnesium free seawater (CMFSW) . . . . .	211
7.3.3	Low melting temperature agarose . . . . .	211
7.3.4	Rhodamine-phalloidin . . . . .	212
7.3.5	DAPI . . . . .	212
7.3.6	Thioglycolate . . . . .	212
7.3.7	Pronase . . . . .	212
7.3.8	anti- $\alpha$ -tubulin antibody . . . . .	213
7.3.9	Goat anti-mouse IgG secondary antibody . . . . .	213
7.3.10	Preparation of the chemical inhibitors . . . . .	213
7.3.11	Protease K . . . . .	215
7.3.12	Zamboni's fixative . . . . .	215
7.3.13	Phosphate buffered saline (PBS) for protein purification . . . . .	216
7.3.14	Phosphate buffered saline (PBS) for <i>P. dumerilii</i> specimen . . . . .	216
7.4	Software . . . . .	217
7.5	SiR-dye preparation and treatment . . . . .	218
7.6	Microinjection and mounting . . . . .	218
7.6.1	Mounting for live-imaging with light sheet fluorescence microscopy	220
7.6.2	Mounting for live-imaging with spinning disk confocal microscopy	220
7.6.3	Markers for live-labeling of the cytosolic components . . . . .	221
7.7	Immunofluorescence . . . . .	222
7.8	Functional studies by exogenous application of the chemical inhibitors .	222
7.9	Measurement of the spindle inclination angle during spiral cleavage . .	223
7.10	Dechoriation and cell dissociation . . . . .	224
7.11	gDNA extraction . . . . .	224

## Contents

7.12 RNA extraction and cDNA synthesis . . . . .	225
7.13 Gene cloning and mRNA synthesis . . . . .	225
7.14 Protein purification . . . . .	227
7.15 Particle velocimetry analysis, PIV . . . . .	228
7.16 Statistics . . . . .	229

## V Appendix 231

### A Appendix 233

A.1 <i>P. dumerilii</i> maintenance under laboratory conditions . . . . .	233
A.2 <i>P. dumerilii</i> culturing and maturation . . . . .	234
A.3 Cytosolic components distribution in the zygote . . . . .	235
A.4 Phylogenetic analysis of <i>P. dumerilii</i> Par proteins . . . . .	236
A.5 The effects of cytoskeletal inhibitors on cellular behaviors . . . . .	237
A.6 Identified gene sequences and the cloning information . . . . .	239
A.6.1 Optimization of the lifeact construct . . . . .	239
A.6.2 Partitioning detective homologs . . . . .	239
A.6.3 Non-muscle-myosin related proteins . . . . .	249
A.6.4 Actin binding protein . . . . .	257
A.6.5 gDNA fragment and guide RNA sequences for CRISPR-Cas9 transgenesis . . . . .	259
A.7 <i>P. dumerilii</i> immunofluorescence protocol . . . . .	262
A.8 Preparation of the TOP10 competent cell for electroporation . . . . .	265
A.9 Gene cloning . . . . .	267
A.10 Protein expression and purification from bacteria . . . . .	274

## VI Bibliography 277

### Bibliography 279

# List of Figures

1.1	Phylogeny of metazoan with the typical cleavage types . . . . .	5
1.2	The annelid fossil record and <i>P. dumerilii</i> morphology . . . . .	24
1.3	The life cycle of <i>P. dumerilii</i> . . . . .	27
1.4	Comparison of CLSM and LSFM imaging techniques . . . . .	31
1.5	Mitotic spindle machinery during cleavage . . . . .	37
1.6	Contractility regulation of the cell cortex . . . . .	39
1.7	The cell processes to model spiral cleavage . . . . .	45
1.8	Cell polarity of <i>Drosophila</i> neuroblast . . . . .	50
2.1	Early cleavages of <i>P. dumerilii</i> . . . . .	59
2.2	The first embryonic cleavage of <i>P. dumerilii</i> . . . . .	62
2.3	The second embryonic cleavage of <i>P. dumerilii</i> . . . . .	63
2.4	The first spiral cleavage (third embryonic cleavage) of <i>P. dumerilii</i> . . .	65
2.5	Mitotic spindle orientation and division angle measurement of the first spiral cleavage . . . . .	68
2.6	Spindle inclination angle analysis of the first spiral cleavage . . . . .	70
2.7	The second spiral cleavage (fourth embryonic cleavage) of <i>P. dumerilii</i> .	72
2.8	The third spiral cleavage (fifth embryonic cleavage) of <i>P. dumerilii</i> . . .	73
2.9	The fourth spiral cleavage (sixth embryonic cleavage) of <i>P. dumerilii</i> .	74
2.10	Spiral cleavage led to clonal domain formation in <i>P. dumerilii</i> . . . . .	77
2.11	Early lineage tracking of <i>P. dumerilii</i> . . . . .	79
2.12	C and D lineages entered cell division prior to A and B lineages . . . . .	82
2.13	Three initial cleavages of intact or partial <i>P. dumerilii</i> embryos in the absence of the eggshell . . . . .	86
2.14	Development of <i>P. dumerilii</i> embryos without eggshell . . . . .	88
2.15	Localization of Par components in the early <i>P. dumerilii</i> embryo . . . . .	90
2.16	Alternating division axes and nuclei migration during spiral cleavages .	94
3.1	SiR-actin was not suitable for labeling F-actin fibers in the living <i>P.</i> <i>dumerilii</i> embryos . . . . .	99
3.2	Early visualization of the cytoskeletal elements during spiral cleavages .	102
3.3	Localization of <i>P. dumerilii</i> non-muscle-myosin components . . . . .	104

## List of Figures

3.4	Optimization of injected mRNA translation with 5'UTR and 3' terminator	107
3.5	Quantitative analysis of the expression of <i>PduPar6</i> under the regulation of different UTR regions . . . . .	109
3.6	Optimization of Lifeact labeling in <i>P. dumerilii</i> during spiral cleavage .	111
3.7	Lifeact distribution in the <i>P. dumerilii</i> zygote . . . . .	113
3.8	Actin labeling in early <i>P. dumerilii</i> embryos by Lifeact protein injection	116
3.9	Durability of the injected Lifeact-mKate2 protein under live-imaging . .	117
4.1	Actomyosin localization in early <i>P. dumerilii</i> embryos . . . . .	122
4.2	Actomyosin distribution during spiral cleavage . . . . .	124
4.3	Actomyosin distribution in the macromeres and micromeres . . . . .	127
4.4	Cytosolic actomyosin dynamics during cell division in living or fixed <i>P. dumerilii</i> embryos . . . . .	129
4.5	Chiral counter-rotational velocity of cortical actomyosin during spiral cleavage . . . . .	134
4.6	The cell long axis dynamics during spiral cleavages . . . . .	137
4.7	Measurement of the cell long axis dynamics between cleavages . . . . .	139
4.8	Cytoskeletal dynamics under chemical inhibitor treatments to the early <i>P. dumerilii</i> embryos . . . . .	147
4.9	Spindle angle measurement of the cytoskeletal element inhibitors treated embryos during the first spiral cleavage . . . . .	150
6.1	Cellular and cytoskeletal mechanisms of the early embryonic cleavages in <i>P. dumerilii</i> . . . . .	196
A.1	<i>P. dumerilii</i> maintenance under laboratory conditions . . . . .	233
A.2	<i>P. dumerilii</i> culturing and maturation . . . . .	234
A.3	Distribution of the cytosolic components in <i>P. dumerilii</i> zygote . . . .	235
A.4	Phylogenetic analysis of the Par proteins . . . . .	236
A.5	The effects of cytoskeletal inhibitors on cellular behaviors . . . . .	237



## List of Tables

2.1 The cell cycles under laboratory incubation condition . . . . .	60
---	----

## List of Equations

4.1 Counter rotational velocity equation . . . . .	132
4.2 Chiral rotational direction equation . . . . .	132



# Abbreviations

<b>CLSM</b>	confocal laser scanning microscopy
<b>CMFSW</b>	calcium magnesium free seawater
<b>DAPI</b>	4,6-diamidino-2-phenylindole
<b>DIC</b>	differential interference contrast
<b>DMSO</b>	dimethyl sulfoxide
<b>dpf</b>	day-post-fertilization
<b>EMTB</b>	ensconsin's N-terminal MT-binding domain
<b>EtOH</b>	ethanol
<b>GFP</b>	green fluorescent protein
<b>H2B</b>	histone 2B
<b>hpf</b>	hour-post-fertilization
<b>hr</b>	hour
<b>IPTG</b>	isopropyl $\beta$ -D-1-thiogalactopyranoside, isopropyl $\beta$ -D-thiogalactoside
<b>LSFM</b>	light sheet fluorescent microscopy
<b>min</b>	minute
<b>mpf</b>	minute-post-fertilization
<b>PFA</b>	paraformaldehyde
<b>Q</b>	macromere quartet, A-D
<b>q</b>	micromere quartet, a-d
<b>ROI</b>	region of interest
<b>SC</b>	spiral cleavage
<b>SD</b>	spiral deformation
<b>sec</b>	second
<b>sGFP</b>	superfolder GFP
<b>SI</b>	spindle inclination
<b>SPIM</b>	selective plane illumination microscopy



# Part I.

## Introduction



# 1. Introduction

## 1.1. Diverse cleavage types in metazoans

All animals with sexual reproduction starts as a zygote, an eukaryotic cell formed by fertilization of two gametes. Although it all begins with a single cell, the adult forms are overwhelmingly diverse. This diversity could be seen much earlier in the life cycle, during embryogenesis. One of the most important advantages to study embryology and put it into a phylogenetic context is that it often shows astonishing similarities between animal groups, which are irreconcilably distinct in adult body plans. Therefore, a rapid growth of new approaches to investigate the evolution of animal morphology has been seen in the latest decades. Evolutionary developmental biology, also known as “Evo-Devo”, is mainly focusing on the comparison of genetic mechanisms during embryogenesis at various phylogenetic levels from microevolutionary (intra-species) to macroevolutionary (across phyla) (Arthur, 2002). In my PhD thesis, I have concentrated on the mechanisms of the first events in development, the embryonic cleavages, to understand the convergence and variety at different levels resulting in certain organismal forms. First, I will introduce the different cleavage types described in metazoans.

## *1. Introduction*

In 1874, Ernst Haeckel defined metazoan as the multicellular animals and protozoa as the single-celled organisms of the animal kingdom (Reynolds & Hülsmann, 2008). With the help of morphological comparison and later molecular phylogenetics, the phylogenetic relationship between animals has been established (Figure 1.1). Although the adult forms are distinct, when considering early embryogenesis, each of the animal clades has a representative early cleavage pattern generating blastomeres in a given orientation.

In holoblastic eggs, the first embryonic cleavage follows the animal-vegetal axis. The second cleavage as well, but perpendicular to the first one, resulting in the four blastomeres localizing in the same plane. The third embryonic cleavage plays a critical role in the spatial arrangement of the blastomeres by different cleavage plane in each organism. The four major holoblastic cleavage types, bilateral, radial, rotational, and spiral cleavage, and the resulting embryonic patterns are described below. Bilateral and radial cleavage are two of the representative cleavage types in Deuterostomia while rotational and spiral cleavage are typical for Protostomia (Figure 1.1).



## 1.1. Diverse cleavage types in metazoans

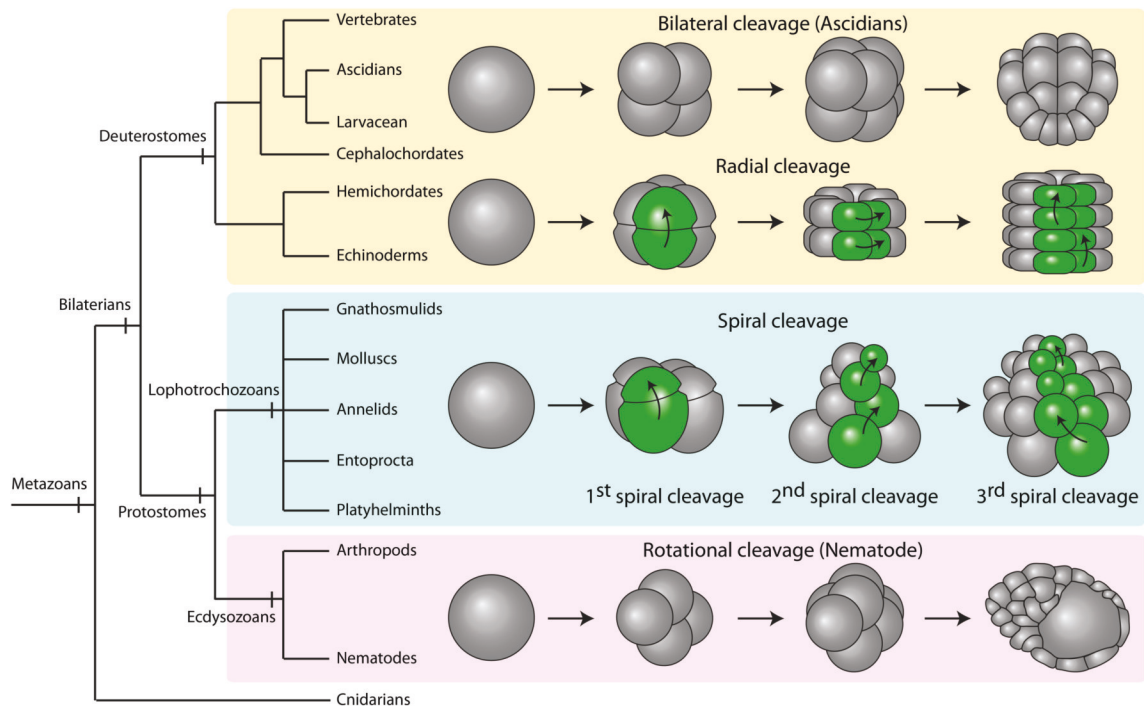


**Figure 1.1.: Phylogeny of metazoan with the typical cleavage types.** The phylogenetic tree is according to the consensus of 18S rRNA sequences (Adoutte et al., 1999). The four typical cleavage types are illustrated according to the animal groups (the colored-boxes at background). One of the four lineages are indicated with green color in radial cleavage and spiral cleavage, demonstrating the division angle alternation in each cleavage and the formation of clonal domains. The arrows indicated the cleavage planes.

### 1.1.1. Bilateral cleavage

Bilateral cleavage is the major type for ascidians. The first embryonic cleavage defines the left and right half of the embryo. The following cleavages use this axis (the animal axis) to produce an embryo with two mirror-imaged halves. Therefore, the embryo eventually gets a midline with clear left-right bilateral symmetry.

## 1. Introduction

### 1.1.2. Radial cleavage

Radial cleavage is the major cleavage type for the deuterostomes (e.g., vertebrates and echinoderms). The first two embryonic cleavages result in the four blastomeres orientated in the same plane. These blastomeres are indeterminate, so all have the potential to develop into the whole organism when dissociated (Gilbert, 2000; Lawrence & Levine, 2006). The third embryonic cleavage occurs with the cleavage plane perpendicular to animal-vegetal axis, and the mitotic spindles parallel to this axis, resulting in two layers of blastomeres on top of each other and aligned along the animal-vegetal axis (Green & Batterman, 2017). The set-up of the cleavage plane leads the axes of the following cleavage, which are either parallel (the even cleavages), or perpendicular (the odd cleavages), to animal-vegetal axis. Eventually, a cylinder-shaped, radial symmetric blastula is formed.

### 1.1.3. Rotational cleavage

Rotational cleavage is the major cleavage type in nematodes, especially well studied in the roundworm *Caenorhabditis elegans*. In this cleavage, there is no standard division axis for all the blastomeres in one cleavage. The first cleavage occurs along the anterior-posterior axis, resulting in two daughter cells in this direction. In the second cleavage, however, one daughter cell divides meridionally while the other one divides equatorially (Rose & Gönczy, 2014).

#### 1.1.4. **Spiral cleavage**

Spiral cleavage is the major cleavage type in lophotrochozoans, also known as spiralian. The first two embryonic cleavages are rather similar to those in radial cleavages. Four blastomeres are located in a plane perpendicular to animal-vegetal axis. However, the third embryonic cleavage occurs with an inclined division angle instead of parallel to the animal-vegetal axis. Therefore, the upper blastomere tier, the micromeres, rotates either clockwise or counterclockwise to the bottom tier, the macromeres, when viewed from the animal pole. From this cleavage, the division angle is no longer a multiple of  $90^\circ$  to the animal-vegetal axis, but it uses the coordinates set by the first spiral cleavage. The blastomeres always rotate between tier. This feature eventually creates a blastula with a spiral-looking arrangement of the blastomeres (Henry et al., 2006; Goulding, 2009). Although spiral cleavage is not the only cleavage type in spiralian, it has been suggested to represent the ancestral mode of development within this clade, because of its broad occurrence (see Section 1.2.2) (Laumer et al., 2019).

Another characteristic of spiral cleavage concerns the cell potency. Unlike the deuterostomes, which are mostly indeterminate developers, determinate development is present in many protostomes, including organisms with rotational cleavage and spiral cleavage (Valentine, 1997). The cell fate is determined early in embryogenesis, meaning that each blastomere has the potential to only develop a part of the organism rather than a complete embryo. Therefore, tracing the cell lineage and investigating the molecular mechanisms are important approaches to understand how the cell fate is determined and how this can affect or be affected by the cleavage pattern during early embryogenesis.

## 1. Introduction

### 1.2. Evo-Devo of spiral cleavage

In this section, the focus is mainly on spiral cleavage. As a shared developmental feature of many animal clades, the convergence and divergence of the mechanisms are compared to reveal the critical steps making spiral cleavage a unique embryogenic type.

#### 1.2.1. Evolutionary relationships of spiralian

Lophotrochozoa is one of the biggest animal clades which contain over one-third of all the animal phyla (Halanych et al., 1995; Aguinaldo et al., 1997; Dunn et al., 2008; Telford & Littlewood, 2009; Laumer et al., 2015). The adult forms of lophotrochozoans are very distinct and they were not considering related. Embryologists discovered however a great similarity in the early embryogenic cleavages, the spiral cleavage, and cellular arrangement between many lophotrochozoan phyla, e.g., polyclad flatworms, nemertean, gnathosmulids, entoprocta, molluscs, and annelids (E. B. Wilson, 1892; Lillie, 1895; Conklin, 1897; Child, 1900). Not all lophotrochozoans exhibit spiral cleavage though. Rotifers, Gastrotricha, Bryozoans, Phoronida, and Brachiopods are reported without the typical spiral arrangement of the blastomeres (Hejnol, 2010). However, the cell fate is set early in development in these organisms and cell fate mapping show similar tissue destination (Vellutini et al., 2017). These are other characteristics of the spiralian development. Still spiral cleavage is thought to represent the ancestral trait of Spiralia, because the spiral arrangement of the blastomeres exist in Gnathifera, Lophotrochozoa, and Rousphozoa, the three main branches of Spiralia as defined by Laumer et al. (2015). A loss or modification of this trait has likely

## 1.2. *Evo-Devo of spiral cleavage*

occurred within the bryozoans, brachiopods, gastrotrichs and rotifers, which don't show any clear trace of spiral cleavage, and within the gnathostomulids (R. J. Riedl, 1969), phoronids (Pennerstorfer & Scholtz, 2012), and entoprocts (Merkel et al., 2012), which exhibit spiral-like characters (Vellutini et al., 2017).

As mentioned before, spiralian development is determinant and the cell fates are set early in development, meaning that a blastomere can only develop into part of an organism. In order to understand the cell fates and the relations of each cell between organisms, the research topic, lineage study, which traces the cells of an embryo during gastrulation and morphogenesis has been active since the end of the 19<sup>th</sup> century. Thanks to the stereotypic cell divisions and similarity in the cell placement, individual blastomere can be traced and compared between spiralian taxa. A surprising conservation of the cell fate of the spiral-cleaving embryos was discovered this way (Guralnick & Lindberg, 2001).

Previous cell lineage studies were based on bright field microscopy and careful observations and tracking of each cleavage. The cell density or lack of transparency set the limit as to how long the cells could be traced. Modern studies have combined injection of a fluorescent dye or genetic material, e.g., mRNA or protein, and fluorescent microscopy to get more details and achieve precise tracking of the lineages for longer (Lyons and Henry, 2014). The details of the application of different fluorescent microscopies are described in Section 1.4. Through careful tracking of the cell lineages, the conserved cell orientation and cell fate specification has been discovered in those animals with typical spiral cleavage.

## 1. Introduction

### 1.2.2. Rosetta stone of spiral cleavage

Two meridional divisions result in the formation of the four blastomeres, A, B, C, and D, which are placed in the plane perpendicular to the animal-vegetal axis. These cells can be equal or unequal in cell size (see Section 1.2.3) (Lambert, 2010). The third cleavage, which is the first spiral cleavage, is asymmetric, creating smaller micromeres at the animal pole (in polyclads, gnathosmulids, entoprocta, molluscs, and annelids) with either clockwise or counterclockwise rotation against the macromeres (Hejnol, 2010). The macromeres segregate micromeres toward the animal pole, and both micromeres and macromeres switch the division axis (clockwise versus counterclockwise) between each cleavage resulting in a spiral looking blastomere displacement when viewing from the animal pole (E. B. Wilson, 1892; Costello & Henley, 1976; Henry & Martindale, 1999; Hejnol, 2010; Lambert, 2010). The descendants of each of the four blastomeres represents one quadrant of the embryo, because of the synchronous cleavage timing and relative symmetry of the A, B, C, and D lineages (also see Figure 2.10).

### 1.2.3. Dorsal-ventral axis determination mechanisms

In spiralian development, the first embryonic axis, animal-vegetal axis, is determined as early as during oogenesis. The second axis, dorsal-ventral axis, is determined by the specification of the D quadrant (Goulding, 2009; Henry & Jonathan, 2015; Lyons et al., 2017). The D lineage gives rise to the dorsal and posterior structures of spiralian (Raven, 1951). There are two mechanisms driving the specification of the D quadrant and the determination of the dorsal-ventral axis. According to the cell size difference of the 4-cell stage embryo, the spiralian can be categorized into two groups, equal or

## 1.2. *Evo-Devo of spiral cleavage*

unequal cleaver. Each group has a unique way of axis determination.

In the equal cleavers, the first two embryonic cleavages are symmetric, resulting in four macromeres of comparable cell size. Because of the symmetry, D quadrant specification is not determined at 4-cell stage, but during the fifth embryonic cleavage (Freeman & Lundelius, 1992), e.g., at 24-cell stage in the gastropods (van den Biggelaar & Haszprunar, 1996). At this stage, the macromere with the greatest cell contact to the neighbor micromeres is determined to be the D lineage (Freeman & Lundelius, 1992; Lambert & Nagy, 2003). This serves as the inductive interaction for D quadrant specification, and the overlaying micromeres receive the signals from the D macromere to determine their cell fates. The MAP kinase pathway mediates this signaling in some spiralian (Lambert & Nagy, 2003). Thus, for those species which undergo two equal cleavages to obtain four blastomeres, it is difficult to tell the cell lineages at 4-cell stage.

In the unequal cleavers, the macromeres have different sizes at 4-cell stage due to the first two asymmetric cell divisions. The D macromere is typically the largest of the four (Freeman & Lundelius, 1992; Lambert & Nagy, 2003). Therefore, the specification of the D macromere occurs during the initial two unequal cleavages. This is likely through a differential distribution of yet unknown key factors into the D macromere (Render, 1989). Therefore, the D quadrant is specified very early in development.

The unequal cleavage can be achieved by two mechanisms. One mechanism involves asymmetric localization of the mitotic spindles thereby off-centering the nuclear positioning (also see Figure 2.2). The astral mitotic spindles, which attach to the cell membrane and to the centrosome, are much shorter on one side of the

## 1. *Introduction*

cell than on the other side. Therefore, the DNA is not positioned at the center of the zygote, leading to the cytokinetic ring being off-centered and to the asymmetric cleavage (McCarthy & Goldstein, 2006). This results in the unequal cytokinesis, leading to a larger and a smaller blastomere. When the asymmetric cytokinesis occurs in both the first and second embryonic cleavage, the biggest blastomere is assigned as the D quadrant. In this scheme, the D lineage is specified and the dorsal-ventral axis is determined as early as in the 4-cell stage. Therefore, it indicates that the symmetry breaking events occur earlier in spiralian with unequal cleavages, and the equal cleavages may be the ancestral mechanism in spiralian development.

The second mechanism does not include the asymmetric spindle positioning, but involves the production of a membrane bound cytoplasmic protrusion, named a polar lobe, during the second embryonic cleavage (Freeman & Lundelius, 1992). The polar lobe forms at the vegetal pole and becomes part of the D macromere, making this cell the biggest of the four and resulting in its specification (Boyer & Jonathan, 1998; Lambert & Nagy, 2003). This mechanism is described mainly in molluscs (Conrad et al., 1990; Henry et al., 2006).

For both equal and unequal cleavers, the D quadrant is already specified at the fifth embryonic cleavage. After carefully tracking the D cell lineage, it was discovered that the fate of the D quadrant is surprisingly conserved. One of the typical examples is the 4d mesentoblast, the mesoderm precursor (Lambert, 2008). Therefore, although nowadays spiral cleavage is understood as a complex of developmental characters, conservation in the underlying mechanisms and fate maps has been discovered by cell lineage tracing and evo-devo studies (Costello & Henley, 1976; Henry & Martindale, 1999; Hejnol, 2010; Lambert, 2010).



## 1.2. Evo-Devo of spiral cleavage

Through comparison of D quadrant specification between equal and unequal cleavers, it also showed that the overall differentiation of the blastomere starts earlier in the unequal cleavers (e.g., compare D specification at 24-cell stage in gastropods versus at 4-cell stage in annelids), indicating that these spiralian develop faster than the equal cleavers. This is also supported by comparing the development speed of these organisms. It takes around 12 hours for the equal cleaving gastropod *L. stagnalis* to enter the sixth embryonic cleavage, but only around 3.5 hours for the unequal cleaving annelid *Platynereis dumerilii* to reach the same stage (Kuroda, 2015) (also see Table 2.1 and Figure 2.11). The early differentiation of the blastomeres and the acceleration of development in the unequal cleavers are now suggested as derived traits to increase the survival rate from the predators during embryogenesis (Boyer & Jonathan, 1998; Dorresteijn & Westheide, 2013).

### 1.2.4. Cellular mechanisms of the first spiral cleavage

Several key cellular events have been observed during the third embryonic cleavage (first spiral cleavage). During metaphase of the first spiral cleavage, typical spiral deformation (SD) of the cell membrane of the macromeres is seen in many spiralian. The cells twist/incline toward the direction of the expected final positions of the micromeres prior to the cytokinetic ring formation. This is especially visible from the animal pole. Together with SD, the mitotic spindles do not orient parallel to the animal-vegetal axis, but incline toward the division direction. This phenomenon is called spindle inclination (SI). SD and SI typically result in the final positioning of the micromere layer with clockwise or counterclockwise rotation compared to the macromere layer (Kuroda et al., 2009).

## 1. Introduction

Not all spiral cleavage patterns result from SD and SI. The mollusc (snail) *Lymnaea stagnalis* has both a dextral and sinistral cleaving strain. The majority of this species use a clockwise rotation of the micromeres during the first spiral cleavage and both SD and SI was detected during this cell cycle. However, in the sinistral cleaving strain with a counterclockwise rotation of the micromeres in the first spiral cleavage, the cell division starts without SD and SI. The mitotic spindles point toward the animal-vegetal axis until the formation of the cytokinetic ring. The micromere rotation is detected during cytokinesis while the cytokinetic ring is closing. This results in a twist of the whole micromere layer toward the final cell position (Kuroda, 2015). Thus, *L. stagnalis* uses different mechanisms for the dextral and sinistral cleaving strains during the first spiral cleavage. Interestingly, another snail *Physa acuta*, which develops only by sinistral cleavage during the first spiral cleavage, follows a mechanism similar to the dextral cleaving *L. stagnalis*. During first spiral cleavage, *P. acuta* uses SD and SI prior to cytokinesis to complete the first spiral cleavage. This shows that the dextral and sinistral cleaving organisms can use the same cellular mechanisms to complete the first spiral cleavage. Moreover, chirality can be reversed by applying external physical force to the cleaving 4-cell *L. stagnalis* (Shibazaki et al., 2004). In other words, SD/SI are not the key components driving chirality, but there are other ways to generate physical force to the macromeres resulting in the proper positioning of the micromeres.

### 1.2.5. Spiral cleavage, a left-right symmetry breaking event

The third animal axis, the left-right axis, is as important as the dorsal-ventral and anterior-posterior axes, during animal development. In the nematode *C. elegans*,

## 1.2. Evo-Devo of spiral cleavage

this event happens with the divisions of the ABa and ABp blastomeres during the third embryonic cleavage. During cytokinesis, both ABa and ABp cells show spindle inclination leading to precise positioning of the daughter blastomeres, ABar, ABal, ABpr, and ABpl, and to a break in the body symmetry (Naganathan et al., 2014). In spiralian, the embryonic chirality can lead to a break in left-right symmetry. A clear example of this can be found in gastropod molluscs (snails). As mentioned above, *L. stagnalis* contains both dextral and sinistral cleaving individuals during the first spiral cleavage. This results not only in different embryonic blastomere orientation, but also in differences in the adult body plan. The dextral and sinistral snails have mirror-imaged left-right body axis, both in the embryo and in the adult. In the adult, this is easily seen by a change in the coiling of the shell. In the dextral strain, the shell rotates in a counterclockwise orientation, but in the sinistral strain, the shell rotates clockwise. This indicates that a difference in the embryonic chirality generated during the first spiral cleavage is sufficient to set up the left-right axis of the organisms (Kuroda et al., 2009).

A change in the embryonic chirality of *L. stagnalis* changes the position of the cells within the embryo. This is reflected in the overall gene expression pattern. For example, *nodal* and *pitx*, which are differentially expressed genes along the left-right body axis in vertebrates (Levin, 2005), are detected in a mirrored position after chirality manipulation (Grande & Patel, 2009; Kuroda, 2014). Overall, this indicates that the first spiral cleavage is important in both body plan determination, and thus influence tissue orientation and animal morphology, in spiralian. However, the physical machinery driving the “TWIST” of the macromeres remain unclear.

## 1. Introduction

### 1.2.6. Molecular mechanisms involved in spiralian development

From the previous sections, it is clear that spiral cleavage and the spiralian development consist of a series of complex actions. Various molecular mechanisms are involved in these processes, some of which have been described with regard to the cell and tissue fate determination and to the molecules guiding the cellular and physical mechanisms during spiral cleavage (Henry & Martindale, 1999; Hejnol, 2010; Lambert, 2010).

#### Cell fate determination

Although the mechanisms underlying axes determination during the first spiral cleavages are not clear, the genetical mechanisms for later development are strikingly conserved among spiralian. The signaling molecules and transcription factors activated during cell differentiation are relatively well-studied. For example, MAPK is activated in the 3D lineage and functions as an organizer in many spiralian (Lambert & Nagy, 2001, 2003; Koop et al., 2007; Henry & Perry, 2008; Vellutini et al., 2017).

Developmental genes expressed in different germ layers are also known in the spiralian development. Here, high conservation in expression is seen for developmental genes expressed in specific tissue and cell types, both within spiralian and compared to ecdysozoans and vertebrates. The neuroectoderm and central nervous system is one of the most extensively described tissues at the molecular level in spiralian for its relevance in the understanding of the evolution of the nervous system (Arendt et al., 2002; Denes et al., 2007; Lauri et al., 2016; Vergara et al., 2017; Handberg-Thorsager et al., 2018). The expression profile of transcription factors such as the *nk*, *pax* and *hox* genes have been described in various spiralian organisms (Denes et al., 2007; Marlow et

## 1.2. Evo-Devo of spiral cleavage

al., 2014). For the mesoderm, markers such as *twist*, *foxc* and *foxf* have been described in various spiralian (Häcker et al., 1995; Gorfinkiel et al., 1999; Thaëron et al., 2000; Zaffran et al., 2001; Nederbragt et al., 2002; Pérez Sánchez et al., 2002; de Rosa et al., 2005; Mazet et al., 2006; Dill et al., 2007; Shimeld et al., 2010; Pfeifer et al., 2013, 2014; Passamaneck et al., 2015; Perry et al., 2015; Vellutini et al., 2017). Also, gut tissues have been described with gene expression profiles for the genes *evx*, *cdx*, *otx*, *gsc* (Martín-Durán et al., 2016). The spiralian larva is segmented and the genetic network involved seems to be conserved with that of arthropods and vertebrates. This way the genes *engrailed*, *pax*, *wnt1*, *hedgehog*, *gbx*, *hox* and *otx* are expressed in a segmented pattern in spiralian (Vellutini & Hejnol, 2016). These studies suggest that the molecular mechanisms for gastrulation, morphogenesis and cell differentiation may be conserved in spiralian, resulting in the lophophore or trochophore larva.

The activation of Wnt signaling pathway is a conserved mechanism for cell fate determination during embryogenesis (Martin & Kimelman, 2009; Steinhart & Angers, 2018; Theka et al., 2019). Wnt induced  $\beta$ -catenin accumulation in the nuclei mediates the activation of the downstream gene transcription, e.g., transcription factors, (MacDonald et al., 2009; Lien & Fuchs, 2014; Liu et al., 2016) of which eventually leads to cell differentiation. It has been shown that transition of  $\beta$ -catenin from the cell membrane to the nuclei controls development in various organisms at various levels. It participates in organizer specification in vertebrates (S. Schneider et al., 1996; Larabell et al., 1997), segmentation of arthropods (Orsulic & Peifer, 1996), endomesoderm determination in ascidian (Imai et al., 2000, 2004), and anterior-posterior cell fate specification in early *C. elegans* embryogenesis (Rocheleau et al., 1999). In planarians, the nuclear version of  $\beta$ -catenin controls the formation of the anterior-posterior axis by specifying posterior characters (Iglesias et al., 2008; Petersen & Reddien,

## 1. Introduction

2008). Therefore, Wnt signaling pathway becomes a potential candidate for cell fate determination during the early spiralian development. In the spiralian annelid *Platynereis dumerilii*, early  $\beta$ -catenin localization was monitored by immunofluorescence with a  $\beta$ -catenin antibody against a *Xenopus*  $\beta$ -catenin peptide (S. Schneider et al., 1996; S. Q. Schneider & Bowerman, 2007). They described a binary activation of the Wnt signaling pathway through a differential nuclear localization of  $\beta$ -catenin as early as at 8-cell stage. Most of the macromeres have larger proportion of nuclear  $\beta$ -catenin comparing to the micromeres, suggesting that there is an activation difference of Wnt signaling between micromeres and macromeres. Moreover,  $\beta$ -catenin nuclear localization is always restricted to the vegetal daughter cells following an animal/vegetal oriented cell division, throughout all the four spiral cleavages. The binary effect serves as a sign of Wnt dependent versus Wnt independent cell fate determination in each of the two daughter cells in each lineage, and may explain the determinant development of spirilians (Costello, 1945; S. Q. Schneider & Bowerman, 2007). It also indicates that the molecular control of the chirality occurs before the first spiral cleavage, since the blastomere behavior is already distinct after that. Interesting, the same nuclear  $\beta$ -catenin segregation pattern is described in nematodes and ascidians (Lin et al., 1998; Hudson et al., 2013), so it seems to be a common mechanism in animals with determinant development.

## Cell polarity

Early cell polarity and division axis determination is mainly studied in the ecdysozoa. In the nematode *C. elegans*, the anterior-posterior polarity is established as early as in the zygote. After fertilization, the microtubule linked to sperm DNA and the cell

## 1.2. Evo-Devo of spiral cleavage

cortex breaks the symmetry of the egg, recruiting Par2 to the posterior cell cortex. Because of the antagonistic behavior of the Par proteins, eventually Par3 and Par6 localize at the anterior, while Par1 and Par2 localize at posterior of the zygote. Pars also influence the distribution of cortical actomyosin (toward anterior) and cytosolic microtubule (anterior-posterior orientation). The polarity of Pars decides the cleavage plane, since the boundary of these proteins forms the cytokinetic ring. This results in the first asymmetric cleavage of the *C. elegans* embryo along the anterior-posterior axis (Nance, 2005; Arata et al., 2000). The distribution of Pars continues to skew the mitotic spindles during the rotational cleavage, positioning each blastomere correctly (Rose & Gönczy, 2014). Early Par polarity is also detected in fly ectoderm (Sun et al., 2001; Hutterer et al., 2004; Bayraktar et al., 2006) and in the ctenophore *Mnemiopsis leidyi* (Salinas-Saavedra & Martindale, 2019). Although the localization of M/Par1 is not clear, M/Par6 does seem to localize asymmetrically until 2-cell stage in the cell contact free area. Then it looks like it's in the entire cortex is labeled until gastrulation, where M/Par6 localizes to the apical cortex of the ectoderm in *M. leidyi* (Salinas-Saavedra et al., 2018). Interestingly, *par* mRNA is detected in transcriptomic data from the oocyte and zygote of the spiral cleaving annelid *P. dumerilii*, but the protein localization is not known (Nakama et al., 2017). Thus, whether Par proteins are critical for polarity set up and/or critical for chirality during spiral cleavage remains unknown.

### Chirality determining molecules

The machinery of spiral cleavage is not well understood, but pioneer studies in molluscs (snails) give clues to what may control the chirality. *LsDia* is a formin-related protein,

## 1. Introduction

Diaphanous, detected in *L. stagnalis* as early as in the zygote (Kuroda et al., 2016). According to the study on different strains (dextral or sinistral), they found that *LsDia1* is critical for spiral deformation (SD) and spindle inclination (SI), which result in the dextral orientation of the micromeres. The sinistral strain, which has a functional *LsDia2* but lacks a functional *LsDia1*, performs micromere rotation leading to counterclockwise rotation of the micromeres (Kuroda et al., 2016). Moreover, in the snails *Physa acuta* and *Indoplanorbis exustus*, only one Diaphanous is identified, which is homologous to *LsDia2*. These species present solely sinistral strains, indicating that *LsDia1* may be critical for a dextral displacement of the micromeres (Kuroda et al., 2016; Abe & Kuroda, 2019).

By investigation of *diaphanous* mRNA segregation during early development, Kuroda et al. (2016) has found that both *Lsdia1* and *Lsdia2* are evenly distributed in the zygote, and no specific localization of them was detected before or during spiral cleavage. Both transcripts are dramatically down-regulated after the first few cleavages. Thus, if *diaphanous* plays a critical role in spiral cleavage, it must take place very early and should influence all the blastomeres since it is evenly distributed, at the mRNA level at least. A more recent study by Davison et al. (2016) reached a controversial conclusion about the expression pattern and function of *diaphanous*. They found that *diaphanous* is largely segregated into one of the four macromeres and that this may be important in symmetry breaking (Davison et al., 2016). Due to the divergent observation and conclusion of the two research articles, it is hard to conclude which are the molecular mechanisms driving spiral cleavage. They do provide a hint to that the left-right symmetry breaking and chirality determination may be controlled by cytoskeletal components and their dynamics during early embryogenesis.



### 1.2.7. First spiral cleavage, key of spiral looking embryo

Summarizing what we know about some of the most common metazoan developmental programs, one extreme contains the indeterminate developers following, e.g., radial cleavage whereas the other extreme contains the determinate developers following, e.g., spiral cleavage. The first two embryonic cleavages of the two cleavage types are very similar, both resulting in the four blastomeres in the same plane. In radial cleavers, the cells keep their potency so all of the four blastomeres have the potential to become clones of the embryo. This is not the case for spiral cleavers. Here, the fate of each blastomere is specified earlier than the third cleavage by a differential segregation or regulation of molecules and the cells can only develop into specific organs or cell types (Costello, 1945).

The major cause of the morphological differences between the embryos of the spiral and radial cleavers occurs at the third embryonic cleavage. SD/SI and blastomere rotation are absent during the third embryonic division in radial cleavage. Therefore, instead of clockwise or counterclockwise rotation of the cell layer, the two tiers of blastomeres line up along the animal-vegetal axis, forming a cube of 8 cells, in radial cleavage (Jeffery, 1992). This division axis serves as a compass for later cleavages, as in spiral cleavage. Both in spiral and radial cleavage, the following cleavage plane is perpendicular to the previous one. However, due to the variation in the third embryonic cleavage, spiral cleavage results in the 45° rotation of the cleavage plane according to animal-vegetal axis, whereas the plane is parallel or perpendicular to this axis in radial cleavage. Therefore, the outcome is eventually a spiral-looking embryo or a cylinder-shaped embryo for respectively spiral or radial cleavers (Figure 1.1). These observations indicate that the first spiral cleavage is the critical step to form the

## 1. Introduction

unique body plan of the spiralian embryos. Thus, elucidating the cellular, molecular, and physical mechanisms setting up this compass is crucial for understanding what causes various embryo forms in evolution.

### 1.3. *Platynereis dumerilii*: a model organism for studying spiral cleavage

Annelids have an interesting position within the metazoan phylogenetic tree. They belong to the lophotrochozoan clade, which contains close to half of the animal phyla (Laumer et al., 2015) and which share a common developmental program, the spiral cleavage. Annelids have a fossil record, which date them back to the Cambrian period and with an adult body plan, which is very similar to nowadays polychaete annelids (Parry & Caron, 2019) suggesting that morphologically they have changed little (Figure 1.2 A,B).

The marine polychaete annelid *Platynereis dumerilii* (Figure 1.2 C) has emerged as a spiralian model organism for embryology at multiple developmental stages and levels and in an evolutionary context (Tessmar-Raible & Arendt, 2003; Raible & Tessmar-Raible, 2014). Research topics covered by laboratories working with *P. dumerilii* includes the gene regulatory networks during early development (Backfisch et al., 2014; Zantke et al., 2014; Chou et al., 2016, 2018), the mechanisms during spiral cleavage (Nakama et al., 2017), cell-lineage tracing and the molecular signature during tissue and cell type specification (Özpolat et al., 2017; Vopalensky et al., 2019), nervous system evolution (Arendt et al., 2004; Handberg-Thorsager et al.,

### 1.3. *Platynereis dumerilii*: a model organism for studying spiral cleavage

2018), neuronal connectomes and behavioral studies (Tosches et al., 2014; Shahidi et al., 2015; Williams & Jékely, 2016; Ayers et al., 2018), molecular control of circadian and lunar rhythm (Zantke et al., 2013; Arboleda et al., 2019; Schenk et al., 2019), and gene regulation of body segmentation and stem cell biology and mechanisms of regeneration (Hofmann, 1975; Prud'homme et al., 2003; Dray et al., 2010; Pfeifer et al., 2012; Gazave et al., 2013; Grimm et al., 2016). *P. dumerilii* has been kept under laboratory conditions since 1953 with commercial food, sea water, artificial day/night and moon light cycle, and temperature control, even far away from the sea. This way its life cycle was successfully closed in the laboratory. In addition, several molecular tools important for developmental studies have been applied to *P. dumerilii*, making it one of the most successful and well-known spiralian model organisms in the field (Zantke et al., 2014).

## 1. Introduction



**Figure 1.2.: The annelid fossil record and *P. dumerilii* morphology.** (A, B) The fossil record of *Canadia spinosa* with biramous parapodia and fascicles of flattened chaetae from dorsal (A) or lateral (B) view. The images were adapted from Parry and Caron (2019). (C, D) The images were adapted from A. H. Fischer et al. (2010). The fully-grown immature *P. dumerilii* (C) and the matured worms (D) showed morphological differences. The immature worm is more transparent with obvious gut visible within its body. The matured male is with red color and the female is with yellow color. Both male and female matured worms have bigger adult eyes (ae). pp: parapodia. Scale bar: 1mm.

### 1.3.1. Life cycle of *Platynereis dumerilii*

*P. dumerilii* is a prototypic spiralian with spiral cleavage. The complete life cycle of *P. dumerilii* contains biphasic life style, divided into a pelagic and benthic phase

### 1.3. *Platynereis dumerilii*: a model organism for studying spiral cleavage

(A. Fischer & Dorresteyn, 2004). The fertilized egg undergoes two unequal divisions, resulting in the four macromeres with various sizes and allowing for an early recognition of the blastomere identity. The early lineage tracing of *P. dumerilii* embryogenesis was done with bright field microscopes (Ackermann et al., 2005) and allowed the construction of a cell lineage tree up to 64 blastomeres. These studies also showed that the first spiral cleavage in *P. dumerilii* is consistently in dextral orientation (Lyons & Henry, 2015). Later dye injections into the early blastomeres revealed the cell fates of the blastomeres in the larva (Özpolat et al., 2017).

A 3-segmented, round-shaped trochophore larva develops after one day of development with a simple brain and a pair of eyes, which are directly connected to the ciliary band. The larva is positive phototactic and swims toward light. Locomotion depends solely on ciliary movements at this stage (Figure 1.3). At 3 days of development, the muscles of the nectochaete larva have differentiated and locomotion is a combination of ciliary and muscle movements. The larva starts to elongate and the number of segments grows, becoming negatively phototactic and seeking down to the bottom of the sea. Next, the larva undergoes the first metamorphosis, the cephalic metamorphosis, where the first body segment transforms into head structures. The juvenile worm has a fully developed gut at this point and starts to eat. When the worm reaches the bottom of the sea, it builds a tube, which offers protection from predators and where it keeps growing over the next months, by adding segments to a posterior growth zone (Figure 1.3).

Starting from 3-month-old, the worm is capable of maturation. Sexual metamorphosis is induced by the moon. In *P. dumerilii*, it happens a few days after the new moon. After maturation, the morphology of the worms become distinct form

## *1. Introduction*

the juveniles. And the male and female worms can be distinguished by morphology at this point (Andreatta et al., 2019). Both the male and female are shorter than the immature worms. The male is white in the anterior and red in posterior, and the female is with yellow body color, which are distinct from the transparency of the juveniles (Rebscher, 2014) (Figure 1.2 D, 1.3). The matured worms swim to the water surface and spawn here. Fertilization is external and depending on the size of the female, 300-500 eggs can be released from each female. Both the male and female worms die after spawning (or within 24 hours after maturation), and the life cycle is then complete.



### 1.3. *Platynereis dumerilii*: a model organism for studying spiral cleavage

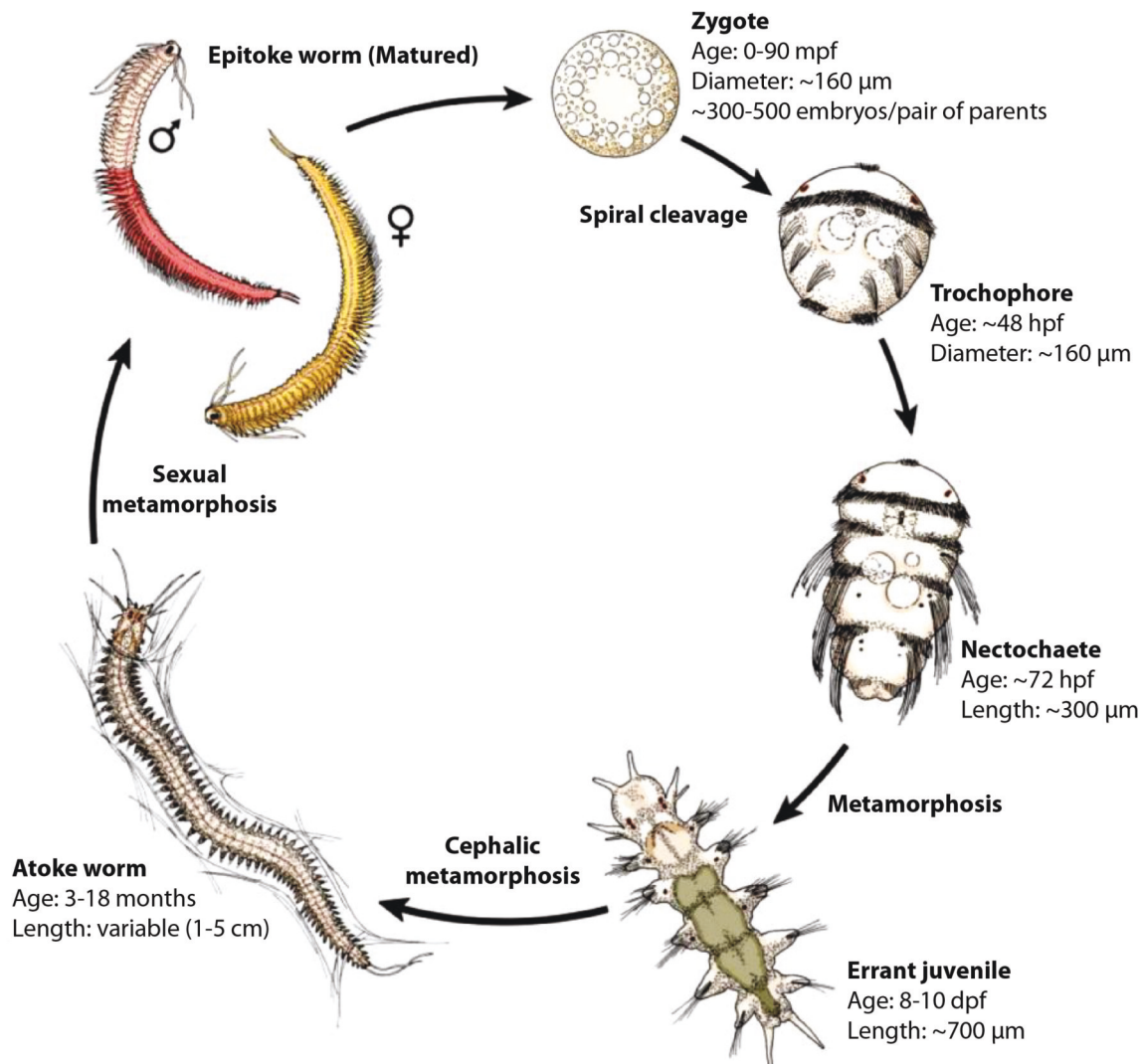


**Figure 1.3.: The life cycle of *P. dumerilii*.** The illustration was adapted from Hauenschild and Fischer (1969). The transparent zygotes with diameter of 160 µm contain nutritional vesicles and oil droplets and undergo the first embryonic division at around 90 mpf. Spiral cleavage occurs from the third embryonic cleavage leading to the blastula. The three-segmented trochophores freely swim at 24-48 hpf with similar larvae size as the zygote. The atoke worm contains around 60 segments dwelling in the self-constructed tubes. The sexual maturation occurs depending on the moon cycle. The matured worms have very distinct morphology and swimming behavior from the atoke worms. The females are yellow and the males are white in the anterior and red in the posterior. Each pair of the matured worm can lay around 300 eggs and all are fertilized simultaneously.

## 1. Introduction

### 1.3.2. Available research tools for *Platynereis dumerilii* studies

The described maturation and spawning mechanism of *P. dumerilii* is of great advantage when used for embryogenesis studies. The spawning of the mature worms can be controlled and the exact fertilization time noted. From each pair of mature worms, more than 300 simultaneously fertilized eggs can be collected. The following cleavages and development are highly synchronized between the embryos making it easy to capture each cell cycle as well as the phases of each cleavage. The size of the *P. dumerilii* embryo, 160-200 µm in diameter, fits perfectly in standard microscopes. The embryos are extremely transparent and thus suitable for both bright-field and fluorescent imaging. The fast cleaving speed is also an advantage for long-term live-imaging. As an example, the whole spiral cleavage can be monitored within 5 hpf at 18 °C. Therefore, it decreases not only the amount of imaging raw data, but also lowers the risk of photo-bleaching and -toxicity of the embryos by the laser.

Apart from the biological advantages, the available genetic tools for *P. dumerilii* are increasing. First, protocols for detecting gene or protein expression patterns were established (whole-mount *in situ* hybridization and immunohistochemistry (e.g., Jékely and Arendt (2007); Marlow et al. (2014)) along with transcriptomic (Conzelmann et al., 2013; Chou et al., 2018) and genomic (unpublished; access kindly provided by Dr. Arendt, EMBL, Germany) databases becoming available. Recently, the transcriptomes of the whole embryo in different stages, or single cell resolution profile of early cleavages are available, making it much easier to investigate a certain set of regulative pathways in a specific blastomere or in different stages in *P. dumerilii* (Chou et al., 2018). Second, an injection protocol of the zygote and methods for performing functional studies either by drug treatments (e.g., Denes



#### 1.4. Imaging methods for fluorescently labeled samples

et al. (2007); Tomer et al. (2010); Demilly et al. (2013); Handberg-Thorsager et al. (2019)) or by gene perturbation (e.g., Bannister et al. (2014); Williams et al. (2015); Handberg-Thorsager et al. (2018)) came out. Third, introduction of foreign genetic material by transposon based transgenesis was achieved (Backfisch et al., 2013, 2014). The first CRISPR-Cas9 knock-out snail strain opens a window for specific transgene, knock-in, or knock-out studies in spiralian (Perry & Henry, 2015; Abe & Kuroda, 2019), making it possible to target a unique gene or its regulatory element for transgenesis in the future. Fourth, injection of fluorescently labeled mRNAs for labeling distinct cellular compartments transiently together with live-imaging recordings has allowed to construct later developmental cell lineages and to follow the dynamics of cellular processes (Özpolat et al., 2017; Vopalensky et al., 2019). With the knowledge of cell lineage tracking and synchronous development, and the available genetical tools, *P. dumerilii* is emerging to become one of the most powerful model organisms for investigation of the mechanisms behind spiral cleavage. And through study on *P. dumerilii*, it may represent the Evo-Devo connection between vertebrates and the other fast-evolving ecdysozoan models, such as *Drosophila* and *Caenorhabditis*.

#### 1.4. Imaging methods for fluorescently labeled samples

The use of fluorescent microscopy to study live embryogenesis or fixed biological specimens has been one of the most convenient approaches to extract specific details and perform quantitative analysis on the function and morphology of the blastomeres in intact organisms (Pantazis & Supatto, 2014). Because each microscope has a different

## 1. Introduction

spatial and temporal resolution as well as signal-to-noise ratio, different microscopies fit different biological specimens, experimental design, or scientific purposes. With the wide range of microscopic variety, molecular and cellular processes can be imaged *in vivo* with confocal laser scanning techniques, super-resolution techniques, and/or two photon techniques (Combs, 2010; Schermelleh et al., 2010; Ettinger & Wittmann, 2014; Thorn, 2016). These fluorescent imaging techniques use optical sectioning to increase spatial resolution, allowing to image a region of an intact sample without physical sectioning (Lichtman & Conchello, 2005). They also make live-imaging of a developing embryo with precise spatial information possible. Optical sectioning can be achieved in two major ways depending on the design of the light path of the microscopes: With confocal microscopy the whole sample is illuminated and the fluorescent signal is collected from a small region of the sample (Figure 1.4). Light sheet microscopy, on the other hand, illuminates only part of the sample and collect all the information of the illuminated region (Figure 1.4). Below I will describe these two imaging techniques in more details.

#### 1.4. Imaging methods for fluorescently labeled samples

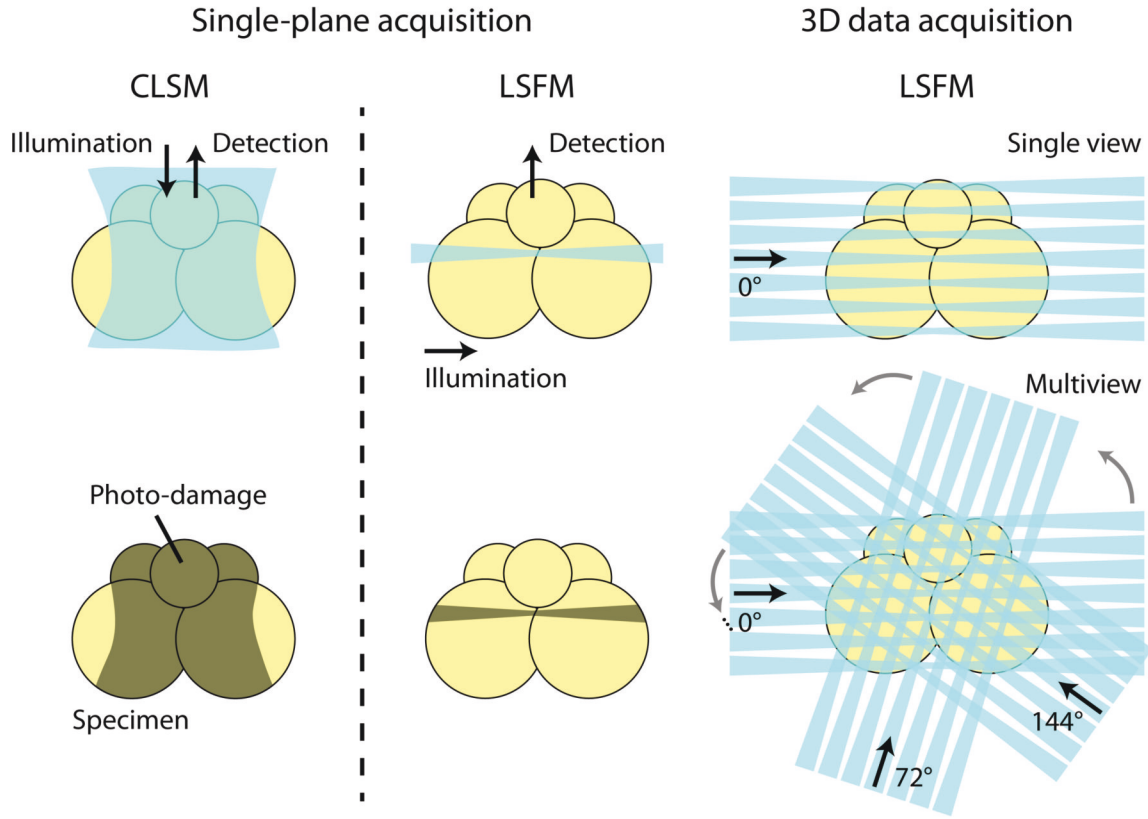


**Figure 1.4.: Comparison of CLSM and LSFM imaging techniques.** The illustration was modified from Keller et al. (2011). Confocal laser scanning microscopy (CLSM) illuminates the whole specimen, therefore, induces greater photo-damage to the sample. Light sheet fluorescence microscopy (LSFM) illuminates only a thin layer of the specimen by shining a sheet of laser beam to the sample. With this strategy, it reduces largely photo-toxicity to the living sample and at the same time reduces the out-of-focus light entering the detection objective. During 3D data acquisition, the sample is imaged from multiple angles. In this study, five views with  $72^\circ$  rotation was used to optimize the image processing efficiency.

Confocal laser scanning microscopy (CLSM) is one of the most popular methods to study cellular and molecular dynamics during embryogenesis. The two major CLSM types are point scanning and spinning-disc. In both systems, optical sectioning is achieved by the pin hole(s) in the light path, allowing only the light in the focal plane passing to the detector (Lichtman & Conchello, 2005). A point scanning

## 1. Introduction

system gives very high image resolution, because the data is collected pixel by pixel. This, however, leads to a low temporal resolution compared to other microscopies. In order to increase the temporal resolution, the background noise will also increase dramatically. Therefore, the point scanning confocal microscopy is mainly used for imaging fixed sample, or for live-imaging of slow biological processes. The idea of spinning disk confocal microscopy was invented in 1960's by Egger, who used a rotating mechanical spinning disc, namely the Nipkow Disc, with thousands of pinholes for imaging (Egger & Petr  n, 1967). The advantage is that multiple points can be imaged at the same time, meaning that the imaging speed is much faster than the point scanning system. However, in both confocal systems, the entire sample is illuminated while imaging, resulting in high photo-bleaching of the fluorophore and photo-toxicity leading to damage of the live sample. Therefore, confocal microscopies are usually limited up to a few hours for live imaging (Icha et al., 2017; Laissue et al., 2017).

Light sheet fluorescence microscopy (LSFM) has recently opened up for the possibility for long-term whole embryo live-imaging of biological processes at high temporal and spatial resolution (Huisken et al., 2004). In contrast to the confocal microscopies, light sheet microscopy only illuminates a small volume of the sample at a time with a sheet of light moving back and forth across it (Huisken et al., 2004; Keller, Schmidt, et al., 2008; Keller et al., 2011). This sheet of light is produced by a pair of objectives in the selective plane illuminative microscopy (SPIM), one of the most popular LSFM systems. The light sheet is created perpendicular to the imaging direction, and always adjusted to the focal plane of the detection objectives. By moving the sample across the light sheet, the whole specimen can be imaged and only the focal plane is illuminated. This reduces the out-of-focus light entering the detection objective, it maximizes the useful information collected, and massively

#### *1.4. Imaging methods for fluorescently labeled samples*

reduces photo-bleaching and -toxicity of the live sample. With these benefits, SPIM allows live-imaging of an embryo for days until it hatches (Keller, Pampaloni, et al., 2008; Chhetri et al., 2015). The separation of the illumination objective creating the light path and the detection objective capturing the images results in a wider combination of flexibilities for imaging (Huisken et al., 2004; Pitrone et al., 2013).

Apart from photo-bleaching and photo-toxicity causing a limitation to imaging with fluorescence microscopes, imaging depth is usually another limiting factor for the imaging system. Unfortunately, most of the embryos are either at the edge of the maximum thickness or above it. Even if the thickness of the sample can be fully covered, image quality reduces drastically when moving through the tissue because of the scattering effect of the tissue between the imaging plane and the objective. To image the entire sample, confocal microscopy is therefore not the optimal solution because the sample can only be imaged from one view. SPIM imaging on the other hand offers the possibility to acquire images from multiple views, thus covering the entire sample. Because the sample is suspended at the center of the imaging chamber and the motor drives its movement for optical sectioning, it can also rotate the sample to achieve the acquisition from a different view. All the positioning, angles, and sectioning information is recorded by SPIM so that each image can be registered forming a 3D reconstructed embryo.

Various open source software joins the processing of the raw images, including Fiji (<http://fiji.sc/Fiji>), micromanager (<https://www.micro-manager.org/>), multiview reconstruction plugins (Preibisch et al., 2010; Schmied et al., 2016), BigDataViewer (<http://fiji.sc/BigDataViewer>), and deconvolution (Preibisch et al., 2014). With the processing pipeline, the raw images are registered and/or fused

## 1. Introduction

and can be visualized from every view-of-interest. The whole volume of the image is isotropic, meaning the data is unbiased by imaging angle and can be post-processed and analyzed with maximum flexibility (Tomer et al., 2010, 2012; Amat et al., 2014, 2015; Stegmaier et al., 2016).

In this study, I used a combination of various microscopies. When the biological interest was a large-scale, long-term process, such as cell positioning, nuclei movement, and lineage tracing, SPIM is introduced to get as much 3D information as possible. The images are acquired by five views with a  $72^\circ$  rotation (Figure 1.4). Therefore, the temporal resolution is not specifically high (90 sec) but the position of the cell components can be carefully observed. On the other hand, when monitoring a fast processing biological mechanism, such as cortical actomyosin dynamics, spinning disk confocal microscopy is used for the following reasons. First, the requirement of temporal resolution is extremely high ( $\sim 5$  sec) as well as special resolution ( $\sim 1 \mu\text{m}$ ). Second, imaging the dynamics of cell cortex requires neither the microscopy with large depth coverage nor from multiple views because cell cortex is a thin layer underneath the plasma membrane. Third, the imaging of the process is relatively short ( $\sim 30$  min). Photo-bleaching is usually not a big issue in this experimental design. Therefore, confocal microscopy especially the spinning disk system suits better in this experiment. By the combination of different techniques, each biological question can be investigated and answered in the most neutral ways.

## 1.5. Cellular processes involved in cleavages

Embryonic cleavages are special cell mitosis types of the pluripotent stem cells (Li et al., 2011; Zdravkovic et al., 2015). The division planes in this process is important for cell positioning and cell fate determination (Homem & Knoblich, 2012). The organization and localization of the cytoskeletal elements determine the division plane, and this plane results in general blastomere position, in some cases, leading to cell fate determination (Homem & Knoblich, 2012; Lu & Johnston, 2013; Smith et al., 2017). The complexity of division plane determination is controlled by various factors, including organization of the mitotic spindle (Pease & Tirnauer, 2011), position of the centrosomes and the nucleus (Kasioulis & Storey, 2018), polarity established by specific proteins (Rose & Gönczy, 2014), closure of the cytokinetic ring (Fededa & Gerlich, 2012), and contractility of the cell cortex (Naganathan et al., 2014). The external disturbance from the eggshell may also contribute to cell orientation and the final position of the blastomeres (Yamamoto & Kimura, 2017). Therefore, all these factors combined give rise to the morphology of the blastula and influence the larval/adult forms.

### 1.5.1. Cell division machinery: Mitotic spindle and DNA

Mitotic spindle is one of the most important cytosolic structure to separate sister chromatids during cell division. It consists of hundreds of proteins with microtubule as majority (Kline-Smith & Walczak, 2004). Microtubules are nucleated from microtubule organizing centers (MTOC) at prophase of each cell division, then attach to the kinetochores of the chromosomes after nuclear envelope breakdown, forming a stable

## 1. Introduction

structure to pull two sets of sister chromatids apart (metaphase) (Figure 1.5). Therefore, the position of DNA/nucleus, the location of MTOCs, and the orientation of the mitotic spindles influence the division plane (Pease & Tirnauer, 2011; Kasioulis & Storey, 2018).

The pulling force of the spindles comes from the motor protein dynein, which connects to the cell cortex, walking along the astral microtubules toward the MTOCs (from plus to minus end), making the microtubules and MTOCs moving toward the plasma membrane and separating the DNA (Lu & Johnston, 2013) (Figure 1.5). Kinesins movement on the kinetochore microtubules from minus to plus end accelerates this process (Fraschini, 2017). The peripheral microtubules connected to actomyosin filaments through Anillin and RhoA activate Rho-dependent contractile ring assembly (anaphase) (D'Avino, 2009). The contraction of the cytokinetic ring eventually splits one cell into two to complete the cell division (telophase).

The location of the nucleus and the centrosomes decide where the mitotic spindles are nucleated and orientated at the beginning of mitosis. However, cytokinesis and the pulling force of the mitotic spindles are highly dependent on the cell cortical dynamics, which is the other critical factor of cell division (Labbé et al., 2003; Rose & Gönczy, 2014) (Figure 1.5).



## 1.5. Cellular processes involved in cleavages

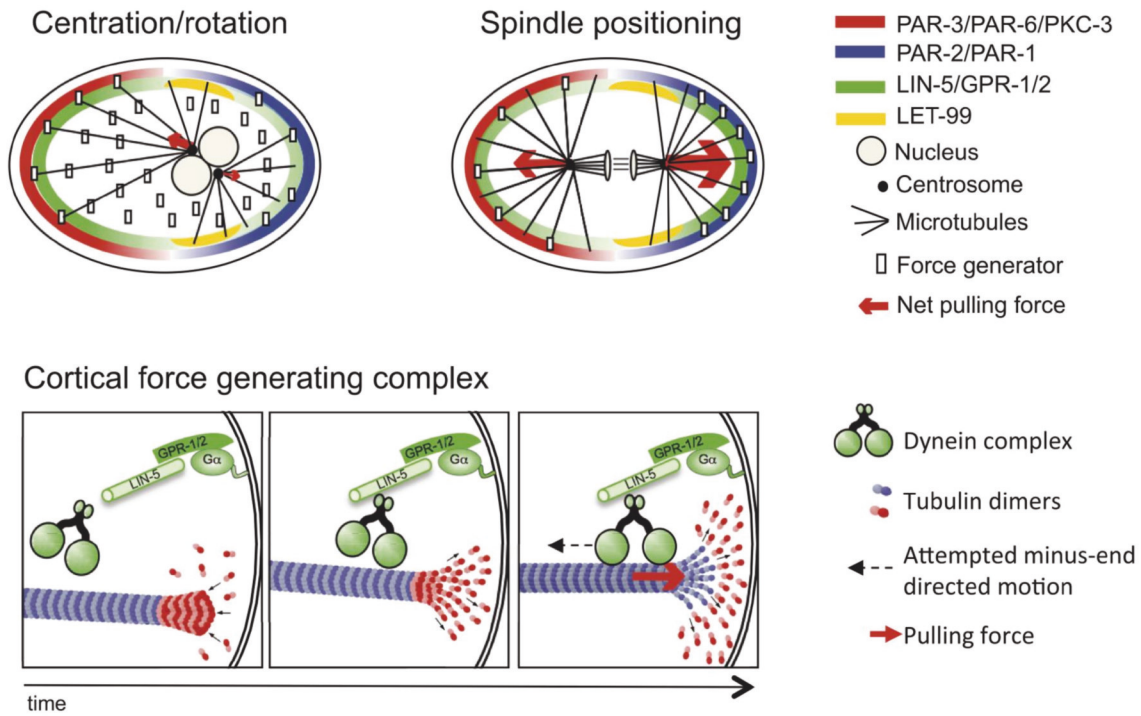


**Figure 1.5.: Mitotic spindle machinery during cleavage.** The illustration was adapted from Rose and Gönczy (2014). The mitotic spindles are nucleated from the MTOCs and the division plane is adjusted during the cleavage by cell cortical components. Dynein moves along the microtubule generates the pulling force and therefore separates the sister chromatids.

### 1.5.2. Cell division machinery: Cell cortex

Cell cortex, also known as the actin or actomyosin cortex, abundant with F-actin filaments, the motor protein myosin, and actin binding proteins, is a layer (in the range of 100 to 1000nm thick) of cytoplasmic proteins located at the inner layer of the cytoplasmic membrane (Chugh & Paluch, 2018). The cell cortex is connected to the membrane through ERM proteins, modulating the membrane behavior and properties (Fehon et al., 2010; Salbreux et al., 2012). The proteins of the cell cortex undergo

## *1. Introduction*

rapid turnover, resulting in the highly reflexive and plastic property, which is essential to its function. Actin filaments connect to each other through spectrin, forming a mesh-like structure with continuous remodeling by polymerization, depolymerization, and branching (Unsain et al., 2018). The regulation of cortical dynamics is achieved by several proteins. These proteins alter not only the structures of the actin cortex, but also the function of it to the cell shape and processes (Figure 1.6).

## 1.5. Cellular processes involved in cleavages

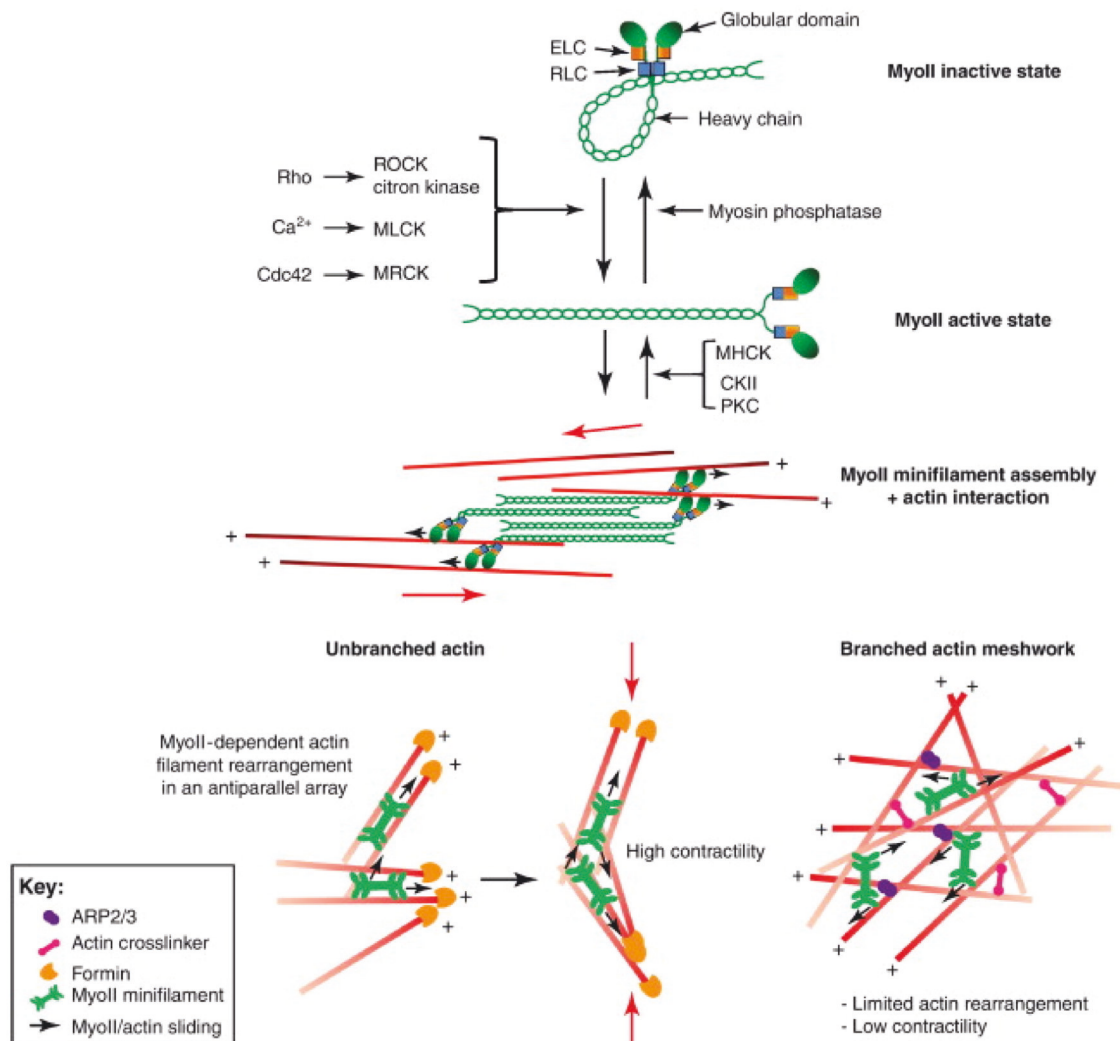


**Figure 1.6.: Contractility regulation of the cell cortex.** The illustration was adapted from Levayer and Lecuit (2012). Myosin can be activated by Rho and moves along the actin filaments toward the plus end, resulting in actomyosin contractility. Various actin binding proteins, such as Arp2/3 or Formin, change the structure of the actin meshwork and therefore changes contractility.

## 1. Introduction

### **Formin**

Formin is responsible for one of the two Rho-GTPase mediated actin polymerization process by interacting with the fast-growing end, barbed end, of the actin filaments (Evangelista et al., 2003). It is characterized by the three formin homology (FH) domains, FH1, FH2, and FH3. FH1 is a proline-rich domain which interacts with many proteins such as profilin and Src homology 3 proteins (Uetz et al., 1996). FH2 domain contains actin nucleation-promoting activity (Goode & Eck, 2007). It is also required for the self-assembly of formin proteins by direct binding of the FH2 domains of each other, as well as binding to actin filaments for regulating actin polymerization (Takeya & Sumimoto, 2003; Shimada et al., 2004). FH3 domain is required for directing formins to specific location, such as to mitotic spindle (Kato et al., 2001). Some formins contain a Dia-autoregulatory domain, DAD. This domain is reported inducing actin filament formation and stabilizing microtubules (Litschko et al., 2019). Therefore, through the direct binding ability of the FH2 domain to actin and microtubules, Formin facilitates the alignment of microtubules along actin filaments (Palazzo et al., 2001; Bartolini & Gundersen, 2010).

### **Myosin**

Myosin is a motor protein super family consisting of various subtypes, which mainly participates in muscle contraction and/or motility processes of the cells (Coluccio, 2007). These motor proteins drive actin-based motility through ATP-dependent pathways (A. K. Wilson et al., 1992; Iwase et al., 2017). Most myosins contain the head, neck, and tail domains and present as dimers (Craig & Woodhead, 2006; Holmes,

### 1.5. Cellular processes involved in cleavages

2008). The head domain has F-actin binding activity and can change its conformation by hydrolyzing ATP, making the dimer walk on the actin filament toward the plus end (Murphy et al., 2001; H. Yu et al., 2007). The neck domain is the linker to transduce the force generated by the motor domain. It also binds to the myosin light chains which regulates myosin macromolecular complex. The tail domain interacts with cargo molecules or other myosin subunits, which generally regulates motor activity (Janssen et al., 2017; Shrivastava et al., 2019).

Myosin II is the myosin causing muscle contraction in muscle cells, and the non-muscle-myosin represents the myosin II (Nmm) found in non-muscle cells, which regulates mainly contractility of intracellular F-actin network (Krendel et al., 1999; Chen et al., 2010; Kasza & Zallen, 2011; Wang et al., 2017). It contains two heavy chain with a N-terminal head, a neck, and a C-terminal tail domain. The coiled-coil morphology of the tail makes two myosin II binding to each other (Vicente-Manzanares et al., 2009). There are four myosin light chains (Mlcs), two regulatory light chains (Rlcs) and two essential light chains (Elcs), associated to the heavy chain in the neck domain (Taubman et al., 1987; Hernandez et al., 2007; H. Yu et al., 2016; Logvinova & Levitsky, 2018). Fluorescent labeling of Nmm, Rlcs, or Elcs is usually used to monitor myosin function and dynamics (Naganathan et al., 2014; Münster et al., 2019). Through the labeling, the mobility of the cytoplasmic structures mediated by Nmm can also be measured, such as cortical actomyosin flow and cytokinetic ring contraction (Naganathan et al., 2014; Pimpale et al., 2019).

## 1. Introduction

### **Arp2/3**

Arp2/3 is a protein complex consists of seven subunits, mainly plays roles in F-actin regulation (Robinson et al., 2001). Two of the seven components, actin-related protein ARP2 and ARP3, have similar conformation to monomeric actin, and can serve as a nucleation center for new F-actin on the existed filament (Welch et al., 1997). Arp2/3 creates branches of F-actin with a  $\sim 70^\circ$  angle (Figure 1.6). Actin nucleation driven by Arp2/3 is activated by WASP proteins, which binds to the plasma membrane and start nucleation of actin through Arp2/3 (Wegner et al., 2008; Padrick et al., 2011). Therefore, it makes the actin filament close or attached to the plasma membrane, forming a strong cell cortex.

### **Rho-mediated cell cortical mechanics**

Cell cortex is responsible for a variety of cellular processes, such as the formation of filopodia and lamellipodia, cell rounding during mitosis, cell shape changing, cytokinetic ring formation contraction, and cell polarity establishment (Chugh & Paluch, 2018). Energy is required for all of the above functions. The Rho family of small GTPase is known to regulate these actin-based cortical machineries (Hall, 1998; Sit & Manser, 2011; Spiering & Hodgson, 2011). RhoA is found responsible to drive the contraction of the actin filaments, such as the stress fibers, in the non-muscle cells (Tojkander et al., 2012; Girouard et al., 2016). The activated/inactivated forms of RhoA, RhoA-GTP or RhoA-GDP, is facilitated by GEF and GAP, respectively. Then RhoA-GTP activates formins (or Diaphanous) and Rho-associated coiled-coil forming kinase (ROCK) (Evangelista et al., 2003; Pellegrin & Mellor, 2007). Formin directly induces

### 1.5. Cellular processes involved in cleavages

F-actin nucleation and polymerization. ROCK facilitates phosphorylation of Mlc, thus triggers the motor function of myosin on actin filament, resulting in actomyosin contraction (Pellegrin & Mellor, 2007).

#### Cortical actomyosin flow

Rho-mediated actomyosin contractility induces not only the formation of the cytokinetic ring, but also the closure of the ring (Kamijo et al., 2006; Mangione & Gould, 2019). Due to the helical structure of actin filament, the mesh-like cortical structure, and the active movement of myosin on two actin filaments, the contraction of the actin fibers results in a pulling tension of the cortex, and an active torque which rotates the whole cell cortex (Naganathan et al., 2014). The combination of the two forces give rise to the cortical actomyosin flow (Kron & Spudich, 1986; Sase et al., 1997; Beausang et al., 2008). The sum up of these mechanical forces generated by actomyosin contractility results in the counter rotation of the cell cortex, namely chiral flow, in a cell. It is detected during early embryogenesis of *C. elegans* before the first embryonic cleavage, establishing and maintaining the anterior-posterior actomyosin polarity. And during cytokinesis, the chiral flow is a key factor to set up the division plane (Naganathan et al., 2014).

#### 1.5.3. Factors for cleavage plane determination

Embryonic cleavages are a series of precise cell divisions making the blastomeres located at their destined places. Every cell cycle is well controlled to make sure the division plane is set according to the embryonic axes. There are fundamental rules for

## *1. Introduction*

cleavage plane determination, which in theory also explains how an embryo achieves its embryonic form (Figure 1.7) (Brun-Usan et al., 2017).



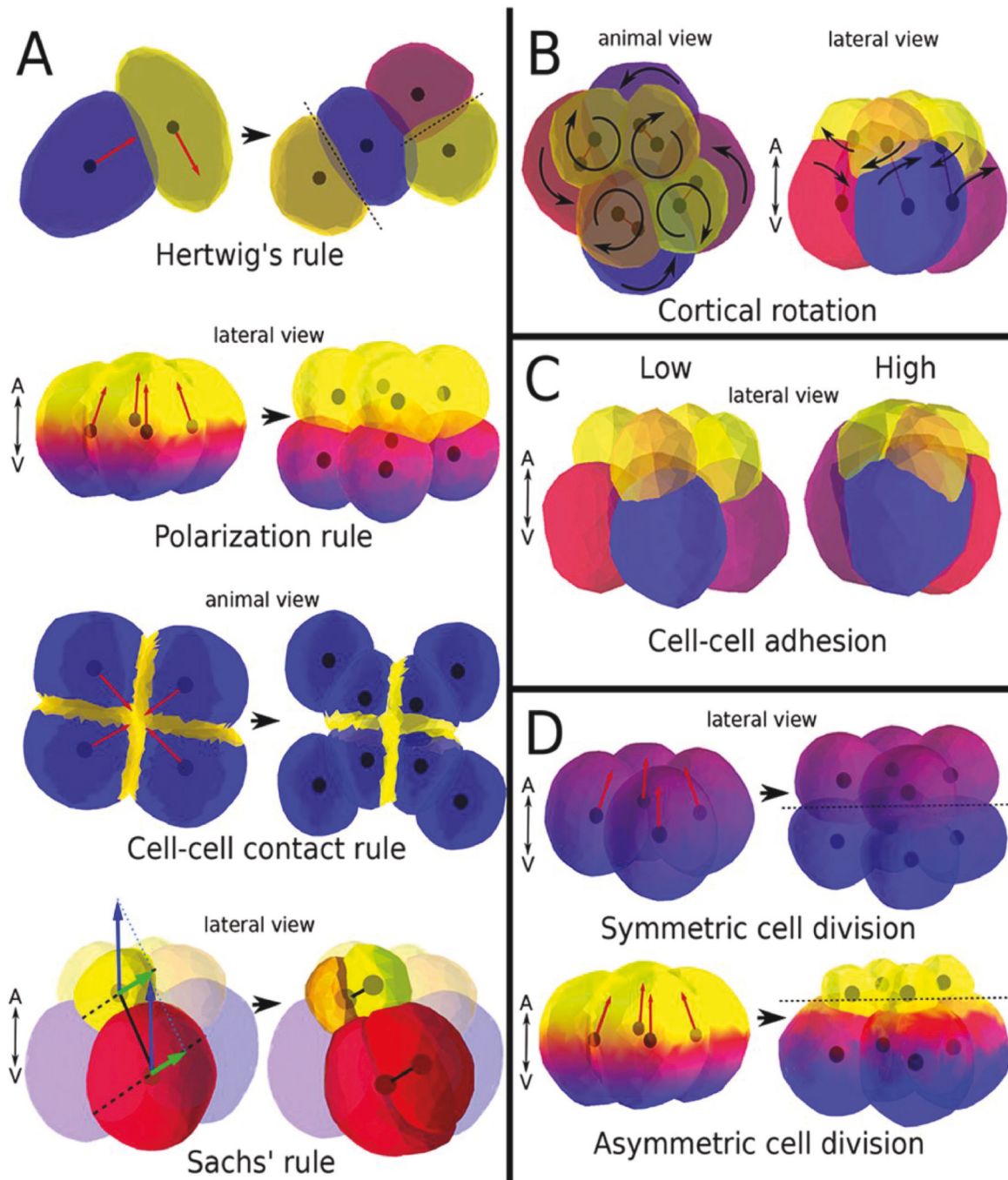


**Figure 1.7.: The cell processes to model spiral cleavage.** The figure was adapted from Brun-Usan et al. (2017). These rules and cellular processes were proposed to contribute to spiral cleavages and to generate a spiral looking embryo. By tuning the level and combinations of these rules, different embryo morphology of spiralian phyla can be modeled *in silico*.

## 1. Introduction

### Hertwig's rule

This rule describes that cells tend to divide with the plane perpendicular to their longest axis (Minc & Piel, 2012). The longest axis can be determined already by the shape of the eggshell. For example, the first embryonic cleavage of *C. elegans* embryo follows anterior-posterior axis, which is the longest axis of the egg itself. For spiralian, spiral deformation of the snails plays a role to change the longest axis from animal-vegetal axis to the dextral orientation and thus, determine the final cleavage plane (Meshcheriakov, 1978).

### Polarization rule

The cellular components, such as maternal mRNAs, proteins, or cytoskeletal components, can be polarized according to the embryonic axes to segregate specific materials into different blastomeres for cell fate determination (Homem & Knoblich, 2012). The direction of polarity is influenced by the cell surroundings, asymmetrical inheritance of oocyte cytosol, or active segregation of the molecules (Lu & Johnston, 2013; Smith et al., 2017). Cells tend to divide perpendicularly to the direction of the polarity, splitting the polarized molecule to one of the two daughter blastomeres (Brun-Usan et al., 2017). One explanation is that usually the cell elongates toward the polarized pole, thus, this axis becomes the longest axis and the division follows Hertwig's rule (Rogulja et al., 2008). The polarized molecules, e.g., actomyosin cortex, may orientate mitotic spindles as well (Freeman & Lundelius, 1982; Lu & Johnston, 2013; Rose & Gönczy, 2014).

*C. elegans* zygote is a great example to demonstrate the polarization rule.

### 1.5. Cellular processes involved in cleavages

The centrosomes of the fused zygotic nucleus are originally orientated perpendicular to the final division plan. However, the Par polarity as well as cortical actomyosin polarity lead the mitotic spindle aligned along the anterior-posterior axis, resulting in the first asymmetric cleavage (Rose & Gönczy, 2014). Therefore, the polarized molecules determine the division plane as well as to segregate themselves and/or the cell fate determinants unevenly into the daughter blastomeres (Venkei & Yamashita, 2018).

#### **Cell-cell contact rule**

The embryo contains multiple cells packed in limited space. The cells contact each other with various cell junctions to communicate and share molecules (Lecuit & Lenne, 2007; Sandersius & Newman, 2008). It has been shown in the spiralian *Tubifex* that the cells cleave toward where the cells contact each other (Takahashi & Shimizu, 1997). It's hypothesized that the cell adhesion changes the cortex beneath that region, resulting in the stabilization of the astral microtubules and therefore, increase the cortical contractility (Hertzler & Clark, 1992; Goldstein, 1995; Théry & Bornens, 2006).

#### **Sachs' rule**

Due to the typical duplication and migration of the centrosomes, the location of the centrosomes is perpendicular to the previous cell cycle. This alternating position leads the assembly of the mitotic spindle thus perpendicular from one cell division to the previous one (Théry & Bornens, 2006; Minc & Piel, 2012)). It is shown with the *in*

## 1. Introduction

*vitro* cultured cell lines, as well as in spiral and radial cleavage (Morris et al., 1989; Pierre et al., 2016).

### Cortical actomyosin counter rotation

As mentioned in the previous section, myosin creates a contractile tension and a rotational torque when walking along actin filaments. The sum up of the force generates a flow of the whole cell cortex. This flow is detected counter-rotating between the anterior and the posterior halves in the *C. elegans* embryo (Naganathan et al., 2014). It results from the gradient of actomyosin along the anterior-posterior axis, which leads to a gradient of the torque, therefore creates a chiral flow orthogonal to the direction of the actomyosin gradient. It's been shown that the chiral flow rate is controlled by myosin activity as well as upstream Rho GEF/GAP activity (Naganathan et al., 2014).

Although the general division axis is determined by the other rules, actomyosin chiral flow creates an extra input to tune the final cleavage plane. The embryonic cleavage from four to six cells of *C. elegans* is also the left-right symmetry breaking event. It's been shown that the chiral flow rate determines the spindle inclination angle during this cleavage. And it's mediated by upstream Rho activity. With greater Rho activity, the chiral flow is stronger, resulting in a greater inclination angle during cytokinesis. Therefore, it suggests that cortical actomyosin counter rotation is one of the components to adjust the final cleavage plane for daughter blastomere positioning, which affects cell fate and the symmetry of the organism during embryogenesis (Naganathan et al., 2014).

### Physical constraint by the eggshell

Many organisms have their embryo develop in a protective eggshell surrounding the blastomeres. While cells divide and migrate in the embryo, the eggshell serves as an external contact which not only restricts the embryo in a given space, but also provides a specific shape for the blastomere to migrate or to follow and therefore the unique embryonic morphology is formed (Yamamoto & Kimura, 2017). It's been shown both with *in silico* simulation and experiments with *C. elegans* embryo that, when the ratio of the major and minor axis of the oval-shaped eggshell is changed, the rotational cleaving blastomeres are no longer positioned as in the wildtype (Yamamoto & Kimura, 2017). Moreover, the eggshell of the *C. elegans* embryo is essential for symmetry breaking during the 4-cell stage (Yamamoto & Kimura, 2017). These indicate that the connection between the blastomeres and the eggshell, and the physical constraint given by it may influence cleavage plane, cell positioning, and embryonic morphology.

To sum up, the plane determination rules guide generally how a blastomere defines its division plane within the embryo. And while the cleavage progresses, the dynamic cell cortex and the eggshell give extra input to adjust the final plane, resulting in the proper cleavage type of the organism.

#### 1.5.4. Influence of division plane to cell stemness

The switch between stemness maintenance or differentiation in the stem cells is depending on the inheritance of the fate-determining factors, which are unevenly distributed in or around the stem cell (Campanale et al., 2017; Jossin et al., 2017; Toledano & Jones, 2008). The division plane decides the orientation of the two daughter

## 1. Introduction

stem cells in the tissue or in the embryo, which affects how the cell fate determining factors are segregated. Therefore, different division planes give rise to distinct stem cell actions, producing more stem cells, or providing differentiating progenies (Venkei & Yamashita, 2018).

*Drosophila* neuroblast (NB) is one of the best-known examples that the division plane determines cell fate (Doe & Bowerman, 2001; F. Yu et al., 2006; Prehoda, 2009; Gallaud et al., 2017). The fate-determining factors (Numb, Prospero, Miranda, Staufen and *prospero* mRNA) are polarized to the basal side of the NB (Figure 1.8). Cell division takes place normally following polarization rule, which segregates these determinants only into the basal daughter cell (Figure 1.8). This cell starts differentiation and becomes ganglion mother cells (GMCs). The apical fate-determining factor producing NB remains at its position, ensuing reproducing GMCs by segregating these factors accordingly and divides perpendicularly to the apical-basal axis (Venkei & Yamashita, 2018).

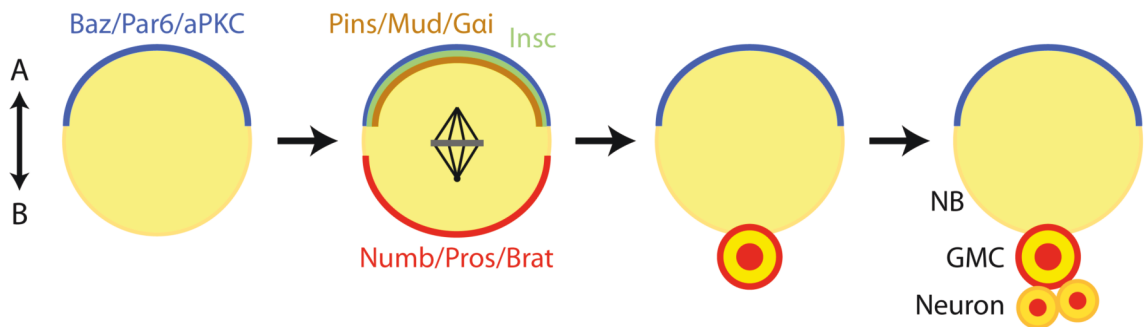


**Figure 1.8.: Cell polarity of *Drosophila* neuroblast.** The illustration was adapted from Homem and Knoblich (2012). The division of the neuroblast (NB) follows apical-basal axis. The polarity proteins are located at either sides of the NB and are segregated to the daughter cell, resulting in its differentiation into GMC.

The normal division of NB leads to the renewal of NB and produces a

GMC. The well-controlled orientation makes sure of the proper apical-basal polarity, maintenance of the source NB, and the correct output GMC rate. However, when the tumor suppressor genes, e.g., *lgl*, *dlg*, and *scribd*, are mutated, the basal polarity is changed. This makes an ectopic division plane parallel to the apical-basal axis and results in both daughter cell inheriting the apical part of the NB. Therefore, it creates two NBs, instead of one NB and one GMC. The dysregulation eventually leads to the lethal giant larvae phenotype because of uncontrolled stem cell proliferation (Venkei & Yamashita, 2018).

To sum up, cleavage plane is determined by a series of well-controlled cellular and molecular components. This plane leads to proper cell positioning in the embryo to form the precise organismal morphology, and more importantly, to regulate the cell behavior and cell fates during development.

## 1.6. Objectives

Spiral cleavage is described in the previous sections. However, the detailed biophysical mechanisms remain unclear. In this study, I aim to develop the fast labeling and live-imaging techniques. And with these tools, I can investigate early spiral cleavages of *P. dumerilii* in finer scales.

## 1. Introduction

### 1.6.1. Develop the labeling techniques for studying early embryogenesis

Cleavage pattern and early cell lineage were revealed with bright-field microscopy (Ackermann et al., 2005). In this study, I aim to label the nuclear DNA, cytoskeletal elements, and cytoplasmic membrane from the early cleavages, and with the help of light sheet microscopy, to track cell lineages with higher temporal and spatial resolution, therefore to better resolve each cleavage as well as how the cytoskeletons and the nucleus cooperate during the cleavage.

Different labeling techniques are required for different experimental purposes. A combination of chemical dye, mRNA, or fluorescent protein injection will be used in this project to optimize the labeling. Since spiral cleavage occurs from the third embryonic cleavage, the potential acceleration methods for protein expression will also be investigated by optimization of the DNA constructs. Although it may not be the best labeling technique for all the experimental design, the aim is to find relatively fast and stable methods for labeling and live-monitoring spiral cleaving machinery.

### 1.6.2. Decipher the mechanisms of spiral cleavage

Spiral cleavage is a complex developmental process requiring cooperation in various levels including cellular, molecular, and physical machineries. I Aim to investigate spiral cleavage in all these levels with various biological scales in this study. In large scale, monitor the cell positioning will acquire the global picture of the spiral arrangement during *P. dumerilii* embryogenesis. Lineage tracing will establish the



## 1.6. Objectives

timeline of each cleavage and reveal the cell division properties of each blastomere.

In the intermediate scale, the cytoskeletal dynamics will be observed to find out the relationships of each cytoskeletal element, e.g., nuclear DNA, mitotic spindle, and cell cortex, and their roles in spiral cleavage. The chemical inhibitors targeting those cytoskeletal elements will be used to investigate the importance of each molecule/structure to spiral cleavage, therefore to find the critical molecules driving the whole process.

In the micro scale, I will focus on the cortical actomyosin dynamics, which has been shown playing an essential role in left-right symmetry breaking in various systems. Through deciphering whether actomyosin chiral flow occurs during spiral cleavage of *P. dumerilii*, this physical force generating mechanism may be concluded as a conserved cleavage plane determinant for different cleavage types upon Evo-Devo.



Part II.

Results



## 2. Early development of *P. dumerilii*

In this study, I particularly focused on the early spiral cleavages of *P. dumerilii*. It's although a conserved cleavage type for the spiralian with particular cell division and orientation pattern, the detailed cytoskeletal events involved are unclear. To understand it, I started analyzing the first two asymmetric cleavages, which lead to spiral cleavage, with immunofluorescence targeting the cytoskeletal elements, to characterize the cellular properties in a global view.

### 2.1. Synchrony of the first six embryonic cleavages

To perform the mating and fertilization of *P. dumerilii* processes under laboratory conditions and have the real-time control of the embryogenesis, the matured males and females were collected into small cups pairwise with a thin layer of natural seawater. After the mating behavior was observed and both worms spawned, the worms were removed and the cup was filled with natural seawater to prevent polyspermy of the

## 2. Early development of *P. dumerilii*

eggs. One batch of eggs contained 300-500 embryos considered fertilized simultaneously. The embryos were incubated at 18 °C for fertilization envelope formation and pronuclei fusion. If the eggs were fertilized properly, a thick jelly layer separates each zygote and the zygotes are spherical. The jelly layer was removed by washing the embryos on a mesh, which collects only the embryos onto it. With this physical method, the embryos were separated from the secreted jelly with minimal disturbance.

The timing of the early *P. dumerilii* cleavages have been documented (Ackermann et al., 2005), but since the developmental speed of the *P. dumerilii* embryos is controlled by the temperature (A. H. Fischer et al., 2010), I wanted to repeat these experiments under our laboratory conditions. The embryos were incubated in a chamber slide filled with natural seawater and the development of the *P. dumerilii* embryos was monitored by bright-field microscopy. Under these conditions, the embryos survived throughout the live-imaging and developed into trochophore larvae by 24 hpf, indicating that the development was normal. The live-recordings were captured at a 30-second temporal resolution covering half of the embryos from the animal pole (Figure 2.1). The time of cytokinesis were annotated for the first six embryonic cleavages (Table 2.1). Fertilization of the embryos was considered simultaneous due to the small volume for mating and spawning in the culturing cup, confirming that the cleavages between individuals were highly synchronous under a given incubation condition. The first cell cycle took around 100 min, including fertilization, meiosis of the egg, polar body formation, fusion of the pronuclei (at around 60 mpf), and processes of the first cleavage. Starting from the second division, each cell cycle took around 30 min (at 18 °C).

## 2.1. Synchrony of the first six embryonic cleavages

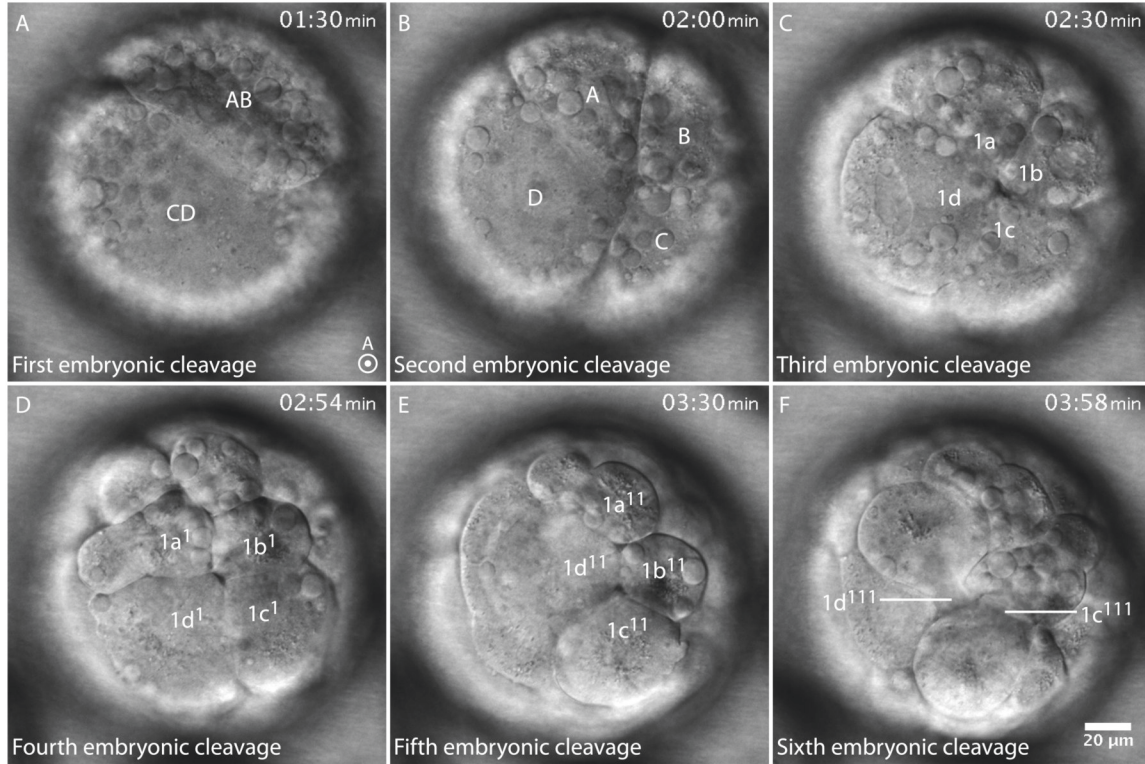


**Figure 2.1.: Early cleavages of *P. dumerilii*.** The embryos were incubated at 18°C and imaged from the animal pole with the wide-field DIC microscope. The development was recorded with a 30-second temporal resolution. The 50 µm from the animal pole toward the center of the embryo was projected. (A) The first unequal cleavage occurred at 90-100 mpf. (B) The second unequal cleavage occurred at 120-130 mpf. (C) The third embryonic cleavage (the first spiral cleavage) from 4 to 8 cells occurred at 150-160 mpf. (D) The fourth embryonic cleavage (the second spiral cleavage) from 8 to 16 cells occurred at 180-190 mpf. (E) The fifth embryonic cleavage (the third spiral cleavage) from 16 to 32 cells occurred at 210-220 mpf. (F) The sixth embryonic cleavage (the fourth spiral cleavage) from 32 to 64 cells occurred at 240-250 mpf. The identity of the blastomeres at the animal pole were labeled. The format of the timestamp is hr:min. Scale bar: 20 µm.

## 2. Early development of *P. dumerilii*

**Table 2.1.: The cell cycles under laboratory incubation condition**

Cell cycle	Development time	Description
1-2 cell	90-100 mpf	First embryonic cleavage
2-4 cell	120-130 mpf	Second embryonic cleavage
4-8 cell	150-160 mpf	First spiral cleavage
8-16 cell	180-190 mpf	Second spiral cleavage
16-32 cell	210-220 mpf	Third spiral cleavage
32-64 cell	240-250 mpf	Fourth spiral cleavage

The embryos were incubated at 18 °C and the divisions were captured by live-imaging with bright-field microscopy.

## 2.2. Orientation of the cytoskeletal elements

Because the time of cleavages were precisely captured, the phases of each cell cycle can also be predicted. Therefore, before live-monitoring the cytoskeletal dynamics, I've chosen to fix the embryos at each cleavage, as shown in Tabel 2.1, and immunostained the cellular components. With the design, although the images are fixed, it gave me a global view with very strong and clear signal to describe the whole process and let me target the potential cleavages for further investigation. This is also the first documentation of detailed investigation of early cleavages in *P. dumerilii* based on the phases of cell cycle by immunofluorescence.



### 2.2.1. The first two asymmetric embryonic cleavages

The first two cleavages in *P. dumerilii* were asymmetric, giving rise to the four macromeres, A, B, C and D, with different sizes as already observed by bright-field microscopy (Figure 2.1). However, this imaging technique did not reveal the intracellular processes during the cleavages. To look into the cellular processes during each cleavage, I fixed the embryos at various time points according to Table 2.1 to cover each cell cycle. Microtubules were labeled by immunofluorescence with a commercial antibody against  $\alpha$ -tubulin. The plasma membrane and DNA were labeled with respectively the dyes phalloidin and DAPI. Early observation was the segregation of cytoplasmic material in the zygote. Before the onset of mitosis, the ooplasm largely localized to the animal pole, whereas the oil droplets and the nutritional vesicles moved to the vegetal pole of the zygote (Figure 2.2 D, also see Appendix A.3 for detailed images). A similar segregation process happens in Medaka and is dependent on actin and tubulin (Webb et al., 1995). Currently, the mechanism leading to this segregation in *P. dumerilii* is not known. During mitosis of the zygote, my immunostainings showed that the chromosomes were off-centered during the metaphase at the animal pole (Figure 2.2 A). Both the polar and astral mitotic spindles in the larger cell half of the zygote, the future CD cell, were longer and spread wider than the spindles in the other daughter cell, the future AB cell (Figure 2.2 A). The mitotic spindles at each pole shortened at anaphase leading to a segregation of the chromatids into the two daughter cells (Figure 2.2 B). The cleavage furrow was first detected at the animal pole of the embryo between the separated DNA and the spindles (Figure 2.2 C,D). Therefore, the ingression of the cleavage furrow first separated the mitotic spindles and the nuclei and finally closed at the vegetal pole to complete the cell division (Figure 2.2 E-G). The cleavage furrow

## 2. Early development of *P. dumerilii*

formation was accompanied by an accumulation of actomyosin to this area (Figure 2.2 C-G). Thus, because of the off-centered DNA, the asymmetries in the length of the mitotic spindles, and the off-centered closure of the cleavage furrow, the two-cell stage embryo was constituted of a smaller AB cell and a bigger CD cell (Figure 2.2 H).

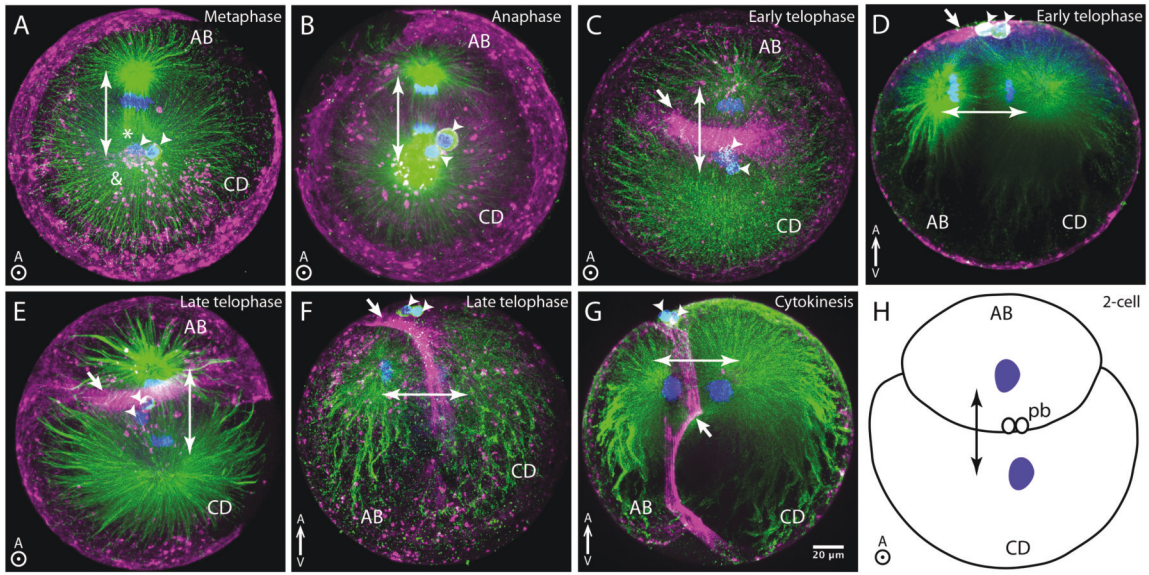


**Figure 2.2.: The first embryonic cleavage of *P. dumerilii*.** The embryos were incubated at 18°C and fixed at 90-100 mpf. Microtubules were labeled with anti- $\alpha$ -tubulin antibody (green). The cell membrane was labeled with phalloidin (magenta) and the nuclei with DAPI (blue). (A) The DNA aligned asymmetrically in the zygote during metaphase. (B) The DNA was separated during the anaphase (double-headed arrow). (C, D) The ingression of the cytokinetic ring initiated at the animal pole (arrow). Actomyosin accumulated at the furrow (arrow). (E, F, G) The ingression continued toward the vegetal pole and finally separated the chromosomes into the AB and CD cells. The polar mitotic spindles were labeled with asterisks and the astral mitotic spindles with &. Arrowhead: polar body. Arrow: cytokinetic ring. Double-headed arrow: cleavage direction. A-C, E, H: animal view. D, F, G: lateral view. Scale bar: 20  $\mu$ m.

After the first division, the centrosome duplicated in each cell and move along the nucleus until they were at opposite positions ( $180^\circ$ ) across the nucleus. Therefore, the second embryonic cleavage was perpendicular to the first (Figure 2.3 A). As during

## 2.2. Orientation of the cytoskeletal elements

the previous cleavage, the DNA and mitotic spindles were off-centered in the both cells, but more prominent in the CD cell (Figure 2.3 A,B). The cleavage furrows were first detected at the animal pole and again they closed at the vegetal pole (Figure 2.3 C). Due to the asymmetric divisions, the cell sizes of the four macromeres in *P. dumerilii* were unequal. The D macromere was by far the biggest, followed by the C macromere and the A macromere was slightly bigger than the B macromere (Figure 2.3 D). This is conserved as the observation of Ref. The four macromeres were aligned in the plane perpendicular to the animal-vegetal axis.

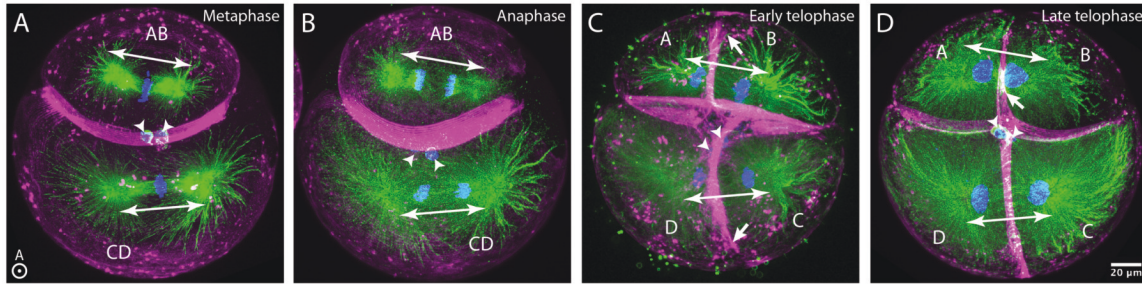


**Figure 2.3.: The second embryonic cleavage of *P. dumerilii*.** The embryos were incubated at 18°C and fixed at 120-130 mpf. Microtubules were labeled with anti- $\alpha$ -tubulin antibody (green). The cell membrane was labeled with phalloidin (magenta) and the nuclei with DAPI (blue). All the images were captured from the animal view. (A) The division was synchronous and the DNA was aligned asymmetrically in each cell during metaphase. (B) The chromosomes were separated during anaphase (double-headed arrow). (C, D) The ingression of the cytokinetic ring initiated at the animal pole (arrow) and was visible during the telophase (C) and cytokinesis was finished earlier in CD cell than in AB cell (D). Arrowhead: polar body. Arrow: cytokinetic ring. Double-headed arrow: cleavage direction. Scale bar: 20  $\mu$ m.

### 2.2.2. The first spiral cleavage of *P. dumerilii*

The third embryonic cleavage is also known as the first spiral cleavage in the spiralian. The general division axis follows the animal-vegetal orientation, giving rise to four

## 2. Early development of *P. dumerilii*

micromeres (smaller blastomeres) at the animal pole and four macromeres (larger blastomeres) at the vegetal pole. However, the division plane inclines during this cleavage resulting in a final micromere position, which is rotated dextral or sinistral to the macromeres. This final twist in the cell position within the embryo is specific to the spiralian (Kuroda, 2014). The division orientation in *P. dumerilii* is dextral during the first spiral cleavage (Nakama et al., 2017). In order to investigate the dynamics of the mitotic spindles during the first spiral cleavage, the embryos were fixed at each mitotic phase of the division and the cytoskeletal components were labeled as in the previous section.

The initial stages of the first spiral cleavage follow a typical cell division. The orientation of the spindles is in general parallel to the animal-vegetal axis so that the inclination of the mitotic spindles was not obvious during metaphase by histological observations (Figure 2.4 A,B). The position of the chromosomes was closer to the animal pole (Figure 2.4 B). The cytokinetic ring was detected during the late metaphase/early anaphase and the position of the cytokinetic ring were generated closer to the animal pole (Figure 2.4 C-E). Thus, it resulted in the asymmetric division. The DNA was segregated into micromeres and macromeres by the mitotic spindles starting at early anaphase (Figure 2.4 D). Interestingly, the DNA separation started a bit earlier in the C and D macromeres than in the A and B macromeres (Figure 2.4 C-E). The second half of the mitotic phases (anaphase and telophase) were characteristic to the spiralian. Here, an inclination of the spindles was observed during anaphase and telophase by histochemistry, leading to a tilted cell division axis (Figure 2.4 D-F). The spindle inclination was accompanied by a deformation in the cell membrane during telophase (Figure 2.4 G). All the four macromeres showed a dextral orientation of the spindles (when looking from the animal pole, Figure 2.4 F-H). This became more



## 2.2. Orientation of the cytoskeletal elements

obvious through the closure of the cytokinetic ring. The cell division was asymmetric because of the polarized localization of the chromosomes and the cytokinetic ring toward the animal pole (Figure 2.4 B-D). This resulted in four smaller micromeres positioned in a shifted, dextral manner comparing to the larger daughter macromeres (Figure 2.4 H) and marked the end of the first spiral cleavage in *P. dumerilii*.

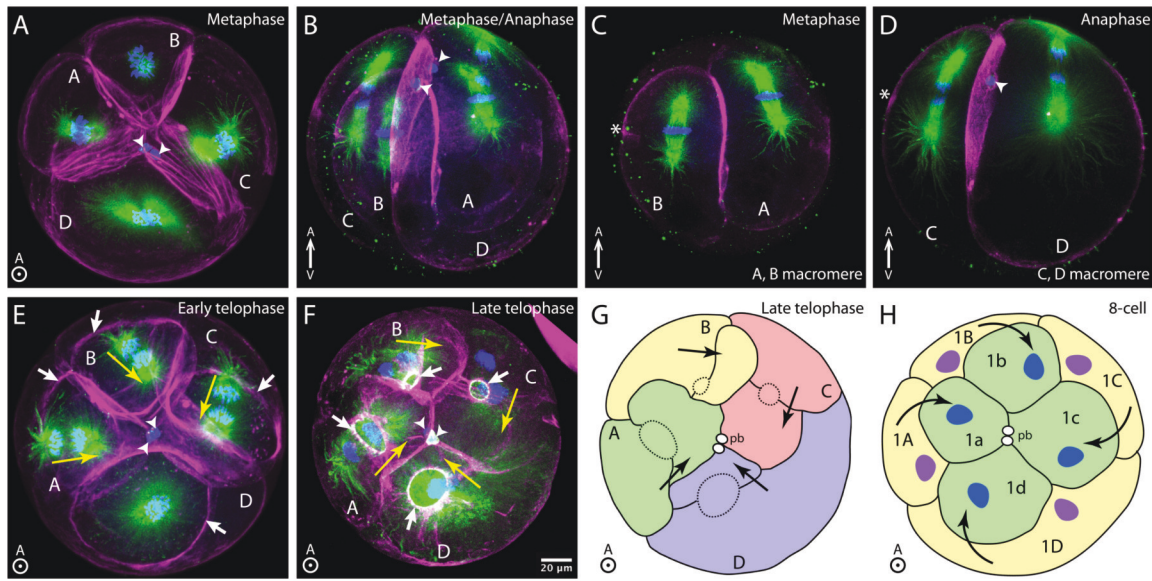


**Figure 2.4.: The first spiral cleavage (third embryonic cleavage) of *P. dumerilii*.** The embryos were incubated at 18°C and fixed at 150-160 mpf. Microtubules were labeled with anti- $\alpha$ -tubulin antibody (green). The cell membrane was labeled with phalloidin (magenta) and the nuclei with DAPI (blue). (A, B) The microtubules were aligned along animal-vegetal axis during metaphase. (C, D) C and D macromeres entered anaphase earlier than A and B macromeres. Actomyosin started to accumulate for forming the cytokinetic ring during metaphase/anaphase. Asterisk: Accumulation of actomyosin at the cell cortex. (E, F) Cytokinetic ring was clearly visible during telophase and the closure positioned the micromeres in a dextral manner. (G) The illustration of panel (F) showed division direction and closure of the cytokinetic ring. (H) The illustration of an 8-cell embryo with the orientation of the micromeres (1a-1d) and macromeres (1A-1D). Arrowhead: polar body. Arrow: cytokinetic ring. Yellow/Black arrow: cleavage direction toward the animal pole. A, E-H: animal view. B-D: lateral view and C and D showed half of the embryo. Scale bar: 20  $\mu$ m.

## 2. Early development of *P. dumerilii*

A long-standing question has been which mechanism contributes to the spiral cleavage and what gives the spiral cleavage its twist. The observed spindle inclination and cell deformation during the first spiral cleavage are interesting processes to explore. The cell deformation in *P. dumerilii* was detected at telophase, where the cytokinetic ring was also clearly seen. As for the mitotic spindles, the inclination angle were measured from multiple embryos in each phase of division in order to monitor how the mitotic spindle inclines to achieve the first spiral cleavage (Figure 2.5 A). The scripts used to measure the inclination angle were written by Dr. Benoit Lombardot from the Scientific Computing Facility of the MPI-CBG, Germany. The plugin works with Fiji. All the image stacks were captured by point-scanning confocal microscopy from the animal pole and the mitotic spindle, DNA, and plasma membrane were labeled and visualized in three separate channels. To measure the inclination angle of the embryos, two directional vectors were required; one along the embryo axis and the other along the spindle axis. The membrane labeling was used to segment each embryo and the polar bodies to mark the animal pole. Therefore, the embryo axis was determined by the vector going through the center of the embryo and toward the animal pole. With regard to the spindle axis, the spindle positions needed to be tracked. For that, the position of the DNA was used as a reference point. The two points with the highest intensity around the DNA in the microtubule channel was considered as the positions of two microtubule-organizing centers (MTOCs) (as shown in Figure 3.2). The direction of the spindle axis vector was from the macromeres at the vegetal pole to the micromeres at the animal pole. Therefore, a vector linking the MTOC spot closer to the vegetal pole with the one closer to the animal pole, defined the mitotic spindle vector ( $V_s$ ). With the two direction vectors, the spindle inclination angle can be measured precisely. If the spindle was not inclined, the spindle axis pointed toward

## 2.2. Orientation of the cytoskeletal elements

the embryo axis, giving the inclination angle theta,  $\theta$ , a zero-degree output. The angle was defined positive when the spiral cleavage was dextral orientation. Contrary, the value was negative when the orientation was sinistral (Figure 2.5 A).

All the four macromeres had dextral inclination during the first spiral cleavage (Figure 2.5 B). When the measurements of the spindle inclination angle were grouped as their identity (A, B, C, and D macromeres), the mean value of A, B, C, and D were  $28.849^\circ$ ,  $34.891^\circ$ ,  $20.813^\circ$ , and  $61.686^\circ$  in dextral direction, respectively. The inclination angle of D macromere was significantly larger than A, B, and C macromeres. The inclination angles of the A, B, and C macromeres didn't show significant difference between each other.

To understand in which phase of the division the spindles inclined, the inclination angles were grouped according to cell cycle phases (Figure 2.5 C). The angle was not significantly toward either directions during prophase (average of  $2.261^\circ$  dextral). However, the dextral orientation of the division angle was detected from the metaphase (average of  $34.167^\circ$ ). Moreover, the angle increased throughout the division ( $45.690^\circ$  for anaphase and  $53.133^\circ$  for telophase).

## 2. Early development of *P. dumerilii*

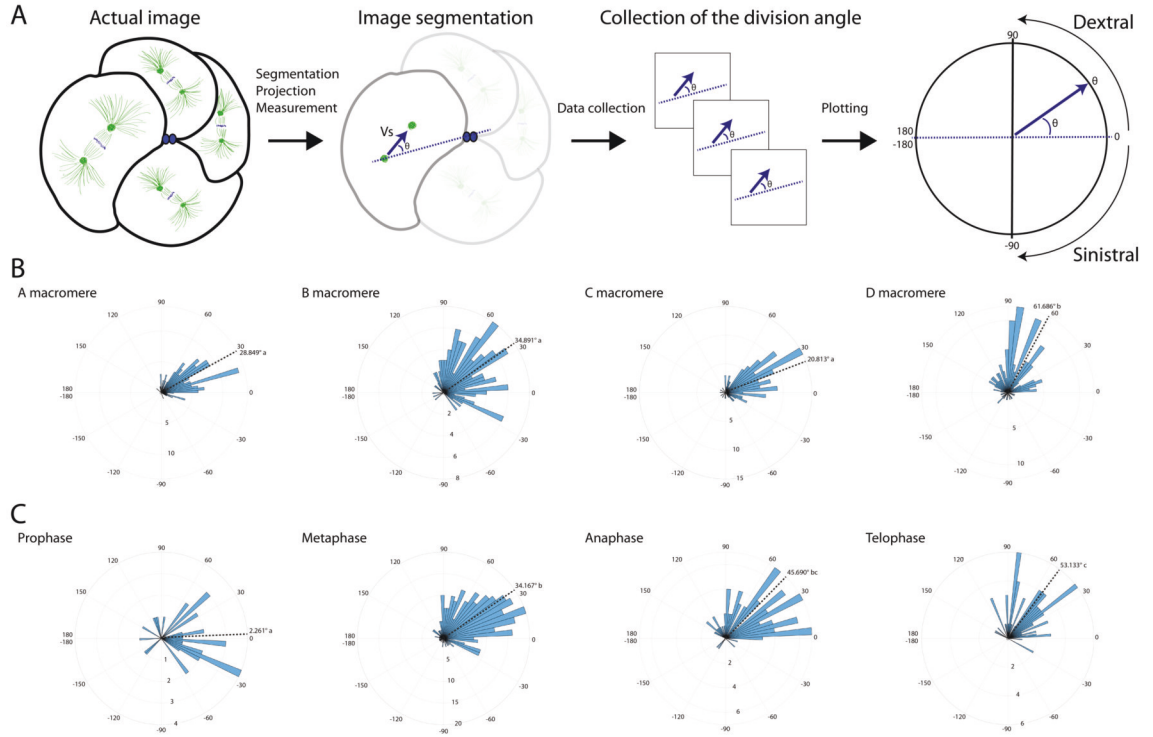


**Figure 2.5.: Mitotic spindle orientation and division angle measurement of the first spiral cleavage.** (A) Schematic overview of the pipeline of the angle measurement. The images were taken from the animal pole. A Fiji-based script was used to determine the embryo axis and mitotic spindle vector ( $V_s$ ) used for the calculation of the division angle. The angles were plotted onto polar-histograms to illustrate the division axes and angles.  $\theta$ : inclination angle. (B) The division angle measurements of the A, B, C, and D macromeres revealed that all the four macromeres performed a dextral orientation of the mitotic spindle during the first spiral cleavage. The division angles of B and D macromeres were greater than A and C.  $n(A)=132$ ,  $n(B)=129$ ,  $n(C)=138$ ,  $n(D)=141$ . The dashed lines indicated mean value. The alphabets behind the average angle indicated statistical difference of the groups. (C) The division angle measurements of all the four blastomeres in each division phase. The dextral orientation of the mitotic spindle was detected from metaphase with increasing angles in anaphase and telophase.  $n(Prophase)=36$ ,  $n(Metaphase)=332$ ,  $n(Anaphase)=92$ ,  $n(Telophase)=80$ . The dashed lines indicated the mean value. The alphabets behind the average angle indicated statistical difference of the groups.

The spindle inclination angle measurements were grouped by each macromere and its phase to understand if any macromeres lead the inclination in a specific phase



## *2.2. Orientation of the cytoskeletal elements*

during the first spiral cleavage (Figure 2.6). It showed that D macromere contained greater inclination angle during metaphase (average of  $57.063^\circ$ ) and telophase (average of  $85.874^\circ$ ), suggesting that D macromere may guide the initiation of spindle inclination as well as play the leader role for the dextral orientation of the first spiral cleavage.

These observations indicated that the first spiral cleavage started without the mitotic spindle inclination, but rather with the mitotic spindle oriented perpendicular to the previous cell division. It is later that the spindles inclined in a dextral manner, either actively (by cytoskeletal elements, see Chapter 4) or passively (by the physical constraint from the eggshell, see Section 2.4), resulting in the clockwise rotation of the micromeres. The order of and importance of the cytoskeletal elements during this cleavage can be analyzed by chemical inhibition experiments. The detailed approach please see Section 4.5.

## 2. Early development of *P. dumerilii*

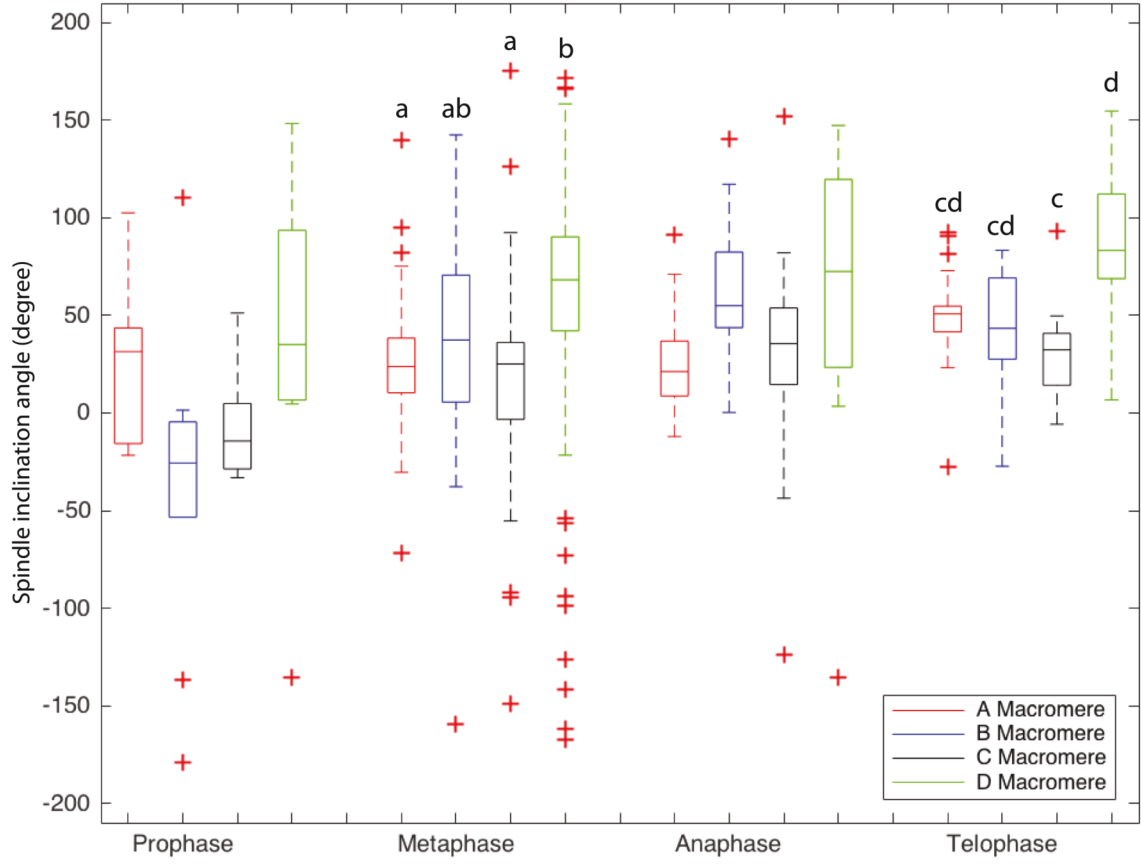


**Figure 2.6.: Spindle inclination angle analysis of the first spiral cleavage.** The measurement was done by the method shown in Figure 2.5. The data was grouped by the macromeres and the phases during the first spiral cleavage. An increasing trend of spindle inclination angle was observed according to the phases of mitosis. D macromere had the greatest inclination angle during both metaphase and telophase.  $n(\text{A.Prophase})=11$ ,  $n(\text{B.Prophase})=10$ ,  $n(\text{C.Prophase})=7$ ,  $n(\text{D.Prophase})=8$ ,  $n(\text{A.Metaphase})=77$ ,  $n(\text{B.Metaphase})=82$ ,  $n(\text{C.Metaphase})=85$ ,  $n(\text{D.Metaphase})=88$ ,  $n(\text{A.Anaphase})=25$ ,  $n(\text{B.Anaphase})=20$ ,  $n(\text{C.Anaphase})=24$ ,  $n(\text{D.Anaphase})=23$ ,  $n(\text{A.Telophase})=19$ ,  $n(\text{B.Telophase})=17$ ,  $n(\text{C.Telophase})=22$ ,  $n(\text{D.Telophase})=22$ .

### 2.2.3. **Spiral cleavages divide the embryo into clonal domains**

Following the first spiral cleavage, more regular cell division patterns followed with division axes, which were perpendicular to the previous division axes. In contrary of the first, cell deformation was not detected in the micromeres during the second to fourth spiral cleavage (Figure 2.7, 2.8, 2.9). Cell deformation was detected only in the macromeres during the second to fourth spiral cleavage at telophase with asymmetric cell division (Figure 2.16). The second, third and fourth spiral cleavages were still termed spiral, because of the final displacement of the micromeres compared to the daughter (micromere and macromere) cells leading to a spiral looking arrangement of the blastomeres when looking from the animal pole (Figure 4.2).

During the second spiral cleavage, the spindles oriented in a sinistral manner in all the blastomeres (Figure 2.7, yellow arrows). The final spindle position was determined as early as at the metaphase of this cleavage. Both the micromeres (Figure 2.7 B) and the macromeres (Figure 2.7 C) images showed the same orientation. The closure of the cytokinetic ring also indicated that the cleaving direction was sinistral (Figure 2.7 D-G). In contrast of the previous cleavages, the cleavage furrow wasn't organized from one side of the cell, and the closure of the cytokinetic ring was symmetric at the cleavage furrow. The spindle orientation and cleavage axis resulted in a 16-cell embryo with four layers of blastomeres (Figure 2.7 H, indicated with different color codes).

## 2. Early development of *P. dumerilii*

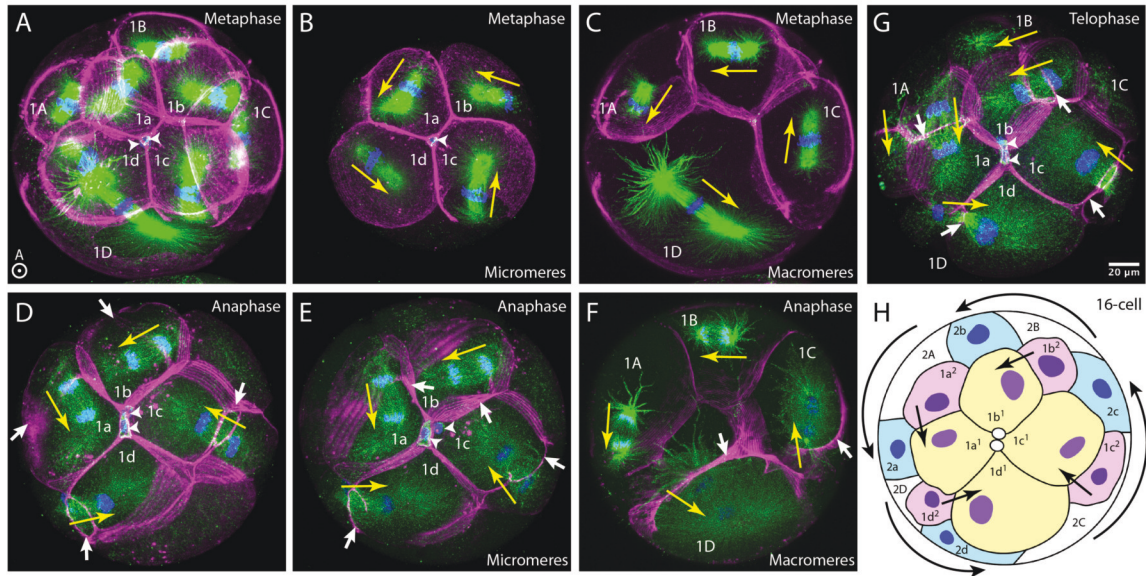


**Figure 2.7.:** The second spiral cleavage (fourth embryonic cleavage) of *P. dumerilii*. The embryos were incubated at 18 °C and fixed at 180-190 mpf. Microtubules were labeled with anti- $\alpha$ -tubulin antibody (green). The cell membrane was labeled with phalloidin (magenta) and the nuclei with DAPI (blue). All the images were captured from the animal view. (A-C) Z-projection of the whole embryo (A), the micromere layer (C), or the macromere layer (D) from the animal pole showed the metaphase of the division with mitotic spindle orientation in each cell. (D-F) Z-projection of the whole embryo (D), the micromere layer (E), or the macromere layer (F) from the animal pole showed the anaphase or early telophase of the division with mitotic spindle orientation and cytokinetic ring closure of each cell. 1C and 1D macromeres entered telophase earlier than 1A and 1B. (G) All blastomeres entered telophase. The Z-projection showed four micromeres and two macromeres with their division axes. (H) The illustration of a 16-cell embryo with the orientation of the micromeres and macromeres (2A-2D). Arrowhead: polar body. White arrow: cytokinetic ring. Yellow/Black arrow: cleavage direction toward the animal pole. Scale bar: 20  $\mu$ m.

The division orientation shifted between each spiral cleavage and thus, the cleavage axis and spindle orientation of the third and the fourth spiral cleavages were with dextral and sinistral rotation, respectively (Figure 2.8, 2.9). The spindle orientation was decided as early as during metaphase (Figure 2.8 A, 2.9 A). The four

## 2.2. Orientation of the cytoskeletal elements

daughter micromeres at the animal pole (Figure 2.9 B,C, indicated with green color code) were smaller than the other blastomeres and were known to develop into the apical tuft, a brain region of the trochophore larva. Interestingly, C and D lineages entered cell division earlier than A and B lineages throughout all the four spiral cleavages (Figure 2.4 E,F, 2.7 D, 2.8 B,C, 2.9 B). For detailed analysis please see Figure 2.12 and lineage tracking data (Figure 2.11) in Section 2.3.

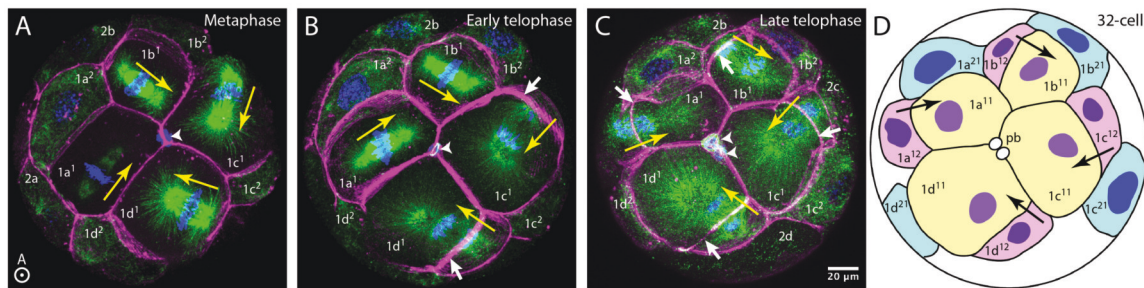


**Figure 2.8.: The third spiral cleavage (fifth embryonic cleavage) of *P. dumerilii*.** The embryos were incubated at 18 °C and fixed at 210-220 mpf. Microtubules were labeled with anti- $\alpha$ -tubulin antibody (green). The cell membrane was labeled with phalloidin (magenta) and the nuclei with DAPI (blue). All the images were captured from the animal view. Part of the embryo was projected showing 1a<sup>1</sup>, 1b<sup>1</sup>, 1c<sup>1</sup>, and 1d<sup>1</sup> micromere (1q<sup>1</sup> quartet). (A) The spindle orientation was decided as early as in metaphase of these micromeres. (B, C) 1c<sup>1</sup>, and 1d<sup>1</sup> blastomere entered telophase earlier than 1a<sup>1</sup> and 1b<sup>1</sup> blastomeres. (H) The illustration of part of a 32-cell embryo with the orientation of the micromeres at animal pole. Arrowhead: polar body. Arrow: cytokinetic ring. Yellow/Black arrow: cleavage direction toward the animal pole. Scale bar: 20  $\mu$ m.

The spiral looking embryo with four quadrants was best visible at 64-cell stage. Most of the micromeres kept dividing with alternating, spiral pattern after 64-cell. There were also signs for bilateral division pattern, e.g., 2d<sup>112</sup> and 4d blastomere (Kitamura & Shimizu, 2000). The cell cycle was arrested in the 4A-4D macromere (4Q quartet) after the fourth spiral cleavage. The cell lineages tracking of the later stages were done by Dr. Mette Handberg-Thorsager, which showed that the 4C

## 2. Early development of *P. dumerilii*

and 4D macromeres divided again, independently, to 5C and 5D at respectively 9:57 hpf and 10:36 hpf. 5D then divided to form a sixth quadrant 6D at 17:04:30 (Handberg-Thorsager et al., unpublished).

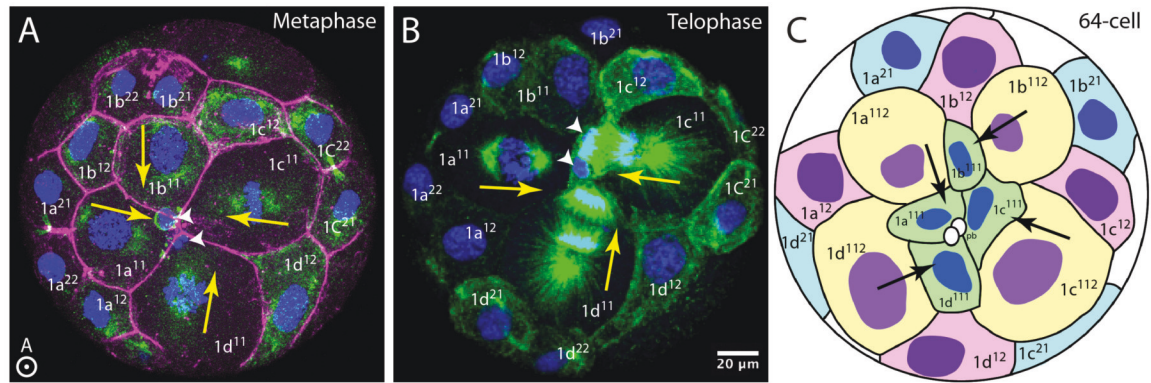


**Figure 2.9.: The fourth spiral cleavage (sixth embryonic cleavage) of *P. dumerilii*.** The embryos were incubated at 18 °C and fixed at 240-250 mpf. Microtubules were labeled with anti- $\alpha$ -tubulin antibody (green). The cell membrane was labeled with phalloidin (magenta) and the nuclei with DAPI (blue). All the images were captured from the animal view. Part of the embryo was projected showing the micromeres at the animal pole. The 1c<sup>11</sup>, and 1d<sup>11</sup> micromeres entered metaphase (A) and telophase (B) earlier than 1a<sup>11</sup>, and 1b<sup>11</sup> micromeres. (C) The illustration of part of a 64-cell embryo with the orientation of the micromeres at animal pole. Arrowhead: polar body. Arrow: cytokinetic ring. Yellow/Black arrow: cleavage direction toward the animal pole. Scale bar: 20  $\mu$ m.

## 2.3. Live-imaging and lineage tracking of *P.*

### *dumerilii* spiral cleavages

The immunostainings of the fixed embryos helped me describe the first two cleavage and the spiral cleavage processes with multiple fluorescent markers. To gain insight into the blastomeres and intracellular dynamics during spiral cleavages, I performed mRNA injections into the zygote and live-imaged the embryo development. I wanted



### 2.3. Live-imaging and lineage tracking of *P. dumerilii* spiral cleavages

to first confirm the old cell lineage studies (Ackermann et al., 2005; Vopalensky et al., 2019) with newer technology and dissect the early cell lineages in depth with regard to the cell cycles. I injected mRNAs encoding for *lyn-gfp* (labels the plasma membrane) and *h2b-mCherry* (labels the histone of the DNA) into the zygote and subsequently, starting from 4-cell stage, live-imaged the whole embryo at culturing temperature (18°C) by light sheet fluorescence microscopy (LSFM). I imaged from 5 angles to cover the entire embryo and to ensure that the image registration would work. The temporal resolution was 90 sec, which was enough for cell tracking. The Fiji plugin Multiview-Reconstruction (Preibisch et al., 2010) using beads as reference points was used for the image registration and fusion. The fused images were isotropic, which allowed full-range observation and tracking of the cell lineages. The fluorescent signal developed within two cell cycles thus from 4-cell stage, the nuclei of the four macromeres were detected and tracked. I used the Fiji plugin MaMuT (Wolff et al., 2018) to manually track the cell lineages of two embryos starting from 4-cell stage (A, B, C, and D macromeres) for four cell cycles (until 64-cell stage).

#### 2.3.1. Clonal domain formation

We know from the literature (Shibazaki et al., 2004; Grande & Patel, 2009; Lambert, 2010; A. H. Fischer et al., 2010; Girstmair & Telford, 2019) that the spindle inclination during the first spiral cleavage and the alternating cleaving axes throughout the four spiral cleavages lead to an embryo with a spiral looking cellular organization when observing the embryo from the animal pole (Figure 2.10). Formation of the four quadrants is a stereotypic feature during spiralian development (Ackermann et al., 2005; Girstmair & Telford, 2019; Vopalensky et al., 2019). It's also seen by projecting

## 2. Early development of *P. dumerilii*

the four tracts of the four macromere lineages. With my live-imaging recordings of developing embryos, all the cell identities can be tracked and annotated. The tracking started at 4-cell stage, each of which can easily be identified as A, B, C or D macromere based on their sizes and positions. The D macromere is the biggest macromere, the C macromere is the second biggest, the B macromere is opposite to the D macromere, and the A macromere is opposite to the C macromere. Looking from the animal pole, the macromeres were thus organized A-B-C-D along a clockwise direction. The lineage tracts of each blastomere was color-coded to easily distinguish each blastomere cell lineage. The position of the DNA during cell division was used to indicate the cleavage orientation in the live-imaging movies. These were comparable with the fixed images, indicating that the injection of mRNAs and live-imaging have little disturbance to the embryo development. The projection of all the tracts together with the 4-cell stage showed that each lineage formed a clonal domain, which occupied a quadrant of the embryo (Figure 2.10 C). Interestingly, we knew from later cell lineages by Dr. Mette Handberg-Thorsager that this clonal distribution is maintained in the brain in the 1 dpf trochophore larva (Vopalensky et al., 2019).



### 2.3. Live-imaging and lineage tracking of *P. dumerilii* spiral cleavages

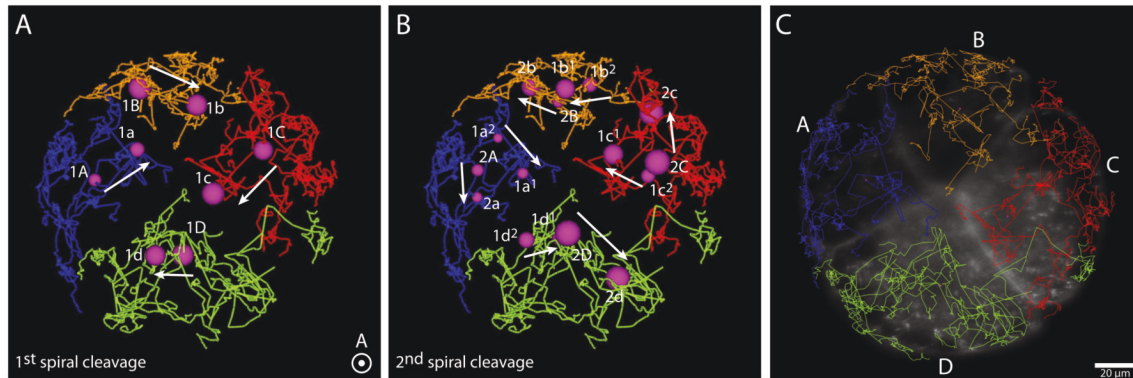


**Figure 2.10.: Spiral cleavage led to clonal domain formation in *P. dumerilii*.** (A, B) The first two spiral cleavages were plotted against the entire cell lineage tracts from A, B, C and D. (C) Tracks of the four lineages from 4-cell to 64-cell were plotted on top of the actual A, B, C, and D macromeres, revealing the clonal domain formation in *P. dumerilii* early development. The positions of the DNA of the first two spiral cleavages were shown with magenta spheres, and the cleavage orientation was indicated with arrows. The tracks and the image were taken from animal view. Scale bar: 20  $\mu\text{m}$ .

#### 2.3.2. Variation of cell cycles during *P. dumerilii* early cleavages

Initially, the early *P. dumerilii* cell lineages were described by observing through a bright-field microscope (Ackermann et al., 2005). My *P. dumerilii* cell lineages covering spiral cleavage and based on fluorescent markers has allowed me to study the exact division timing and synchrony in more details (Figure 2.11). The first two spiral cleavages were relatively synchronous. The D blastomere divided slightly earlier than the other three blastomeres. In the third and the fourth spiral cleavage, not all the blastomeres divided at the same time, but the correlated lineages from each quadrant showed high synchrony in cell cycle, e.g.,  $1a^{11}$ ,  $1b^{11}$ ,  $1c^{11}$ , and  $1d^{11}$ , or  $1q^{11}$  in short. Moreover, the cell lineage tree showed that the micromeres closer to the

## 2. Early development of *P. dumerilii*

animal pole tended to divide earlier. However, unlike the trend of the micromeres, the macromeres, which are located at the vegetal pole, divided earlier than some of the micromeres. 3D blastomere divided the first among all the blastomeres in the fourth spiral cleavage. The 2d lineage also performed faster cell cycle in the 2q quartet, suggesting that the D lineage is potentially leading/guiding the cleavages during *P. dumerilii* early development. Thus, my cell lineages confirmed older cell lineage studies, but also contributed with new knowledge into the asynchronous behavior of some of the macromeres and micromeres.

### 2.3. Live-imaging and lineage tracking of *P. dumerilii* spiral cleavages

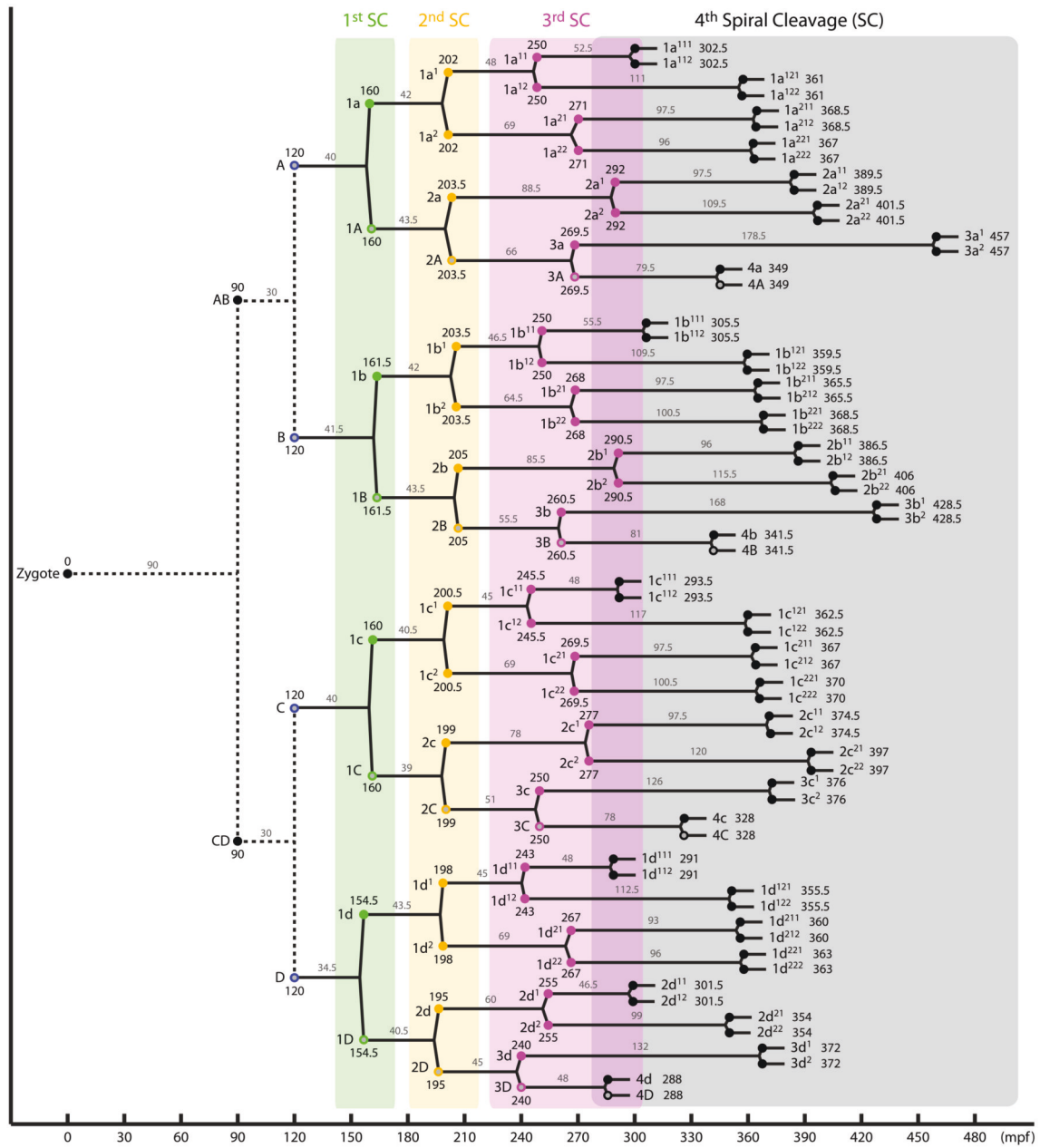


Figure 2.11.: Early lineage tracking of *P. dumerilii*.

**Figure 2.11.: Early lineage tracking of *P. dumerilii*.** The embryo was labeled with *lyn-mCherry* and *h2b-gfp* mRNA and live-imaged with Zeiss Z.1 SPIM from 4-cell stage at 18°C. 5 z-stacks with a 72° rotation of each view were taken and the images were registered and fused with Fiji Multi-view reconstruction plugin. The cell lineage

## 2. Early development of *P. dumerilii*

of the two initial divisions prior to spiral cleavage were based on the observations from DIC imaging and fixed, immunostained embryos (dashed lines). The resulting A, B, C, and D macromeres were tracked using live-imaging recordings, at a temporal resolution of 90 sec, of fluorescently labeled nuclei (H2B-GFP) and the tracking and annotation software MaMuT. The numbers at the nodes indicated the actual time of division. When two sets of chromosomes can be observed in mitosis, they were defined as two cells and the branch of the lineage was created. The numbers above the lines indicated the time span from one division to the next. Each spiral cleavage was color-coded both the nodes and the background color. Green, first spiral cleavage (SC); yellow, second SC; magenta, third SC; grey, fourth SC. Each node was annotated with the cell identity. The macromeres were indicated with grey circles in the nodes. Each lineage was indicated next to the node.

Asynchrony in the cleavages was not only shown with the cell lineage tree, but also observed by immunostaining (Figure 2.12 A,B), DIC imaging (Figure 2.12 C-F) and live-imaging, where the zygote was injected with mRNAs encoding for H2B-mCherry, Lyn-mCherry, and EMTB-3xGFP (Figure 2.12 G-J). The asynchrony during the first spiral cleavage was relatively slight. All the four macromeres started cell division at the same time. However, the D blastomere entered telophase prior to the other three blastomeres (Figure 2.12 A). The C blastomere entered telophase after D but before A and B (Figure 2.12 B). This resulted in a slight difference in division time mapped in the lineage tree (Figure 2.11). The asynchrony of the second, third, and fourth spiral cleavage can be captured with live-imaging. It is observed with DIC microscope revealing that the nuclear envelope breakdown happened earlier in 1c and 1d blastomeres of the second spiral cleavage, and in 1c<sup>1</sup> and 1d<sup>1</sup> blastomeres of the third spiral cleavage, suggesting that the asynchrony was not due to the interference of mRNA injection into the embryos (Figure 2.12 D,F). Recruitment of the cytoskeleton was also asynchronous during spiral cleavages. 1a<sup>1</sup> and 1b<sup>1</sup> were at prophase when 1c<sup>1</sup> and 1d<sup>1</sup> blastomeres entered metaphase, and the difference continued throughout the

### 2.3. Live-imaging and lineage tracking of *P. dumerilii* spiral cleavages

division, resulting in the earlier separation of the DNA in the anaphase and telophase of  $1c^1$  and  $1d^1$  (Figure 2.12 G,H). The asynchrony increased in the fourth spiral cleavage, leading to the earlier completion of  $1c^{11}$  and  $1d^{11}$  than  $1a^{11}$  and  $1b^{11}$  blastomeres (Figure 2.12 I,J). Therefore, although the asynchrony of the sister lineages in each cell cycle was very little, the difference accumulated resulting in the diverse cell cycle as shown in the lineage tracking data (Figure 2.11). The cell cycle variety increased also in the fourth spiral cleavage and this may be a consequence of or may lead to cell fate specification.

## 2. Early development of *P. dumerilii*

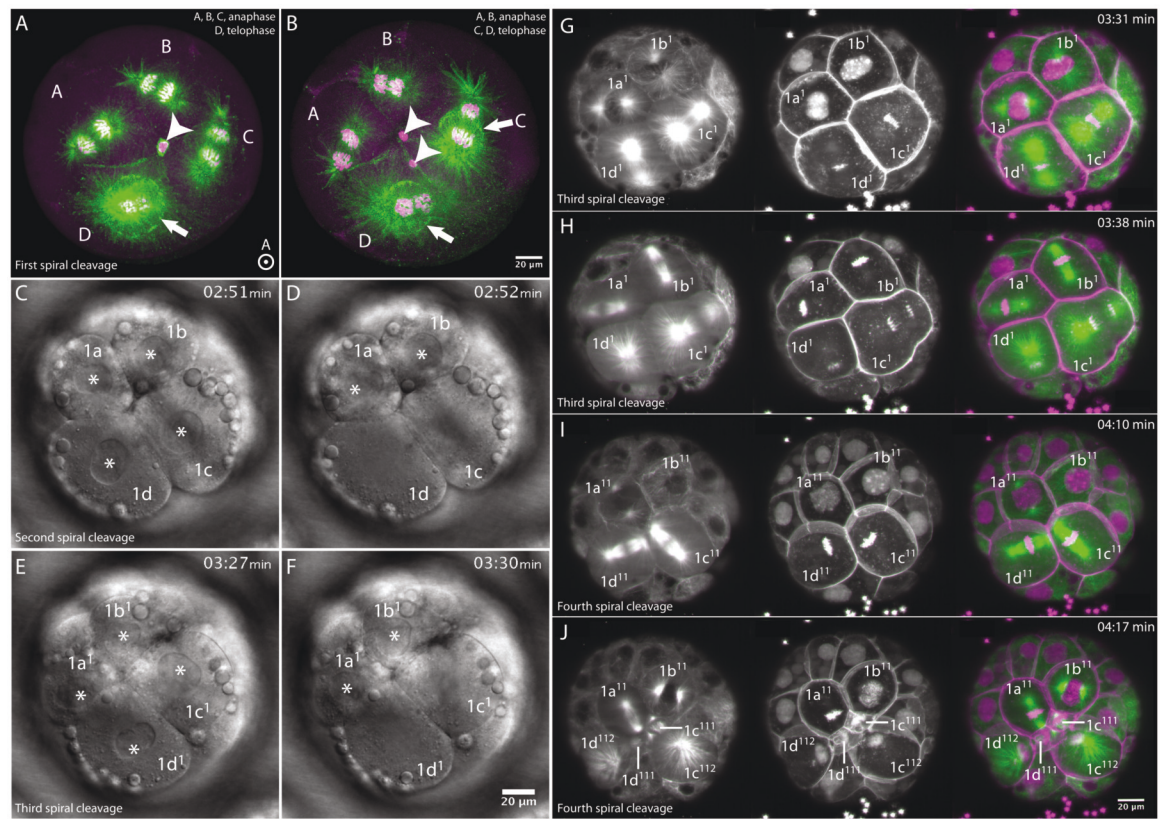


**Figure 2.12.: C and D lineages entered cell division prior to A and B lineages.** All the images were taken from the animal view. (A, B) The embryos were incubated at 18°C and fixed at 90-100 mpf. Microtubules were labeled with anti- $\alpha$ -tubulin antibody (green) and the nuclei with DAPI (magenta). (A) The cytokinetic ring occurred in D prior to A, B, and C macromeres. (B) C and D blastomeres entered telophase while A and B blastomeres were still in anaphase. (C-F) The embryos were live-imaged with DIC microscope. Nuclear envelope breakdown occurred earlier in 1c and 1d blastomeres during the second spiral cleavage (C and D) and in 1c<sup>1</sup> and 1d<sup>1</sup> blastomeres during the third (E and F) spiral cleavage. (G-J) Microtubule (green), nuclei (magenta), and plasma membrane (magenta) were labeled by mRNA injection and live-imaged by SPIM. The images were taken from the third spiral cleavage. The microtubules were shown in the left panels, plasma membrane and nucleus in the middle panel, and the merge of the three in the right panel with microtubule in green and the other two components in magenta. 1c<sup>1</sup> and 1d<sup>1</sup> blastomeres entered metaphase and anaphase prior to 1a<sup>1</sup> and 1b<sup>1</sup> blastomeres during the third spiral cleavage (G and H) and the fourth spiral cleavage (I and J). The format of the timestamp is hr:min. Asterisk: nucleus. Scale bar: 20 μm.



#### 2.4. Cell autonomy of spiral cleavage and determinate development

In summary, a spiral looking embryo is achieved through the following cellular processes. First, the synchronous cleavages of the first three embryonic divisions with the spindle inclination, resulting in an 8-cell embryo with 4 micromeres and 4 macromeres and a dextral rotation between them (Figure 2.2, 2.3, 2.4). Second, the perpendicular cell division and thus cell organization between each spiral cleavage and synchronous division timing results in an embryo, which is divided into four clonal domains. Each quadrant and clonal domain represents one for the four cell lineages (Figure 2.10). Therefore, a spiral looking embryo is achieved after four spiral cleavages (Figure 2.9). However, in a finer timescale, I demonstrated that the cell cycle of each lineage was not exactly the same. D lineage possesses the fastest cell cycle. C lineage was the second, and A and B lineage were the last. The difference between the lineages was within one cellular event during the mitosis, e.g., 1c<sup>11</sup> and 1d<sup>11</sup> were in the metaphase while 1a<sup>11</sup> and 1b<sup>11</sup> were in the prophase. Therefore, the general synchrony of each lineage during each spiral cleavage is preserved, and the blastomeres also undergo specification during *P. dumerilii* early embryogenesis.

## 2.4. Cell autonomy of spiral cleavage and determinate development

The spiralian are described as determinate developers with a developmental strategy executed through mainly cell autonomous processes (Costello, 1945). Various of the cellular mechanisms of spiral cleavage have been described in gastropods (Shibazaki et al., 2004; Kuroda et al., 2009; Davison et al., 2016; Kuroda, 2014). Also, it was demonstrated that the chirality can be manipulated through physical interference of

## 2. Early development of *P. dumerilii*

an 8-cell gastropod embryo (Kuroda et al., 2009; Kuroda, 2014). In another phylum of animals with determinate development, the nematodes, it was reported that the cell orientation is influenced by the presence and shape of the eggshell (Yamamoto & Kimura, 2017). This all suggests that the relative position of the cells is not only controlled by the blastomere itself, but may also be influenced by the physical constraint from the outside of the embryo.

To investigate if the dextral orientation of the cells in *P. dumerilii* spiral cleavage is cell autonomous, or if the physical constraint executed by the eggshell plays a role in positioning the cells, the embryos were dechorionated during zygotic stage, and allowed to develop in natural seawater. Three batches of embryos (50-100 embryos in each biological replicate) were examined and most of the dechorionated zygotes processed through the first two asymmetric divisions as the wild type embryos, resulting in 4 macromeres in a plane with the D macromere the biggest (Figure 2.13 A-C). Cytosolic components (ooplasm versus lipid droplets and yolk granules) segregated as in the wild type embryo. The nutritional oil droplets were positioned toward the vegetal pole of the embryos, while the nuclei were visible at the animal pole (Figure 2.13 C, marked with the asterisks). Also in the 4-cell embryos, the A and C macromeres contacted each other at the animal pole (Figure 2.13 C) as was seen in the wild type embryos (Figure 2.4 A). This indicated that the establishment of the embryo animal-vegetal axis was independent of the eggshell.

The first spiral cleavage was described in Section 2.2.2 and contained a rotation in the division plane, which resulted in the dextral orientation of the micromeres. The dechorionated embryos were incubated on the glass petri dishes covered by natural seawater at 18 °C. In the dechorionated embryos, the animal pole was attached to



#### *2.4. Cell autonomy of spiral cleavage and determinate development*

the bottom of the glass petri dish, but the cells could still move in the water. The first spiral cleavage was asymmetric with the smaller micromeres forming in a dextral orientation, as in the wild type embryos (Figure 2.13 D, indicated by arrows). Thus, the division plane was not influenced by the dechoriation and the dechorionated embryos had clearly two layers of blastomeres, the micromeres and the macromeres. However, the blastomeres formed a spherical structure without the eggshell in comparison to the oval shape in the wild type embryos. The rotational, alternating cleavage planes were observed during the second to the fourth spiral cleavage as well, suggesting that the spiral cleaving capability itself was not influenced by the physical constraint from the eggshell.

The physical constraint can be generated from outside of the embryo through a mechanical force generator or a molecular linker between the eggshell and the embryo. Alternatively, this constraint can be obtained through molecular interactions between the blastomeres. To investigate if all of the four macromeres are required to perform proper spiral cleavage, the embryo was dissociated at 4-cell stage and a partial embryo was further cultivated in natural seawater. I dissociated the C and D blastomeres from the embryo and imaged the A and B blastomeres. The division plane of the partial embryo was the same as the intact, wild type embryo. The 1a micromere was located to the left of the 1A macromere and 1b is in the back of 1a and 1B (Figure 2.13 E,F). This indicated that the division axis of both 1a and 1b was in a dextral orientation. Therefore, it suggested that the spindle inclination and division plane determination leading to spiral cleavage do not depend on an entire embryo or all the four blastomeres being in contact. I have here shown that A and B blastomeres can perform spiral cleavage in the absence of C and D blastomeres, which indicated that spiral cleavage may be a cell autonomous event.

## 2. Early development of *P. dumerilii*

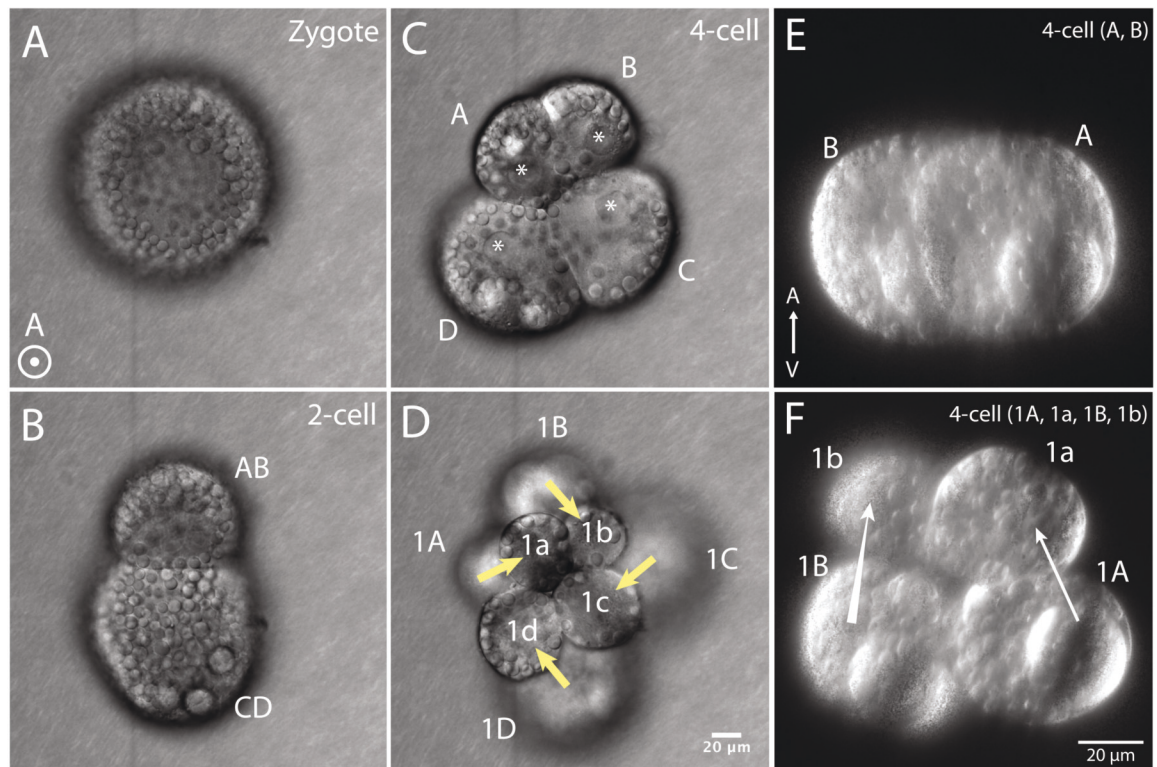


**Figure 2.13.: Three initial cleavages of intact or partial *P. dumerilii* embryos in the absence of the eggshell.** Intact (A-D) and partial (E-F) embryos were monitored. (A-C) The dechorionated zygote (A) underwent two asymmetric divisions (B, C) generating A, B, C and D macromeres as in the wild type embryo. (D) The embryo performed a clockwise rotation of the micromeres in the third cleavage (first spiral cleavage), as in a wild type embryo. (E) The macromeres were dissociated at 4-cell stage. The A and B macromeres, still together, were recorded during the first spiral cleavage. (F) The micromere (1a, 1b) positions in the 4-cell embryo (1A, 1a, 1B, 1b) were shifted in a dextral orientation compared to the macromeres (1A, 1B) following the first spiral cleavage in a similar manner as in the intact 8-cell embryo. A-D were imaged from the animal pole. E and F were imaged from the side view. Scale bar: 20 µm.

To investigate whether the embryogenesis is influenced after dechorionation, or if the eggshell is crucial to the morphology and the function of the larva later in embryogenesis, the dechorionated zygotes were incubated in the natural seawater at 18 °C till 24 hpf. If the embryo stays intact, it develops as the wild type into a

#### 2.4. Cell autonomy of spiral cleavage and determinate development

free-swimming larva (Figure 1.3). Both the final four oil droplets (one per macromere) and the ciliated band can be seen (Figure 2.14 A, indicated by the arrow), indicating the cell differentiation and positioning was not affected. However, without the presence of the eggshell, the blastomeres were easily dissociated during development. Therefore, many partial embryos were observed. As the arrowheads showed in Figure 2.14 A, the partial embryo with one oil droplet in the tissue suggested it contained only one of the four macromeres. The dissociated blastomeres can only develop into partial embryo, indicating that the cell fates were determined early in development. Some dissociated cells developed into tissues with the ciliated cells (Figure 2.14 B), which were mobile in seawater, suggesting that both the macromeres and micromeres had their fates determined early in development.

Although the eggshell did not play a critical role during spiral cleavage, it did have crucial function for *P. dumerilii* embryogenesis. As mentioned above, absence of the eggshell led to weaker cell contact and in many cases, cell dissociation during development. The eggshell kept all the blastomeres to form an intact larva. Moreover, the naked blastomeres becomes sticky and attached to the external substance when the eggshell was absent. When two or more zygotes attached to each other, the embryos conjoined each other (Figure 2.14 C). The conjoined larvae have functional organs, but the tissue was connected between larvae. Therefore, the larvae cannot swim and died eventually. These results suggested that the blastomeres do interact with the external substances, and the eggshell played a critical role to keep the individual intact and proper development during embryogenesis.

## 2. Early development of *P. dumerilii*

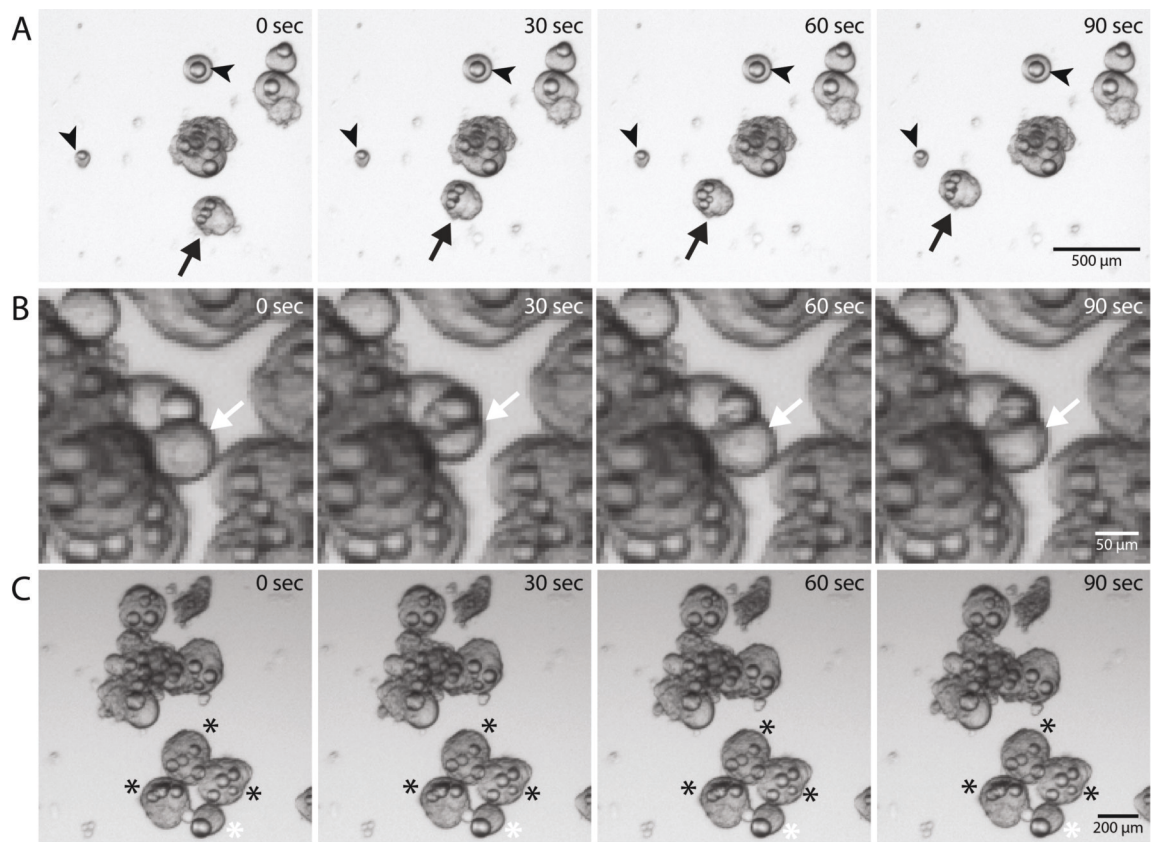


**Figure 2.14.: Development of *P. dumerilii* embryos without eggshell.** The zygotes were decorionated at the zygote stage and incubated in natural seawater at 18°C until 24 hpf. Time-lapse movie recorded by bright-field microscopy of the *P. dumerilii* development started from 24 hpf. (A) The free swimming larva was indicated with an arrow. Two partial embryo with one oil droplet in the tissue were indicated with the arrowheads. Scale bar: 500 μm. (B) Multiple larvae were conjoined during development due to lack of the eggshell. The asterisks indicated that three larvae (black) and one partial embryo (white) were conjoined. Scale bar: 200 μm. (C) A partial embryo with the differentiated ciliated cells was able to rotate and move (white arrow). Scale bar: 50 μm.

## 2.5. Early polarization of the *P. dumerilii* embryo

Axes establishment is one of the first events during embryogenesis. Different embryo may use different mechanisms to set the embryonic axes (Jeffery, 1992; Gotta & Ahringer, 2001; Nakamoto et al., 2011; Takaoka & Hamada, 2012; Wotton et al., 2015). In *P. dumerilii*, the animal and vegetal poles are determined upon fertilization. The sperm entry point forms vegetal pole and the opposite position of the zygote becomes then the animal pole (Nakama et al., 2017). To investigate if the embryo polarity is also built at the molecular level, the *P. dumerilii* par genes were identified, cloned, and fused with the fluorophores for mRNA injection. One *Pdupar1*, one *Pdupar3*, one *Pdupar4*, and one *Pdupar6* genes were identified from the transcriptome database (Section 7.4) and cloned (Appendix A.4, A.6). Since no antibodies against the *P. dumerilii* Par proteins were available, I wanted to investigate the protein localization by mRNA injections. The coding region of each gene was cloned into pCS2+ plasmid with the fluorophore, *sgfp*, coding region at the 3' end. The *Pdupar* mRNAs were *in vitro* transcribed and co-injected into the zygote with the mRNA for a nuclear marker *h2b-mCherry*. The embryos were incubated for 8 hr at 18 °C for signal development. *PduPar1* and 4 did not show any specific localization in the embryos. *PduPar3* localized slightly to apical and largely to the lateral cytoplasmic membrane, especially in the micromeres (Figure 2.15 A). *PduPar6* was in the cytosol and at the cell membrane (also largely lateral) in the micromeres (Figure 2.15 B). Very little signal was detected at the basal plasma membrane. Generally, the signal was higher in the micromeres. The macromeres, which were at the vegetal pole, had lower *PduPar6* localization and *PduPar3* was barely detected. This result showed a molecular polarity from the animal pole to vegetal pole of *P. dumerilii* embryo, by largely segregated the *Pdupar* mRNAs



## 2. Early development of *P. dumerilii*

into micromeres, or active degradation of the Par3/6 proteins in the macromeres. The localization of Par3/6 to apical and lateral plasma membrane also indicated that Par may be involved in cell polarity establishment during the early development of *P. dumerilii*.

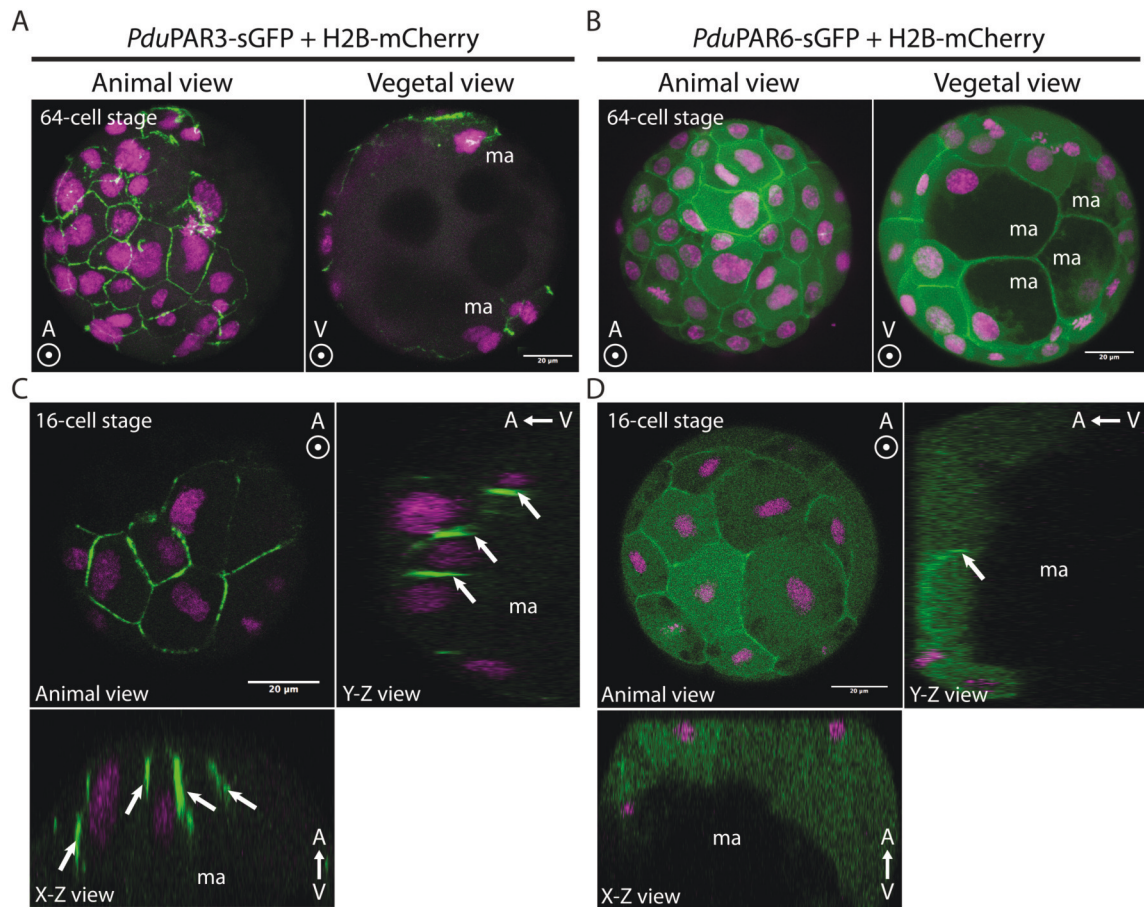


**Figure 2.15.: Localization of Par components in the early *P. dumerilii* embryo.** *Pdupar3* or *Pdupar6* mRNA (in green) was injected into the zygote together with the nuclear marker *h2b-mCherry* mRNA (magenta). (A) *PduPar3* was localized to the plasma membrane in the micromeres at the animal pole. (B) *PduPar6* was localized to the plasma membrane and the cytosol in both the micromeres and macromeres. (C, D) The orthogonal view showed that *PduPar3* and *PduPar6* were largely localized to the cell periphery as well as toward the animal pole. Arrow: *PduPar3/6* expression. ma: macromere. The cells without labeling were micromeres. Scale bar: 20 μm.

## 2.6. Cellular and intracellular dynamics during spiral cleavages

The difference in Par localization between the micromeres and macromeres implied that the micromeres and macromeres may have different cell behavior during embryogenesis. This difference was not only seen in the molecular expression, but also in the migration of the nuclei and the cellular component distribution. The nuclei of the micromeres stayed at the center of the cell at the animal pole through the four spiral cleavages (Figure 2.16 E-H). However, the nuclei of the macromeres showed a much more dynamic behavior. Localized toward the apical side of the macromeres, the nuclei alternated in position between the left versus right side of the cell between each spiral cleavage (Figure 2.16 I-P). Further, the nuclei tracking showed that the nuclei of the macromeres traveled further in distance than the micromeres (Figure 2.16 A-D).

The movement of the nuclei in the macromeres may be passive due to the movement of the whole cell or due to the production of a force in the cytoplasm, which carries the nuclei along with it. Alternatively, the nuclei movement could be active within the cells. To investigate the dynamics of the nuclei position within the cell, a combination of mRNAs encoding for cytoskeletal components, DNA, and plasma membrane were injected into the zygotes. As described in the previous sections, spiral cleavage contained alternating orientation of the division axes, both in the micromeres and macromeres. However, the mechanisms to achieve this was different between the micromeres and macromeres. In the micromeres, the nuclei stayed at the center of the cell, and the mitotic spindle changed direction to achieve the alternating division axes. Therefore, the movement of the nuclei in the cell tracking was due to the migration of

## 2. Early development of *P. dumerilii*

the micromeres (Figure 2.16 A-D). On contrary, the nuclei of the macromeres were at the side of the blastomere and migrated in the cell between each spiral cleavage. The cytoskeletal components (non-muscle-myosin regulatory light chain, *PduRlc1* and F-actin, detailed comparison see Section 4.2) concentrated around the nuclei, migrating with them between the divisions (Figure 2.16 I-P). Strikingly, an accumulation of the actin around the nuclear envelope took place right before nuclear envelope breakdown at the beginning of mitosis (Figure 4.4, see Section 4.2.2). These experiments were performed together with Dr. Mette Handberg-Thorsager.

Actin is clearly an important cellular factor during the cell cycle. A molecular player, which often forms a complex with actin in the cell cortex, is non-muscle-myosin (Matzke et al., 2001; Maddox & Burridge, 2003; Sedzinski et al., 2011; Stewart et al., 2011; Levayer & Lecuit, 2012; Alvarado et al., 2013; Biro et al., 2013; Carvalho et al., 2013; Maliga et al., 2013; Beach et al., 2014; Billington et al., 2015; Murrell et al., 2015; Ennomani et al., 2016; Maître et al., 2016; Chugh & Paluch, 2018). I therefore cloned and tested the localization of the 6kb large *P. dumerilii* non-muscle-myosin, *Pdunmm*, by mRNA injections. Unfortunately, the fluorescent signal was only visible after the spiral cleavage period. This could be because it did not localize to any cellular structure during early development or because of protein conformation issues. At 24 hpf, *PduNmm* signal was visible and localized to the cell cortex (Figure 3.3 C, see Section 3.2.3). Taken together, the alternating division axes in the macromeres relied on a combination of nuclei migration, re-organization of the cytoplasmic actomyosin and organization of the mitotic spindle. Further, the movement of the nuclei in the cell tracking was largely dependent on intracellular migration.

Based on my observations, we now had some first indications that the



## *2.6. Cellular and intracellular dynamics during spiral cleavages*

micromeres have different gene expression, cell polarity, molecular distribution, and mitotic mechanisms compared to the macromeres. All of these findings resulted in the completion of the spiral cleavage. However, how the spindles inclines and how the final cleavage plane is determined at the molecular and physical level, remain unsolved. To approach these questions, it is necessary to visualize the cytoplasmic components as early as during spiral cleavage to investigate the molecular mechanisms of it.

## 2. Early development of *P. dumerilii*

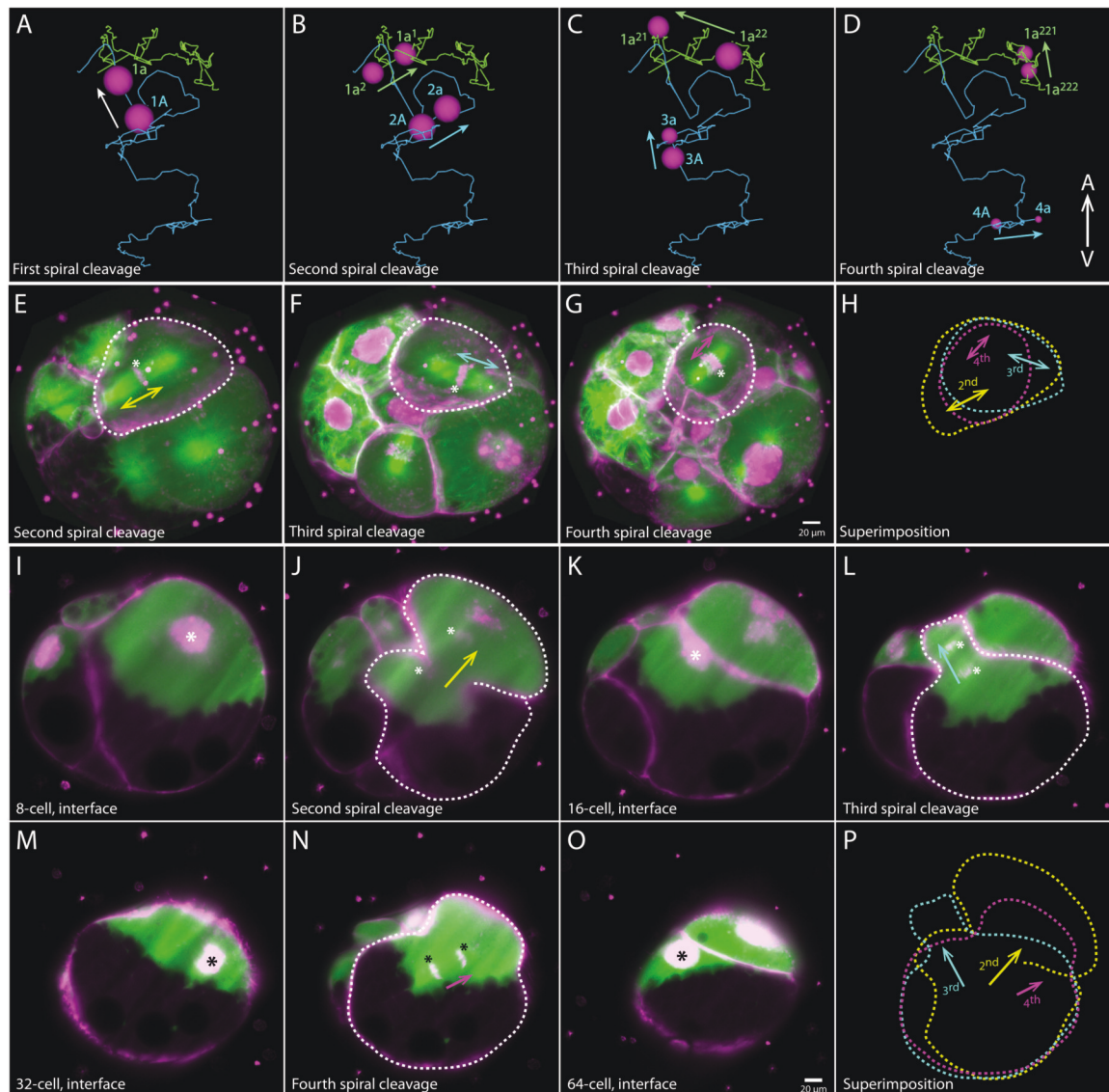


**Figure 2.16.: Alternating division axes and nuclei migration during spiral cleavages.**

**Figure 2.16.: Alternating division axes and nuclei migration during spiral cleavages.** (A-D) Nuclei tracking of the A lineage. The traces of the 4A macromere and the  $1a^{22}$  micromere were showed. The micromere tract was labeled with the green line and the macromere with the blue line. The division axes were indicated with arrows. (E-G) The zygote was injected with *h2b-mCherry* and *lyn-mCherry* mRNA to mark the nuclei and plasma membrane (magenta) and *emt6-3xgfp* mRNA to mark

## 2.6. Cellular and intracellular dynamics during spiral cleavages

the mitotic spindles (green). The outline of the micromere was illustrated with a dashed line. The division axes were indicated with double-headed arrows. (H) Superimposition the division axes of the three spiral cleavages in E-G. (I-O) The zygote was injected with *h2b-mCherry* and *lyn-mCherry* mRNA to mark the nuclei and plasma membrane (magenta) and *rlc1-sgfp* (non-muscle-myosin regulatory light chain 1 conjugated with sgfp) mRNA to label non-muscle-myosin. The outline of the micromere is illustrated with the dashed line. The division axes were indicated with arrows pointing toward the micromere side. (P) Superimposition the division axes of the three spiral cleavages in J, L, and N. Asterisk, DNA. All the images were taken from the side view. Scale bar: 20  $\mu\text{m}$ .



### 3. live-imaging of cytoskeleton dynamics during early *P.* *dumerilii* spiral cleavage

The progress of developing the methods to label cytoskeletal components in early *P. dumerilii* spiral cleavages is described in this chapter. For the early visualization of the cytoskeletal components, the following methods were optimized and investigated: chemical dye soaking or injection into the zygote (Section 3.1), mRNA injection of the cytoskeletal components conjugated with fluorescent protein (Section 7.13), optimization of the expression and labeling of the target genes in early development (Section 7.13), synthetic peptides injection for labeling cytoskeletal component and stability examination during live-imaging (Section 3.4).

### 3.1. Chemical dyes fail to label microtubule or actomyosin for live-imaging

One approach to label the very first cleavages of a zygote, is by soaking and immediate uptake and incorporation of a fluorescently labeled chemical dye by the zygote. To this end, I tested SiR-actin or SiR-tubulin to label the cytoskeletal components during early embryogenesis as which has been done in *C. elegans* spermatocytes (Hu et al., 2019) and various cell lines for live-imaging the cytoskeletal dynamics or for structural studies (Lukinavičius et al., 2014; Melak et al., 2017). The chemical dyes were used by either soaking the permeabilized zygotes (started at 60 mpf) in the dye or by injection of the dye into the zygote (at 60 mpf).

For the soaking experiment, 10  $\mu$ M verapamil was included in the soaking solution (total volume of 500  $\mu$ L) to block the calcium channels of the zygote and potentially decrease the expulsion of the SiR-dye from the cells. After a 4-hour soaking treatment of either 1  $\mu$ M of SiR-actin or SiR-tubulin, the fluorescent signal was hardly detected in the developing embryos (Figure 3.1 B). The injection of these dyes showed similar results (Figure 3.1 A). However, if the embryos were fixed (at 8-cell stage) prior to the treatment, and soaked with SiR-actin for 30 min, it showed a clear actomyosin labeling of the cell cortex and the nuclear envelope of the dividing blastomeres (Figure 3.1 C). Therefore, I hypothesized that the chemical was first taken up, but then actively removed from the embryos even in the presence of verapamil. To test this hypothesis in more details, the developing embryos were soaked in SiR-actin for 4 hr, started from 60 mpf, then 1  $\mu$ L of 16% PFA (= 0.032% PFA) was added to the 500  $\mu$ L) soaking solution, which killed the embryos in 30 sec but was not enough to fix the sample. The

### 3.1. Chemical dyes fail to label microtubule or actomyosin for live-imaging

sample was continuously imaged before and after the addition of PFA. Interestingly, the fluorescent signal, which was not detected in the live embryos after 4 hr of SiR-dye soaking, started to be seen at the cell cortex 10 min after the embryos were sacrificed (Figure 3.1 D). This indicated that the SiR-dye did label the cytoskeletal elements but was actively expelled by the living embryo. Thus, live-imaging of cytoskeletal dynamics with SiR-dyes in *P. dumerilii* is not possible, unless a blocker for the active removal of the SiR-dyes is found, which does not interfere with development.

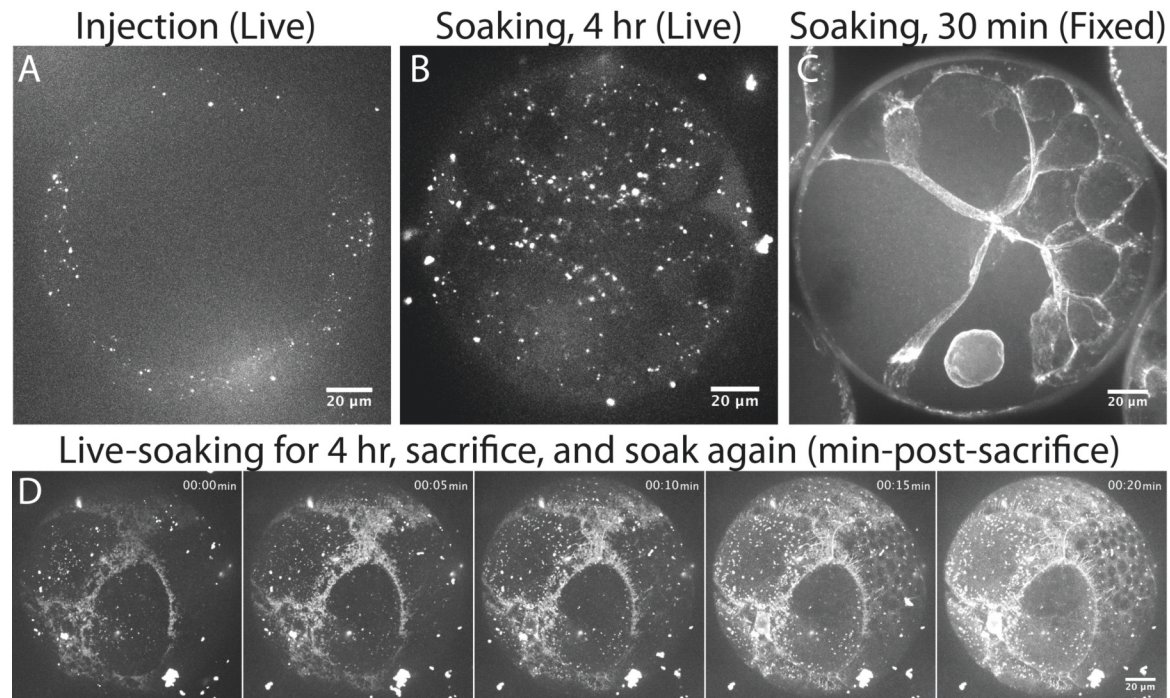


**Figure 3.1.: SiR-actin was not suitable for labeling F-actin fibers in the living *P. dumerilii* embryos.** (A, B) Intended labeling of F-actin fibers with SiR-actin in the live-developing embryos by injection (A) or following 4 hr of soaking (B). (C) SiR-actin dye labeled F-actin in the fixed embryos. The signal became visible within 30 min of soaking the fixed embryo in the SiR-actin dye. (D) Following the 4 hr treatment with SiR-actin (from B), the embryos were sacrificed by PFA, but continuously soaked in SiR-actin. The labeling of actin became visible within 10 min and continued improving. Time indicated minutes-post-sacrifice. The format of the timestamp is hr:min. Scale bar: 20 µm, n>100.

## 3.2. Labeling of cytoskeleton by gene cloning and mRNA injection

To visualize cytoskeletal components during spiral cleavage, actin binding peptide Lifeact, various non-muscle-myosin components, and the microtubule binding domain ensconsin (EMTB) were targeted and investigated in sequence level. The sequences of the homologous genes from other organisms (mouse, *D. melanogaster*, *C. elegans*, and *Capitella teleta*) were aligned and the conserved motifs of each gene were used to search for the homologous *P. dumerilii* genes by using the BLAST tool of the *P. dumerilii* transcriptomic database (Arendt lab, Heidelberg, Germany). The full coding region of each gene were cloned into the expression vector pCS2+ between the SP6 promoter and the SV40 poly-A signal allowing for synthesis of the full-length mRNAs. The DNA and protein sequences were listed in the Appendix A.6.

The *in vitro* transcribed mRNAs (200ng/μL) were injected into *P. dumerilii* zygotes and the embryos were incubated at 18 °C until 2-cell stage, then mounted in 0.6% low melting temperature agarose/seawater and imaged by spinning disk confocal microscope or SPIM.

### 3.2.1. Microtubule

EMTB is a microtubule binding protein. To visualize microtubule dynamics with EMTB, I used an expression construct with microtubule binding-domain of ensconsin (EMTB) from human (amino acids 18-283 of GenBank reference sequence X73882) conjugated to three GFPs (this construct was kindly provided by Norden lab, MPI-CBG,



### 3.2. Labeling of cytoskeleton by gene cloning and mRNA injection

Germany). The mitotic spindles in the *P. dumerilii* embryos with injected *emt6-3xgfp* mRNA were visible at 4-cell stage (Figure 3.2). The signal intensity got stronger throughout the spiral cleavage.

### 3. live-imaging of cytoskeleton dynamics during early *P. dumerilii* spiral cleavage

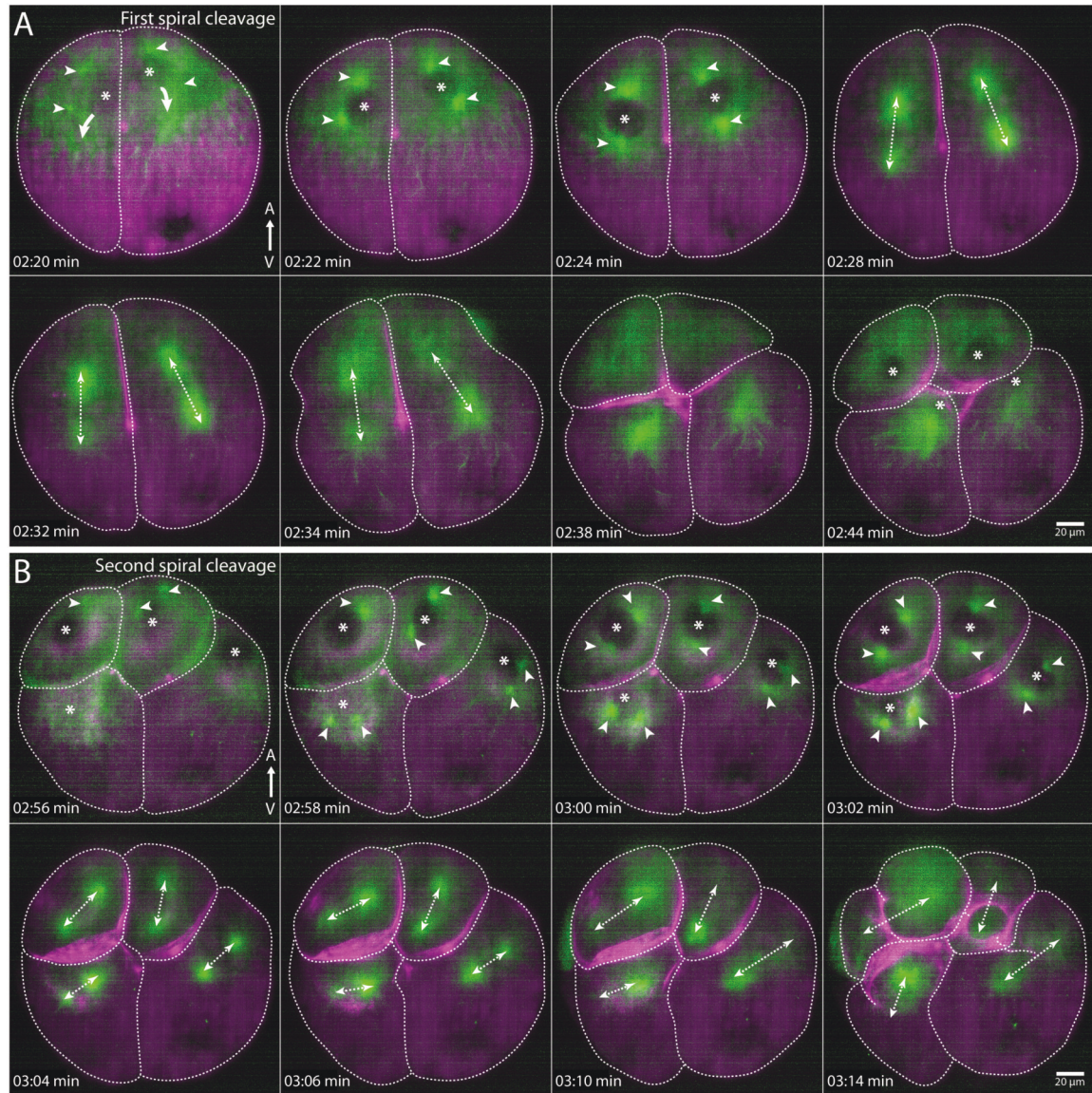


**Figure 3.2.: Early visualization of the cytoskeletal elements during spiral cleavages.** The zygote was injected with *emt6-3xgfp* (green) and *lifeact-mKate2* (magenta) mRNAs and imaged by SPIM. The expression of Lifeact can be detected but the intensity was not strong enough for further analysis. (A) MTOCs and the spindles were visualized from the first spiral cleavage. (B) The fluorescent signal increased through development. Arrowhead: MTOC. Asterisk: nucleus. Double-headed arrow: orientation of the mitotic spindles. All the images were taken from the side view and half of the embryo was projected. The format of the timestamp is hr:min. Scale bar: 20  $\mu\text{m}$ .

### 3.2.2. Actin

Lifect is a 17 amino acid peptide which binds to F-actin (J. Riedl et al., 2008). I used a construct with Lifect conjugated to a fluorophore at the 3' end and cloned it into pCS2+ to synthesize the mRNA. The small size of Lifect resulted in fast translation of the mRNA and the fluorescent signal was seen as early as at 4-cell stage at the cell cortex. However, the intensity was not strong enough for protein dynamic analysis during spiral cleavage. The optimization of Lifect expression in *P. dumerilii* is shown in Section 3.3.

### 3.2.3. Non-muscle-myosin

Non-muscle-myosin (Nmm) is an actin-binding protein involved in generation of the cell contractility. Generally, it consists of non-muscle-myosin heavy chain, the regulatory, and the essential light chains (Holmes, 2008). I searched the *P. dumerilii* transcriptomic database for the orthologs and was able to annotate two essential light chains (*elc1* and *2*), two regulatory light chains (*rlc1* and *2*), and the non-muscle-myosin II heavy chain (*nmm*) in *P. dumerilii*. The full-length sequences of the five genes were cloned and sequenced. For the sequence information please see Appendix A.6. *sgfp* was conjugated to the 3' end of each gene and the mRNAs were synthesized. For comparison with the homologous gene in *D. melanogaster*, *Pduelc1* and *2* are homologous to *cytoplasmic myosin light chain*, and *Pdurlc1* and *2* to *spaghetti squash*.

I injected the mRNAs related to non-muscle-myosin with the hope that this way I could label the actomyosin during spiral cleavage. Whereas the *PduElcs* are not visible in the early *P. dumerilii* embryos, the fluorescent *PduRlc* proteins were

### 3. live-imaging of cytoskeleton dynamics during early *P. dumerilii* spiral cleavage

visible from 4-cell stage, but the signal was weak and without specific localization. Both *PduRlc1* and *PduRlc2* were abundant in the cytosol and partially labeled the cell cortex at 48 hpf (Figure 3.3 A). However, the signal intensity and labeling of the myosin-light-chains were not strong enough for further analysis. The injected non-muscle-myosin heavy chain (*PduNmm*) localized to the cell cortex, but it was hardly visible before 64-cell stage (Figure 3.3 B). However, the 24 hpf embryos showed strong cell cortex localization signal of *PduNmm* (Figure 3.3 C). This indicated that actomyosin was presence at the cell cortex, but a better tool for live-monitoring its dynamics during early development needed to be developed.

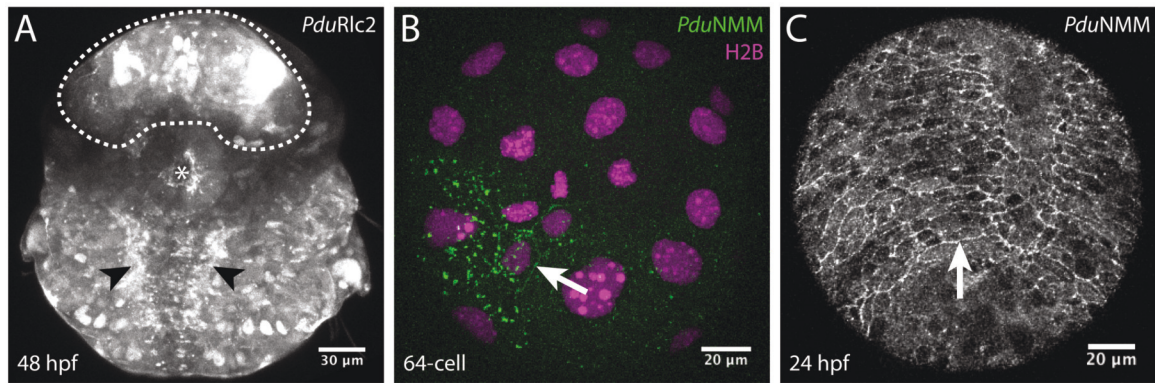


**Figure 3.3.: Localization of *P. dumerilii* non-muscle-myosin components.** The mRNA of the non-muscle-myosin regulatory light chain 2 (*Pdurlec2*) or heavy chain (*Pdunmm*) conjugated with *sgfp* was injected into the zygotes. (A) *PduRlc2* was localized to most of the cells of the embryo at 48 hpf. Particularly, the ventral nervous system (arrowhead), stomodeal (asterisk) and brain regions (dashed line) were distinguished. (B) *h2b-mCherry* (magenta) and *Pdunmm* (green) mRNA were co-injected into the zygotes. *PduNmm* signal was detected in a part of the embryo at 64-cell stage. The localization to the cell cortex was indicated by arrows. (C) The cell cortex was labeled (arrow) with *PduNmm* at 24 hpf. Scale bar: 30 μm (A) and 20 μm (B, C).



### 3.3. Sequence optimization increases fluorescent signal of the injected mRNA

In order to optimize the injected mRNA expression in terms of increasing translation efficiency and mRNA stability, various 5'UTRs and 3' terminators were tested. Based on a work in *D. melanogaster* (Pfeiffer et al., 2012), I constructed a combination of different UTR regions in the pCS2+ expression plasmid, I synthesized and injected the mRNAs into the *P. dumerilii* zygote and I quantified the fluorescent intensity for each construct at 8 hpf. I tested two Kozak sequences, syn21 and L21, upstream of the coding region. syn21 (5'-AACTTAAAAAAAAAAATCAAA-3') is a synthetic 21 bp, AT-rich sequence, designed as a combination of Cavener consensus sequence with elements from the *Malacosoma neustria* nucleopolyhedrovirus (*MnNPV*) polyhedron gene. L21 (5'-AACTCCTAAAAAACCGCCACC-3') is the 21 bp sequence immediately preceding the initiation codon of the lobster tropomyosin gene. Both syn21 and L21 increase the transgene signal level in *D. melanogaster* either through an increase in translation or because of an increased stability of the transcribed mRNA (Pfeiffer et al., 2012).

From the same study, it was shown that the 3'UTR of *Autographa californica* nucleopolyhedrovirus *p10* gene promoted polyadenylation more efficiently than SV40, and that poly-A tail was important for mRNA stability and translation. Therefore, I compared the original 3' terminator (SV40) on the pCS2+ plasmid with p10 by replacing SV40 with p10 3'UTR.

*Pdupar6-sgfp* was chosen as the reporter because of its cytosolic signal during early *P. dumerilii* development, thereby facilitating the quantification of the

### 3. live-imaging of cytoskeleton dynamics during early *P. dumerilii* spiral cleavage

fluorescent intensity (Figure 3.4 A). Therefore, the sGFP intensity measurements were used as a proxy for the amount of *PduPar6* protein. Either syn21 or L21 were cloned immediately preceding the initiation codon of *Pdupar6*. As control experiments, the original pCS2+ construct was used, or the original *Pdupar6* 5'UTR (5'-TCGGCTCC AATGTGGAATTTACCTGGATTTAACCGGTGACCAAGCCCTGGAGGAGGG CAAAAAGTCATCTACG-3') was cloned into pCS2+ plasmid. The 3' terminator p10 was compared in the original pCS2+ plasmid together with *Pdupar6-sgfp* (Figure 3.4 A).

The plasmids were linearized, the mRNAs *in vitro* transcribed, and the concentration adjusted to 600ng/ $\mu$ L with nuclease-free water for storage at  $-80^{\circ}\text{C}$ . The injection mix was freshly prepared containing 200  $\mu\text{g}/\mu\text{L}$  *Pdupar6* mRNA and 200  $\mu\text{g}/\mu\text{L}$  *h2b-mCherry* mRNA. H2B expression served as the loading control to normalize the expression of the target *PduPar6*-sGFP. The injected embryos were fixed at 8 hpf and immediately imaged with confocal microscopy. It was clear that the sGFP intensity was higher in both syn21 or L21 5'UTR containing groups (Figure 3.4 B). However, the p10 3' terminator did not seem to increase the expression level of the injected mRNA in *P. dumerilii*.

### 3.3. Sequence optimization increases fluorescent signal of the injected mRNA

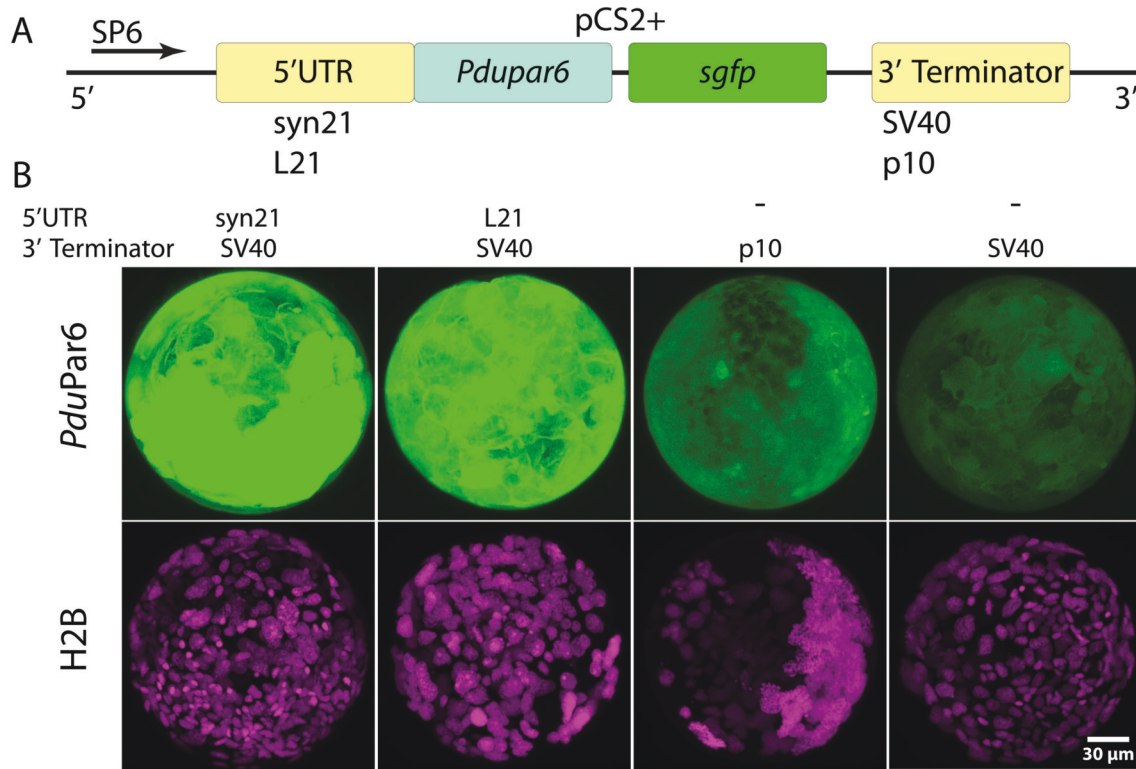


**Figure 3.4.: Optimization of injected mRNA translation with 5'UTR and 3' terminator.** (A) Scheme of the construct designing showed that either syn21 or L21 5'UTR was constructed in front of the start codon of *Pdupar6* coding sequence. Either the original SV40 terminator of pCS2+ or p10 3' terminator was cloned at the terminator site of pCS2+ plasmid. (B) Expression level of *PduPar6* in *P. dumerilii* embryos. A mixture of the *Pdupar6-sgfp* and *h2b-mCherry* mRNA was injected into *P. dumerilii* zygote and imaged at 8 hpf. The brightness was normalized according to the expression of H2B-mCherry. Scale bar: 30 μm.

To quantify the increment of the injected mRNA signal, the fluorescent intensity of the translated protein was plotted as a relative value. In Fiji, I defined the region of interest covering the whole embryo on a maximum intensity projection of the imaged z-stack. I measured the average fluorescent intensity of H2B-mCherry as well as the target *PduPar6*-sGFP separately. The intensity of *PduPar6*-sGFP readout was divided by the H2B-mCherry signal to normalize the injection variation of each

### 3. live-imaging of cytoskeleton dynamics during early *P. dumerilii* spiral cleavage

specimen. These calculations were plotted in Figure 3.5. Next, all the normalized values were compared with the SV40 group, that was with the 5' and 3'UTR regions of the original pCS2+ construct. The normalized sGFP intensity of the SV40 group was set to 1. The fluorescent intensity of the syn21 or L21 containing construct was  $2.93 \pm 0.22$  or  $2.47 \pm 0.16$  times as bright as the SV40 control. syn21 5'UTR gave higher signal comparing to L21 5'UTR. Substitution of SV40 by p10 did not significantly change the expression of the protein comparing to their correlated groups (syn21 + p10 group was  $2.66 \pm 0.06$  and L21 + p10 group was  $2.28 \pm 0.27$ ). The construct with the original 5'UTR of *Pdupar6* didn't show significant change of the fluorescent signal ( $0.68 \pm 0.03$ ) compared to the SV40 control group, indicating that the specific 5'UTR, syn21 or L21, boosted protein production in *P. dumerilii* embryos.



### 3.3. Sequence optimization increases fluorescent signal of the injected mRNA

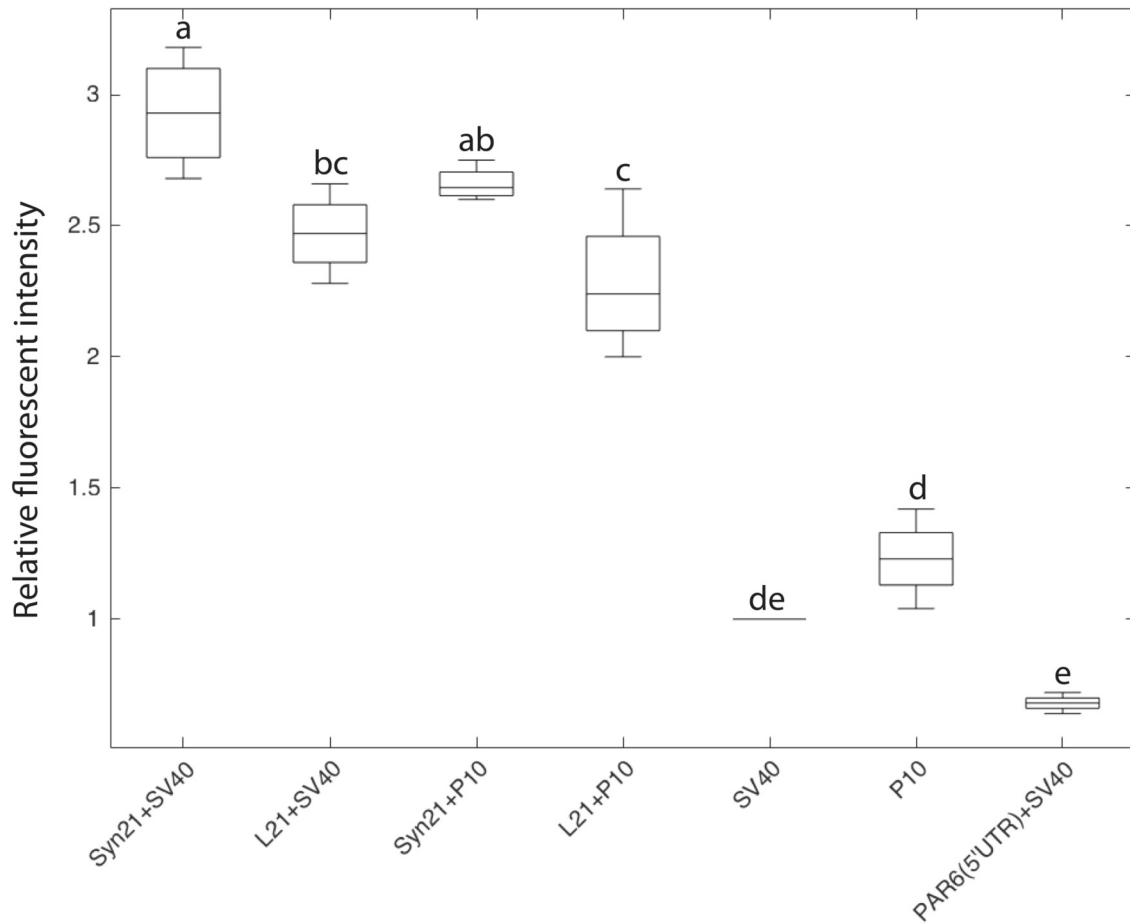


**Figure 3.5.: Quantitative analysis of the expression of *PduPar6* under the regulation of different UTR regions.** A combination of different 5'UTRs (syn21, L21, original 5'UTR of pCS2+ or the 5'UTR of *Pdupar6*) and 3' terminators (SV40 or p10) were constructed and tested by mRNA injections into the *P. dumerilii* zygotes. The mRNAs were co-injected with *h2b-mCherry* mRNA as standard. The relative fluorescent intensity of *PduPar6*-sGFP/H2B-mCherry was calculated and further divided by the value of the SV40 control. The alphabets above each box indicated statistical difference of the groups. The final values were plotted. Biological replicate n=4.

The data showed that the constructs with syn21 or L21 may accelerate the injected mRNA expression probably either through an increased in protein translation and/or mRNA stability. Moreover, syn21 increased the potential to detect the target

### 3. live-imaging of cytoskeleton dynamics during early *P. dumerilii* spiral cleavage

protein in early *P. dumerilii* embryos, because it resulted in the strongest signal level among all the constructs. Therefore, syn21 was added to the lifeact construct to label actomyosin and investigate its dynamics in early spiral cleavages.

A third sequence optimization that I evaluated, was the linker region between the target gene and the fluorescent protein. In most of the mRNAs, which I used this evaluation did not seem to be necessary, since the localization was consistent. However, my experience with the different Lifeact constructs, which I tested was that depending on the downstream fluorophore, the localization to the actin fibers could be more or less well-defined. Lifeact is a small peptide (17 amino acids). Therefore, the conformation of the conjugated fluorescent protein may affect the binding affinity of Lifeact in the actomyosin complex. To determine the optimal Lifeact construct for live-imaging in *P. dumerilii*, I tested two different linker sequences between Lifeact and the fluorophore, and various fluorophores (mKate2, mCherry, eGFP, sGFP, mNeonGreen) located at the C-terminus of Lifeact. Regarding the linker region, the short linker was part of the multiple cloning site of pCS2+, and the optimal linker was codon optimized for *C. elegans* transgenic Lifeact expression (Figure 3.6 A). The two linkers gave different, but overlapping, actomyosin labeling patterns. The short linker labeled largely extracellular components such as the filopodia connecting the blastomeres and the eggshell (Figure 3.6 C). Further, the cell cortex was slightly labeled and the actomyosin network was hardly visible. The linker optimized for *C. elegans* (“optimal-linker”) resulted mainly in cell cortex labeling as well as partial cytosolic distribution (Figure 3.6 B). From phalloidin staining in fixed embryos (e.g., Figure 2.4), I expected the F-actin labeling of the cell cortex and abundant at cytokinetic ring during cell division, thus verifying the fluorescent stainings observed in the living embryos. Regarding the fluorophores, different fluorophores at the C-terminus of the fusion proteins also led to differences in

### 3.3. Sequence optimization increases fluorescent signal of the injected mRNA

actomyosin labeling affinity. The constructs with the optimal linker and a GFP, sGFP, mNeonGreen, or mCherry at the 3' end all showed largely filopodia labeling, but very little labeling of the cell cortex (Figure 3.6 D). Contrary, when fluorescently labeling the Lifeact with mKate2, the cell cortex was nicely labeled starting from 4 cell-stage and even individual F-actin fiber can be distinguished (Figure 3.6 B). Therefore, in order to monitor the cortical actomyosin dynamics, the construct with the optimal linker and mKate2 fluorophore (namely *syn21-lifeact-mKate2*) was chosen for further experiments.

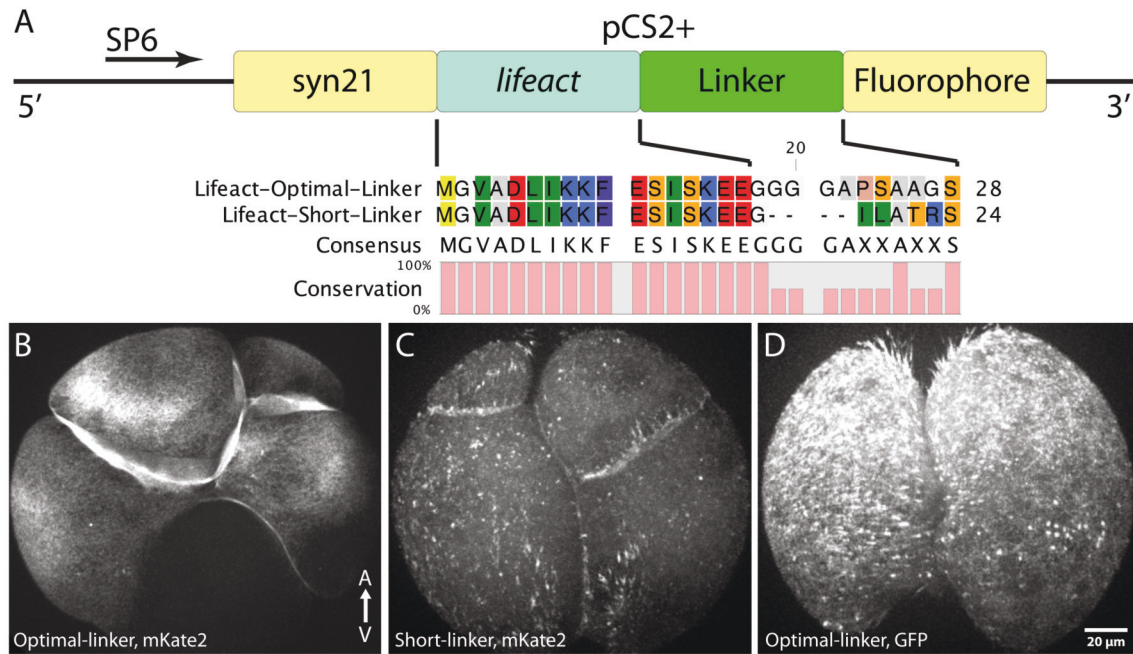


**Figure 3.6.: Optimization of Lifeact labeling in *P. dumerilii* during spiral cleavage.** (A) Construct design for synthesizing mRNA for *lifeact* coupled to a fluorophore. The Kozak sequence *syn21* was conjugated in front of the start codon of *lifeact*. Two linker regions and multiple fluorophores were tested to optimize Lifeact labeling. (B-D) Lifeact localization in the living *P. dumerilii* embryo. Lifeact mRNA with optimal-linker and mKate2 fluorophore was injected in (B), Lifeact mRNA with the short-linker and mKate2 in (C) and Lifeact with the optimal-linker and GFP in (D). The images were taken from the side view. Scale bar: 20 μm.

### 3. live-imaging of cytoskeleton dynamics during early *P. dumerilii* spiral cleavage

To further test how early actomyosin can be labeled by mRNA injection method, equal amount (with a higher concentration of 600ng/ $\mu$ L) of *lifeact-mKate2*, without *syn21* and with the short linker, or *syn21-lifeact-mKate2* mRNA was injected into the zygote at around 60 mpf. In details, the embryos took 60 min to secrete the jelly layer after fertilization and the jelly layer was manually removed by physical filtration. The injection of mRNAs was performed at 60-90 mpf. The first embryonic cleavage took places at around 90 mpf, serving as a sign to terminate the injection and to start mounting the samples for live-imaging. The embryos had maximum 30 min from injection until the first embryonic cleavage to develop the fluorescent signal. The *lifeact-mKate2* construct couldn't give a visible fluorescent signal at 2-cell stage. However, the fluorescent signal was visible as early as in the zygote of the *syn21-lifeact-mKate2* injected embryos (Figure 3.7). And the signal increased throughout the embryogenesis.

### 3.3. Sequence optimization increases fluorescent signal of the injected mRNA

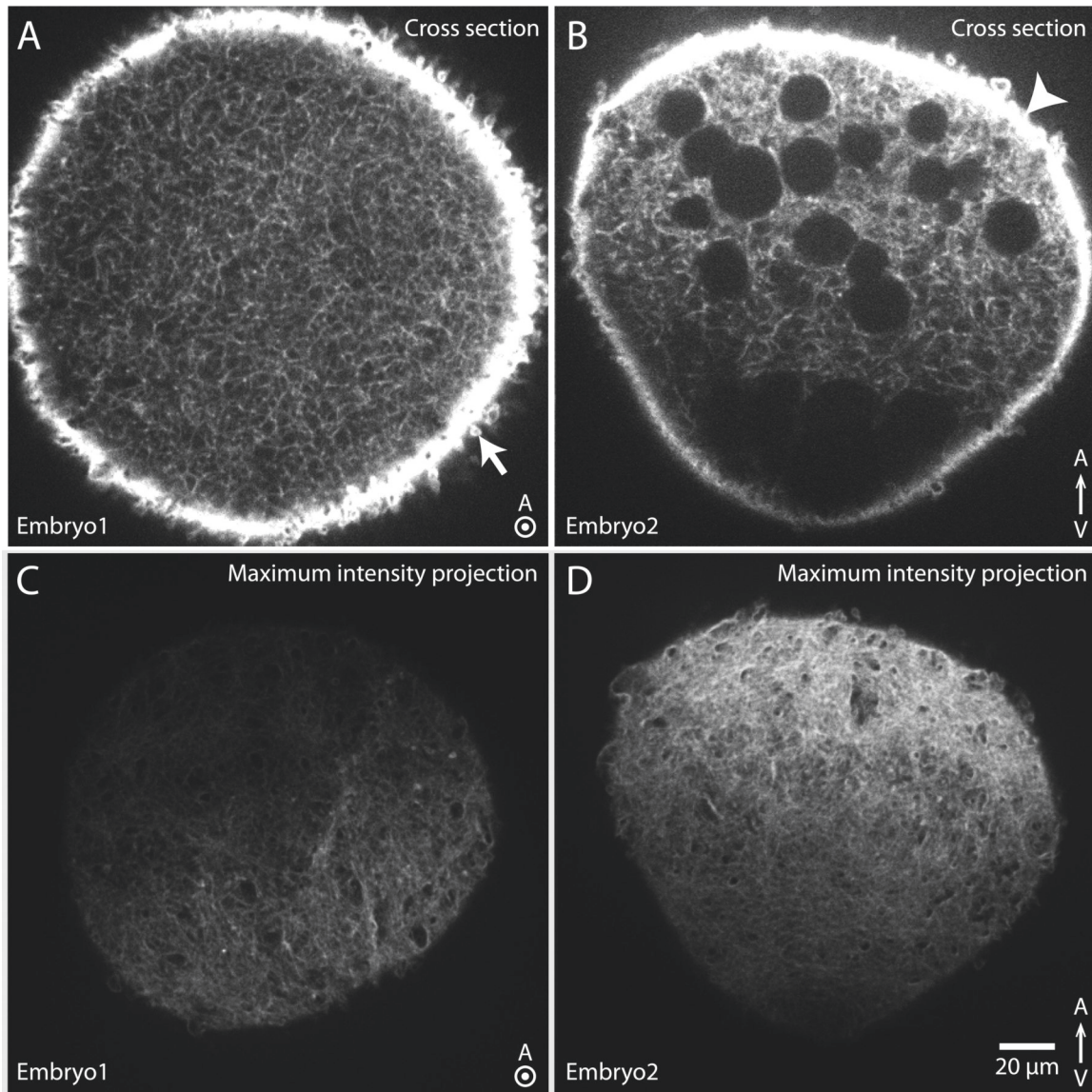


**Figure 3.7.: Lifeact distribution in the *P. dumerilii* zygote.** Injection of large amount of *syn21-lifeact-mKate2* at 60 mpf into the *P. dumerilii* zygotes resulted in a fast visualization of the fluorescent signal while still in the one-cell stage. Two embryos were shown with cross section (A and B) or maximum intensity projection (C and D) imaging from various views. (A, B) Cross section of the two embryos showed both the cortical and the cytosolic actomyosin labeling. The animal pole contained thicker cortical actomyosin as shown in B (arrowhead). Filopodia connected to the vitelline membrane can be observed in A (arrow). (C, D) Maximum intensity projection of the two embryos from A and B gave cell cortex labeling of actomyosin. A and C: animal view. B and D: side view. Scale bar: 20  $\mu$ m.



### 3.4. Protein synthesis and injection for early labeling of actomyosin

As described in the previous section, actomyosin can be visualized at least from 4-cell stage through mRNA injections. However, the fluorescent intensity fluctuated with the amount of mRNA injected. The injected mRNAs needed time to be translated and the fluorescent protein had to mature. Therefore, the fluorescent signal was only slightly detected at the 4-cell stage. The intensity increased throughout the developmental processes, giving brighter, higher resolution images in the later stages. *syn21-lifect-mKate2* mRNA injection is then useful for monitor overall *P. dumerilii* spiral cleavage, as well as the cytoskeletal dynamics in the later spiral cleavages, but limited for quantitative measurements during early spiral cleavage (starting at 4-cell stage).

To visualize actomyosin earlier in development, I developed an alternative labeling approach by directly injecting the fluorescently labeled Lifect peptide and thus skipped the protein translation process inside the zygote. There were two methods to synthesize Lifect peptide conjugated with a fluorescent compound. In the first method, Lifect was synthesized through a chemical reaction (Sequence: GVADLIKK FESISKEEGGGGAPSAAGSK) with the optimal linker at the C-terminus. Then, the first methionine of the peptide was removed and an additional lysine was included at the C-terminus of the peptide for further fluorescent dye conjugation. The peptide was next conjugated with TRITC fluorescent dye at the last lysine (Figure 3.8 A). The peptide was diluted to 10 µg/µL and stored at  $-80^{\circ}\text{C}$ . A second method relied on synthesizing the identical Lifect-mKate2 peptide with the optimal linker as produced

### 3.4. Protein synthesis and injection for early labeling of actomyosin

from the mRNA construct. In this case, the *lifeact* with the optimal linker and mKate2 (*6xhis-lifeact-mKate2*) was sub-cloned into the expression vector pET30a. A six-histidine site was included at the 5' end of *lifeact* for protein purification. The protein expression was done by bacteria and the fluorescence could be detected directly in the bacteria culture before purification. The induced Lifeact-mKate2 protein was then purified, diluted to 2 µg/µL and stored at  $-80^{\circ}\text{C}$  (Figure 3.8 B-D).

The Lifeact-TRITC peptide or Lifeact-mKate2 purified protein (diluted to 500ng/µL) was injected into *P. dumerilii* zygotes and imaged at the desired developmental stages. The Lifeact-TRITC protein showed barely any signals at the cell cortex (Figure 3.8 A). However, the cortical actomyosin was seen right after the injection with Lifeact-mKate2 purified protein and the signal persisted (Figure 3.8 B,C). The fluorescent signal could be imaged for up to 6 hr covering the four spiral cleavages when imaging with a broad time interval (60 sec/time point or longer) (Figure 3.9 A). This indicated that the embryogenesis was normal after Lifeact protein injection. However, to monitor and measure the cortical actomyosin dynamics during spiral cleavage, high temporal and spatial resolution imaging was necessary. Therefore, when imaging at a temporal resolution of 5-8 sec, the injected protein persisted only for up to 30 min covering one spiral cleavage (Figure 3.9 B). The injected protein localized mainly to the cell cortex, and the actomyosin network was clearly labeled (Figure 3.8 C). Other F-actin structures in the cells were also labeled such as the cytokinetic ring during the first spiral cleavage (Figure 3.8 C) and an actin accumulation around the nucleus prior to nuclear envelope breakdown (Figure 3.8 B). These observations coincided perfectly with the F-actin labeling in the fixed embryos (Figure 4.4 B) and indicated that the Lifeact-mKate2 recombinant protein is a powerful tool for investigation of actomyosin dynamics during early spiral cleavage.

### 3. live-imaging of cytoskeleton dynamics during early *P. dumerilii* spiral cleavage

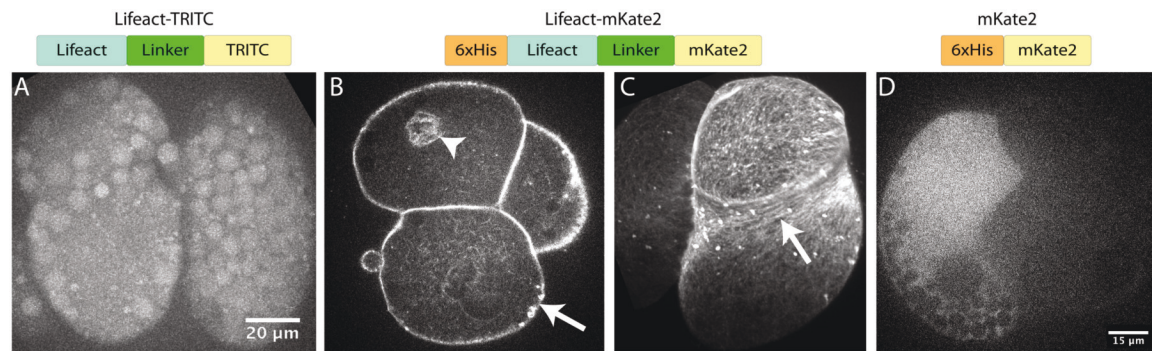


**Figure 3.8.: Actin labeling in early *P. dumerilii* embryos by Lifeact protein injection.** (A) Injection of chemically synthesized Lifeact conjugated to TRITC into the zygotes did not label actin in the living *P. dumerilii* embryo during 4-cell stage. (B-C) Synthesized and purified Lifeact-mKate2 protein was injected into the *P. dumerilii* zygote. The Lifeact-mKate2 protein labeled the different actin components of the cells at 4-cell stage: actin fibers of the cell cortex (arrow) and actin accumulation around the nucleus prior to nuclear envelope breakdown (arrowhead). (D) Control experiment with mKate2 protein injections into the *P. dumerilii* zygote. No specific cellular localization was observed. The panel C showed an optical cross section while A, B, and D were the projected images showing the whole cells. Scale bars: 20  $\mu\text{m}$  (A), 15  $\mu\text{m}$  (B-D).



### 3.4. Protein synthesis and injection for early labeling of actomyosin

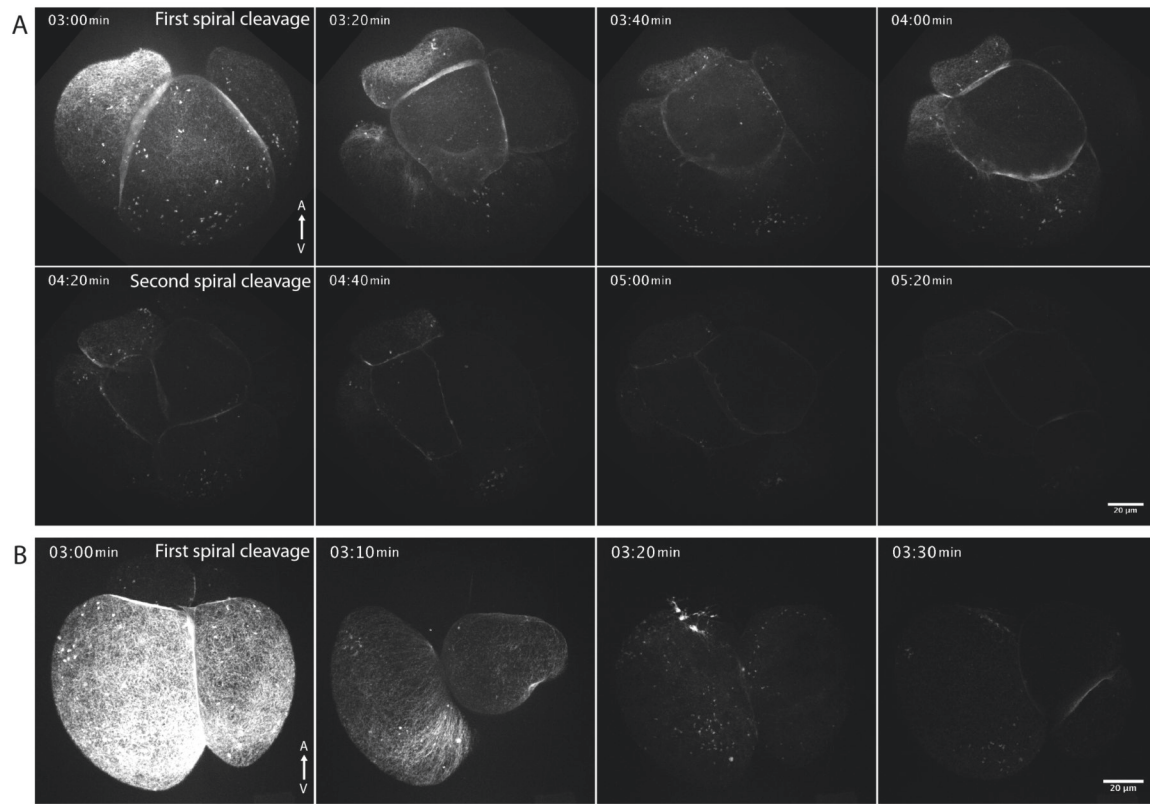


**Figure 3.9.: Durability of the injected Lifeact-mKate2 protein under live-imaging.** (A) Lifeact-mKate2 protein was injected into the zygote and the imaging was started at the 4-cell stage with a 30-second temporal resolution. The fluorescent signal can be observed for more than 2 hr of continuously imaging but it decreased through time. (B) When the injected embryos were imaged with a 5-second temporal resolution, the fluorescent signal decreased dramatically during the 30 min of imaging. The first spiral cleavage was captured within the time span. The images were taken from the side view. The format of the timestamp is hr:min. Scale bar: 20 μm.



## 4. Contribution of actomyosin to *P. dumerilii* spiral cleavage

In the previous chapters, I have described the dynamics of cytoskeletal elements during spiral cleavage. Next, I wanted to understand the function of these elements during spiral cleavage. I was particularly interested in the role of the actomyosin cortex, since striking changes in the cell shape took place during spiral cleavage.

Both the synthetic Lifeact-mKate2 protein and *syn21-lifeact-mKate2* mRNA can label actomyosin of the early embryos. But different strategy was selected for different experimental purposes. In this chapter, the live-recorded movies were achieved by mRNA injection, which performed better signal intensity throughout long-term imaging. For particle image velocimetry analysis, both the protein and mRNA injected embryos were included to achieve the best signal-noise quality.

#### 4. Contribution of actomyosin to *P. dumerilii* spiral cleavage

### 4.1. Actomyosin distribution analysis in early developing *P. dumerilii* embryos

Imaging of the early development of the *P. dumerilii* embryos by regular mRNA injection into the zygote was not successful due to the relatively short cell cycle of the embryos, which caused low expression of the fluorescent protein under investigation. To overcome this, I designed the mRNA construct *syn21-lifeact-mKate2* (described in Section 3.3), which resulted in an increased translation efficiency (*syn21*) and protein binding/stability (optimal-linker) and allowed for an early visualization of actomyosin in the *P. dumerilii* embryos.

#### 4.1.1. Asymmetric actomyosin distribution during the first two embryonic cleavages

Important cytoskeletal arrangements took place in the two asymmetric divisions of the zygote immediately prior to spiral cleavage (Section 2.2.1). Therefore, I wanted to study this in the living embryo. Large volume of *syn21-lifeact-mKate2* mRNA (concentration of 600ng/μL) was injected into the zygote to reach a detectable fluorescent level of actomyosin before the first cell division. This labeling strategy allowed me to visualize both the cortical and cytosolic F-actin in the zygote. The cortical actomyosin labeling was much brighter than the cytosolic F-actin proportion (Figure 3.7 A,B). Moreover, cortical actomyosin is localized asymmetrically with a greater segregation toward the animal pole compared to the vegetal pole (Figure 3.7 B). Maximum intensity projections showed the same, but also that cortical actomyosin of the *P. dumerilii*

#### 4.1. Actomyosin distribution analysis in early developing *P. dumerilii* embryos

embryo formed a dense fibrous network (Figure 3.7 C,D). The cytosolic actomyosin network enveloped the nutritional vesicles and might play a role in reorganizing/moving the cellular compartments during early embryogenesis (Figure 3.7 B).

Injectations with lower *syn21-lifeact-mKate2* mRNA concentration (200ng/ $\mu$ L) resulted in higher viability, around 80%, of the injected embryos. The Lifeact-mKate2 signal of the normally developing embryos remained low during the first cleavage, but it was clear that the cortical actomyosin segregated asymmetrically within the blastomeres (Figure 4.1). Both in the AB and CD blastomeres, the actomyosin was largely located at the animal pole and at the side of the embryo (Figure 4.1 A,B). The cytokinetic ring formed at the actomyosin-abundant side of the blastomere during the second asymmetric embryonic cleavage, resulting in the bigger A and D cell, respectively (Figure 4.1 C). More Lifeact-mKate2 protein has matured after the cleavage, which resulted in an increase in the actomyosin signal at 4-cell stage (Figure 4.1 D). The asymmetric distribution of actomyosin toward the animal pole was also detected in all the four macromeres, and the cell contact had higher actomyosin signal (Figure 4.1 D). From the phalloidin stained fixed embryos in Figure 2.4, I described that the asymmetric cytokinetic ring formation started from the animal pole during the first two spiral cleavages, which was the actomyosin-abundant side of the blastomeres. These observations indicated that actomyosin may play a role in defining cell asymmetry, both in the first two asymmetric embryonic cleavages as well as in the first spiral cleavage.

#### 4. Contribution of actomyosin to *P. dumerilii* spiral cleavage

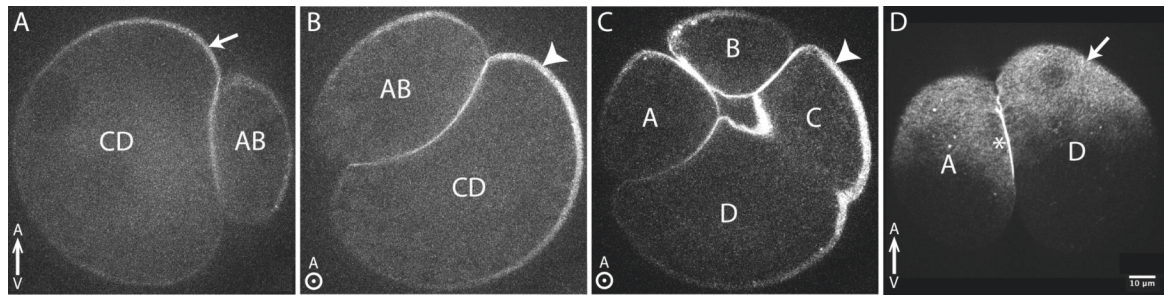


**Figure 4.1.: Actomyosin localization in early *P. dumerilii* embryos.** (A, B, C) Actomyosin was visualized from 2-cell stage with asymmetric distribution. It was largely distributed at the animal pole (A, arrow) as well as toward the future B and C cell side (B and C, arrowhead). (D) Actomyosin was distributed largely toward animal pole (arrow) and the cell contact (asterisk) at the 4-cell stage. A, D: side view. B, C: animal view. Scale bar: 10  $\mu$ m.

##### 4.1.2. Actomyosin labeling by Lifeact during spiral cleavage

After the injection of (200ng/ $\mu$ L) *syn21-lifeact-mKate2* mRNA and continuously imaging, the Lifeact-mKate2 expression still increased during spiral cleavage, making the observation and measurement of actomyosin dynamics more reliable. Actomyosin was more abundant at the cell contact of the 4-cell embryos, and prior to the cell division it accumulated around the cleavage furrow (Figure 4.2 A). A change in cell division axes became apparent as a deformation in the cell boundary between the four macromeres was detected (Figure 4.2). The cytokinetic ring was abundant in actomyosin from the telophase until the end of the first spiral cleavage (Figure 4.2 Telophase). The actomyosin in the micromeres were evenly distributed at the cell cortex in each blastomere throughout the spiral cleavages (Figure 4.2 B-D).

To summarize, when providing Lifeact-mKate2 to the zygote by mRNA injections, the fluorescent signal of Lifeact-mKate2 increased for each cell cycle. I did

#### 4.1. Actomyosin distribution analysis in early developing *P. dumerilii* embryos

not observe asymmetric mRNA segregation between the blastomeres because all the cells showed fluorescent signal. The injected embryos developed into trochophore larvae, and the fluorescent signal was visible for more than five days of development, indicating that the mRNA, injection, and the imaging processes did not dramatically influence *P. dumerilii* embryogenesis. These results also suggested that *syn21-lifect-mKate2* mRNA injection for actomyosin labeling was a potential method for long-term tracking of the actomyosin dynamics without interfering with the development of the larvae.



#### 4. Contribution of actomyosin to *P. dumerilii* spiral cleavage

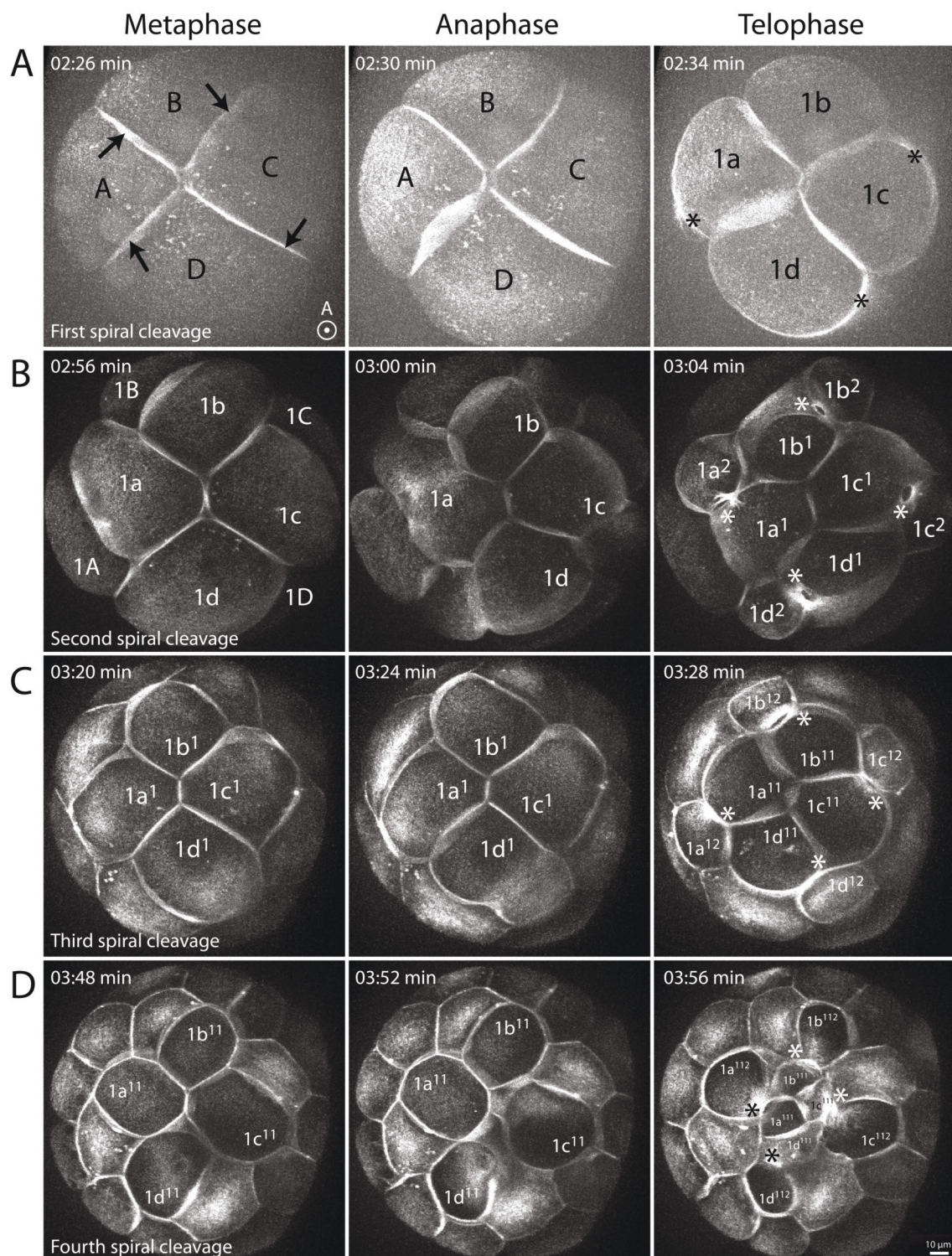


Figure 4.2.: Actomyosin distribution during spiral cleavage.



## 4.2. Actomyosin dynamics during cell division in micromeres and macromeres

**Figure 4.2.: Actomyosin distribution during spiral cleavage.** The embryo was injected with *syn21-lifeact-mKate2* mRNA into the zygote and imaged with spinning disk confocal microscopy from 4-cell stage and during spiral cleavage. (A) The first spiral cleavage. (B) The second spiral cleavage. (C) The third spiral cleavage. (D) The fourth spiral cleavage. (A-D) The expression of Lifeact-mKate2 was visible at 4-cell stage, especially at the cell-cell contact sites (A, arrow). The signal increased through time, and the cytokinetic ring was observed during the telophase of this cleavage, indicated with the asterisks. (B-D) The Lifeact-mKate2 expression increased throughout the development and it didn't interfere the embryogenesis. The blastomeres at the animal pole were labeled with cell lineage IDs. The images were taken from the animal view. The format of the timestamp is hr:min. Scale bar: 10  $\mu$ m.

## 4.2. Actomyosin dynamics during cell division in micromeres and macromeres

Since actomyosin can be monitored from at least the beginning of the spiral cleavage, how it contributed to the blastomeres behavior was investigated. Here I showed the divergent actomyosin behaviors in the micromeres and macromeres (Section 4.2.1), which may play a role in the differences of the cell division of these blastomeres, and a conserved, novel function of actomyosin in both micromeres and macromeres, which may trigger cell division during early *P. dumerilii* cleavages (Section 4.2.2).

### 4.2.1. Distribution of cortical actomyosin during cell division

In Section 2.6, I have shown that the cellular behavior of cell division of the micromeres and the macromeres was different. The micromeres had perpendicular cell division axes between consecutive cell divisions, while the nuclei of the macromeres migrated

#### 4. Contribution of actomyosin to *P. dumerilii* spiral cleavage

from one side of the cell to the other side between each spiral cleavage (Figure 2.16). To understand whether the actomyosin distribution and dynamics are also different between micromeres and macromeres, I live-imaged *syn21-lifeact-mKate2* mRNA injected embryos from the lateral view to cover both cell types.

The actomyosin distribution was homogenous in the cell cortex of the micromeres during the interface (Figure 4.3 A). An accumulation of actomyosin to the cytokinetic ring was only observed during cytokinesis. The actomyosin distribution in the macromeres was different from the micromeres. Both the cytosolic and cortical actomyosin was localized at the animal side of the macromere, where the nucleus was located during the interface (Figure 4.3 A). When the cell divided, a clear actomyosin-abundant region was detected toward the animal pole of the embryo, whereas a lack of actomyosin was observed at the vegetal side of the macromeres (Figure 4.3 A,B). Moreover, the boundary of the actomyosin-abundant region was the location, where the cytokinetic ring was formed (Figure 4.3 B). The asymmetry remained until the end of the cytokinesis, and a major proportion of actomyosin was segregated into the daughter micromere (Figure 4.3 C). Following cytokinesis, the daughter macromere expressed cytosolic actomyosin, which localized around the nucleus (Figure 4.3 D). Because the nucleus of the macromere was at the animal side of the it, the expressed actomyosin was also localized at the animal side. Therefore, the macromere kept actomyosin asymmetry for the next spiral cleavage.

#### 4.2. Actomyosin dynamics during cell division in micromeres and macromeres

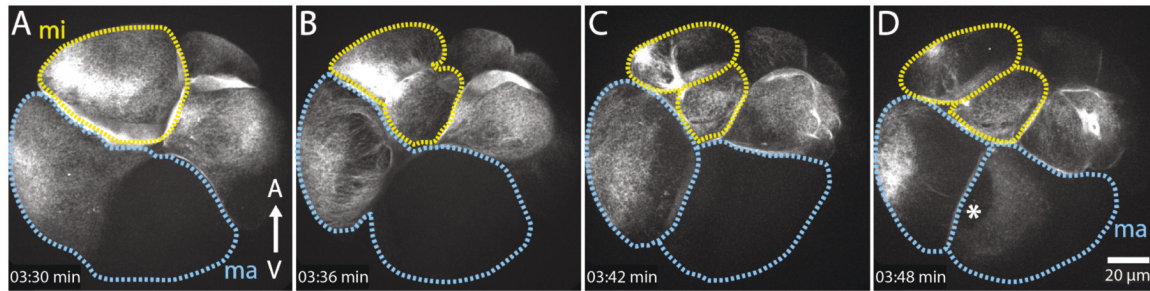


**Figure 4.3.: Actomyosin distribution in the macromeres and micromeres.** The zygote was injected with *syn21-lifeact-mKate2* mRNA to label actomyosin. The third spiral cleavage was captured and a macromere (ma) was marked with a blue dashed line while a micromere (mi) with a yellow dashed line. Both the cortical and cytosolic proportion of actomyosin can be detected but cortical was predominant in the projected images. The signal around the newly formed nucleus (D, asterisk) was an example of the cytosolic actomyosin since the macromere side lacked of cortical actomyosin during division. The images were taken from the side of the embryo. Asterisk: nucleus. Dashed line: cell outline. The format of the timestamp is hr:min. Scale bar: 20  $\mu\text{m}$ .

##### 4.2.2. Cytosolic actomyosin accumulates at the nuclear envelope before cell division

Cytosolic actomyosin dynamics was also correlated to the cell cycle. There was no specific actomyosin localization at the interface. However, when the cells entered the prophase of cell division, dramatic actomyosin accumulation at the nuclear envelope was detected prior to the nuclear envelope breakdown (Figure 4.4 A). The actomyosin was recruited from every direction surrounding the nuclear envelope and this process decreased substantially the cytosolic actomyosin pool. The recruitment of actomyosin took around 10 min and it's released following nuclear envelope breakdown occurring within the next 2 min. A homogeneous actomyosin distribution was observed, indicating that the nuclear envelope was no longer presence. The accumulation of cortical

#### 4. Contribution of actomyosin to *P. dumerilii* spiral cleavage

actomyosin was detected during the anaphase and the cytokinetic ring formed a few minutes after to complete the cell division. To verify the accumulation of cytosolic actomyosin by Lifeact-mKate2 labeling, the fixed embryos were stained with phalloidin at the prophase of cell division while nuclear envelope breakdown was progressing. I observed that the nuclear envelope became actin-rich with the recruitment of the mitotic spindles, indicating that Lifeact-mKate2 indeed labeled actin fibers in *P. dumerilii* (Figure 4.4 B). Actomyosin labeled with SiR-actin dye showed the same result (Figure 3.1 C). Thus, my *syn21-lifeact-mKate2* mRNA construct allowed for fast tracking of actomyosin dynamics during early embryogenesis. In *P. dumerilii*, this has allowed me to describe the cortical and cytosolic actomyosin dynamics with relation to cell division in micromeres and macromeres.



#### 4.2. Actomyosin dynamics during cell division in micromeres and macromeres

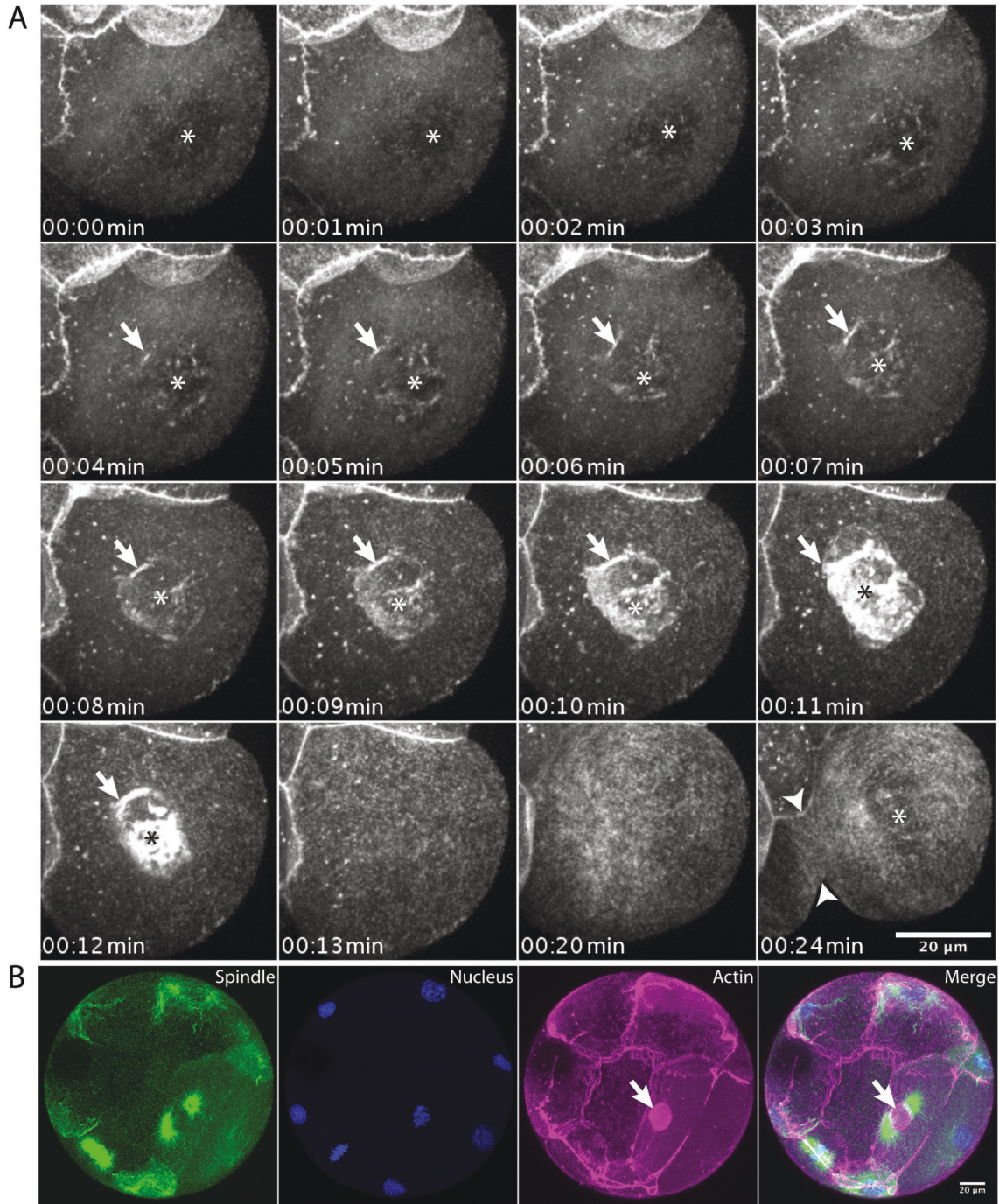


Figure 4.4.: Cytosolic actomyosin dynamics during cell division in living or fixed *P. dumerilii* embryos.

#### 4. Contribution of actomyosin to *P. dumerilii* spiral cleavage

**Figure 4.4.: Cytosolic actomyosin dynamics during cell division in living or fixed *P. dumerilii* embryos.** (A) Embryos were injected with *syn21-lfeact-mKate2* mRNA and imaged at 32-cell stage. Actin accumulated at the nuclear envelope before the nuclear membrane breakdown and the event lasted around 10 min. The cytokinesis started followed by the nuclear envelope breakdown. The cleavage furrow was indicated with the arrowhead. Asterisk: nucleus. (B) The accumulation of F-actin was stained in the fixed specimen with phalloidin staining. The mitotic spindles were labeled with anti- $\alpha$ -tubulin antibody by immunofluorescence (green) and the nuclei were labeled with DAPI (blue). The accumulation occurred during prophase of cytokinesis. Arrow: the accumulation of F-actin at the nuclear envelope. The format of the timestamp is hr:min. Scale bar: 20  $\mu$ m.

### 4.3. Quantitative analysis of actomyosin dynamics during the first spiral cleavage

Actomyosin is the key cytoskeletal component to generate the mechanical forces for cell deformation and division plane determination. In *C. elegans*, actomyosin counter rotations play a critical role in setting up the division plane in the 4-cell embryo leading to the left-right symmetry breaking event (Naganathan et al., 2014). Therefore, I wanted to investigate whether the cortical actomyosin dynamics contributes in the division plane determination during the first spiral cleavage, which is the key factor of the chirality in spiralian.

To be able to track the cortical actomyosin movement in real-time, the embryos were injected with fluorescent *lfeact* mRNA or protein into the zygote. The criteria for selecting the appropriate labeling strategy was that the fluorescent signal had to be bright enough for quantitative measurements at 4-cell stage, stable for long-term live-imaging, and not affecting embryogenesis significantly. Various

#### 4.3. Quantitative analysis of actomyosin dynamics during the first spiral cleavage

fluorophore conjugated *lifeact* mRNAs with different UTR modifications have been tested as described in Section 3.3. Of these, the *syn21-lifeact-mKate2* mRNA construct showed the earliest (1-cell stage) and highest stable fluorescence expression (Figure 4.1). Furthermore, purified Lifeact-mKate2 protein, which was expressed in bacteria, labeled actomyosin as early as in the zygotes. Although the fluorophore amount was fixed after the inject, the signal was bright enough for 30-minute live-imaging at a 5-second temporal resolution (Figure 3.9). Therefore, both the mRNA and protein were selected for investigating actomyosin dynamics in *P. dumerilii*.

After injection, the embryos were mounted in 0.4% agarose and incubated at 18 °C until 4-cell stage. The embryos were imaged with a 5-second temporal resolution covering 30  $\mu\text{m}$  with 0.5  $\mu\text{m}$  optical section. The Lifeact-mKate2 protein injected embryos were imaged for 30 min until the end of the first spiral cleavage. The *syn21-lifeact-mKate2* mRNA injected embryos were imaged until the end of the fourth spiral cleavage. Each blastomere captured was re-orientated with the Fiji plugin BigDataViewer to view the image stack from the cytokinetic ring. Then the images were projected with maximum intensity method. Therefore, each blastomere had a unique view from the side of it. The digital correction of the observation plane also made the tracking and analysis of actomyosin dynamics around the cytokinetic ring more precisely.

Particle image velocimetry (PIV) is a technique to measure fluid flows (Willert & Gharib, 1991). The Grill lab, MPI-CBG, Germany, has adapted PIV to analyze the cortical actomyosin dynamics (Naganathan et al., 2014; Pimpale et al., 2019). For the calculations of the actomyosin dynamics during spiral cleavage in *P. dumerilii*, the selected time frames were based on the cell cycle events of each blastomere, starting from

#### 4. Contribution of actomyosin to *P. dumerilii* spiral cleavage

the anaphase, where an accumulation of actomyosin around the forming cytokinetic ring was seen, till the telophase of the cell division, where the ingression of the cleavage furrow was detected. The analytic area was defined relative to the cytokinetic ring. Two opposing rectangular region-of-interests parallel to the cytokinetic ring were defined and the velocity vectors from each region were summed up to get a proxy for the flow orientation around the cytokinetic ring (Figure 4.5 A-D). The component of the vector parallel to the cytokinetic ring was measured and the actomyosin counter rotational velocity was calculated with the following equations:

$$\vec{V}_c = \vec{g}_1 \times \vec{V}_{1y} + \vec{g}_2 \times \vec{V}_{2y} \quad (4.1)$$

**Equation 4.1.: Counter rotational velocity equation.** The direction of the velocity vectors  $\vec{V}_{1y}$  and  $\vec{V}_{2y}$  are corrected by the directional vectors  $\vec{g}_1$  and  $\vec{g}_2$ . Therefore, the result represents the counter rotational velocity  $\vec{V}_c$ .

$$|\vec{g}_1| = |\vec{g}_2| = 1 \quad (4.2)$$

**Equation 4.2.: Chiral rotational direction equation.** The directional vectors  $\vec{g}_1$  and  $\vec{g}_2$  are both with the value of 1 pointing toward opposite directions.

The asymmetric distribution of cortical actomyosin in the macromeres made it difficult to analyze the counter rotation at the macromere side (with weaker signal) of the cytokinetic ring (example see Figure 4.3). Furthermore, the macromeres of the fourth spiral cleavage were located inside of the embryo. The micromeres at the animal pole and the oil droplets in the macromeres at the vegetal pole also made it difficult to image cortical actomyosin of these macromeres (3Q blastomeres) no matter from which



#### 4.3. Quantitative analysis of actomyosin dynamics during the first spiral cleavage

direction. Therefore, neither imaging from the animal pole nor from the vegetal pole gave qualified images for PIV. For these given reasons, only the macromeres during the first to third spiral cleavage, and the micromeres of the second to the fourth spiral cleavage were analyzed from a lateral view (Figure 4.5 B).

PIV showed that both the macromeres of the 4-cell (A, B, C, and D) and the 8-cell (1A, 1B, 1C, and 1D) stage performed cortical actomyosin counter rotation during cell division. The cortical actomyosin generated  $2.437 \pm 0.595$   $\mu\text{m}/\text{min}$  counter rotational velocity in the macromeres of the first spiral cleavage, and  $2.816 \pm 2.406$   $\mu\text{m}/\text{min}$  in the second spiral cleavage. Actomyosin also showed a significant counter rotational pattern during the second spiral cleavage in the micromeres ( $2.882 \pm 0.922$   $\mu\text{m}/\text{min}$ ), but not in the third and the fourth spiral cleavage (Figure 4.5 E). These observations indicated that the behavior of the macromeres and the micromeres may be different during cell division. The actomyosin of the macromeres may actively tune the division axis, while the micromeres have the division angle set during the interface and divide passively according to the previous cleavage. These calculations suggested that the macromeres are the main actors in creating an inclination in the cell division axis during spiral cleavage, whereas the micromeres follow an usual cell division pattern.

#### 4. Contribution of actomyosin to *P. dumerilii* spiral cleavage

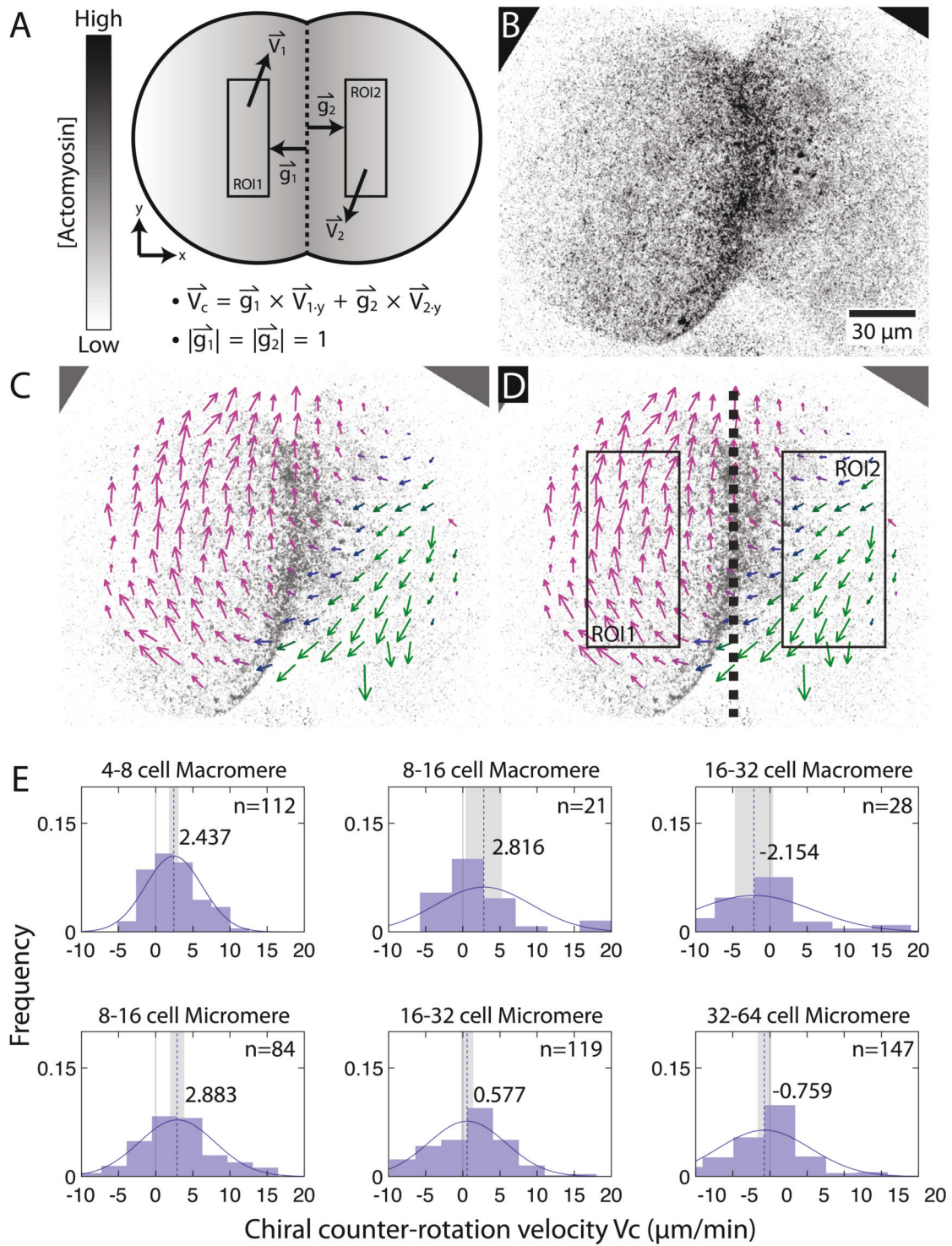


Figure 4.5.: Chiral counter-rotational velocity of cortical actomyosin during spiral cleavage.

#### 4.4. Mitotic spindle inclination during spiral cleavage

**Figure 4.5.: Chiral counter-rotational velocity of cortical actomyosin during spiral cleavage.** Actomyosin was labeled with *syn21-lifeact-mKate2* mRNA or Lifeact-mKate2 protein and imaged at the first spiral cleavage with a 5-8 second temporal resolution and 0.5  $\mu\text{m}$  optical sectioning covering 30  $\mu\text{m}$  thickness. (A) The scheme of particle image velocimetry (PIV) with the modified PIVlab by the Grill lab in MPI-CBG, Germany. The gray gradient illustrated actomyosin concentration. Two regions of interest, ROI1 and ROI2, with the width of 7.5  $\mu\text{m}$  and length of visible cortical actomyosin in the images located at either side of the cytokinetic ring. Each ROI started 3  $\mu\text{m}$  from the cytokinetic ring to prevent the bias from the ingression of the ring. Seven time frames (data points) during cytokinesis were analyzed from each biological replications. At least three biological replications were analyzed in each group (shown in E).  $\vec{g}_1$  and  $\vec{g}_2$  directional vectors were taken into account to calculate counter rotational flow rate. The velocity in y axis ( $\vec{V}_1y$  and  $\vec{V}_2y$ ) were responsible for  $\vec{V}_c$ . (B) An example image during cytokinesis showed actomyosin gradient. Scale bar: 30  $\mu\text{m}$ . (C) Chiral velocity ( $V_c$ ) was measured and plotted from the image. Magenta and green arrows showed velocity vectors in different y directions. (D) ROIs were plotted on (C). (E)  $\vec{V}_c$  of various blastomeres during each spiral cleavage were plotted with mean (the blue dashed lines) and 95% SEM (gray area). The numbers in each graph indicated the mean  $V_c$  value.

#### 4.4. Mitotic spindle inclination during spiral cleavage

In Section 2.2.2, I've shown that the mitotic spindles inclined during the first spiral cleavage (Figure 2.4), and the perpendicular division axes were detected during the second through the fourth spiral cleavage forming a spiral looking embryo with the four clonal domains, one for each blastomere lineage (Figure 2.7, 2.8, 2.9, 2.10). The quantitative measurements of the cortical actomyosin dynamics revealed that the counter rotation at the cytokinetic ring was detected in the macromeres (Figure 4.5). This indicated that the macromeres contributed with the major biophysical forces

#### 4. Contribution of actomyosin to *P. dumerilii* spiral cleavage

for cell positioning resulting in the spiral cleavages. Combining these observations, I hypothesized that the cortical actomyosin counter rotation may actively position the spindles and thus determine the final division plane in the macromeres.

To investigate real-time spindle inclination within each spiral cleavage, the embryos were injected with *lyn-mCherry* and *emt6-3xgfp* mRNA and imaged with a 30-second temporal resolution from the animal pole. Both the plasma membrane and the mitotic spindles can be detected from the 4-cell stage (Figure 3.2). The four blastomeres at the animal pole of each spiral cleavage were investigated. As described in Figure 4.6, it showed that during the first spiral cleavage, the angles of the macromeres were less during the metaphase and increased along the progression of cell division (Figure 4.6 A). The cell deformation can also be seen at the anaphase and telophase of this cleavage, resulting in the dextral positioning of the micromeres (Figure 4.6 A). This was in accordance with the observations and description in the previous chapters (Chapter 2 and 3) based on various experimental and imaging techniques. Therefore, the cytoskeletal dynamics was active and played critical roles in the macromeres of the first spiral cleavage. However, as shown in Figure 4.5, actomyosin counter rotation was not observed in the micromeres of the third and fourth spiral cleavages. Therefore, I hypothesized that the division axes are determined prior to these cell divisions, and the cell division proceeds to separate the daughter micromeres. The movies showed that the division plane was pre-determined in the micromeres. The inclination angle remained unchanged throughout cytokinesis. Following cytokinesis one micromere was separated into two daughter micromeres along the cell long axis determined in the interface (Figure 4.6 B-D).



#### 4.4. Mitotic spindle inclination during spiral cleavage

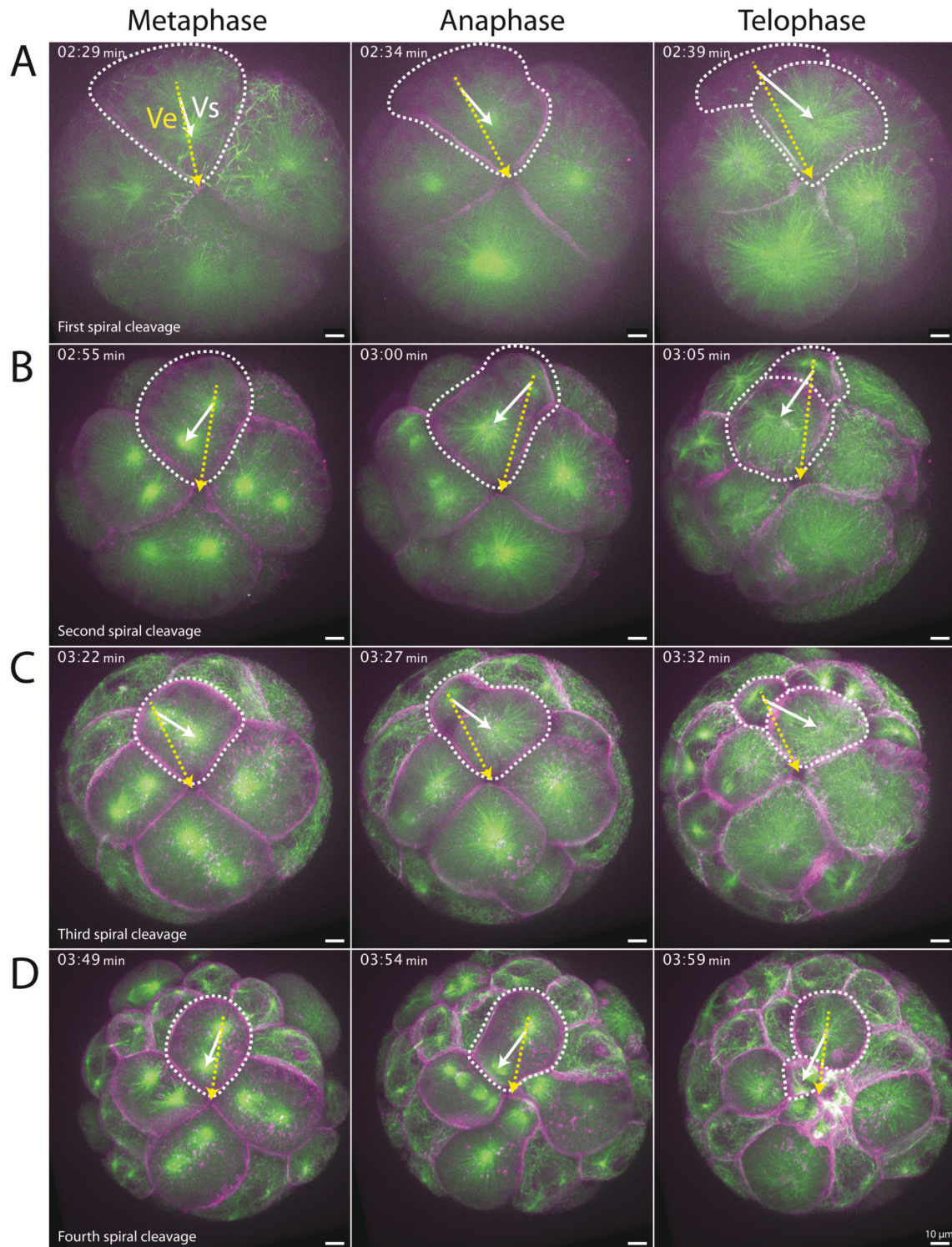


Figure 4.6.: The cell long axis dynamics during spiral cleavages.

#### 4. Contribution of actomyosin to *P. dumerilii* spiral cleavage

**Figure 4.6.: The cell long axis dynamics during spiral cleavages.** The zygotes were injected with the membrane marker *lyn-mCherry* and microtubule marker *emt看-3xgfp* and live-imaged from the animal view. (A-D) The mitosis of the four spiral cleavages was captured. The cell outline of the B lineage was marked with the white dashed lines. The long axis of the cell and the mitotic spindle vector was indicated with the white arrow (Vs). And the reference embryonic axis toward the animal pole was marked with the yellow dashed arrow (Ve). The format of the timestamp is hr:min. Scale bar: 10  $\mu\text{m}$ .

To measure the progress of the spindle inclination during spiral cleavage, I defined two directional vectors inside the embryo and calculated the spindle inclination angle. The embryonic vector (Ve) was defined as the vector from the outer mitotic spindle toward the center of the embryo (Figure 4.6, yellow dashed lines), and the spindle vector (Vs) was defined as the vector from the outer mitotic spindle toward the inner one (Figure 4.6 A-D, white dashed lines). The spindle inclination angle was then the angle between the two vectors. The spindle inclination angle of the macromeres during the first spiral cleavage and the micromeres at the animal pole during the second to the fourth spiral cleavage were measured and plotted on Figure 4.7. The inclination angle was significantly increased from the metaphase ( $12.63^\circ \pm 7.16^\circ$ ), anaphase ( $24.93^\circ \pm 8.88^\circ$ ), to telophase ( $32.63^\circ \pm 9.13^\circ$ ) in the macromeres (Figure 4.7, red boxes). However, the angle was set up in the micromeres during the metaphase ( $27.51^\circ \pm 3.69^\circ$  during the second,  $26.84^\circ \pm 3.22^\circ$  during the third, and  $21.24^\circ \pm 2.95^\circ$  during the fourth spiral cleavage), which were greater than the initial inclination angle of the macromeres during the first spiral cleavage, and remained constant throughout the cytokinesis (Figure 4.7, blue, black, and green boxes). The inclination angle of the micromeres at the fourth spiral cleavage was slightly decreased, from  $21.24^\circ \pm 2.95^\circ$  to  $17.94^\circ \pm 2.45^\circ$  due to the movement of the neighbor blastomeres. The cell axis was not changed during the division. With these measurement, it was claimed that

#### 4.4. Mitotic spindle inclination during spiral cleavage

the physical actomyosin counter rotational force was generated from the macromeres, resulting in the inclination of the mitotic spindles and cell division plane determination, leading to the spiral cleavage in *P. dumerilii*.

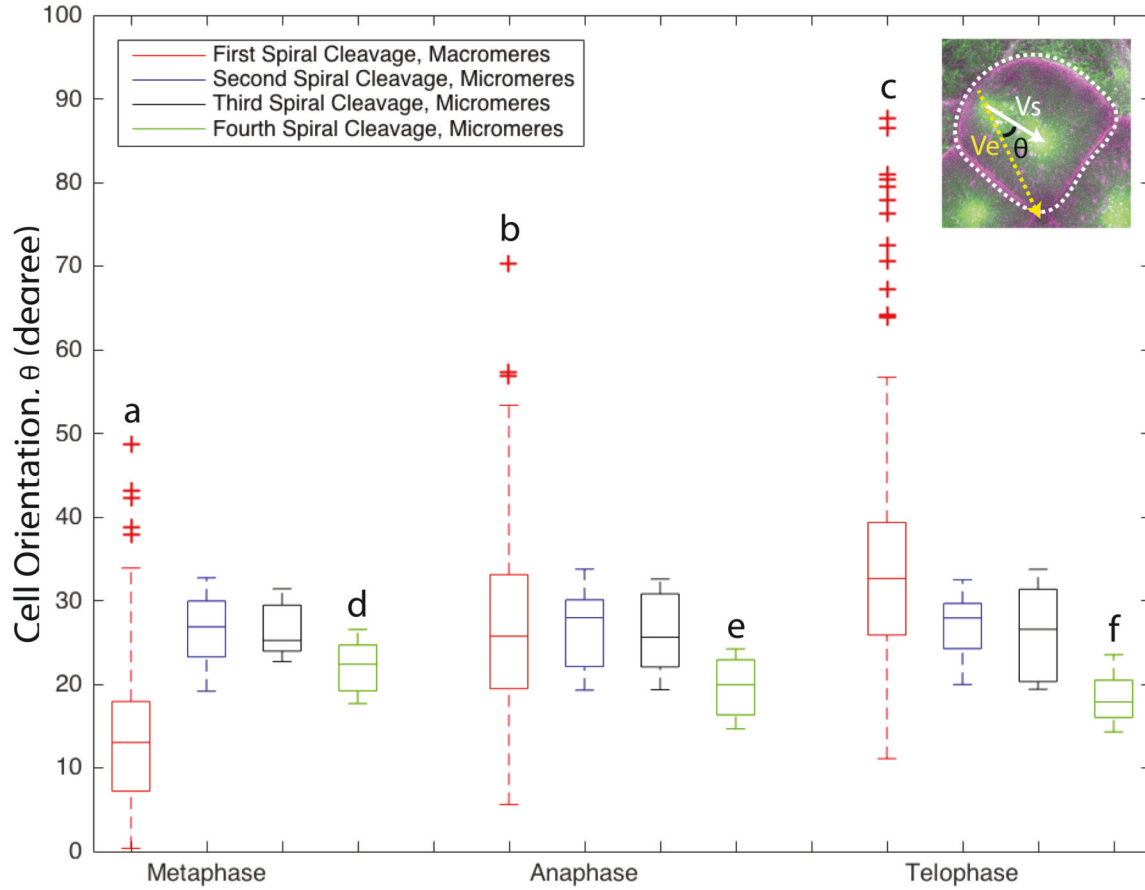


**Figure 4.7.: Measurement of the cell long axis dynamics between cleavages.** (E) The cell orientation  $\theta$  was defined as the angle between  $V_e$  and  $V_s$ , illustrated at the top right corner of the plot (also indicated in Figure 4.6). A, B, C, and D macromeres were analyzed during the first spiral cleavage (red boxes). Moreover, the micromeres located at the animal pole of the second, third, and fourth spiral cleavages were measured and plotted with the blue, black, or green boxes, respectively.  $n(\text{First.Metaphase})=328$ ,  $n(\text{First.Anaphase})=167$ ,  $n(\text{First.Telophase})=251$ , for all the rest groups,  $n=36$ .

## 4.5. Contribution of the cytoskeletal components to the first spiral cleavage

As shown in Section 2.2.2, the mitotic spindles inclined during the first spiral cleavage (Figure 2.5, 2.6). The inclination started from the metaphase throughout the whole cell division (Figure 2.5 C). Then the perpendicular division axes were observed during the remaining three spiral cleavages suggesting that different cellular mechanisms might control the first spiral cleavage versus the subsequent spiral cleavages, resulting in an embryo with four clonal domains and whose blastomeres had a spiral looking orientation when looking from the animal view (Figure 2.10). It showed that the spindle inclination was mainly detected during the first but the second to the fourth spiral cleavage (Figure 4.6, 4.7). And  $V_c$  was detected mainly in the first two spiral cleavages (Figure 4.5). Therefore, here I focused on the mechanisms controlling the first spiral cleavage to understand the relationship of each cytoskeletal component in this process.

### 4.5.1. The chemical treatments targeting cytoskeletal elements

The shift in cell positioning during the first spiral cleavage was achieved by a combination of an inclination of the mitotic spindle, a deformation of the cell membrane, and the closure of the cytokinetic ring (Kuroda, 2014). These cellular processes required cytoskeletal elements including microtubules and actomyosin (Shibasaki et al., 2004). To elucidate whether spindle inclination or cell orientation determination is required for spiral cleavage to occur, the embryos were treated with exogenously applied chemicals



#### 4.5. Contribution of the cytoskeletal components to the first spiral cleavage

targeting microtubule, actin, or myosin.

To disrupt microtubule function, the commonly used drugs in cell biology colchicine and nocodazole were selected. Colchicine binds to soluble tubulin and form tubulin-colchicine complexes. These poorly reversible complexes then bind to the end of microtubules and stop microtubule elongation. Therefore, colchicine arrests microtubule growth. Moreover, it promotes microtubule depolymerization at high concentration. It's been used for cell cycle studies since it results in cell cycle arrest in the metaphase (Taylor, 1965). Nocodazole disrupts microtubules by binding to  $\beta$ -tubulin, thus interfering with tubulin polymerization. It's been largely used in cell biological studies, especially for flow cytometry, because it makes cell cycle arrest in G2/M phase (Blajeski et al., 2002). Therefore, either colchicine or nocodazole was applied to the developing *P. dumerilii* embryos to elucidate the roles of microtubule in spiral cleavage.

Actomyosin is asymmetrically distributed from 1-4 cell stage and in the macromeres of *P. dumerilii* (Figure 4.1, 4.3). And it plays critical roles in maintaining or changing the cell shape (Roh-Johnson et al., 2012), in cytokinesis (Kitanishi-Yumura & Fukui, 1989; Sedzinski et al., 2011; Cheffings et al., 2016; Spira et al., 2017; Dekraker et al., 2018), in cell polarity (Wedlich-Soldner et al., 2003; Munjal & Lecuit, 2014; Autenrieth et al., 2016; Raman et al., 2018; Saha et al., 2018), and in positioning of the cytosolic components (Ma & Taylor, 1994; Even-Ram et al., 2007; Joo & Yamada, 2016). To investigate which components of actin filaments and actomyosin are crucial to spiral cleavage, various commonly used chemicals, latrunculin A, CK-666 and SIMFH2, were applied to *P. dumerilii* embryos. Latrunculin A is a toxin produced by the sponge *Latrunculia* and *Negombata*, which binds to actin monomers at the

#### 4. Contribution of actomyosin to *P. dumerilii* spiral cleavage

barbed side of the actin filaments where actin nucleation takes place. Therefore, it blocks the end of F-actin and prevents polymerization. This F-actin disruption is then sufficient to make morphological changes to the mammalian cells (Coué et al., 1987). CK-666 is a chemical targeting the actin cytoskeleton regulator Arp2/3 complex. Two of the Arp2/3 subunits, the Actin-related-protein Arp2 and Arp3 resemble monomeric actin structure and serves as nucleation positions, binding to the existing filament and forming new actin filaments. Therefore, the connection of the branched actin forms the actin network. CK-666 binds to Arp2/3 to stabilize the inactive state of the complex, and therefore it inhibits the formation of actin branching structures. It's been used for studying the function of Arp2/3 and its influence on the F-actin network (Nolen et al., 2009; Hetrick et al., 2013). SMIFH2 is an inhibitor targeting Formin homology 2 domain. Formins are a group of Rho-effector proteins involved in actin polymerization, especially in the formation of parallel actin fibers forming close to the cleavage furrow during cell division. SMIFH2 therefore inhibits Formin-mediated actin assembly by disrupting Formin dependent processes (Rizvi et al., 2009; Isogai et al., 2015).

Regarding the inhibition of the motor protein non-muscle-myosin or its related pathways, several commonly used chemicals such as blebbistatin and Y-27632 were used to treat the *P. dumerilii* embryos. Blebbistatin is a myosin II inhibitor, which inhibits myosin ATPase activity and interferes with actomyosin-based motility. It binds between the nucleotide binding pocket and the actin binding cleft of myosin in an actin detached conformation (Shu et al., 2005). Y-27632 is a chemical used to interfere rho-associated protein kinase (ROCK) signaling pathways, which selectively inhibits p160<sup>ROCK</sup>. ROCK catalyzes myosin light chain phosphorylation, resulting in actin fiber contraction. It affects cellular function in multiple levels, including cell morphology, G1/S cell cycle transition, and cytokinesis (Ishizaki et al., 2000; Narumiya

#### 4.5. *Contribution of the cytoskeletal components to the first spiral cleavage*

et al., 2000).

The chemicals were dissolved in the recommended solvents (EtOH or DMSO, see Section 7.3.10) to make the stock solution, then they were diluted with natural seawater to 2x of the working concentration just before the beginning of the experiment to prevent aggregation or decomposition. First, the embryos were incubated in one volume of natural seawater. Then, they were mixed with one volume seawater containing the 2x concentrated chemical at the beginning of the 4-cell stage, around 120 mpf, for 20 min until the embryos in the mock control group started to divide. The embryos were fixed and the cytoskeletal elements were labeled by immunofluorescence or chemical dye staining.

##### **4.5.2. Cell division axis is not affected upon microtubule depolymerization**

In the mock controls, the mitotic spindles oriented in the direction of animal-vegetal axis at the metaphase and inclined in a dextral manner throughout the first spiral cleavage (Figure 4.8 A) as described in Section 2.2.2. Nocodazole treated embryos lost the mitotic spindles due to the tubulin depolymerization effect of the chemical. Partial microtubule signal remained in the 0.005  $\mu\text{M}$  nocodazole treated embryos, but no microtubules were detected under 0.01  $\mu\text{M}$  nocodazole treatment (Figure 4.8 B,C). The nuclei of A and B macromeres were closer to each other, as in the C and D macromeres, indicating that the nucleus migration to each end required the presence of microtubules (Figure 4.8 B,C). Without the pulling forces from the mitotic spindles at the end of the second embryonic cleavage, the nuclei cannot be positioned to the center

#### 4. Contribution of actomyosin to *P. dumerilii* spiral cleavage

of the daughter macromeres at 4-cell stage and remained closer to the position as in the previous cell cycle. However, the cytokinetic ring was detected at the right position without the presence of the mitotic spindles, indicating that the cell division plane was irrelative to the presence of the mitotic spindles during the first spiral cleavage (Figure 4.8 B,C). When the embryos were injected with the *syn21-lifeact-mKate2* mRNA and microtubule marker *emt6-3xgfp* mRNA into the zygote, soaked in 0.005% colchicine and live-imaged, the mitotic spindles were not detected due to the tubulin depolymerization effect of the colchicine, but the cell division plane was present in a dextral manner as in the controls (Figure 4.8 D, also see Appendix A.5 for detailed experimental design). The inclination of the long axes of all the four blastomeres were observed as in the control. Although the cell division was not achieved due to lack of mitotic spindle, the potential of dextral orientation of the division axes and the accumulation of actomyosin for cytokinetic rings indicated that, first, the animal-vegetal orientation of the cell was decided very early in the cell cycle during 4-cell stage. And second, the initiation of spiral cleavage (division axes inclination) was not mainly controlled by the microtubules nor the mitotic spindles.

#### 4.5.3. Cortical actomyosin is essential for cell deformation and microtubule orientation

In mock control embryos (0.5% EtOH), the cortical actin was clearly labeled during the first spiral cleavage (Figure 4.8 E). On the contrary, phalloidin staining (labeling actin) was weaker or not visible and the cell division did not complete when the embryos were treated with latrunculin A at two concentrations (0.75  $\mu$ M and 1.5  $\mu$ M latrunculin A). This indicated that latrunculin A successfully interfered with actin

#### 4.5. Contribution of the cytoskeletal components to the first spiral cleavage

polymerization resulting in the abolishment of the actin network. Although actomyosin was interfered, the mitotic spindles formed and were nicely labeled by immunostaining (Figure 4.8 F,G). However, the spindle orientation was randomized both in the 0.75  $\mu$ M and 1.5  $\mu$ M latrunculin A treated groups. It was shown in Figure 4.8 F that the abnormal spindle orientation of A and B macromeres and, A, B, D macromeres in Figure 4.8 G. When the embryos were injected with the cytoplasmic membrane marker *lyn-gfp*, microtubule marker *emt6-3xgfp*, actomyosin marker *syn21-lifect-mKate2*, and nucleus marker *h2b-mCherry* mRNA into the zygote and live-imaged while soaked in 0.75  $\mu$ M latrunculin A at 4-cell stage for one cell cycle, it showed that the division of the nuclear DNA was still processed, however, the division axes were randomized as shown in the fixed embryos (Figure 4.8 H, also see Appendix A.5 for detailed experimental design). Moreover, unlike the normal cell deformation and cleavage axes determination in the abolishment of microtubule, the long cell axes of the macromeres remained parallel to the animal-vegetal axis and no inclination was observed when treated with latrunculin A (Figure 4.8 H). An interesting observation was that usually the effects of latrunculin A was more severe to A and B blastomeres than to C and D (Figure 4.8 F-H). This may be due to the cell size difference so that the chemical effects on the bigger C and D blastomeres were less severe than on the smaller A and B blastomeres. When the embryos were treated with CK-666, not all the blastomere showed abnormal division axes. The effect of it to division angle was milder than Latrunculin A and many embryos showed normal cleavage at 4-cell stage (Figure 4.8 I). This may due to that CK-666 interfered the branch formation of the F-actin network so only a subgroup of actin structure was affected, or the penetrance of this chemical was not as efficient as other chemicals. On the other hand, the division axis was not affected under SMIFH2 treatment (Figure 4.8 J). However, this could be because of

#### 4. Contribution of actomyosin to *P. dumerilii* spiral cleavage

the low solubility of SMIFH2 in seawater. Therefore, the chemical may have less effect than the expectation and under other biological conditions at the same concentration. These observations indicated that both the orientation of the mitotic spindles and the final division axis were highly dependent on the contribution of cortical actomyosin, resulting in the dextral blastomere organization of the first spiral cleavage.

The contribution of the motor protein myosin in actomyosin was tested by treatments with the chemicals, blebbistatin or Y-27632. Blebbistatin has a low solubility in seawater, therefore the effect varied from embryo to embryo. In the embryos which were affected by the chemical, cortical actomyosin was hardly detected with phalloidin staining, and the mitotic spindle orientation was abnormal, as in the latrunculin A treated groups (Figure 4.8 K). The Y-27632 treated embryos showed a change in the cell division plane. Abnormal mitotic spindle orientation was observed in A and B macromeres. The division plane was perpendicular to the animal-vegetal axis, rather than parallel to it. Although C and D macromeres showed parallel division axis to the animal-vegetal axis, cell deformation was not observed, indicating that the daughter micromeres might not shift in position in a dextral orientation compared to the macromeres (Figure 4.8 L). These observations indicated that myosin activity was also crucial for proper first spiral cleavage. Taken together, the treatments with chemicals interfering with the actomyosin cortex indicated that actomyosin played critical roles to determine the division plane, orientation of the mitotic spindles, and cell positioning during the first spiral cleavage.



#### 4.5. Contribution of the cytoskeletal components to the first spiral cleavage

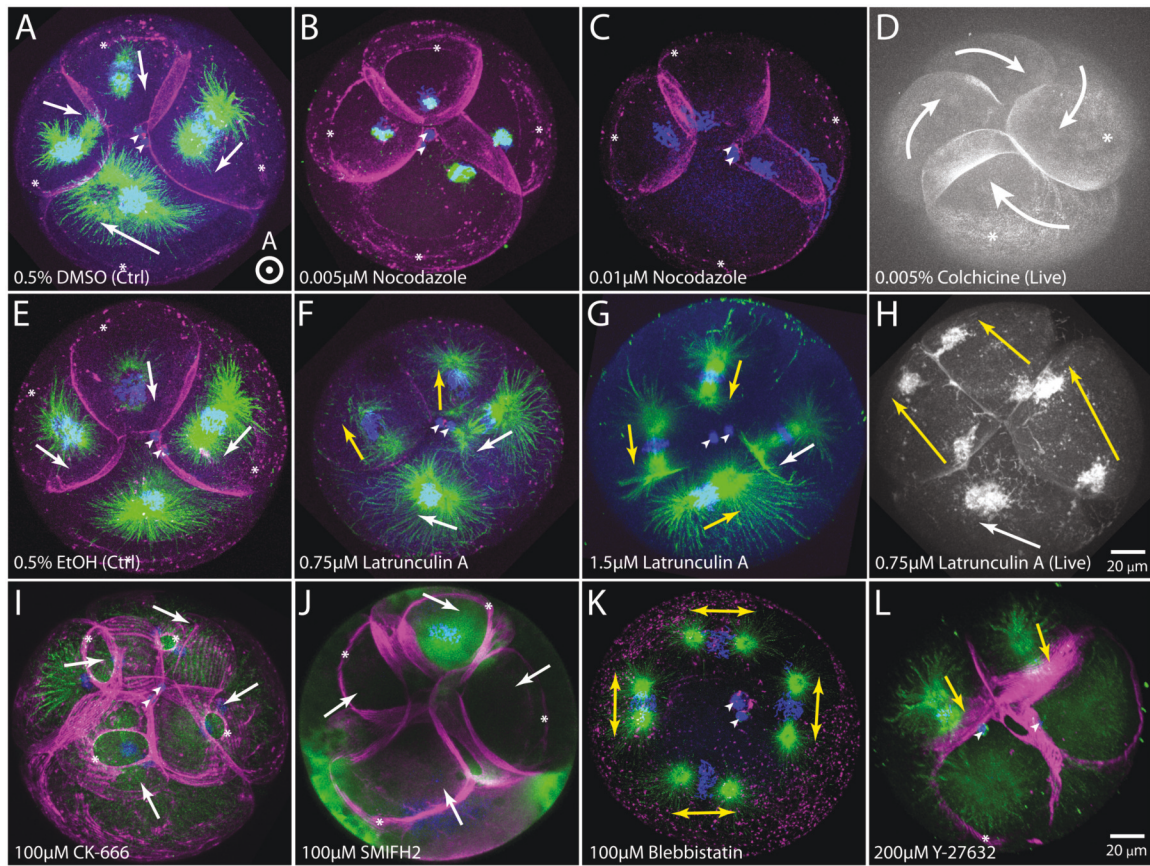


**Figure 4.8.: Cytoskeletal dynamics under chemical inhibitor treatments to the early *P. dumerilii* embryos.**

**Figure 4.8.: Cytoskeletal dynamics under chemical inhibitor treatments to the early *P. dumerilii* embryos.** The embryos were treated with various cytoskeletal inhibitors or myosin inhibitors at the 4-cell stage for 20 min. Then the embryos were fixed and stained with the microtubule maker, DAPI, and phalloidin and imaged by confocal microscope. (A, E) The normal *P. dumerilii* embryos performing the first spiral cleavage showed a dextral spindle inclination of all the macromeres (arrow indicated). (B, C) The embryos treated with 0.005  $\mu\text{M}$  (B) or 0.01  $\mu\text{M}$  (C) nocodazole showed microtubule depolymerization. Microtubule was detected around the MTOC at the low-dose nocodazole group (B) and there was no microtubule signal detected with a high-dose treatment (C). The cytokinetic ring was indicated with the asterisk. (D) Live-imaging of the colchicine treated embryo injected with the membrane marker *lyn-mCherry* mRNA showed that the blastomeres had the potential to perform a dextral orientation of the micromeres without the presence of the mitotic spindles. The curved arrows indicated the division axes. (F, G) The



#### 4. Contribution of actomyosin to *P. dumerilii* spiral cleavage

embryos were treated with 0.75  $\mu\text{M}$  (F) or 1.5  $\mu\text{M}$  (G) latrunculin A at the 4-cell stage for one cell cycle. The mitotic spindles showed random orientation, indicated by the yellow arrows. The white arrows indicated normal orientation of the spindles. (H) Live-imaging of the latrunculin A treated embryo injected with the membrane marker *lyn-mCherry*, spindle marker *emt6-3xgfp*, and DNA marker *h2b-mCherry* mRNA. (I, J) Neither CK-666 nor SMIFH2 showed dramatic division plane alternation during the first spiral cleavage. The dextral orientation of the cleavage plane, the position and closure of the cytokinetic ring were similar to the normal embryos. (K) The spindles were abnormally positioned, perpendicular to the animal-vegetal axis, under 100  $\mu\text{M}$  blebbistatin treatment. The yellow arrows indicated the spindle axes. There was no obvious animal-vegetal orientation of the spindles, therefore, the arrows were double-headed. (L) Both the orientation of the mitotic spindle and the division plane of the cytokinetic rings were interfered by 200  $\mu\text{M}$  Y-27632 treatment. The yellow arrows indicated the abnormal mitotic spindles orientation and the asterisks indicated the position of the cytokinetic rings. For all the tested chemical treatments, more than 80% of the specimens showed the phenotype ( $n > 100$ ). Scale bar: 20  $\mu\text{m}$ .

##### 4.5.4. Mitotic spindle angle in the absence of microtubules or cortical actomyosin

The spindle inclination angle of the chemical treated embryos (Figure 4.8) were measured and plotted as described in Figure 2.5 A. The control group showed major dextral inclination (average angle of  $36.813^\circ$ ) of the mitotic spindles (Figure 4.9 A). The data of the control group was taken from Figure 2.5 and all the four macromeres were pooled together. Therefore, this is the average spindle inclination angle of all the division phases among the four macromeres during the first spiral cleavage. The groups treated with the microtubule inhibitors (nocodazole or colchicine) were not measured, because of the abolishment of the microtubules. Embryos treated with latrunculin A showed a random distribution of the mitotic spindles (average spindle angle of  $0.65^\circ$ ). Around half of the spindles performed dextral inclination and the other half a sinistral

#### *4.5. Contribution of the cytoskeletal components to the first spiral cleavage*

inclination (Figure 4.9 B). This indicated that when actomyosin was interfered, the spindles were unable to position properly during the first spiral cleavage. The effect was milder in the CK-666 treated embryos (average spindle angle of  $10.029^\circ$ ) but still showed significant difference to the control group. Some spindles showed sinistral orientation after CK-666 treatment (Figure 4.9 C). This may be due to that CK-666 affects Arp2/3, which interferes with actin branching. Therefore, instead of a complete abolishment of the F-actin network, only a subset of actin structure was influenced, resulting in a partial abnormal mitotic spindle orientation. Although the solubility of blebbistatin, which inhibits ROCK activity, was lower in seawater and precipitated during treatment, it interfered division axes during 4-cell stage. The inclination angle (average of  $11.573^\circ$ ) was significantly less than the control group when treated with blebbistatin (Figure 4.9 D). Taken together, a decrease in the cortical actomyosin or its motor activity led to an abnormal spindle angle and consequently abnormal cell division axis. This can be a result of a lack of active spindle positioning by the actomyosin cortex.

To sum up, the chemical treatment experiments have shown that the first spiral cleavage can be divided into a series of events: first, the mitotic spindles were organized along the animal-vegetal axis, giving this cleavage a general division axis. Second, cell deformed during anaphase and this re-orientated the cell long axis. Third, the mitotic spindle inclined into a dextral manner, coupled by cell deformation and cytokinetic ring formation. Fourth, separation of chromosome mediated by microtubule led the cell components to the micromeres or macromeres. Fifth, the cytokinetic ring closure and further rotation of the whole micromere layer (by cell deformation) increased the spindle inclination angle in telophase. And sixth, the four micromeres were properly positioned through the motion of cytokinesis resulted in the completion

#### 4. Contribution of actomyosin to *P. dumerilii* spiral cleavage

of the first spiral cleavage (also summarized in Figure 6.1 in Section 6.1).

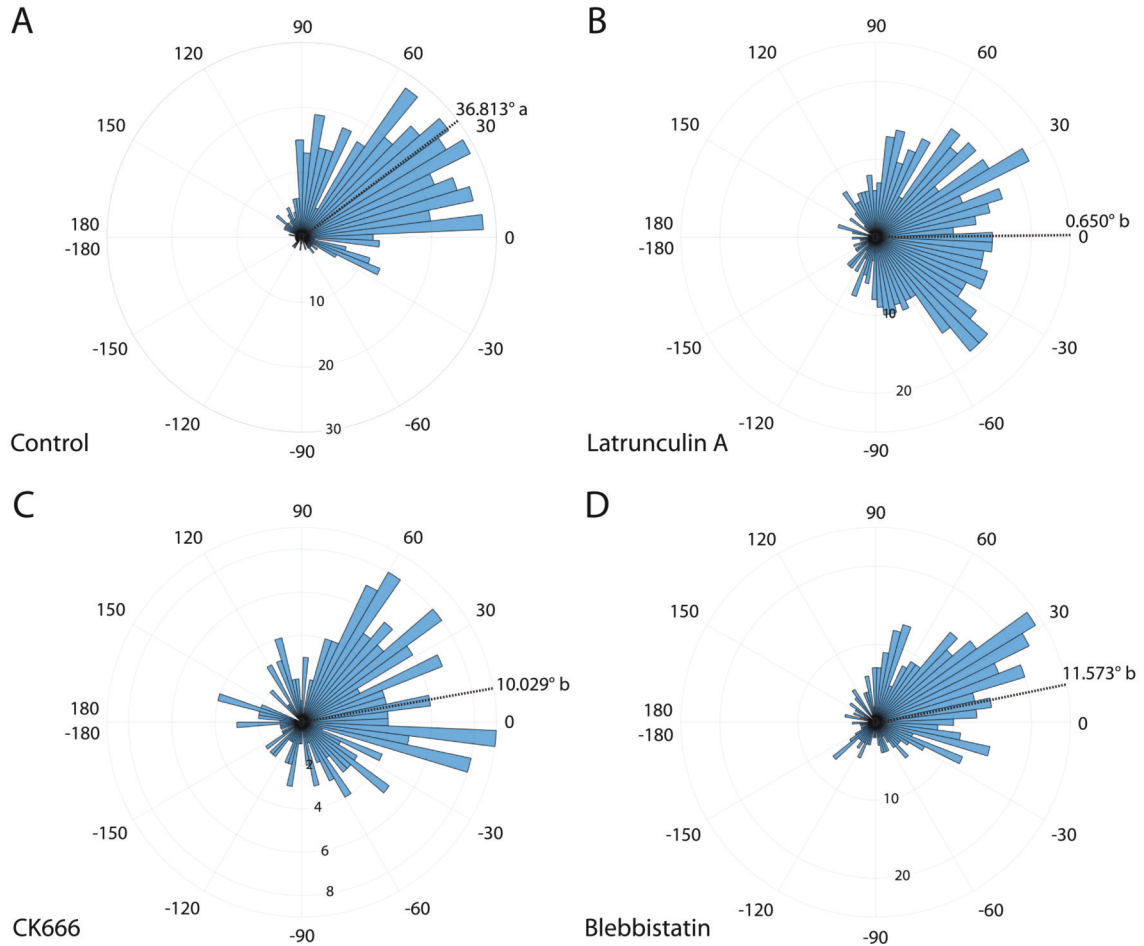


**Figure 4.9.: Spindle angle measurement of the cytoskeletal element inhibitors treated embryos during the first spiral cleavage.** The embryos were treated with the inhibitors at the 4-cell stage for one cell cycle and fixed. Microtubule, DNA, and the plasma membrane were stained and imaged with the confocal microscope. The spindle inclination angle was measured as the method described in Figure 2.5. (A) The spindle inclination angle of the normal embryos. The data was collected from all the macromeres of Figure 2.5. Most of them showed dextral orientation. (B) With latrunculin A treatment, the mitotic spindles performed random distribution in the blastomeres. (C) The spindle inclination angle decreased after CK-666 treatment. (D) The spindle inclination angle decreased after blebbistatin treatment. The dashed lines indicated the mean inclination angle. The alphabets behind the average angle indicated statistical difference of the groups.  $n(\text{Control})=540$ ,  $n(\text{Latrunculin A})=630$ ,  $n(\text{CK-666})=206$ ,  $n(\text{Blebbistatin})=457$ .

## Part III.

# Discussion and Conclusions



## 5. Discussion

Embryogenesis is a complex process starting from the zygote through rapid cell cycles, cleavages, producing a cluster of cells, blastomeres, and finally grow into a functional individual with differentiated cells forming various tissue, organs, and biological systems. These processes require not only molecular and cellular signals, but also biophysical mechanisms to achieve proper cell position and cell fate determination (see Introduction 1.5). In spiralian, the molecular signature of cells is well studied especially regarding transcription factors and cell specific factors during later developmental stages. For example, it's been shown in *P. dumerilii* that the typical brain specification gene, *otx*, is expressed anterior to the first segment defined by *engrailed*-expressing cell. And the four segments of the embryo show the expression boundary of *gbx*, *hox1*, *hox4*, and *hox5*, respectively (Steinmetz et al., 2011). The expression of these molecules controls the differentiation of cells into different cell types and give the cell their function, e.g., neurotransmitters or cell membrane receptors such as GPCRs. However, less is known regarding to the cellular and biophysical processes during the spiralian development. During my PhD thesis I thus wanted to gain insight into the cellular and biophysical mechanisms during the development of the spiralian *P. dumerilii*. I wanted to focus on the early development, the spiral cleavage, which is crucial for the initial setting up

## 5. Discussion

of the body plan. Here I will present the main results and discuss them with respect to what is known in other spiralian and phyla.

### 5.1. Visualization of the protein dynamics at early spiralian embryogenesis

Spiral cleavage starts from the third embryonic cleavage, which divides each of the four macromeres into a micromere at the animal pole and a macromere at the vegetal pole. The relative position of the micromeres and the macromeres determines the division direction of the remaining spiral cleavages. In *L. stagnalis*, it has been shown that with external mechanical force against the first spiral cleavage, the division as well as the following division axes and the whole animal chirality can be reversed (Kuroda et al., 2009). Therefore, the biophysical influences on cell division may play a critical role on the chirality of spiral cleavage. Biophysical processes are dynamic, so to study cell positioning and the biophysical mechanisms behind, I wanted to perform mainly live-imaging recordings and follow externally introduced fluorescent cellular markers. To image the protein dynamics as early as at 4-cell stage, the best approach would be to create transgenic animals with the target gene conjugated with a fluorophore. A few transgenic spiralian lines are available, but they were generated using transposable elements (Backfisch et al., 2013, 2014; Zantke et al., 2014). Considering the low output of the gene editing with transposable element, the effort to generate the transgenic lines and the generation time to obtain enough sexually maturing worms to be able to cross two transgenic animals, and the various candidates of cytoskeletal elements targeted for investigation, I focused on mRNA or fluorescent protein injection into the zygote



### 5.1. Visualization of the protein dynamics at early spiralian embryogenesis

and monitored embryogenesis. This strategy is easier and time-wise more efficient to monitor multiple cytoskeletal components during embryogenesis. However, it requires not only the embryos to develop normally after microinjection under live-imaging, but also the experimental set-up to optimize the expression level of the injected mRNAs or the stability of the injected proteins during early stages.

#### 5.1.1. Different microscopy approaches for live-imaging of spiral cleavage

A number of different microscope set-ups exist for live-imaging of the development. Each set-up has its own advantages. I tested different set-ups, but finally chose to use two approaches: light sheet fluorescence microscopy (LSFM) for whole-embryo imaging or spinning disk confocal microscopy for fast-imaging (see Introduction 1.4).

In order to capture the isotropic images of the whole embryo throughout development, the embryos were mounted in agarose/seawater and live-imaged by LSFM in an incubation chamber filled with seawater and set to 18 °C. Previous studies have shown that *P. dumerilii* embryos can be long-term live-imaged by light sheet laser beam and hatch afterward (Handberg-Thorsager et al., unpublished). This indicates that the early development is barely interfered, at least for the embryos chosen and imaged, by injection into the embryos and live-imaging by LSFM. However, due to the fast development of *P. dumerilii* embryos and the fact that imaging from five illumination directions is required to reassemble an isotropic image, the highest possible temporal resolution of this imaging technique is 90 sec, which is enough for tracking the early cell lineage and record the overall cellular processes taking place during cell

## 5. Discussion

division, but too slow to quantify the dynamics of the cytoskeletal elements. Therefore, spinning disk confocal microscopy was applied to examine actomyosin dynamics.

The spinning disk confocal microscopy is able to examine the embryos from one chosen direction. Each frame can cover a 20-30  $\mu\text{m}$  depth with 0.5  $\mu\text{m}$  optical sectioning. The frame rate is about 5-8 sec depending on the total depth of the image stack. With these settings, actomyosin dynamics can be recorded and analyzed by partial image velocimetry. However, due to the high scanning rate and the high laser power, the fluorescent signal usually decreases within a short time. This makes it difficult to live-image the actomyosin dynamics during the entire spiral cleavage. Therefore, in order to increase the imaging durability and the signal intensity, I have designed some strategies to optimize actomyosin expression in early *P. dumerilii* embryos, which I will discuss below.

### 5.1.2. Optimization of transient fluorescent labeling during spiral cleavage

It has been reported that injection of the mRNA encoding for a fusion protein with a fluorescent protein is successfully translated in the *P. dumerilii* embryo (Özpolat et al., 2017). However, most of the studies focused on the later stages such as segmentation or organ specification (Özpolat et al., 2017), giving the mRNA enough time to get translated and the protein to mature to obtain a strong fluorescent signal. When the scientific interest, as mine, comes to earlier stages such as spiral cleavage, the studies are mostly done by imaging the fluorescently labeled fixed embryos (S. Q. Schneider & Bowerman, 2007; Lambert, 2010; Pfeifer et al., 2014; Nakama et al., 2017). Therefore,

### 5.1. Visualization of the protein dynamics at early spiralian embryogenesis

in order to live-image the spiral cleavage and monitor its molecular dynamics during my thesis, I had to first develop a technique to optimize the fluorescent protein expression for early visualization. In this study, I have tested three ways for early visualization of the target genes, with special interest in the actomyosin, by chemical dye staining, by mRNA injection or by fluorescent protein injection into the zygote.

#### **The effects of the UTRs for protein expression in *P. dumerilii***

The mRNA injection method was mainly used for cell lineage studies of *P. dumerilii* (Özpolat et al., 2017; Vopalensky et al., 2019). The target genes were cloned into pCS2+ plasmid, which contains a SP6 promoter in front of its multiple cloning site. The fluorophore gene can be conjugated either at the 5' or the 3' terminus of the cloned open reading frames. The linearized plasmid is *in vitro* transcribed with SP6 transcriptase into mRNA and then injected into the embryos. Translation takes place within the embryos, meaning that the earlier the injection is done, the earlier the fluorescent signal is seen. The injection settings are already optimized so that the embryos cannot be injected even earlier with the current protocol. Injection with higher concentration of the mRNAs was also tested, however, large amount of exotic mRNA is toxic and lethal to the embryos. Therefore, boosting the translation efficiency becomes one of the potential methods to obtain a stronger fluorescent signal in a short developmental time.

In *Drosophila*, it was reported that specific 5' enhancers as well as the 3' termination signals increase the transgene expression (Pfeiffer et al., 2012). In my work, I tested syn21 and L21 5'UTRs, and p10 and SV40 termination signals in *P. dumerilii*. syn21 is a synthetic enhancer and L21 is the enhancer of the lobster tropomyosin gene.

## 5. Discussion

Both of them are reported to act in cis to increase translational efficiency (Pfeiffer et al., 2012). In this study, either of the two sequences (syn21 and L21) were designed to be conjugated right before the start codon of the *Pdupar6* open reading frame to test the translational acceleration ability. Comparing to absence of any 5'UTR, or with the *Pdupar6* 5'UTR, both syn21 and L21 enhancers increased the fluorescent signal intensity by at least 1.5 times. This suggests that the translation efficiency is increased by the presence of either syn21 or L21 5'UTR. It is not surprising that the p10 3' terminator did not increase the fluorescent signal. First, the exchange of SV40 terminator by p10 didn't increase the fluorescent intensity, indicating that p10 doesn't increase the mRNA stability. Second, it's reported that the 3' terminator increases transcription efficiency (Bönisch et al., 2007). The injected mRNAs were *in vitro* transcribed, therefore, only its stability and the translation efficiency play roles on the protein expression level. I thus chose syn21 as 5'UTR and SV40 as 3'UTR to construct the optimized mRNAs for increased protein translation.

### **Multiple approaches for labeling actomyosin in early *P. dumerilii* embryos**

One of my scientific interests in this thesis is to investigate the cytoskeletal dynamics and its contribution to spiral cleavage. I have tested three methods, which are commonly used to label actomyosin for live-imaging: chemical dye staining, mRNA injection, and fluorescent protein injection. SiR-actin was reported to label F-actin in various cell lines (Lukinavičius et al., 2014; Melak et al., 2017; Hu et al., 2019). However, neither by soaking nor by injection of the chemical dye into the embryos labeled F-actin in *P. dumerilii*. The labeling of SiR-actin was also not seen with presence of verapamil, an L-type calcium channel blocker which acts as a broad-spectrum efflux-pump inhibitor

### 5.1. Visualization of the protein dynamics at early spiralian embryogenesis

to avoid the expulsion of the dye from the cell. However, the labeling was detected when the fixed embryos were soaked in SiR-actin, indicating that the chemical does bind to F-actin, but was actively removed by the embryos. This could be resulted from novel pumps of the embryos, which couldn't be inhibited by verapamil, actively remove SiR-dye from the cytosol. Or the calcium channel is so strong that verapamil is insufficient to block its activity.

Various genes for actomyosin labeling were cloned and *in vitro* transcribed to mRNA followed by injection into the zygote. However, most of the myosin components, such as the essential light chains and the regulatory light chains, did not show a high resolution labeling of actomyosin even in the later stages of embryogenesis. The myosin heavy chain (*Pdunmm*) does label actomyosin nicely. However, due to its 6kb open reading frame, it is hard to detect *PduNmm* expression until 64-cell stage. It is therefore not practical to use it as an actomyosin indicator to study spiral cleavage in *P. dumerilii*. An alternative approach to increase the stability of the fluorescent Nmm signal and to insure expression as early as in the zygote, is to develop the transgenic line which contains the open reading frame of the fluorophore at the 3' end of the endogenous gene. I have identified an ~3kb genomic fragment including the last exon of Nmm heavy chain and designed five guide RNAs for CRISPR-Cas9 knock-in strategy (see Appendix A.6). These guide RNAs perform specifically cleaving activity by *in vitro* cutting assay. Moreover, the transgenic *Lsdia* line by CRISPR-Cas9 is successfully developed in *L. stagnalis* (Abe & Kuroda, 2019), indicating that this tool may also be applicable in *P. dumerilii*. However, this is work in progress and thus not an option for my initial work. Consequently, F-actin labeling using Lifeact became the only and the best choice for the experimental purposes.

## 5. Discussion

Although Lifeact is a 17 amino acid peptide, its expression is seen but not strong enough for quantitative analysis during spiral cleavage. To increase the expression level, syn21 was conjugated in front of the open reading frame of *lifeact*. The whole insert including syn21 and lifeact is small enough to be designed in a primer and easily cloned into pCS2+, making the cloning of the 5'UTR conjugated *lifeact* much more straight forward and precise. It is also shown in this study that different linker sequences and sizes between the fluorophore, mKate2, and Lifeact result in dramatic labeling differences. The optimal linker has been used in *C. elegans lifeact* construct showing better actomyosin labeling. I could show that with the optimal linker, both the cortical and cytosolic actomyosin network can be visualized. The labeling is weak, but detectable from two-cell stage and the signal intensity increases throughout development. Therefore, this mRNA construct and injection method is recommended for investigating actomyosin dynamics during spiral cleavage, especially the third and the fourth spiral cleavage.

To achieve the fastest actomyosin labeling after injection, the best way is to reduce the time for translation or skip translation. This is possible by injecting the protein directly. Before constructing Lifeact-mkate2, several other fluorophores were expressed by bacteria and purified for injection. However, most of them precipitated at higher concentration during purification, and did not show fluorescent signal when injected at lower concentration, probably because of misfolding of the protein (data not shown). However, Lifeact-mKate2 with the optimal linker was successfully expressed and purified without any precipitation. The concentrated protein solution can be kept under  $-80^{\circ}\text{C}$  for long-term usage. This opens the door to label actomyosin as early as from the zygote.

### 5.1. Visualization of the protein dynamics at early spiralian embryogenesis

The advantages of protein injection are, first, the fluorescent signal is detected right after the injection. Second, the signal intensity can be tuned by the amount of injection. Therefore, it's much stronger than mRNA injection during the first two spiral cleavages. However, there are limitations for using solely Lifeact fluorescent protein in this study. The input protein amount is fixed, therefore, the fluorescent signal decreases during the time of imaging. I showed that when the embryos were imaged at high temporal resolution (5-8 sec), the injected protein got diminished within 30 min, making it difficult to observe actomyosin dynamics throughout the four spiral cleavages. Moreover, due to the fast decay of the fluorescent signal, the imaging needs to be more precisely targeted to the beginning of the desired cell cycle, making it more challenging for the experimental design.

In summary, both the syn21 containing *lifeact-mKate2* mRNA with the optimal linker and the purified Lifeact-mKate2 protein label actomyosin in *P. dumerilii* embryos from the early stages. The mRNA is more applicable for the third spiral cleavage or later, or for long-term imaging. The fluorescent protein is useful for targeting specific cell cycles or for higher signal intensity in the first or second spiral cleavage. A combinatorial approach, which I started to investigate, is to combine the Lifeact protein injection with mRNA injection, which translates the same end product, so that I would first image the fluorescent protein and subsequently the increasing signal of the translated mRNA.



## 5.2. The cellular processes before and during spiral cleavage

*P. dumerilii*, as the model organism in this study, has many advantages for the investigation of the early stages. The well-controlled maturation, mating, and embryo collection procedures make it possible to precisely monitor embryogenesis from the zygote. The development of the individuals is highly synchronous. This feature makes the examination of embryogenesis from a given developmental stage practical. Although the development is highly synchronous, the developmental speed is relative to the environmental temperature (A. H. Fischer et al., 2010). Therefore, the cleavage time at 18°C is characterized in Table 2.1 to set up a standard timeline for specific divisions. This timeline is also a guideline to capture a certain phase of the cell cycle. By standardizing the incubation temperature and the cleavage timing, different phases during each cell cycle is then captured and examined by fixation and immunofluorescence. The transparency and the moderate size of the embryos are perfect for imaging with various microscopies. The injection procedures are relatively simple and can be done during the zygote stage. various molecules (e.g., mRNAs, proteins, dyes, or chemical inhibitors) can be injected for different experimental purposes. Therefore, the investigation and manipulation of its development can be started from the first two unequal cleavages, providing the first clues of the molecular and cellular dynamics during spiral cleavage of *P. dumerilii*.

### 5.2.1. The first two unequal embryonic cleavages result in four macromeres with different cell sizes and cell fates

Among the spiralian, the first two divisions create eventually four macromeres (A, B, C, and D) which are the source for the four quadrants during spiral cleavage. Different organisms have different ways of achieving the four blastomeres. In general, the cleavages are either equal or unequal generating four cells with similar size or various sizes (Henry & Martindale, 1987; Lambert, 2010). D lineage specification occurs as early as within the first two asymmetric cleavages in the unequal cleaving spiralian, but later at the fifth embryonic cleavage in the equal cleaving spiralian (see Introduction 1.2.3).

Earlier literature (Nakama et al., 2017; A. H. Fischer et al., 2010) and my DIC live-imaging recordings of the developing *P. dumerilii* embryo have shown that the zygote undergoes two unequal cleavages resulting in the largest D cell, the second largest C cell and two smaller A and B macromeres. I've shown that the asymmetric cleavages were done by asymmetric positioning of the mitotic spindles as well as the chromosomes. The asymmetric cleavages make it easier to track the four quadrants and trace their destination. Through monitoring of the development of the dissociated macromeres, I could also confirm that each of the four macromeres gives rise to a part of the embryo, suggesting that the cell fates are determined as early as in the first two cleavages. Costello has shown similar results with *Nereis* embryos that each of the two blastomere during the two-cell stage develops into partial embryo after cell dissociation (Costello, 1945). These conservative observations indicate that the early cell specification occurs through asymmetric cell division and may facilitate the speed

## 5. Discussion

of development.

Immunofluorescence on fixed embryos showed that both of the two asymmetric cleavages not only showed the off-centered mitotic spindles, but also contained asymmetric cytokinetic ring formation procedure. The cytokinetic ring forms according to the position of the mitotic spindles and where the DNA locates. The spindle position sets the cell equator which guides the formation of the cytokinetic ring. However, the accumulation of actomyosin to form the rings was not evenly distributed across the equator, but first detected at the animal pole during early anaphase. The closure of rings was also asymmetric, from the animal pole toward the vegetal pole. This indicates that the cellular component and cytoskeletal elements distribute differently along the animal-vegetal axis as early as in the zygote. This was also confirmed by lifeact mRNA or protein injection and live-imaging, where Lifeact localizes at higher concentration at the animal pole forming a gradient from animal to vegetal pole from zygote to 8-cell stage during early *P. dumerilii* development. Later this gradient is still detected, which is higher in the micromeres and the micromere side of the dividing macromeres throughout the four spiral cleavages. All of the observations have suggested that the animal-vegetal axis, the dorsal-ventral axis, and the cell fate of the four macromeres have been determined as early as in the 4-cell stage. Therefore, the mechanism to determine the left-right axis during spiral cleavage becomes one of the most important remaining puzzles to solve in spiralian development.

### 5.2.2. Early lineage tracking reveals symmetry breaking events

Previous studies of the development in *P. dumerilii* has shown that developmental speed is affected by temperature (A. H. Fischer et al., 2010). I therefore chose to culture the embryos at 18 °C as done by other *P. dumerilii* studies and this way facilitated the comparison of my experiments. Cell tracking is a reliable way to determine the destination of blastomeres in organisms with determinate development. I wanted to follow the early cell lineages in *P. dumerilii* to dissect in details the exact division time and angles of the blastomeres during spiral cleavage and at the same time verify the existing cell lineages based on still pictures and observations through a bright-field microscopy (Ackermann et al., 2005). *P. dumerilii* develops relatively faster than other spiralian (e.g., snails and flatworm *Maritigrella crozieri*). This makes the tracking of the cell lineage harder. High temporal resolved, isotropic and fluorescent images are required for tracking. In Chapter 2 I described that the cell tracking is possible, because the cleavages are conserved between embryos under a given incubation temperature. Therefore, through a combination of bright-field DIC live-imaging, live-imaging of the fluorescently labeled embryos, and using the advantage of easy cell recognition because of different cell sizes, the early developmental cell lineages can be precisely analyzed. It is reported that spiral cleavage is highly synchronous between the four quadrant lineages A, B, C and D during the first three spiral cleavages (until 32-cell stage) (Ackermann et al., 2005). My bright-field live-imaging recordings showed that the micromeres divide synchronous until the fourth spiral cleavage, which gives rise to four small cells responsible for the future apical tuft. The synchrony was also seen in each sub-lineage of micromeres. But the overall synchrony started breaking apart at 16-cell stage. When a more precise cell tracking was done with the Fiji plugin MaMuT based

## 5. Discussion

on fluorescently labeled nuclei, I could describe a detailed timing of each cell cycle event for each lineage. Starting as early as from the first spiral cleavage, it showed that the cell cycle of C and D lineages are slightly shorter than A and B meaning that C and D divide earlier than A and B. At the beginning the difference was little. C and D macromeres enter anaphase prior to A and B during cytokinesis. The difference increases through the spiral cleavage period. However, the actual cytokinesis between the cells is relatively synchronous until 8-cell stage. From 16-cell stage that is during the third spiral cleavage, the cell cycle of each lineage changes dramatically. The fates of the lineages have been examined and reported (Ackermann et al., 2005). Therefore, it explains that the cell cycle changes during the third and the fourth spiral cleavage. For example, the epidermal lineages  $1q^{11}$  divide earlier than most of the other lineages. And the prototroch lineages  $1q^{21}$  and  $1q^{22}$  divide synchronously and are among the first cells to differentiate into the ciliated cells of the ciliary band (Özpolat et al., 2017; Vopalensky et al., 2019). It's also observed that the correlated blastomeres of each lineage (e.g.,  $1a^{21}$ ,  $1b^{21}$ ,  $1c^{21}$ , and  $1d^{21}$ , or  $1q^{21}$  in short) have relative closer cell cycle duration. This indicates that the cell differentiation may start as early as in early spiral cleavage.

In my lineage tracking data, it showed that the macromeres also contain shorter cell cycles than the other lineages. D macromere has the shortest cell cycle among the four macromeres, followed by C. This may indicate the leading and organiser role of the D macromere. Although it's very little known if a specific macromere could lead spiral cleavage, there are many clues of this possibility. First, the division axes change actively with nuclei migration, suggesting that the macromeres may contribute in active cell positioning during spiral cleavage comparing to the micromeres. Second, D macromere shows greatest spindle inclination angle at the first spiral cleavage, and

## 5.2. The cellular processes before and during spiral cleavage

also divides prior to other macromeres. Third, this leading role continues throughout the four spiral cleavages. I plan to do the following experiments in the future to test this hypothesis. One, to dissociate only the D macromere and investigate if the inclination angles of the other macromeres decrease. Two, to inject the chemical which inhibit cell deformation (e.g., latrunculin A) into D macromere and monitor how cells are orientated without the division of the D macromere. If the disruption of spiral orientation of the D macromere does result in the interference of spiral pattern of the other lineages, D macromere is then the guide lineage for spiral cleavage in *P. dumerilii*.

Although C/D lineage always start cell division earlier than A/B lineage, the division timing between C and D lineages (as well as between A and B lineages) are highly synchronous, shown by my lineage tracking and imaging of the living/fixed embryos. The later cell fate mapping revealed by Ackermann showed that the 1a<sup>11</sup> and 1b<sup>11</sup> lineages develop into left and right epidermal, ventral-brain, and gland cells, respectively. The 1c<sup>11</sup> and 1d<sup>11</sup> lineages have similar bilateral symmetric cell fates (Ackermann et al., 2005). Therefore, the synchrony of the pairs of lineages, e.g., C and D lineage, may indicate that the first hint of bilateral symmetry establishment in spiralian could occur at the first spiral cleavage. However, it's been shown in snails that the left-right asymmetry factor Nodal/pitx pathway is not activated until 32-49 cell stage (Grande & Patel, 2009; Kuroda, 2015; Martín-Durán et al., 2016; Vellutini et al., 2017). To investigate if these factors are segregated earlier than the first spiral cleavage, I plan to further analyze the single cell RNAseq data of early *P. dumerilii* embryogenesis (Vellutini et al., unpublished). This may help to understand the maternal influence of symmetry breaking in spiralian.

## 5. Discussion

In summary, in *P. dumerilii* the first two embryonic cleavages (until four macromeres) and the first two spiral cleavages (4-8 and 8-16 cells) are relatively synchronous. The breaking of synchrony is largely observed from the third spiral cleavage. And the synchrony is preserved according to left-right body axis, serving as a sign of left-right symmetry. These observations also suggest that, if the cytoskeletal element controlled dextral orientation of the micromeres plays a critical role in spiral cleavage, it should contribute during the first two spiral cleavages. Due to the synchrony of the first two spiral cleavages, the coordination of actomyosin or other cytoskeletal elements may affect much more efficiently to the whole micro-/macromere orientation, resulting in the dextral orientation of *P. dumerilii* embryos.

### 5.2.3. Cellular mechanisms contributing to spiral cleavage

From snails it is known that spiral cleavage can initiate in a dextral or sinistral division orientation and that the different handedness results from different cellular mechanisms (Shibazaki et al., 2004; Kuroda et al., 2009; Kuroda, 2015). An initial dextral orientation of the micromeres is dominant in some snail species, e.g., *L. stagnalis* (Kuroda, 2015). Here, the mitotic spindles incline during the metaphase of the first spiral cleavage. Further, the cells deform to create space for cell positioning. With these settings, the division plane is determined before cytokinetic ring formation, suggesting that the cell orientation changes during the interface of the 4-cell stage. Therefore, the micromere layer is already dextral oriented once cytokinesis occurs. However, about 20% of the individuals contain sinistrally oriented micromeres. Interestingly, the cellular mechanism is different from the dextral. First, there is no cell deformation detected during metaphase and second, at first the mitotic spindles are oriented



## 5.2. The cellular processes before and during spiral cleavage

toward the animal pole, along the animal-vegetal axis. When cytokinesis occurs, the cytokinetic ring orients perpendicular to the animal-vegetal axis, leading to a neutral division at the beginning. However, at the end of cytokinesis, a rotation of the micromere layer occurs together with the inclination of the mitotic spindles, leading to the sinistral chirality. Therefore, in this model, the key influence to chirality happens at the end of cytokinesis. In my thesis work, I wanted to understand which mechanism is used in other spiralian and if there is a consensus depending on the handedness. Sinistral division orientation have only been described within molluscs, so I focused on describing the cellular mechanism behind the dextrally dividing annelid *P. dumerilii*. Further, I added the dynamic aspect to the study to be able to quantify and thus understand the biophysical mechanisms during cleavage.

Through imaging of the fixed embryos and measurement of the mitotic spindle inclination at each phase during the first spiral cleavage, I showed that the spindles are assembled almost parallel to animal-vegetal axis. Only little cell deformation was detected at metaphase and anaphase. The plane of the cytokinetic rings is perpendicular to the animal-vegetal axis upon their formation at the beginning of anaphase. These features follow the sinistral model of *L. stagnalis*. However, starting from the formation of the cytokinetic ring and during the closure of the ring, the inclination angle of the mitotic spindle increases dramatically. The plane of the cytokinetic ring also inclines while closing for the dextral orientation of the micromeres. These observations follow the dextral model in snails, where the division plane is orientated toward dextral. The inclination happens later in *P. dumerilii*. Instead of at metaphase as in the dextral strain of *L. stagnalis*, the major spindle inclination takes place during telophase in *P. dumerilii*. Considering when the spindle inclination is maximized for the first spiral cleavage, the major biophysical influence from the

## 5. Discussion

cellular structures should play a role during cytokinesis.

Spiral cleavage is described to have alternating division axes between each cell cycle (Brun-Usan et al., 2017; Girstmair & Telford, 2019). When the first spiral cleavage performs a dextral, clockwise rotation of the micromeres, such as in *P. dumerilii*, the following cleavage performs a sinistral, counterclockwise rotation of the cell layer with respect to the animal pole. There are two possible cellular mechanisms specifying the direction of cell division resulting in the alternating division axes. Hertwig's rule describes that a cell should divide perpendicularly to its longest axis (Brun-Usan et al., 2017). It explains part of the spiral cleavage pattern by connecting the shape changes of the cells and the specific direction of the division plane (Brun-Usan et al., 2017). By observing the spiral cleavages of *P. dumerilii*, especially the micromeres, it showed that the longest axis changes between each cleavage. The cleavage divides a cell into two, splitting at the longest axis. Consequently, this makes the shorter axis longer in the daughter cell and change the cleavage plane in the next spiral cleavage. The long axis of the macromere is not obvious, and the nuclei migrate during the interface. Therefore, Hertwig's rule couldn't be easily observed in the division of the macromeres. Secondly, Sachs' rule describes that cells divide at certain angles to the previous cell division. The rule has been proposed to be a result of duplication and migration of the centrioles along the nuclear envelope between cell divisions. This migration forms a  $90^\circ$  angle between each division and thus, affects the position of the mitotic spindle toward perpendicularity (Brun-Usan et al., 2017). Both in the micromeres and the macromeres it's been observed that the centrioles duplicated and migrated to form a perpendicular division comparing to the previous division. Interestingly, the duplication and migration of the centrioles was not affected by the actomyosin inhibitor latrunculin A. The nucleus showed the potential of perpendicular

## 5.2. The cellular processes before and during spiral cleavage

division axis alternation without obvious cell shape/axis change (see Appendix A.5). This indicated that Sachs' rule may be dominant over Hertwig's rule in *P. dumerilii* cleavages. But in general, the combination of these two rules can explain the cellular mechanisms of the alternating division angles between spiral cleavages. And this is the key feature in spiral cleavage to form the clonal domain of the four quadrants.

Spiralians are not the only animal clade with the alternating division axes and clonal domain formation. Also in echinoderms, which relies on radial cleavage, it was shown that the alternating divisions and clonal domain formation occur (Hahn, 1998). The echinoderms have their third embryonic division along the plane parallel to the animal-vegetal axis. Then, the next cleavage plane is perpendicular to the previous one. Therefore, the embryo shapes in a cylinder form as a consequence of radial cleavages. If we compare the two division strategies, spiral cleavage and radial cleavage, the key difference to diverge the early embryonic pattern lies in the division plane during the third cleavage. Mitotic spindle inclination is observed in the first spiral cleavage (that is the third embryonic division), but not during the later spiral cleavage. However, this inclination is enough to set up the initial plane and guide the next cleavages. With this initial inclination, every spiral cleavage gives rise to a layer of cells localized between the two cells of the previous layer, rather than a layer of cells located on top of the other layer as during radial cleavage. In summary, the spindle inclination during the third embryonic division in spiralians (spiral cleavage model) does not happen during the third division in echinoderms (radial cleavage model) and thus leads to a different embryo geometry. Figure 1.1 shows the illustrations of embryonic patterning and this comparison is indicated with green color code. I will therefore put more focus on discussing the first spiral cleavage, which seems to play a critical role in creating the specific cell orientation.

#### 5.2.4. Body handedness formation and potential physical force triggering spiral cleavage

The left-right symmetry breaking is one of the key events to determine embryonic axes. In spiralian, this is described to happen at the third embryonic cleavage, also known as the first spiral cleavage. Taking snails as models, *L. stagnalis* has both dextral (dominant) and sinistral (recessive) micromere orientation during the first spiral cleavage, leading to right- or left- handed chirality of the animal as well as the shell (Shibazaki et al., 2004). *P. acuta*, on the other hand, is a sinistral dominant species, using the same cellular mechanism as in the dextral *L. stagnalis* (Kuroda, 2015). It is claimed that the spiral cleavage led left-right symmetry breaking event in snails plays a critical role in the body plan determination. Although it is a critical step in development, different organisms do not have conserved mechanisms to achieve their chirality. For example, spindle inclination and cell deformation are seen in the dextral strain of *L. stagnalis*, but not in the sinistral strain. However, the sinistral dominant *P. acuta*, these cellular mechanisms are detected during the first spiral cleavage. This indicates that the upstream molecular mechanisms controlling spiral cleavage can be more complicated. Although the upstream signals may come from different levels, it was reported in *L. stagnalis* that the chirality can be changed by applying physical constraint to the blastomeres into the opposite direction, but the effect is not heritable (Kuroda et al., 2009; Kuroda, 2014, 2015). Therefore, it suggests that the last key component driving the first spiral cleavage is a mechanical force, and the other spiral cleavages follow the coordination set at the first one, resulting in the total reversed body plan. The mechanical force can be generated either intrinsically by the motor proteins and cytoskeletons of the cell, or extrinsically by the eggshell

## 5.2. The cellular processes before and during spiral cleavage

attached to the blastomeres (Münster et al., 2019).

In my thesis work, I wanted to examine both how the intracellular biophysical force is generated and contribute to the first spiral cleavage, and whether the blastomeres interact with the eggshell and the potential of the extracellular substances influence it. *P. dumerilii* embryo develops in a relatively small space inside of the egg (Figure 2.1). In embryos injected with fluorescent *lyn* or *lifeact* mRNA, or when F-actin was labeled with SiR-actin, it can be seen that the blastomeres interact with the eggshell by filopodia (Figure 3.7, 3.6, 3.1). Therefore, the mechanical force may not only be generated by the cytoskeletal elements which orientated the cell axis in its destined order, but also from the interaction between the blastomeres and the external barrier which positions the cells for specific chirality. My results do not support this however. Here I show that the embryos successfully complete the first spiral cleavage in a dextral manner with all the eight blastomeres located normally after the eggshell is removed. This indicates that spiral cleavage does not require the outside physical constraint. Moreover, the extrinsic force can instead be generated by the neighbor blastomeres as physical cell contact and cell movement during division (Galli & van den Heuvel, 2008; Brun-Usan et al., 2017). My cell dissociation experiments showed that the division plane and potential to undergo spiral cleavage does not require the physical contact of the whole four blastomeres. This suggests that the first spiral cleavage, which serves as a compass for the chirality, is triggered by intrinsic, cell autonomous physical forces.

Above I mentioned how the external force is enough to change the chirality in snails, and shown in my work that the eggshell is not essential in the first spiral cleavage. This indicates that the extracellular mechanical force is sufficient to introduce the chirality, but is not required since the intracellular organization of the cytoskeletal

## 5. Discussion

elements has already decided the natural division orientation. However, it was reported in *C. elegans* that different shapes of the eggshell create different constraint to the blastomeres, resulting in different cell orientation, both by prediction and experiments (Yamamoto & Kimura, 2017). Moreover, it was also modeled and proved by experiments that the eggshell plays a critical role in the body plan formation in early *C. elegans* development. ABa and ABp blastomeres become indecisive when the cleavages are done in absence of the eggshell, and since their cell arrangement does not allow for determining their cell identity, they are both called ABd blastomeres (Yamamoto & Kimura, 2017). This indicates that the blastomere orientation, axis formation, and early embryonic morphology are also influenced by the mechanical force from the extrinsic space constraint in some cases or in other organisms.

Although the eggshell is not required for *P. dumerilii* left-right symmetry breaking event, the first spiral cleavage, it is however required for the later development. It's been shown with *in silico* modeling that the cell-cell contact is important to make the blastomeres correctly positioned in spiralian development. When the cell-cell interaction factor and the adhesion factor are changed, the overall embryo shape becomes abnormal later in development (Brun-Usan et al., 2017). In my eggshell removal experiments, if the embryos developed without the presence of the eggshell, some of them form cone shape instead of normal spherical embryos. The micromeres keep dividing but don't migrate toward the vegetal pole because the space is not restricted by the eggshell. Therefore, epiboly couldn't take place and the macromeres remain exposed at the vegetal pole. The same result was also modeled by Brun-Usan et al. (2017). In some cases, the macromeres detach from each other resulted by the intense cell connection of the micromeres, as predicted in the computer-based modelling (Brun-Usan et al., 2017). In summary, the eggshell is important for cell migration and

### 5.3. Molecular basis and mechanical force generation of spiralian development

positioning during later stages in *P. dumerilii* embryogenesis. These preliminary data match the prediction and explains the function of the filipodia attached to the eggshell. To further test this hypothesis, I plan to change the extracellular substance, e.g., to embed the eggshell-free embryos in low melting temperature agarose, and monitor the overall embryo shape and cell positions in the later stages.

## 5.3. Molecular basis and mechanical force generation of spiralian development

It's been shown in this thesis that actomyosin contributed to spiralian development in various scales. Here in this section I wanted to discuss the molecular linkage of this mechanical force generator to the cell fate determinants, leading to early cell fate specification, and how the mechanical force affected blastomere orientations and behaviors, resulting in specific embryo patterning across evolution.

### 5.3.1. Cell fate determination and mechanogenetics of spiralian

*P. dumerilii* as an unequal-developer, the first two cleavages result in the four macromeres with various sizes. Each macromere has its own cell fate, both in the intact embryo or after cell dissociation at 4-cell stage. The asymmetric formation of the cytokinetic ring is observed in both cleavages. Through optimization of Lifeact construct expression, I showed that F-actin is asymmetrically localized at the cortex



## 5. Discussion

of the smaller daughter cell. It indicates not only that the cytokinetic ring can be generated off-centered, but also that the molecules, e.g., actomyosin, may segregate asymmetrically toward one of the two blastomeres and may contribute to early cell identity determination (Munro et al., 2004; Cowan & Hyman, 2007). Moreover, the *Pdupar* genes were also monitored to be localized to the animal pole throughout spiral cleavages. The animal pole enriched Par localization indicates that the blastomeres contain different molecular features and the Par genes may play a role segregating the polarity molecules to the micromeres later in the development (Nance & Zallen, 2011; Hoege & Hyman, 2013; Rose & Gönczy, 2014; Lang & Munro, 2017; Rodriguez et al., 2017). Together with Dr. Bruno C. vellutini and Dr. Mette Handberg-Thorsager we are currently performing single-cell RNA-seq experiments on dissociated blastomeres from 1-cell to 32-cell stage. This will provide us with candidate genes for cytoskeletal proteins involved in cell division and cell polarity and with genes for cell determination.

From my work and from previous work in *Nereis sp.* (Costello, 1945) it is known that, when the cells are dissociated, each blastomere can only develop into partial embryo, which follows the original lineage of the very blastomere (Ackermann et al., 2005). This indicates that the cell fates are determined in the early embryogenesis and may be independent to the localization of the cells in the embryo. It has also been shown that the bryozoan *M. membranacea*, a spiralian, which lacks of spiral cleavage, has very similar cell fates within each lineage compared to other prototypic spiralian (Vellutini et al., 2017). Although the cleavage pattern of bryozoans is closer to bilateral cleavage and absence of spiral orientation of the blastomeres, it is shown signs of molecular basis of early cell identity. For example, MAPK pathway, a putative underlying signaling in spiralian such as molluscs, (Lambert & Nagy, 2001, 2003; Henry et al., 2007; Koop et al., 2007) is detected solely in the 3D blastomere during

### 5.3. Molecular basis and mechanical force generation of spiralian development

28-cell stage in *M. membranacea*, which is similar to the pattern found in equal-cleaving molluscs (Koop et al., 2007; Lambert & Nagy, 2003). Therefore, it was concluded that despite the modified spindle orientation and cleavage pattern, bryozoans keep a quadrant-based embryo with mostly similar blastomere fates compared to other spiralian (Martín-Durán et al., 2016; Vellutini et al., 2017). It is also shown that the 3D macromere acquires its identity before the 24-cell stage in both the equal- (e.g., *Lymnaea*) and unequal- (e.g., *Ilyanassa*) cleaving gastropods, indicating that the cell fate may be determined before or during cleavages even if the A-D macromeres have same cell size and similar behavior in the embryo (Lambert & Nagy, 2003; Lambert, 2008; Goulding, 2009; Goulding & Lambert, 2016). Moreover, it has been reported that Wnt signaling pathway is activated asymmetrically in only one of the two daughter cells from 8-cell stage in *P. dumerilii*, indicating that the molecules triggering cell fate determination are activated in specific lineages as early as during the first spiral cleavage (S. Q. Schneider & Bowerman, 2007). All of the above observations suggest that neither the localization nor the relative size of the blastomeres play a critical role in cell fate determination, despite the molecular machinery for cell differentiation may be activated already during the first embryonic cleavages.

Spiral cleavage acts as the first left-right axis determinant during spiral cleavage. It was previously demonstrated that the chirality can be reversed by applying external force to the blastomeres during the first spiral cleavage (Kuroda et al., 2009; Kuroda, 2014, 2015). However, the reserved body plane is not inheritable. The manipulated individuals with mirrored left-right axis do not reproduce the offspring with the same feature (Kuroda et al., 2009; Kuroda, 2014, 2015). Therefore, it was proposed that the chirality of spiral cleavage is a genetical, but not epigenetical, heritable trait triggered by mechanical force within the embryo (Kuroda et al., 2009;

## 5. Discussion

Kuroda, 2014, 2015). Once the chirality is decided, the molecules with left-right spatial difference are localized/expressed based on the body plane. The *nodal* and *pitx* genes for example act downstream of the chirality determining marker and are expressed in 2c blastomere, with ectoderm fate, at 33-49, or 49-64 cell stage in snails (Grande & Patel, 2009). When chirality is reversed by micromanipulation at 8-cell stage, the *nodal* and *pitx* expression pattern are also reversed, indicating that the blastomere arrangement at the 8-cell stage determines the zygotic Nodal signaling pathway (Kuroda et al., 2009).

Despite the downstream signals controlled by handedness-determination are easily monitored, the upstream signals giving rise to this “mechanogenetics” remain unclear (Kuroda et al., 2016). With forward genetics using pure dextral or sinistral strain of *L. stagnalis*, diaphanous-related Formins are identified as candidates for chirality in snail spiral cleavage (Kuroda et al., 2016). There are two subtypes of diaphanous in *L. stagnalis*, *LsDia1* and *LsDia2*. These genes contain the conserved domains of diaphanous Formin, participating in actin nucleation and polymerization, microtubule stabilization, and can bind to Rho GTPases and Formins (Kuroda et al., 2016). It’s been shown that the *LsDia1* is expressed in the dextral snail strain, but hardly expressed throughout the development in the sinistral strain. *LsDia2* is expressed both in the dextral and sinistral strains from the zygote but the level decreases dramatically during the early stages. Neither *LsDia1* nor *LsDia2* show any spatial expression patterns in Kuroda’s study. However, *LDia2*, which is *LsDia1* in Kuroda’s study, identified by Davison et al. (2016), showed a localization pattern as early as from the zygote to a 4-cell embryo by asymmetrical segregation of the transcripts. They claimed that *LDia2* is exclusively expressed in one of the four macromeres during 4-cell stage, which is contradicted to the conclusion of the other

### 5.3. Molecular basis and mechanical force generation of spiralian development

article. Therefore, the upstream signals controlling the chiral force generation is still unclear. Unfortunately SMIFH2, the Formin inhibitor, has low solubility in seawater so that I couldn't conclude its effect on *P. dumerilii* spiral cleavage. But this could be a future target to for investigation.

#### 5.3.2. Evolutionary conserved mechanism during left-right symmetry breaking by active cortical actomyosin counter rotation

In *P. dumerilii*, I've observed the animal-vegetal orientation of the mitotic spindles during the metaphase of the first spiral cleavage. Then the spindles skewed in the dextral manner to have the correct micromere positioning. And later during cytokinesis, the micromeres rotated to their final positions. The biophysical mechanisms driving this series of cellular processes were illustrated in nematodes. Cortical actomyosin dynamics and its role during development have been extensively studied in *C. elegans* (Munro et al., 2004; Cowan & Hyman, 2007; Rose & Gönczy, 2014; Naganathan et al., 2014; Lang & Munro, 2017; Pimpale et al., 2019). Actomyosin labeling by either Non-muscle-myosin II (NMY-2::GFP) or F-actin (Lifeact::tagRFP-T) transgenic lines and tracking of their dynamics represent the cortical actomyosin movement and was done at various stages during cell cycle. When they quantified the actomyosin movement in the axis perpendicular to A-P axis before or during cytokinesis, a flow in the cell cortex toward one direction in the anterior part was measured, while a flow in the opposite direction in the posterior part during the interface of the zygote was observed. This created a chiral flow in the cell cortex. The difference of the

## 5. Discussion

flow speed vector is defined as counter rotational velocity ( $V_c$ ) (Naganathan et al., 2014). Moreover, myosin activity was shown to be crucial to chiral flow.  $V_c$  is decreased when myosin regulatory light chain is knocked-down (*mlc-4* KD). Since myosin activity is affected by Rho/ROCK pathway, they also tuned Rho-GEF (*ect-2*) or Rho-GAP (*rga-3*) activity by RNAi and concluded that  $V_c$  is dependent on Rho activity (Naganathan et al., 2014).

Cortical actomyosin counter rotation was not only detected in the zygote, but also from 4 to 6-cell stage in *C. elegans*, which is when the handedness of the embryo is determined (Naganathan et al., 2014). The mitotic spindles of ABa and ABp blastomeres incline  $\sim 20^\circ$  during cytokinesis, resulting in the bilateral symmetry breaking of *C. elegans*. Counter rotation is detected with similar  $V_c$  as in the zygote, and Rho GEF/GAP affects  $V_c$  as well. Interestingly, when  $V_c$  is decreased by *ect-2* RNAi, spindle inclination also decreases. Likewise, inclination angle is increased when  $V_c$  is increased by *rga-3* RNAi. Therefore, the authors concluded that actomyosin plays a critical role for spindle inclination, division angle determination, and left-right symmetry breaking in *C. elegans* (Naganathan et al., 2014).

The cellular behavior of what I observed during the first spiral cleavage in *P. dumerilii* is similar as the rotational cleavage in *C. elegans* 4-cell embryos. First, the mitotic spindles were organized along the animal-vegetal axis, like the initial spindle status of ABa and ABp cell. According to the polarization rule, cells should divide perpendicularly to the direction of the molecular gradient (Brun-Usan et al., 2017). In *P. dumerilii*, there is an actomyosin gradient along the animal-vegetal axis at the 4-cell stage. When the gradient is interfered by soaking the embryos in the actin depolymerizing agent, latrunculin A, at the 4-cell stage, the mitotic

### 5.3. Molecular basis and mechanical force generation of spiralian development

spindles orientate perpendicularly to animal-vegetal axis. Therefore, it indicates that actomyosin gradient may serve as a guide for initial animal-vegetal orientation of the mitotic spindles. Second, spindle inclination is observed during cytokinesis, which is similar to the skew of the mitotic spindles during *C. elegans* 4-cell stage. Third, cortical actomyosin counter rotation is detected during the anaphase to telophase of the first spiral cleavage in *P. dumerilii*, as during the division of the *C. elegans* ABa and ABp cells. Most of the decisive cellular and actomyosin events and their order are highly similar between *P. dumerilii* first spiral cleavage and *C. elegans* bilateral symmetric breaking cleavage at 4-cell stage. Although the two species are distant in evolution and the cleavage types are much different from each other, the mechanisms contribute to left-right symmetry breaking are very similar, indicating that the physical mechanisms to tune cell division angle and cell orientation may be conserved throughout evolution. Interestingly, cortical actomyosin counter rotation is also detected in the micromeres at 8-cell stage, which does not show obvious spindle inclination during cleavage. This suggests that counter rotation may have other roles in this division.

The cascade of cell deformation, spindle inclination, and micromere rotation during the furrow ingression in the first spiral cleavage was studied in the snail *L. stagnalis* by chemical inhibitor treatments. The dextral strain, which contains cell deformation as well as spindle inclination prior to cytokinesis, shows that cell deformation is not affected by nocodazole (inhibits microtubule polymerization), however, spindle inclination is neutralized when the embryos are treated with latrunculin A (inhibits actin polymerization) (Shibazaki et al., 2004). The sinistral strain neither shows cell deformation nor spindle inclination, but perform micromere rotation during the furrow ingression at 4-cell stage. When these embryos are treated with low dose of

## 5. Discussion

latrunculin A, micromere rotation is diminished, but the cytokinetic ring does form. These data indicate that actin-related cellular events such as, spindle orientation, cell shape changing, and cell movement are crucial for spiral cleavage (Shibazaki et al., 2004).

As mentioned in the previous sections, cell deformation of *P. dumerilii* is not as prominent as in *L. stagnalis*, and the spindle inclination occurs later during the anaphase to telophase transition and the micromere rotation is detected during cytokinesis. The mechanism of the first spiral cleavage of *P. dumerilii* may be a mixture of the dextral and sinistral *L. stagnalis* strains, but closer to the sinistral model. Although *P. dumerilii* embryos show only little cell deformation, it is still clear that the cells do not deform under latrunculin A treatment, but deform in the same direction and even more dramatically under nocodazole or colchicine treatment. Moreover, spindle positioning is randomized by latrunculin A treatment. The functional data seems to suggest that spindle positioning depends on cortical actomyosin. However, further investigation needs to be done to deduce whether it's an active mechanism where the spindles bind to the cortex and are moved along the cortex (Howard & Garzon-Coral, 2017) or a passive mechanism where a cytoplasmic flow, generated by the flow in the cortical actomyosin, moves the spindles through the cytoplasm (Niwayama et al., 2011).

The role of the cortical actomyosin counter-rotations on the lack of cell deformation during cytokinesis and micromere positioning upon latrunculin A treatment is difficult to be measured since the fluorescent labeled Lifeact normally used for the quantifications will not be visible and fluorescently labeled *non-muscle-myosin* mRNA is not visible during spiral cleavage by mRNA injection method. Alternative drugs to

### 5.3. Molecular basis and mechanical force generation of spiralian development

target the actomyosin cortex are the myosin inhibitors Y-27632 or blebbistatin. These treatments showed that spiral cleavage also requires myosin activity. Combining these functional data with the measurements on cortical actomyosin counter rotation during the first spiral cleavage indicate that the cortical actomyosin plays a role both in cell deformation and in micromere rotation during furrow ingression. And these processes seem to be crucial for *P. dumerilii* first spiral cleavage.

In *P. dumerilii*, B and D macromere have greater spindle inclination angles comparing to A and C macromere. This may indicate that, first, different macromeres have different contributions to spiral cleavage. Second, B and D macromeres may contain greater  $V_c$  leading to greater spindle skew. Third, Different cell identities and cellular compartments involved in this process lead to the variability in  $V_c$  between the macromeres at 4-cell stage. Since Formin (*LsDia1* and *LsDia2*) is essential for handedness determination in the snail *L. stagnalis*, I wanted to test the role of the Formins in *P. dumerilii*. Unfortunately, because of experimental limitations, it was hard to conclude whether Formin participates in *P. dumerilii* spiral cleavage; the Formin inhibitor SMIFH2 has low solubility in seawater, but could be maybe improved by directly injection into the embryo in the future. Likewise for CK-666, which inhibits Arp2/3. Therefore, although embryos under CK-666 treatment show less spindle inclination, the importance of the Arp2/3 complex of the F-actin network during spiral cleavage in each macromere needs further investigation.



### **5.3.3. Cellular and molecular differences between micromeres and macromeres**

The spiral looking embryo is generated not only by the first two embryonic cleavages and the first spiral cleavage, but also as a result of at least a few more cleavages (also spiral) with proper cell positioning. In this study, I have investigated the cell lineage and their orientation for up to 64-cell stage, covering six embryonic cleavages with four spiral cleavages. Regarding the first two asymmetric embryonic cleavages, the cellular and molecular mechanisms have been discussed in the previous sections. The asymmetric distribution of the cortical actomyosin may contribute in the asymmetric divisions. An animal-vegetal gradient of actomyosin guides initial spindle orientation. Cortical actomyosin counter rotation results in cell deformation, spindle inclination, and micromere rotation during cytokinesis of the first spiral cleavage.

As discussed in Section 5.2.3, the blastomeres might follow Sachs' rule between each cleavage. To determine this, it is important to know if the division axes are set based on the first spiral cleavage and all the remaining spiral cleavages use it as a compass, or whether there are other molecular mechanisms included in the second to fourth spiral cleavage. Therefore, latrunculin A was used to disturb actomyosin from 4-cell stage for a few cell cycles. Interestingly, although the mitotic spindles localized ectopically, perpendicular to the animal-vegetal axis, in the macromeres, and the nuclei divided without cytosol separation, the blastomeres seemed to follow Sachs' rule (the perpendicular organization of the spindles between each cleavage) even when cytokinesis was interfered by latrunculin A (Appendix A.5). The chaos of initial mitotic spindle organization indicates that actomyosin gradient and function

### 5.3. *Molecular basis and mechanical force generation of spiralian development*

play a critical role in setting up a general orientation, animal-vegetal orientation, for the spindles. And the later divisions use this coordinate and Sachs' rule to perform rotational division plane, eventually resulting in the spiral looking embryo.

Macromeres and micromeres differ not only in cell size and fate, but also in the way of division. Starting from the first spiral cleavage (4-cell stage), macromeres include most of the vegetal pole into their larger daughter cell. Therefore, the nuclei of these blastomeres are always located closer to the animal pole. The nutritional vesicles and oil droplets are then located at the vegetal side of the macromeres. This creates a major difference between the macromeres and micromeres, the macromeres have animal-vegetal polarity by their cellular component distribution while the micromeres do not have obvious cell asymmetry and the nucleus localize to the center of the cell. Also, the cortical actomyosin is asymmetrically localized to the future micromere side and the cytosolic non-muscle-myosin is largely segregated into the daughter micromeres during every division of the macromeres. These asymmetries are not observed during the division of the micromeres. Moreover, spindle orientation and dynamics as well as nuclei positioning are also distinct between macromeres and micromeres. My live-imaging recordings showed that the micromere nuclei locate to the center of the cells and follow Sachs' rule during spiral cleavage. Little nuclear movement is seen in the interface and no division angle changing is observed during cleavage. However, the macromere nuclei migrate with the cytosolic non-muscle-myosin and actin during the interface, and the division angle is determined both by Sach's rule and the final position of the nuclei. Since cortical actomyosin is asymmetrically distributed in the macromeres and migrate with the nuclei, it may suggest that both cortical actomyosin and the cytosolic proportion of non-muscle-myosin and actin contribute to the determination of the final position of the nuclei and the division angle.

## 5. Discussion

The measurement of actomyosin chiral flow ( $V_C$ ) between micromeres and macromeres showed that counter rotation is mainly detected in the first two spiral cleavages, especially in the macromeres. Interestingly, under long-term chochicine treatment and live-imaging, the cells deform first dextral, then sinistral, without actual cytokinesis (see Appendix A.5). It's not clear if these abnormal blastomeres can be considered as macromeres processing two cell cycles. But this might be an indication that actomyosin counter rotation actively change the division plane in macromeres during the first two spiral cleavages. Moreover, It has been reported that the separation of cytoplasm and oil droplets are controlled by respectively actin and microtubules in Medaka, *Oryzias latipes*, eggs (Webb et al., 1995). considering that macromeres inherit most of the oil droplets and the nutritional vesicles at the vegetal pole, perform active chiral flow, and guide spiral cleavage plane, it indicates that the microtubules at the vegetal side between the oil droplets may serve as anchors and help to determine the division angle and result in the dynamic cellular behaviors of the macromeres in *P. dumerilii*.

Interesting, I observed an accumulation of F-actin on the nuclear envelope before cell division both in micromeres and macromeres. This is one of the most unexpected, but interesting findings in this study. What is the role of this F-actin during cell division? A similar observation is known from other marine organisms *Nematostella vectensis*, sand dollar (echinoderm) and other polychaetes (Jacobsohn, 1999; DuBuc et al., 2014; Chun et al., 2018). It has been suggested that the accumulation may help nuclear envelop breakdown and guide asters of the mitotic spindles at prometaphase (Jacobsohn, 1999). However, the detailed mechanisms resulting in F-actin accumulation and its function remain unclear. *P. dumerilii* embryos and the optimized *lifeact* constructs make this system one of the best to answer this question. Moreover, the

### 5.3. *Molecular basis and mechanical force generation of spiralian development*

phenomenon does not occur in all types of cell division across species. It is only observed in the above model systems, during embryogenesis, specifically. Therefore, it can be assumed that the accumulation does not play a general role in cell division, but is essential in certain processes and is crucial for early cleavages in these species. The fast recruitment, assembly, and collapse of F-actin on the nuclear envelope may be achieved by novel cytoskeleton homeostatic mechanisms. Consequently, investigation the mechanisms of F-actin accumulation may identify unknown cytoskeletal functions in cell biology and embryology.

In summary, the differences between micromeres and macromeres may result from the variation in cell size, cell composition, the distribution of the organelles and molecules, and cell asymmetry. Furthermore, it results in the proper positioning of the micromeres divided from the macromeres during the second to fourth spiral cleavage, which is as equal important as setting up the coordinates of the division angle in the first spiral cleavage.

#### **5.3.4. Evolutionary speculations on the effects of cytoskeletal machineries to embryonic patterning**

In this thesis, I've shown the embryonic pattern formation of *P. dumerilii* in different levels, including blastomere orientation, intracellular molecular distribution, organelle migration, cytoskeleton dynamics, and cortical actomyosin dynamics, resulting in the animal-vegetal, dorsal-ventral, and left-right axis determination, and leading to the spiral cleavages, which eventually determine the embryonic pattern. By comparing different snail strains, as discussed previously, different actin nucleator

## 5. Discussion

Formin homologues, *LsDia1* or *LsDia2* of *L. stagnalis*, result in dextral or sinistral chirality (Kuroda et al., 2016; Abe & Kuroda, 2019). Therefore, we could speculate that the biophysical force is generated by actin contractility, with various upstream Rho-mediated pathways, e.g., Formins or Myosins.

Some spiralian phyla lack of clear trace of spiral cleavage, such as bryozoans, show very distinct embryonic patterns with conserved cell fates (Vellutini et al., 2017). Although the detailed mechanisms driving these cleavage patterns remain unclear, the lineage studies of bryozoans indicate that the cleavage patterns, at least in some species, affects the embryonic and/or adult morphology, without changing the cell fates. We can therefore speculate that, the change of division patterns may be caused by upstream molecule distribution, resulting in different cell orientation and actomyosin contractility. Further investigation of actomyosin dynamics are required to confirm it (see Section 6.2).

I've shown the conservation of actomyosin counter rotational flow mediated left-right symmetry breaking between the ecdysozoan *C. elegans* and lophotrochozoan *P. dumerilii*. It's also been shown that the spindle orientation in some cells depends on actomyosin activity during ascidian embryogenesis (Negishi & Yasuo, 2015). The mechanistic conservation found in these determinate developers indicate that these cellular and cytoskeletal mechanism I've concluded in *P. dumerilii* may be generally used to determine the final plane of cell division, or at least in some divisions which the division axis plays a crucial role, in the broader animal groups.

Lastly, does Rho-mediated actomyosin-based contractility also contributes in embryonic cleavage plane determination in the indeterminate developer, such as echinoderms, insects, or vertebrates? It's been shown that a wave of Rho activity

### 5.3. Molecular basis and mechanical force generation of spiralian development

and F-actin polymerization were observed both in frogs and echinoderms embryos (Bement et al., 2015), which is similar to *C. elegans* zygote (Naganathan et al., 2014). And actomyosin-based cell chirality, mediated by Myosin ID, determines left-right asymmetry in *Drosophila* embryos (Inaki et al., 2016, 2018). These suggest that the actomyosin mediated division axis determination, which I showed in this thesis, may be a conserved machinery across phyla and developmental types. But as a butterfly effect, a small difference of upstream signals, interacting proteins, or dominant motor proteins, tunes slightly the cleavage plane, eventually resulting in a dramatic variation in embryonic patterning across metazoans.



## 6. Conclusions, open questions, and future directions

### 6.1. Summary and conclusions

Here, I will summarize and conclude on the main findings of my PhD thesis. The cellular, cytoskeletal, and biophysical mechanisms are illustrated in Figure 6.1. To visualize the protein dynamics during early spiralian development, I established transient fluorescent labeling strategies by optimized mRNA constructs (Section 3.3) or protein injections (Section 3.4) and I determined the optimal imaging strategies for each of the individual biological questions in my thesis. This way, I used light sheet microscopy (SPIM) for whole-embryo imaging and spinning disk confocal microscopy for high-speed live-imaging and quantitative measurements.

Once the technical aspect was overcome, I live-imaged and described the spiralian development including the initial two asymmetric cell divisions leading up to spiral cleavage (Section 4.1.2). This also allowed me to track the cell lineage of the spiralian development (Section 2.3.2). I showed that the division of the blastomeres



## 6. Conclusions, open questions, and future directions

are simultaneous during the first four embryonic cleavages, then the cell cycle became diverse between each blastomere with D lineage dividing first, then C, B and A. But in general, the correlated blastomeres of each quadrant had similar cell cycle length, which was corresponding to the symmetry of the four quadrants. This was both examined with fixed embryos and live-imaging. These features of each lineage or blastomere was determined as least at 4-cell stage in development so that each blastomere had its only fate and cell cycle (Section 2.4).

One of the biggest technical achievement in this study was to live-image molecular dynamics with fluorescent microscopies of the early *P. dumerilii* embryos. Various genetic strategies including mRNA injection, optimization of the translation efficiency of the mRNA construct, and fluorescent protein injection, have set a variety of live-imaging tools for studying early embryogenesis (Chapter 3). In summary, syn21 can boost translation efficiency so that less mRNA was needed to achieve a visible fluorescent intensity and gave less abnormal effect to the embryos after injection. Although fluorescent Lifeact protein has relative short durability for live-imaging, it opened a window for instant imaging right after injection. The Combination of the two approaches, mRNA and protein injections, will be the way to live-image the entire spiral cleavage.

Observation and imaging of non-muscle-myosin at early developmental stages is challenging because all the injected mRNAs targeting non-muscle-myosin (Nmm) essential and regulatory light chains do not show clear localization, and the heavy chain gene is too large to give a strong fluorescent signal during spiral cleavage (Section 3.2.3). However, one approach to increase the stability of the fluorescent *PduNmm* signal and to insure expression as early as in the zygote, is to develop the transgenic

## 6.1. Summary and conclusions

line which contains the open reading frame of the fluorophore at the 3' end of the endogenous gene. With the fluorescent *Pdunmm* transgenic line, it would be much more efficient to further investigate and manipulate actomyosin activity before and during spiral cleavage in the future.

By *lifeact* mRNA or protein injection into the zygote, actomyosin distribution was seen from 1-cell stage (Section 3.3). It was shown that actomyosin distribution before 4-cell stage was largely located toward the animal pole forming a cortical actomyosin gradient along the animal-vegetal axis. The asymmetric distribution of actomyosin was not only seen along the animal-vegetal axis, but also at the dividing macromere cortex which destined to be daughter micromeres (Section 4.2.1). Interestingly, actomyosin accumulated shortly around the nuclear envelope right before its breakdown during cell division. This phenomenon occurred in every cell division of every blastomere and was confirmed by phalloidin staining in the fixed embryos (Section 4.2.2). It's function in *P. dumerilii* needs further investigation (see Section 6.2).

Starting from 4-cell stage, actomyosin was always asymmetrically localized to the micromere side of the dividing macromere, giving rise to daughter blastomeres with smaller cell size throughout spiral cleavage (the micromeres). Therefore, the asymmetric actomyosin distribution may serve as a sign for, first, the division orientation determination, second, asymmetric cytokinetic ring formation and, third, asymmetric cell division, where the smaller blastomere inherits more cortical actomyosin.

When focusing on the first spiral cleavage, the mitotic spindles were organized originally in the direction of the animal-vegetal axis, guided by asymmetric distribution of actomyosin along this axis. Very little cell deformation was observed at the cell

## *6. Conclusions, open questions, and future directions*

periphery at the beginning of anaphase. At the same time, the formation of the cytokinetic ring was observed, and massive spindle inclination occurred (Section 2.2.2). My drug treatment experiments targeting actin and tubulin polymerization have shown that cell deformation, the final orientation of the mitotic spindles, and the micromere rotation during telophase required actomyosin activity. However, cell deformation did not require the presence of the mitotic spindles (Section 4.5). Furthermore, the dextral orientation of the micromeres was likely generated by intrinsic forces because neither removal of the eggshell nor partial dissociation of the embryo disturbed the division axis determination (Section 2.4). At the molecular dynamics level, quantitative analyses showed that cortical actomyosin counter rotated during the cytokinetic ring closure, together with the inclination of the mitotic spindles (Section 4.3). Further, actomyosin was necessary for spindle orientation and development of the final cell division axis. In summary, actomyosin may play as a critical mechanical force generator to control the cell orientation, division axis and to bring the mitotic spindles to their destined positions.

Through a comparison of the blastomere behavior by live-imaging and cell lineage tracking, it became clear that the macromeres had different cellular properties and behaviors to the micromeres (Section 4.2). First, the macromeres inherited most of the vegetal pole including the nutritional vesicles and the oil droplets, resulting in the off-centered nuclei positioning toward the animal pole, while the micromeres had their nuclei located at the center of the cell. Second, nuclei migration and repositioning in the macromeres was observed between two spiral cleavages, whereas the nuclei of the micromeres remained at the center of the cell throughout spiral cleavage. Third, the spindle orientation in the micromeres between each spiral cleavage followed Sachs' rule, but in the macromeres it was more complicated. The position and orientation of the

### *6.1. Summary and conclusions*

spindles were controlled by the migration of the nuclei, the anchor point of the spindles to the vegetal pole and to the actomyosin-rich cell cortex closer to the animal pole, and Sachs' rule. Fourth, all of the four spiral cleavages of the macromeres were asymmetric cell divisions, both by the cell volume and by the molecular distribution. The daughter micromeres originating from a division of the macromeres were always smaller, but with larger proportions (relative to the cell size) of the cytoskeletal molecules segregated (e.g., cortical and cytosolic actomyosin). However, the two daughter cells originating from a parent micromere had similar levels of cytoskeletal molecules segregated during division. The cell size difference of the micromere divisions was not as significant as the macromeres. It's most like a combination of symmetric and asymmetric divisions, but none of them was as obvious as the asymmetric divisions of the macromeres. Therefore, the asymmetry of the micromere size requires further measurement if needed. In summary, macromeres had distinct cellular and molecular behaviors to micromeres in the second to the fourth spiral cleavage. These actions most likely contributed to a proper cell positioning resulting in the spiral looking embryo.

## 6. Conclusions, open questions, and future directions

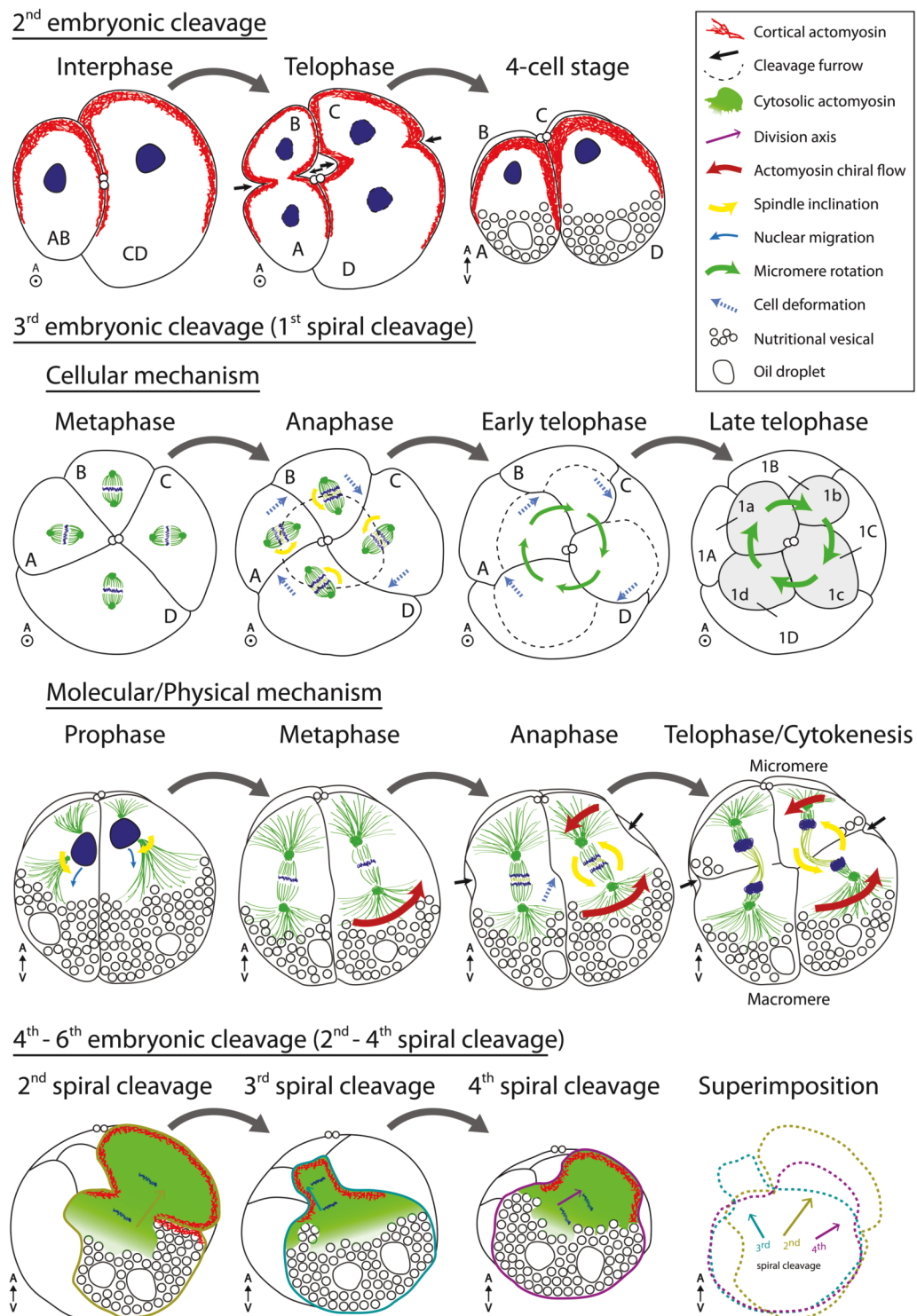


Figure 6.1.: Cellular and cytoskeletal mechanisms of the early embryonic cleavages in *P. dumerilii*.

**Figure 6.1.: Cellular and cytoskeletal mechanisms of the early embryonic cleavages in *P. dumerilii*.** The cellular and molecular/physical mechanisms of the first two asymmetric embryonic cleavages and the first four spiral cleavages are summarized with illustrations. The first two embryonic cleavages showed asymmetric cytokinetic ring formation as well as asymmetric actomyosin distribution, resulting in the asymmetric cleavages. The first spiral cleavage started with parallel orientation of the mitotic spindle to the animal-vegetal axis. Little cell deformation was observed during early anaphase, but mainly seen during telophase, together with micromere rotation. Cortical actomyosin chiral counter rotation played a role during cytokinesis, resulting in spindle inclination and micromere positioning to achieve the left-right symmetry breaking. The macromeres of the second, third, and fourth spiral cleavage were highlighted in the illustration. The nutritional vesicles and oil droplets were located at the vegetal pole of the micromeres, so as in 4-cell stage. Cytosolic actomyosin, cortical actomyosin, and the nuclei were located toward the animal pole, resulting in the asymmetric divisions with smaller micromeres. The superimposition showed nuclear migration and rotational division axis of these macromeres during these spiral cleavages.

## 6.2. Open questions and future directions

With my thesis work, I have initiated a description of the mechanisms underlying spiral cleavage to a large extent based on live-imaging fluorescent recordings of the development of the annelid *P. dumerilii* to include the dynamic aspect of this division pattern. One of the biggest and novel findings has been the description of a physical mechanism, counter-rotation in the actomyosin cortex, which drives the early spiral cleavages. This discovery has naturally raised many new questions.

One question is, which is the relationship between the left-right symmetry breaking morphogens and the actomyosin-related spiral orientation of the blastomeres? In *C. elegans* embryos, the expression of Wnt pathway genes, which affect left-right body axis establishment (Pohl, 2011; Sawa & Korswagen, 2013; Naganathan et al., 2014),

## 6. Conclusions, open questions, and future directions

also has an influence on the chiral flow rate  $V_C$ . Five Wnt components were investigated and four (*dsh-2*, *gsk-3*, *mig-5*, *mom-2*) showed reduced  $V_C$  under RNAi conditions. It's suggested that the link between the genes, which affect left-right symmetry breaking and counter rotating cortical flows, may be propagated through Rho signaling, since Wnt-induced signals, in many other systems, transduce through Rho GTPase to promote actomyosin contractility (Naganathan et al., 2014). This supports that chiral counter-rotating flows participate in left-right body axis establishment. Therefore, the investigation of this type of Wnt components may help understand the roles of the cortical actomyosin counter rotations in spiralian.

The second question is, what are the unique or differential molecular features between each blastomere during spiral cleavage? Previous work in the early *P. dumerilii* embryos has shown that  $\beta$ -catenin localizes to nucleus in only one of the two daughter cells following a cell division, indicating that Wnt signaling pathway participates in early spiralian development possibly in the regulation of expression or segregation of genes (e.g., transcription factors), which gives the cell its identity (S. Q. Schneider & Bowerman, 2007). We have started to look into the differential and conserved expression profiles of individual blastomeres during spiral cleavage to understand which genes are involved in the spiral cleavage and in cell fate specification taking place during spiral cleavage. In particular, we would like to investigate if the differentially expressed genes have an impact on spiral cleavage (the division pattern itself or the cell fate) or if they are a result of spiral cleavage. To this purpose, I, Dr. Bruno C. Vellutini and Dr. Mette Handberg-Thorsager (Tomancak lab, MPI-CBG, Dresden, Germany) are performing single cell RNAseq of various stages during spiral cleavage and earlier: the oocyte, the zygote, at 2-, 4-, 8-, 16- and 32-cell stages. The genes with following temporal (1-3) or spatial (4,5) expression features are of special

## 6.2. Open questions and future directions

interest: 1) genes with increasing expression level from zygote to 32-cell stage, 2) genes with decreasing expression level from zygote to 32-cell stage, 3) genes fluctuating in transcript levels between each cleavage, 4) genes largely segregated/expressed only in micromeres during spiral cleavage, 5) genes largely segregated/expressed only in macromeres during spiral cleavage. Whole-mount *in situ* hybridization will be used to validate the gene expression patterns of the selected candidates by RNAseq. Further, mRNA injections of the full-length candidate genes for cytoskeletal genes fused to a fluorescent marker, will show, where these proteins are localized within the blastomere and give a hint to whether these could be important for the spiral cleavage, e.g., if they are asymmetrically distributed within a blastomere or segregate differently between blastomeres. Functional studies by knocking-down of the gene of interest or by exogenous drug treatment against the protein can then validate its role during spiral cleavage. The result of this project should be able to target the upstream/downstream signaling pathways and molecular segregation related to spiral cleavage, therefore identify the cell fate determinants of each blastomere, and opens a window to investigate the molecular difference between macromeres and micromeres.

A third question concerns which is the cause and consequence of the behavioral differences between micromeres and macromeres? Here, the follow-up plan is to image and calculate  $V_C$  of each macromere during cell division of the first spiral cleavage and of the later cleavages if possible. The Actomyosin  $V_C$  differences between blastomeres have been shown in *C. elegans* embryos and suggested to participate in cellular rearrangement (Pimpale et al., 2019). From my thesis work, we know that B and D blastomeres have greater division angles than A and C blastomeres at 4-cell stage. It may result from the difference of active chiral counter rotation, making the final division angle distinct.  $V_C$  difference between micromeres and macromeres during the



## 6. Conclusions, open questions, and future directions

same cell cycle may also help deducing the mechanism of cell behavior and molecular distribution within these blastomeres. Moreover, through comparing  $V_C$  of the same macromere at different cleavages, it is possible to decipher the mechanisms driving nuclei migration, asymmetric actomyosin distribution, and division angle determination of these macromeres during the second to the fourth spiral cleavage. Finally,  $V_C$  is detected not only previous to cell division in the macromeres at 4- and 8- cell stage, but also in the micromeres of the 8-cell stage. However, spindle inclination during cytokinesis is not observed in these micromeres. Global monitoring of each blastomere may discover more roles of actomyosin chiral flow to the cells and embryo.

mRNA injection is one the most efficient ways to large-scale investigate the candidate genes contributing to spiral cleavage. In my study, I've targeted actomyosin as the critical component during this process. Therefore, to perform a high-throughput cortical actomyosin dynamics observation and to compare the  $V_C$  between each blastomere, a stable transgenic line may be required in the future. I showed that although *syn21-lifeact-mKate2* mRNA injection had clear actomyosin labeling, *Pdunmm-sgfp* mRNA couldn't give enough fluorescent signal for analysis during spiral cleavages. Moreover, because the large size of *Pdunmm*, the injected mRNA was usually unevenly distributed. Each blastomere had different fluorescent level of *PduNmm-sGFP*. This makes  $V_C$  quantification more difficult. As the motor protein of actomyosin, monitoring *PduNmm* dynamics could give more details of counter rotational flow during spiral cleavage. My preliminary tests on the guide RNAs indicated that it's possible to generate a stable *Pdunmm-gfp* transgenic line by CRISPR-Cas9 technique and continue the  $V_C$  measurements based on this line (see Section 6.1). The transgenic line may create a window to investigate the chiral flow and asymmetric actomyosin distribution in details, and to achieve high-throughput

## 6.2. Open questions and future directions

live-imaging of the chemical treated or gene expression manipulated (e.g., through dsRNA or morpholino injection) embryos. The *Pdunmm-gfp* transgenic embryos can further be used to examine which are the physical properties of the blastomeres including cell tension and cortical actomyosin turnover by laser ablation manipulation to the cell cortex.

In this project, I discovered the cellular and biophysical mechanisms driving spiral cleavage resulting in the specific embryonic pattern in *P. dumerilii*. The cellular events and the sequence of cytoskeletal events were compared with the spiral cleavage of other spiralian, e.g., gastropods, showing both conservation and divergence with different models. Then by discovering actomyosin as an essential component for cell orientation during this process and further investigation, I've shown the counter rotational actomyosin flow may be the biophysical force generator during the first and the second spiral cleavages, leading to proper cellular axis determination. At the end of my thesis, I want to address this model to broader evolutionary perspectives. To which extend are the described mechanisms, especially the physical mechanism, conserved?

First, within the organism, I would perform all the quantitative actomyosin  $V_C$  measurements with symmetric and asymmetric cleavages in *P. dumerilii* to understand the extend of cellular mechanistic conservation. Second, among spiralia,  $V_C$  was detected in the unequal cleaver, *P. dumerilii*, and similar cellular mechanisms were observed in the equal cleaver, *L. stagnalis*. Therefore, to measure  $V_C$  and monitor actomyosin dynamics with other spiralian may help to understand the extend of usage and conservation of this physical mechanism during embryogenesis of lophotrochozoans. Third, to look into other phyla with determinate development, such as the ascidians

## *6. Conclusions, open questions, and future directions*

(bilateral cleavage), or phyla following indeterminate development such as echinoderms (radial cleavage) would allow for evolutionary comparison of developmental mechanisms across phylogeny and between deuterostomes and protostomes, eventually generate a global picture of how a biophysical machinery may contribute to embryo patterning among metazoans.

## Part IV.

# Materials and Methods



## 7. Materials and Methods

### 7.1. Culture

#### 7.1.1. *P. dumerilii* animal culturing

*P. dumerilii* is a seawater living annelid spiralian following typical dextral spiral cleavage during embryogenesis. The animal life cycle is enclosed under the laboratory conditions, the sexual maturation process is well studied and can be controlled with artificial light supporting the natural circadian and lunar rhythm (Appendix A.1). Due to the establishment of the system, the fertilization of the eggs as well as the quality control of the embryos also follow standard protocols, making it easier and more stable for early embryogenesis researches and allows for comparisons with other laboratories working with *P. dumerilii*. The embryos are highly transparent and the size is moderate (160-200  $\mu\text{m}$ ), which are suitable for microscopy. Moreover, the fast-developmental processes make live-imaging feasible and data processing much faster. After short-term protease treatment, the eggshell of *P. dumerilii* can be penetrated with the glass needle and the embryos microinjected with a foreign substance and this manipulation does not interfere with its development. With these experimental advantages and

## 7. Materials and Methods

techniques, *P. dumerilii* becomes one of the best-known model organism to examine early spiral cleavage with live-imaging.

*P. dumerilii* was kindly provided by Dr. Arendt's laboratory, EMBL, Heidelberg, Germany, which has an established inland culture. We cultured *P. dumerilii* at MPI-CBG, Germany, following the protocol by Dorresteyn et al. (1993) with a few modifications to facilitate the maintenance of the worms by few users. The culturing seawater is changed every 14 days. The larvae younger than seven days old were fed with living green algae (*Tetraselmis sp.*, provided by University of Göttingen). Instead of growing the algae in flasks, we grew them on agar plates (see *Tetraselmis sp.* algae culturing). The adult individuals were fed with ground fish food (TetraMin Flake Food for all tropical fish, Tetra, Germany) or ground *Spirulina* flakes (Tropical, Germany) three times per week. A 12-hour light period was included in the day-night cycle in the worm facility to facilitate the circadian rhythm of the worms. The sexual maturation of the worms depends on the moon. Therefore, a moon, in form of a light bulb, was installed in the worm facility. Two days prior to the natural full moon, our artificial moon was turned on for six consecutive days. Sexual maturation happens when the moon was turned off that was right after new moon. For an overview of the laboratory culturing condition of *P. dumerilii*, see Appendix A.2.

The gender of the sexually matured worms can be distinguished and males and females were collected into separate small cups with seawater and kept at 18 °C incubator until mating. For fertilization to occur, a male and a female were transferred into a cup half-filled with seawater. On the notice of the proximity of the opposite sex, they would spread sperm and eggs into the water and fertilization would take place in the water column thus outside the adult. The seawater was exchanged to

remove excess sperm and the fertilized eggs were incubated at 18 °C. During the initial approximately 40 min of development, a protective mucus layer was excreted from the zygote. To use the embryos for experiments, this jelly layer was removed mechanically by filter the seawater through a 40 µm filter at 50-60 mpf. The zygotes are 160-200 µm in diameter and were retained in the filter. The embryos were washed with 1L of seawater to remove the remaining jelly and collected into petri dishes for further experiments. At all times, the embryos were kept covered with seawater.

### 7.1.2. *Tetraselmis sp.* algae culturing

*Tetraselmis sp.* was provided by the University of Göttingen in the test tubes with agar/seawater. The algae can be cultured in flasks in seawater, or on the agar plates made from seawater. The latter option was chosen for the reason of easy maintenance, harvest for feeding, and passage. To make the agar plates, 3% agar in 250mL ddH<sub>2</sub>O was autoclaved and kept in a 50 °C water bath. At the same time, a 250mL, 2x concentrated seawater (prepared from seawater powder, Tropic Marin Sea Salt, to 68‰) was warmed up to 50 °C in the same bath. 10mL of fertilizer (Guillard's (F/2) Marine Water Enrichment Solution 50x, G9903, Sigma-Aldrich) was added to it, and the solution was mixed with the agar solution to reach a final volume of 500mL, resulting in a 1.5% agar solution in 34‰ seawater. The fertilizer-containing agar solution was poured into 6-cm petri dishes and 500mL volume was enough for making 40 plates and stored at 4 °C.

Before passage the algae, the plates were placed at room temperature for 1 hr followed by a 15 min UV-light exposure for sterilization because the 2x concentrated



## 7. Materials and Methods

seawater was not (and not able to be) autoclaved. The algae was picked with the sterilized inoculation ring and homogenized in the filtered seawater and plated on the agar plates. The plates were incubated at room temperature with light for two weeks until the algae were visible and ready to be used as food for *P. dumerilii*.

### 7.1.3. Moon cycle and feeding

An example moon cycle (August 2015) and routine culture maintenance protocol was given in Appendix A.1. Briefly, feeding was done every Monday, Wednesday, and Friday. Every second Wednesday the seawater was changed entirely to keep the environment clean. The moon, a light bulb in the laboratory condition, was turned on two days prior to the actual full moon and turned off four days after it. Therefore, the worms received a 24-hour light exposure instead of 12-hour light-dark cycle for 6 nights. The maturation processes of the worms were synchronized after sensing this light signal and started to mature after the artificial moon was turned off and the 12-hour light-dark cycle was applied again. Therefore, the harvest period was the three weeks between the two moon cycles. The artificial moon doesn't need to follow the actual moon cycle. It can also be shifted by weeks to the actual moon cycle. A summary of the moon cycle, feeding, cleaning, and matured worm collection was shown in Appendix A.2. The recording started six months after this culture protocol was applied. And an 8-month recording (October 2015 - June 2016) is plotted showing that there were enough matured worms (around 8 pairs per day) for daily experimental purposes.

## 7.2. Equipment

The equipment used in this thesis is listed below with the brands and applications.

Method	Equipment	Brand	Application
Gene cloning	PCR machine	Eppendorf MasterCycler EP Gradient S	DNA amplification
	Electroporator	Bio-Rad Gene Pulser Xcell	Transformation
Microinjection	Needle puller	Flaming/Brown Micropipette Puller, P-97, Sutter Instrument	Transform capillary into microinjection needle
	Microinjector	FemtoJet Eppendorf	Generate pressure for microinjection
	Cooling stage	MPI-CBG workshop	Keep the embryos at 13 °C
	Light microscope	Leica IL LED, 4x and 10x objectives with S80/30 condenser	Microinjection
	Micromanipulator	FemtoJet Eppendorf	Microinjection
Imaging	Point scanning confocal microscope	Zeiss 780, C-APOCHROMAT 40x/1.2W objective	fixed stained specimen
	Spinning disk confocal microscope	Andor Revolution WD Borealis Mosaic, Olympus UPLSAPO 60x 1.3S objective	Live-imaging of actomyosin dynamics
	Light sheet fluorescence microscope	Light sheet Z.1, Zeiss Plan APOCHROMAT 20x 1.0W DIC objective	Live-imaging of embryo development and cell tracking
Protein purification	Spectrophotometer	Ultrospec 2100 pro, Amersham Biosciences	Measure bacteria culture concentration
	Homogenizer	Avestin Emulsiflex C-5, ATA Scientific Instruments	Homogenize bacteria culture

## 7. Materials and Methods

	Affinity column	HisTrap column, Cat. No. 17524801, GE Healthcare	Purify 6xHis-lifeact-mKate2 protein
	Gel filtration column	HiLoad superdex 200 16/60, Cat. No. 28989335, GE Healthcare	Size selective chromatography

### 7.3. Reagents and solutions

Reagents, solutions, and culture medium were either pre-prepared as stock solution and stored at low temperature, or freshly prepared for their optimal activities. The formula and procedures of making the reagents are listed in this section.

#### 7.3.1. Seawater for *P. dumerilii* culture

The culturing seawater was composed of 25% of artificial seawater (Tropic Marin Sea Salt, dissolved in water to 34‰), 25% of Caribbean natural seawater (NutriSeaWater), and 50% of Atlantic natural seawater (Original Meerwasser). In details, 195g of the artificial seawater powder was mixed with 5L of reverse osmosis water and dissolved for 30 min with stirring. Then the 5L of artificial seawater was mixed with 5L of Caribbean natural seawater and 10L of Atlantic natural seawater. The salinity of the mixed seawater was 34-35‰.

### 7.3.2. Calcium magnesium free seawater (CMFSW)

The calcium magnesium free seawater used in this project was modified from TCMFSW by Schneider and Bowerman (2007). The composition of CMFSW was 50mM Tris, 495.1mM NaCl, 9.7mM KCl, , 27.6mM NaHCO<sub>3</sub>, 5.0mM EDTA, pH8.0. After all the components were dissolved, the solution was filtered with 0.22µm filter to sterile and kept at room temperature.

### 7.3.3. Low melting temperature agarose

The low melting temperature agarose (Cat. No. 50101, SeaPlaque Agarose, Lonza) was used to embed the embryos for live-imaging. Therefore, the salinity was adjusted to 34-35‰. Either 0.4% (for mounting on the glass-bottomed petri dishes for spinning disk microscopy) or 0.6% (For mounting in the glass capillary for SPIM) of low melting temperature agarose was mixed with filtered seawater and heated with a lid to prevent water evaporation. If water evaporates during heating, fill the ddH<sub>2</sub>O to reach original volume. The solution was aliquoted and kept at 4 °C for maximum 2 weeks. Before use, the aliquot was placed at 80 °C for 10 min to melt, then incubated at 34 °C for at least 30 min. Both 0.4% and 0.6% low melting temperature agarose didn't solidify at 34 °C. The melting efficiency drops dramatically when the solution is re-used. Therefore, a fresh aliquot was melted every time before the experiments.

## *7. Materials and Methods*

### **7.3.4. Rhodamine-phalloidin**

300 units Rhodamine-phalloidin (Cat. No. R415, Life Technologies) was dissolved in 1.5mL methanol, aliquoted, and stored at  $-20^{\circ}\text{C}$ . The solution was kept on ice without exposure to light before use.

### **7.3.5. DAPI**

DAPI (Cat. No. D1306, Thermo Fisher Scientific) was dissolved in ddH<sub>2</sub>O to 20mg/mL, aliquoted, and stored at  $-20^{\circ}\text{C}$ . The solution was kept on ice without exposure to light before use.

### **7.3.6. Thioglycolate**

Thioglycolate (Cat. No. T0632, Sigma-Aldrich) was dissolved in CMFSW to 1% by vigorously vortex right before use. The solution was freshly prepared each time and was mixed with CMFSW to reach the working concentration of 0.5%.

### **7.3.7. Pronase**

Pronase (Cat. No. 10165921001, Roche) was dissolved in CMFSW at 0.5% by vigorously vortex right before use. The solution was freshly prepared each time and was mixed with CMFSW to reach the working concentration of 0.25%.

### 7.3.8. anti- $\alpha$ -tubulin antibody

anti- $\alpha$ -tubulin antibody, DM1 $\alpha$ , mouse monoclonal, (Cat. No. T9026, Sigma-Aldrich) was aliquoted in the volume of 5  $\mu$ L and stored at  $-20^{\circ}\text{C}$ . A fresh aliquot was used each time. The primary antibody solution contained 1:5000 of DM1 $\alpha$  in 2.5% Sheep serum/PTw and was pre-absorbed for 1 hr at room temperature before mixing with the sample.

### 7.3.9. Goat anti-mouse IgG secondary antibody

Goat anti-mouse IgG secondary antibody, Alexa Fluor 488 (Cat. No. A28175, Thermo Fisher Scientific) was kept at  $4^{\circ}\text{C}$  without exposure to light. The secondary antibody solution contained 1:500 of the antibody in 2.5% Sheep serum/PTw and was pre-absorbed for 1 hr at room temperature before mixing with the sample.

### 7.3.10. Preparation of the chemical inhibitors

The solvent and stock concentration for each chemical are listed below. Each chemical was dissolved in the fume chemical hood in the bottle which was shipped with it to achieve optimal efficiency. After adding the solvent to the chemical, the solution was incubated on ice on a shaker with gentle agitation for 10 min for the dissolving process. The chemicals were aliquoted in the volume of 2  $\mu$ L and stored at  $-20^{\circ}\text{C}$ . Fresh aliquots were melted on ice for 10 min and the 2x concentrated soaking solution was made (see Section 4.5) right before use. The rest of the chemical was discarded.

## 7. Materials and Methods

Chemical	Solvent	Stock, working conc.	Function	Source
Colchicine	EtOH	5%, 0.005%	Depolymerize microtubules and inhibit tubulin polymerization	Sigma-Aldrich, C9754
Nocodazole	DMSO	1mg/mL, 0.01 $\mu$ M	Inhibit tubulin polymerization, High conc.: induce microtubule depolymerization, Low conc.: alter microtubule dynamics without depolymerization	Sigma-Aldrich, M1404
Latrunculin A	DMSO	1mg/mL, 1.5 $\mu$ M	Inhibit actin polymerization	Sigma-Aldrich, L5163
CK-666	DMSO	10mg/mL, 100 $\mu$ M	Inhibit actin assembly mediated by actin-related protein Arp2/3 complex	Sigma-Aldrich, SML0006
Blebbistatin	EtOH	20mM, 100 $\mu$ M	Inhibit myosin II ATPase activity	Sigma-Aldrich, B0560
Y-27632	H <sub>2</sub> O	10mg/mL, 200 $\mu$ M	Inhibit ROCK activity	Sigma-Aldrich, Y0503
SMIFH2	DMSO	10mg/mL, 100 $\mu$ M	Inhibit Formin-mediated actin assembly by inhibition of Formin homology 2 domains	Sigma-Aldrich, S4826

### 7.3.11. **Protease K**

100mg Protease K (Cat. No. P2308, Sigma-Aldrich) was dissolved in 5mL ddH<sub>2</sub>O on ice for 10 min, resulting in a 2% solution, aliquoted into 75  $\mu$ L, and stored at  $-20^{\circ}\text{C}$ . An aliquot was placed on ice for 5 min for melt without decreased enzyme activity. The aliquot was then mixed with 30mL seawater to reach the final concentration of 0.005% at room temperature right before the treatment.

### 7.3.12. **Zamboni's fixative**

Zamboni's fixative was first published by Stefanini et al. (1967). In this thesis, the working concentration of PFA is modified to 2.5%. The detailed recipe is as follow. Picric acid was diluted in ddH<sub>2</sub>O to 1.3% (saturated solution) and stored at  $4^{\circ}\text{C}$ . All the stock solutions were sterile before preparation of Zamboni's fixative. The composition of Zamboni's fixative: 12.74mL of 0.2M Na<sub>2</sub>HPO<sub>4</sub>, 3.59mL of 0.2M NaH<sub>2</sub>PO<sub>4</sub>, 0.545mL of 1.3% picric acid, and 3.125mL of 16% PFA. Zamboni's fixative was stored at  $4^{\circ}\text{C}$  for maximum 2 weeks. Discard the expired fixative or waste as described below.

Picric acid in Zamboni's fixative can volatile and slowly sublime at room temperature. It's metal picrate salts can constitute an explosion hazard. Therefore, a glass or plastic container is required for Zamboni's waste. Moreover, dry picric acid is sensitive to friction and shock, the liquid in the container should always be filled with a layer of water to prevent high concentration of picric acid.



## 7. Materials and Methods

### 7.3.13. Phosphate buffered saline (PBS) for protein purification

10x phosphate buffered saline: 80g of NaCl, 2.0g of KCl, 14.4g of Na<sub>2</sub>HPO<sub>4</sub>, and 2.4g of KH<sub>2</sub>PO<sub>4</sub> were Dissolved in 800mL of ddH<sub>2</sub>O. Then adjusted the pH to 7.4 and added ddH<sub>2</sub>O to 1L. Sterile the solution by autoclave.

### 7.3.14. Phosphate buffered saline (PBS) for *P. dumerilii* specimen

The 10x phosphate buffered saline was modified to match the cellular property of the marine animals. 70g of NaCl, 62.4g of Na<sub>2</sub>HPO<sub>4</sub>·2H<sub>2</sub>O, and 3.4g of KH<sub>2</sub>PO<sub>4</sub> were first dissolved in 800mL of ddH<sub>2</sub>O (heating is required to dissolve the salts). The pH was then adjusted to 7.4 and filled ddH<sub>2</sub>O to 1L. The 10x PBS was sterile by autoclave and stored at room temperature. The recipes of the PBS containing solutions are listed below.

- 1x PBS: dilute 10x PBS with ddH<sub>2</sub>O and sterile it with 0.22 µm filter.
- PTw: 1x PBS with 0.1% Tween-20
- 5% Sheep serum/PTw: 5% (v/v) sheep serum in PTw

## 7.4. Software

The software used in this thesis is listed with the url link if it's open source program. The Fiji plugins and the scripts for spindle inclination angle measurement were written by Dr. Benoit Lombardot and/or Dr. Robert Haase, Scientific Computing Facility, MPI-CBG, Germany.

Software	Version	Application	Source	Note
Matlab	R2018a	Data analysis	The MathWorks	Proprietary program
Modified PIVLab	—	Particle image velocimetry	Grill lab, MPI-CBG	Matlab script
Zen	Black edition 2012	SPIM Z.1 manipulation, image processing	Zeiss	Proprietary program
Fiji	Fiji/Fiji2	Image processing, analysis	<a href="https://fiji.sc/">https://fiji.sc/</a>	Open source program
Multiview reconstruction	5.0.13	Register and Fuse SPIM images	<a href="https://imagej.net/Multiview-Reconstruction">https://imagej.net/Multiview-Reconstruction</a>	Fiji plugin
MaMuT	v0.27.0	Lineage tracking	<a href="https://imagej.net/MaMuT">https://imagej.net/MaMuT</a>	Fiji plugin
BigDataViewer	3.0.1	Visualize SPIM images	<a href="https://imagej.net/BigDataViewer">https://imagej.net/BigDataViewer</a>	Fiji plugin
<i>P. dumerilii</i> transcriptomic databases	—	Identify gDNA fragments or genes of <i>P. dumerilii</i>	Dr. Arendt lab, Dr. Jékely lab, (Conzelmann et al., 2013)	Online database
spindleOrientation	v0.7	Measure spindle inclination angle	Scientific Computing Facility, MPI-CBG	Python script for Fiji

## 7. Materials and Methods

updateAnimalPole	v1.1	Adjust polar body position recognized by spindleOrientation		
visualiseGeometry	v0.2	Visualize angle measurements by spindleOrientation		

### 7.5. SiR-dye preparation and treatment

SiR-actin (Cat. No. SC001, Spirochrome, Switzerland) or SiR-tubulin (Cat. No. SC002, Spirochrome, Switzerland) was dissolved in DMSO to make 1mM stock solution and was stored at  $-20^{\circ}\text{C}$ . The soaking solution was freshly prepared containing  $1\text{ }\mu\text{M}$  SiR-actin or SiR-tubulin and  $10\text{ }\mu\text{M}$  verapamil in seawater. The embryos were soaked for 4 hr and imaged. In the injection experiment, the injection solution contained  $1\text{ }\mu\text{M}$  SiR-actin or SiR-tubulin and  $10\text{ }\mu\text{M}$  verapamil in ddH<sub>2</sub>O and was sterile by  $0.22\text{ }\mu\text{m}$  filter before use.

### 7.6. Microinjection and mounting

To visualize the fluorescent signal during early developmental stages, the mRNA or protein needs to be injected as early as possible, best in the zygote. For many organisms, the eggshells are too hard for microinjection, or not transparent for monitoring the developmental processes. Therefore, it's necessary to remove the eggshell or prevent its

## 7.6. Microinjection and mounting

formation before injection and live-imaging (Girstmair & Telford, 2019). When using *P. dumerilii* as the model organism, it's not required to remove the eggshell. A mild protease K treatment step is applied to soften the eggshell, followed by microinjection. Prior to injections of the zygotes, A mild 34 sec of 0.005% protease K treatment step is applied to soften the eggshell, followed by washes with 1L of seawater to remove the enzyme and stop the digestion. With this experimental set-up, the embryos remain more natural in the egg, the injection can still be done during zygote stage to maximize the fluorescent signal development, and it gives a possibility to compare the mechanical influence of the eggshell to spiral cleavage (see Section 2.4).

The microinjection protocol was modified from Özpolat et al. (2017). The set-up consisted of an inverted microscope, a home-build cooling stage to keep the embryos at 13 °C during microinjections, a micromanipulator and a FemtoJet Eppendorf microinjector with the injection settings (pi 300 hPa, pc 30 hPa, ti 0.1 sec) (see Section 7.2). Home-pulled needles (Borosilicate thin wall with filament, 1.0mm OD, 0.78mm ID, 150mm L, Cat. No. 300039, Harvard Apparatus) with the pulling settings (Pressure 200, Heat 465 (Ramp + 15), Pull 55, Velocity 70, Time 220) were used for the microinjections. The embryos were aligned on the 2% agar/seawater stage containing a 1mm-thick groove. The mRNAs (200ng/μL) or proteins (500ng/μL) were injected into the zygotes under a 10x objective. Subsequently, the injected embryos were cultured at 16 °C to recover until imaging. At 2-cell stage, the embryos were embedded in the low melting temperature agarose dissolved in seawater for imaging. The low melting temperature agarose was kept in liquid form at 34 °C and allowed to cool down 4 °C before adding to the embryos to not to harm their development. Different mounting protocols were used for different imaging techniques. The detailed mounting and imaging procedures are described below.

## 7. Materials and Methods

### 7.6.1. Mounting for live-imaging with light sheet fluorescence microscopy

The embryos were fluorescently labeled by mRNA injection into the zygotes and recovered at 16 °C in natural seawater. The embryos were mixed with the melted 0.6% low melting temperature agarose/seawater on a glass slide and sucked into the SPIM glass capillary (Cat. No. 701902, Brand) by pulling the metal plunger (Cat. No. 701930, Brand) in the capillary. The mounting agarose contained 3-5% of Merck Millipore Y type Estapor Fluorescent Microspheres beads for the registration purpose in image processing. The capillary was placed horizontally at room temperature for 10 min for the agarose to solidify. The horizontal orientation of the capillary also allowed the animal pole of the embryos facing the side of the capillary, making the angle setting during SPIM live-imaging easier. The capillary can be placed in seawater until the desired developmental stage. The whole-embryo live-imaging was done with the Light sheet Z.1 microscope with Zeiss Plan Apochromat 20x 1.0W DIC objective from 5 angles with a 72° rotation. The images of the two illuminative sources were fused with Zen Imaging Software. Registration and fusion of the 5 angles were done with the Fiji plugin Multiview reconstruction by using the external fluorescent beads as reference points with the cluster computing system in MPI-CBG, Dresden, Germany.

### 7.6.2. Mounting for live-imaging with spinning disk confocal microscopy

The injection and recovery processes are described in the previous sections. Instead of mounting in the capillary, the melted 0.4% low melting temperature agarose/seawater

## 7.6. Microinjection and mounting

was placed at the glass-bottom petri dishes. And the embryos were mixed with the agarose/seawater and pushed to the bottom of the liquid with the desired imaging orientation facing the glass bottom before solidification of the agarose. The petri dish was then incubated on the cooling stage at 13 °C for 5 min for solidification, then filled with seawater for live-imaging. The Andor system (see Section 7.2) was an inverted spinning disk confocal microscopy system which allows imaging from the animal pole because the animal pole faces the bottom naturally. The image stack was taken every 5 sec covered 30  $\mu\text{m}$  with 0.5  $\mu\text{m}$  optical sectioning.

### 7.6.3. Markers for live-labeling of the cytosolic components

The *P. dumerilii* gene cloned in this study are listed in Appendix A.6. Here showed the summary of the mRNA from other species used for labeling the cytosolic components.

Gene	Species	Discription	Target
<i>lyn</i>	<i>H. sapiens</i>	N-terminal chain of non-receptor tyrosine kinase	Plasma membrane
<i>emt6</i>	<i>H. sapiens</i>	Microtubule binding-domain of ensconsin	Microtubule
<i>h2b</i>	<i>M. musculus</i>	Histone 2b	Nuclear DNA

## 7.7. Immunofluorescence

The embryos were fixed with Zamboni's fixative at room temperature for 20 min and washed 5 times with PTw. The fixed embryos were soaked in Milli-Q water for 15 min at room temperature to permeabilize the sample, followed by a 20 min post-fixation with Zamboni's fixative. After a further 5 times of PTw washes, the samples were blocked with 5% sheep serum/PTw at room temperature for 1 hr. The primary antibody (1:5000 dilution) was pre-absorbed in 2.5% sheep serum/PTw and applied to the samples. The samples were incubated in the primary antibody solution at 4 °C for more than 8 hr (overnight) and washed with PTw for 5 times. Then the samples were incubated in the pre-absorbed secondary antibody (1:500 dilution in 2.5% sheep serum) at 4 °C for another overnight. Rhodamin-phalloidin (1:250 dilution) and DAPI (1:200 dilution) were present in the secondary antibody solution if needed. With a further 5 times washes with PTw, the samples were imaged with Zeiss confocal microscope with 40x objective (see Section 7.2). For detailed step-by-step protocol, please see Appendix A.7.

## 7.8. Functional studies by exogenous application of the chemical inhibitors

The chemicals targeting different cytoskeletal elements or motor proteins are commonly used in many species for the study of cell division and other cellular behaviors. The chemical preparation was described in Section 7.3.10. In brief, each chemical was dissolved in the recommended solvent and the stock solutions were stored at  $-20^{\circ}\text{C}$ .

### 7.9. Measurement of the spindle inclination angle during spiral cleavage

They were melted prior to the treatment and kept on ice. The chemicals were diluted in seawater to 2x of the working concentration before the treatment to keep the maximum activity.

The embryos were incubated in the 12-well plate with 500  $\mu$ L of seawater and 50 embryos in each well at 16 °C. Same volume of the 2x concentrated chemical solution was mixed gently with the embryos at the desired stage. The embryos were treated from the beginning of the 4-cell stage, when 80% of the embryos completed the second embryonic cleavage, for 20 min, and fixed with Zamboni's fixative for immunofluorescence. For live-imaging, the embryos were fluorescently labeled by injection at 1-cell stage and the chemicals were treated at 4-cell stage (as described above) and live-imaged by spinning disk confocal microscopy.

## 7.9. Measurement of the spindle inclination angle during spiral cleavage

The embryos were fixed during the first spiral cleavage and the plasma membrane, mitotic spindle, and DNA were fluorescently labeled with Rhodamine-phalloidin, (Cat. No. R415, Thermo Fisher Scientific), DM1 $\alpha$ , and DAPI, respectively. The embryo and cell segmentation, detection of the mitotic spindle, and division angle measurement were done with the Fiji-based script created for *P. dumerilii* four-cell embryos (see Section 7.4). The embryo axis was the axis of the center of the embryo to the polar body. And the mitotic spindle vector ( $V_s$ ) was the direction of the MTOC at the vegetal pole to the one at the animal pole. The inclination angle theta,  $\theta$ , was illustrated in



## 7. Materials and Methods

Figure 2.5 and measured with spindleOrientation plugin.

### 7.10. Dechoriation and cell dissociation

The embryos were incubated at 16 °C until 60 mpf, followed by removal of the jelly layer. Dechoriation was applied at 1-cell stage by soaking with 0.5% thioglycolate and 0.25% pronase in CMFSW for 10 min at room temperature on a 450 rpm shaker. The dechorionated zygotes were washed two times with CMFSW and placed in a new petri dish with natural seawater at 18 °C for imaging. For cell dissociation, the dechorionated embryos were collected at 4-cell stage and the cells were dissociated by gently pipetting in seawater.

### 7.11. gDNA extraction

The source for gDNA extraction was from the tissue of 10 different *P. dumerilii* adults to overcome the cloning difficulties by the polymorphism of the genomic DNA. AllPrep DNA/RNA/Protein Mini Kit (Cat. No. 80004, Qiagen) was used with its user instructions. The extracted gDNA was stored at −80 °C for cloning of the untranslated region or investigation of the certain genomic regions.

## 7.12. RNA extraction and cDNA synthesis

300 embryos were lyzed in 1mL TRIzol reagent (Cat. No. 15596018, Thermo Fisher Scientific) at room temperature for 10 min. The lysate was mixed with 0.2mL of chloroform (Cat. No. 32211, Sigma-Aldrich), homogenized, and placed on ice for 10 min. The samples were then centrifuged at 14000 rpm at 4 °C for 15 min and the upper layer was collected. Same amount of isopropanol (Cat. No. 67-63-0, Merck) was added to the solution and the samples were incubated at −20 °C for 30 min. After centrifugation at 14000 rpm at 4 °C for 30 min and removal of the supernatant, the RNA pellets were washed with 70% EtOH (Cat. No. 64-17-5, VWR Chemicals) and air dried for 20 min. The RNAs were re-suspended with nuclease-free water and stored at −80 °C. The reverse transcriptase SuperScriptIII First-Strand Synthesis SuperMix (Cat. No. 18080-400, Invitrogen) was used to produce the cDNA according to the user manual. 1 µg of total RNA was used as template in each 20 µL reaction mix. The cDNA was stored at −20 °C for gene cloning.

## 7.13. Gene cloning and mRNA synthesis

To clone the genes of interest from *P. dumerilii*, the candidate genes were retrieved from the *P. dumerilii* transcriptomic databases (see Section 7.4) by reciprocal basic local alignment search tool (BLAST) searches. In brief, the desired genes were found by searching with the gene annotations in the databases and further confirmed by BLAST in NCBI and alignment of the open reading frames with the reference homologous genes. The primer sets were designed based on the open reading frames,

## 7. Materials and Methods

the melting temperature, and the secondary structures. For cloning of the open reading frames, the primers had to start from the start codon or ended at the stop codon (see Appendix A.6). Therefore, the sequences and melting temperature ( $T_m$ ) of the primers can only be tuned by the length of them.  $T_m$  was measured with the Basic  $T_m$  calculation by University of the Basque Country (<http://insilico.ehu.es/tm.php>). The range of  $T_m$  was set between 50 – 55 °C and for each primer sets, the difference of  $T_m$  was usually within 1 °C. The other primer quality controls, such as secondary structures and primer dimers, are checked with the OligoAnalyzer by Integrated DNA Technologies (<https://eu.idtdna.com/calc/analyzer>). The primers were ordered from Sigma-Aldrich, dissolved in ddH<sub>2</sub>O to 100  $\mu$ M and stored at –20 °C. For the constructs with syn21 translational regulator conjugated at 5'UTR, it was included in the primer in front of the start codon of the gene and the relative primer parameters were modified accordingly.

The cDNA was used as template with the primer pairs and Phusion DNA polymerase (Cat. No. M0530L, NEB) were used for polymerase chain reaction amplification of the DNA fragments. The PCR products underwent de-phosphorylation and ligated with the linearized pCS2+ plasmids. The ligation products were transformed into the homemade TOP10 competent cells (see Appendix A.8 for preparation of the competent cells) by electroporation. Mini-preparation was done with the QIAGEN mini-prep kit and the plasmids were stored at –20 °C. For detailed step-by-step protocol, please see Appendix A.9.

The mRNAs were *in vitro* synthesized with mMESSAGE mMACHINE SP6 Transcription Kit (Cat. No. AM1340, Thermo Fisher Scientific) following the user manual with the modifications. 1  $\mu$ g linearized plasmid DNA was used as templates

and 37 °C incubation time was extended to 4 hr for optimal mRNA synthesis. If the synthetic mRNA was larger than 5kb, 1  $\mu$ L GTP was added in the 20  $\mu$ L *in vitro* transcription mix. The mRNAs were dissolved in ddH<sub>2</sub>O and the concentration was measured and adjusted to 600ng/ $\mu$ L and stored at –80 °C.

## 7.14. Protein purification

6xHis-Lifeact-mKate2 was cloned in pET30a expression vector (cloning protocol shown in Appendix A.9) and transformed into DH5 $\alpha$  competent cells which contained pRARE plasmid (New England Biolabs). 0.2mM IPTG (Cat. No. 97063-282, VWR) was added when the bacteria culture reached O.D.<sub>600</sub>=0.5 and the culture was shifted to 18 °C with agitation for an overnight. Bacteria were harvested by centrifugation at 5000 rpm for 5 min and re-suspended with lysis buffer (2x PBS, 20mM Imidazole) with 1mM DTT (Cat. No. 97061-338, VWR), 0.1% protease inhibitors cocktail (Bimek), and 0.1% benzonase (MPI-CBG, Germany). The cells were lysed and homogenized by Emulsiflex C-5, Avestin homogenizer. The lysate was centrifuged at 16000 rpm for 30 min to remove the debris. The supernatant was filtered with 0.45  $\mu$ m filter (Cat. No. SLHAM33SS, Sigma-Aldrich) and loaded to HisTrap column (Cat. No. 17524801, GE Healthcare). The column was washed with 10 column volumes (CV) of lysis buffer with 1mM DTT; 5 CV of high salt buffer (6x PBS) with 1mM DTT; and 5 CV of lysis buffer with 1mM DTT. The sample was eluted with elution buffer (2x PBS, 250mM Imidazole) and dialyzed with the dialysis membrane (spectra/por Dialysis membrane 3500MWCO, Spectrum Laboratories) overnight against protein buffer (20mM Hepes pH7.4, 150mM KCl). The dialyzed protein was gel filtrated and

## 7. Materials and Methods

the desired protein size was collected. The detailed protocol is attached as Appendix A.10. The protein can be used after dialysis or further purified by size-exclusion chromatography (Cat. No. 28989335, HiLoad superdex 200 16/60, GE Healthcare), which was used in 6xHis-Lifeact-mKate2 protein purification. The final concentration of the purified protein was adjusted to 3  $\mu\text{g}/\mu\text{L}$  and stored at  $-80^\circ\text{C}$ .

### 7.15. Particle velocimetry analysis, PIV

Particle image velocimetry (PIV) was measured with the modified PIVlab by the Grill lab in MPI-CBG, Germany. The scheme was shown in Figure 4.5. For each biological replicate, selected time frames were analyzed starting from the formation of the cytokinetic ring during anaphase of the cell cycle until telophase, when the ingression of the cleavage furrow was clearly seen. The analyzed area (ROI1 and ROI2) were defined based on the size of the cell and the position were relative to the cytokinetic ring. In details, the ROIs were 7.5  $\mu\text{m}$  in width and the length covered the visible actomyosin signal of the target cell. The position of each ROI located 3  $\mu\text{m}$  from the cytokinetic ring. Three (or more) biological replication were analyzed for each group. The counter rotational vector,  $\overrightarrow{V_1y}$  and  $\overrightarrow{V_2y}$ , which were parallel to the cytokinetic ring, were measured and the flow rate ( $V_c$ ) was calculated with the Equation 4.1 and 4.2.

## 7.16. Statistics

All the numerical data were representative of at least three biological replications. The results were showed as means  $\pm$  standard deviation. One-way ANOVA was performed by Matlab software to determine the statistical significant levels.



Part V.

Appendix





# A. Appendix

## A.1. *P. dumerilii* maintenance under laboratory conditions



**Figure A.1.:** *P. dumerilii* maintenance under laboratory conditions. The example was taken from August 2015. The 1<sup>st</sup> and 29<sup>th</sup> of the month were full moon. The artificial moon was turned on two days prior to the full moon and turned off four days after it. The total moon-on time was six nights. The matured worms were collected during the moon-off state pair by pair and the fertilized eggs were kept for further experimental purposes. The feeding was done three times per week, on Mondays, Wednesdays, and Fridays. And the seawater was changed (for cleaning) every two weeks on Wednesday. With these settings, *P. dumerilii* enclosed the life cycle and can be entirely kept under laboratory conditions. See Appendix A.2 for practical data of maturation.

## A. Appendix

### A.2. *P. dumerilii* culturing and maturation

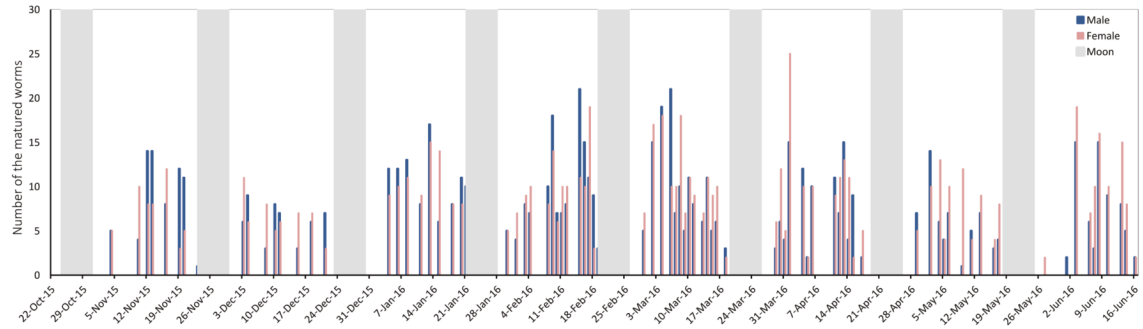


**Figure A.2.: *P. dumerilii* culturing and maturation.** An 8-month record of *P. dumerilii* culture with the matured worms and the moon cycle is plotted. The moon-on state is marked with grey blocks. The matured worms were collected during the harvest period (see Appendix A.1). Although the number of daily matured male and female were not exactly the same, there were on average 8 males and 8 females matured and ready to mate everyday (Culturing size, 50 boxes with 30-70 worms in each box). Therefore, this culturing technique is optimal for spiralian embryological experimental purposes.

### A.3. Cytosolic components distribution in the zygote

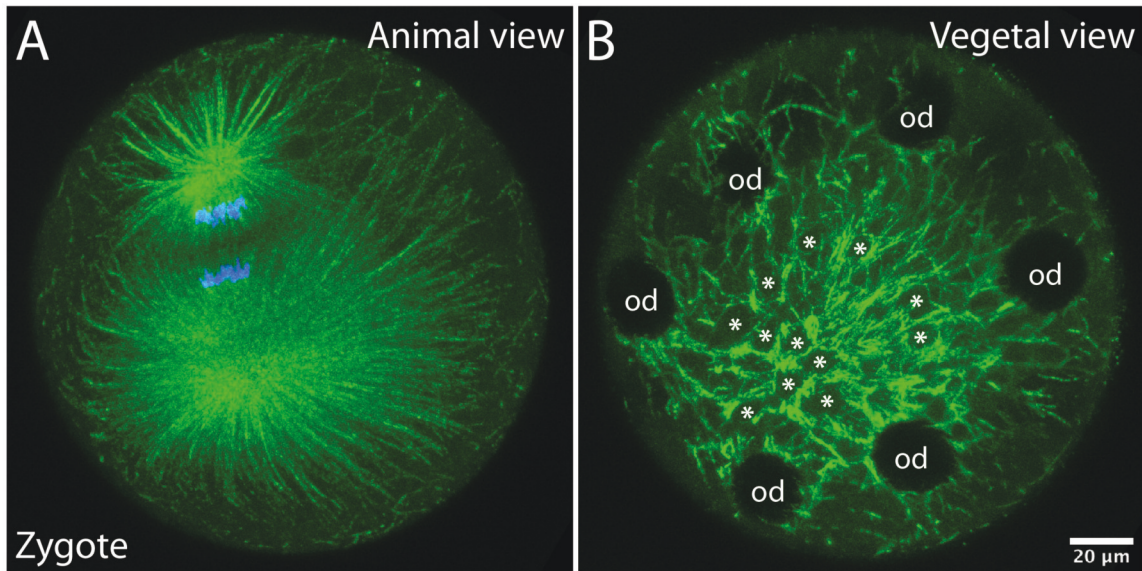


**Figure A.3.: Distribution of the cytosolic components in *P. dumerilii* zygote.** The embryos were incubated at 18 °C and fixed at 90-100 mpf. Microtubules were labeled with anti- $\alpha$ -tubulin antibody (green). The DNA was labeled with DAPI (blue). (A) The Z-projection was done from the animal view covering the animal half of the zygote. The mitotic spindles and chromosomes were seen at the animal half. (B) The Z-projection was done from the vegetal view covering the vegetal half of the zygote. The microtubules were thicker and separated by the oil droplets (od) and nutritional vesicles (asterisk, not all of them were labeled). Scale bar: 20  $\mu$ m.

## A. Appendix

### A.4. Phylogenetic analysis of *P. dumerilii* Par proteins

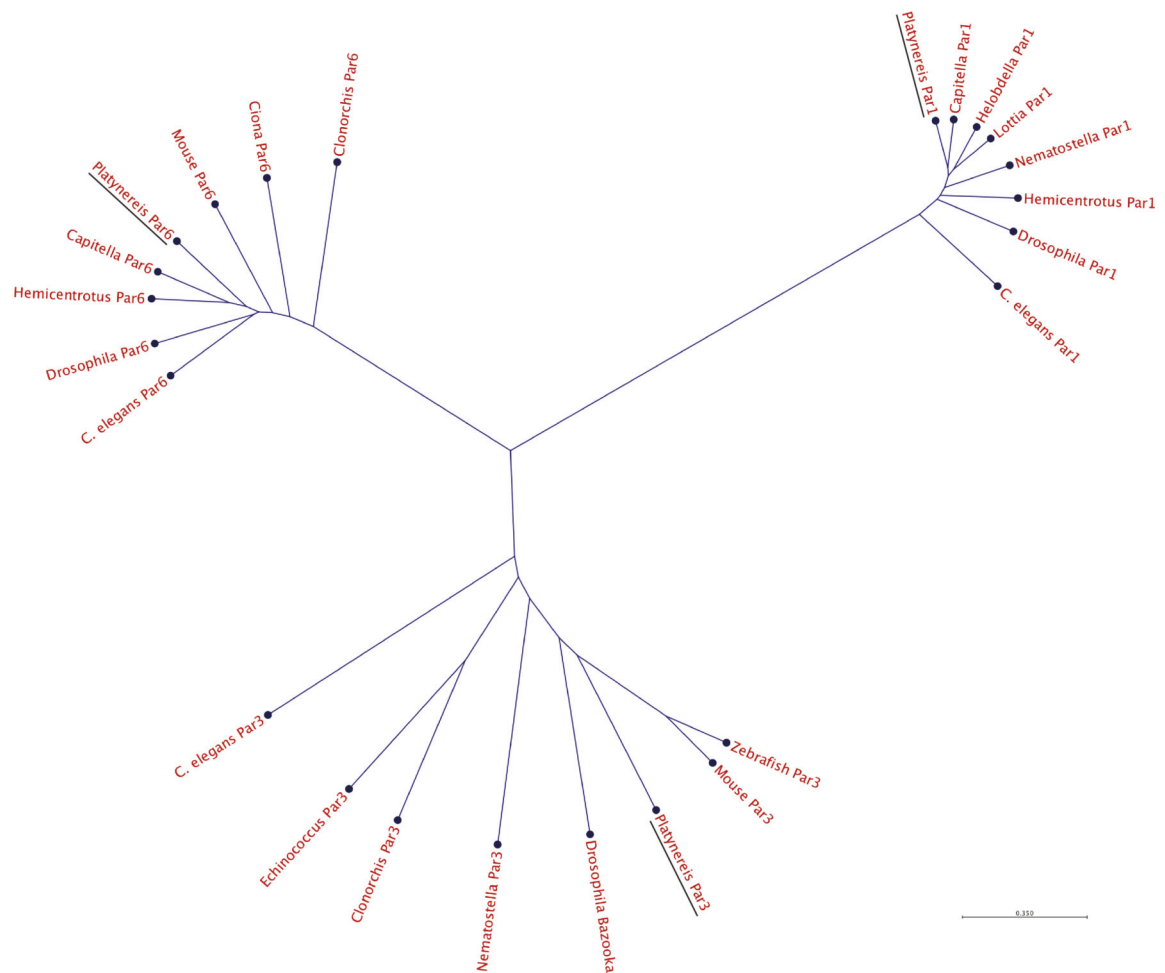


**Figure A.4.: Phylogenetic analysis of the Par proteins.** The full-length protein sequences of Par1, Par3, and Par6 of various animal groups were analyzed. The *P. dumerilii* Par proteins were labeled as *P. dumerilii* Par and marked with bottom lines. Each *Pdu*Par identified was grouped with its homologous genes.

## A.5. The effects of cytoskeletal inhibitors on cellular behaviors

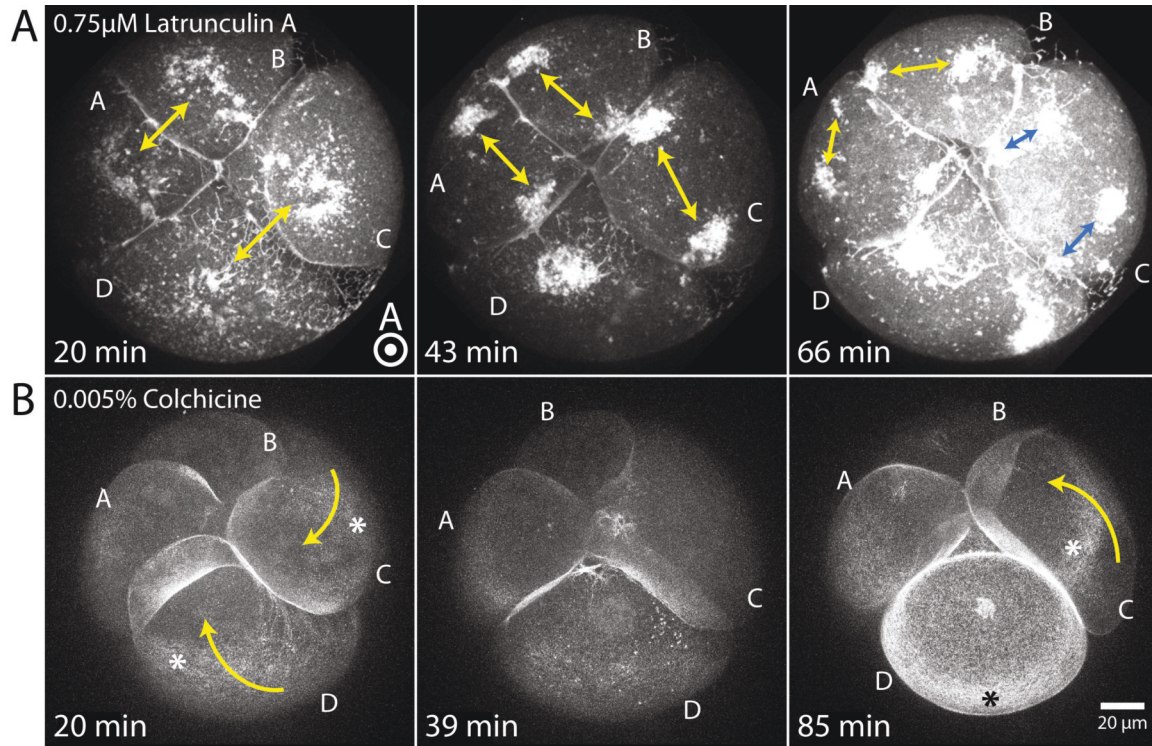


Figure A.5.: The effects of cytoskeletal inhibitors on cellular behaviors.

**Figure A.5.: The effects of cytoskeletal inhibitors on cellular behaviors.** In (A), embryo was injected with *lyn-gfp*, *emt-3xgfp*, *syn21-lifeact-mKate2*, and *h2b-mCherry* mRNA, and in (B), with *syn21-lifeact-mKate2*, and *emt-3xgfp*, into the zygote. Then the embryos were incubated in natural seawater at 18°C until the end of the second embryonic division. When they're observed to be at 4-cell stage, the embryos were transferred to 0.75 μM latrunculin A (A), or 0.005% colchicine (B) and the treatment started (0 min). They're live-imaged by spinning disk confocal microscope from the beginning of the treatments. Both embryos were imaged from the animal view. For the whole time of live-imaging, the embryos were under chemical treatment and therefore, no cell division was observed in terms of splitting a cell into two. However, the dynamics of the sub-cellular structures were monitored. The timestamps indicated the time of chemical treatment and 20 min (left panels) were the beginning of the third embryonic cleavage, also known as the first spiral cleavage in mock control. Half of the embryos were projected with the maximum intensity. (A) Lifeact-mKate2 was first confirmed not localized to the cell cortex by imaging of

## A. Appendix

the mKate2 signal. Therefore, it indicated that latrunculin A functionally inhibited actomyosin. The double-headed arrows at 20 min indicated the direction of the second embryonic cleavage resulting in the four macromeres. Through the time of around two cell cycles (43 min and 66 min), two times of DNA duplication and separation were observed. The direction of DNA separation at 43 min was perpendicular to the previous one (20 min) and also perpendicular to the animal-vegetal axis, indicated by the double-headed arrows. The direction of DNA separation at 66 min was roughly perpendicular to the one at 23 min in A and B cells due to the space restriction of the egg (yellow double-headed arrows). But it showed nicely perpendicular alignment in the C cell, indicated by the blue double-headed arrows. The DNA separation direction was hard to be observed in the D cell because not all the chromatin was seen (due to its large size). By observing the shape of the cell contact, it's concluded that no obvious membrane deformation occurred between cell cycles. (B) It's first confirmed that no mitotic spindle was detected under the treatment by imaging of the GFP signal. Therefore, it indicated that colchicine functionally inhibited microtubules. Although no cytokinesis was observed, the cell deformed in the dextral manner at 20 min as in the mock control (curved arrows). The accumulation of actomyosin at the periphery of the cells were also observed (asterisks). These indicated that the potential of the first spiral cleavage was not affected by interference of microtubule. Moreover, the cell deformation decreased at 39 min of treatment. Strikingly, the division plane switched from dextral to sinistral at 85 min, indicated by the curved arrow. it's also confirmed by the orientation of actomyosin accumulation at 85 min (asterisks). Therefore, these indicated that the cell shape dynamics is irrelevant to microtubule. Scale bar: 20  $\mu\text{m}$ .



## A.6. Identified gene sequences and the cloning information

The DNA and protein sequences of the identified genes are listed below. The primer sequences are **bold**. The start and stop codons are *italic*. The exon sequence of the *Pdunmm* gDNA is **red**. Therefore, the coding region of this exon is from the beginning of the **red** text until the stop codon, which is the italic "*TGA*".

### A.6.1. Optimization of the lifeact construct

#### Lifeact

- DNA sequence

5'-*ATGGGCGTGGCCGATCTGATCAAGAAGTTCGAGAGCATCAGCAAGGA*  
GGAG-3'

- Protein sequence

MGVADLIKKFESISKEE

#### 5'UTR

- **syn21**: 5'-AACTTAAAAAAAAAAAAATCAAA-3'
- **L21**: 5'-AACTCCTAAAAAACCGCCACC-3'
- ***Pdupar6* 5'UTR**: 5'-TGAAAAGAGACAGTTTATCGGCTCCAATGTGGA  
ATTACCTGGATTTAACCGGTGACCAAGCCCTGGAGGAGGGCACAA  
AGTCATCCACG-3'

### A.6.2. Partitioning detective homologs

#### *PduPar1*

- DNA sequence



A. Appendix

5'-**ATGTCTACCA**CGAGAGG**CCCCGCT**GCAAAC**TGTT**CACGAATCTCTC  
ACTTCAGACCATGTCGTTAAAACGACTGATGACAATGCCAAC**CCCTCG**CAT  
TTCGTCTAGGAGCCGAAGTACTGATGAGCCTCACATAGGAAAATACCGA  
TTGATCAAAACCATTGGGAAAGGTA**ACTTCGCTA**AGGTGAAGTTGGCCA  
AACATGTCCCTACAGCTAGAGAGGTTGCCATTAAAATAATTGACAAGGC  
TCAGTTGAATCCATCCAGTCTTCAAAAGTTATACAGAGAAGTGAAAATA  
ATGAAGGTGCTCAATCATCCAAATATAGTTAGGTTGTT**CGAAGT**CATAG  
AAACGGAAAAGACACTTTATTTAGTAATGGAGTATGCAAGTGGAGGGGA  
AGTATTTGATTATTTAGTTGCACATGGGAGAATGAAGGAGAAAGAAGCT  
AGGGCCAAATTCAGACAAATTGTGTCTGCTGTT**CAGTATT**GT**CA**TCAGA  
AGCACATTGTACATAGAGACTTGAAGGCTGAAA**ACTTGTT**ACTAGATGG  
TGATATGAACATCAAAATTGCAGACTTTGGGTTTAGCAATGAGTT**CACG**  
CCGGGAAACAAATTGGACACGTTTTTGTGGTAGTCCTCCTTACGCTGCTC  
CTGAGCTGTTTTCAAGGAAAAAAATATGACGGTCCTGAAGTAGATGTATG  
GAGTTTAGGAGTCATTTTGTATACTCTAGTCAGTGGTT**CCTTGCC**CTTT  
GATGGCCAA**AACTT**AAAAGAATTAAGAGAAAGAGTCCTCAGAGGAAAAT  
ACCGAATCCCATTTTACATGTCAACAGACTGCGAAAATCTTCTTAAGAAA  
TTTTTGGTTCTCAATCCTCAAAAAAAGAGCCAGTTTAGAGACCATTATGAA  
AGACCGCTGGATGAATGTAGGTTATGAAGATAATGAATTAAAGCCTTAC  
AAAGAGCCTCCATTGGGAGACTGACCCCGACGTATAGGGGAAATCATGA  
TCAACATGGGATACTCAAGAAAAGACATCGAAGATTCATTAGTGCAAAA  
TAAATACGATGACATCACGGCGACATATCTATTGTTGGGGAGAAGAAGT  
AATGAGTTGGAAAGTAGTGAGTCAAGATCAGGGAGTAGTCTCTCATTAC  
GCCAACTGCAGATGACCCATCGGCAGAACAGCGAGATGAATGCCAACAG  
TTCGCAGTCACCCTCGCACGGAGGCAGCAAGGTCCAGAGAAGCGTATCG  
GGGTCCAATTCCAAAACCAGACGATCGTCGTTCCGGTGACAACAAAACGC  
CCTCTTCAAAGAACAGTGGTGTGCCTTCCAGTGCCTCATACTAAGCG  
GTCTTCACAAGGAGTAGACAGTGCTTCCAAAGACAATGCTATCTCGGGT  
GGGTCACGGTCGAAGGGACCATCGTCAGGCGGGTCAACGCCCACCTCAT  
CCACTTCAGCCGCCTCTTCCATGCCCCAAGGAGAGTCTCCCAAGATTCTT  
GCTGCAAGCAGTCCTGGCAAAGCGGCCATTCCCAAAAAGCCCCAGTCAA  
AATCGGGAACGGTGGGAGTAACGCGCAGGAACACTTTTGGTTACGGTGA  
TAATAAGGGTCCTGCCATCGAGCGAACAACAAAACACAAACACCGACC

#### *A.6. Identified gene sequences and the cloning information*

CCGTCTTCTAACAATTCAGACTTTTCGAAGTAACATCCCATCCACACCTGC  
CAGCCAGGCCTCTGACGACCGCCCTGCAGCCCGACCTAAGGGTCACCAG  
AAATCTGCCAGCACCTCCCATGCTGTTAGAGACTTGGGCCTTCCGCATG  
CTGAACCTGCTAGTGGGGCTGACCCCTGCGTCAGACGACGACCAGCTC  
CTCGCAGAAGTCGTCGGCGATCCCCGCGTCTCCCATGGCAACCAGACAG  
TTCCCCCGTAGCACCCAGCACGCAGCACATTCCATGCTGGGCAGGTGC  
GTGACCGACGGGCCACGACCAATGCCTACAATGGGCCTGGGGGTCTGCC  
AACACACACGCAGGACACGTCGGCCATGGCGGCTCACAATCGTTTGTCT  
TTCTTCAACAAAATCACCTCCAAGTTCAGCAGGAGGTACGTACCTGGCCA  
AGAACTGGAGCCCAACAGGTCCATGAATGAGAAGGATGTCGGAGGAGGA  
GGAGGTGGCATGGGGGGAGTTGGCCTCGGGGGAGGGGGCCAGCGACCAG  
GTCAAACCGCGATCTCTGCGCTTCACATGGAGCATGAAGACGACCAGCT  
CGATGGACCCTAACGAGATGATGCGGGAGATCCGAAAAGTCCTTGACGC  
TAACAATTGTGACTACGAACAACGGGAAAAGTTCTTACTCCTGTGTGTG  
CACGGGGACCCTAACACGGATAGTTTAGTTCAATGGGAGATGGAGGTCT  
GTAAGCTACCCAGACTGTCTCTAAACGGAGTACGATTCAAGAGAATATC  
TGGCACTTCCATTGGCTTCAAGAACATAGCCTCTAAAAT**TGCCAATGA  
GTTGAAGTTG TGA-3'**

- Protein sequence

MSTTRGPLQTVHESLTSDHVVKTTDDNANPRISSRSRSTDEPHIGKYRLIKTIG  
KGNFAKVKLAKHVPTAREVAIKIIDKAQLNPSSLQKLYREVKIMKVLNHPNIV  
RLFVETETKTLVMEYASGGEVFDYLVAHGRMKEKEARAKFRQIVSAVQY  
CHQKHIVHRDLKAENLLLDGDMNIKIADFGFSNEFTPGNKLDTF CGSPPYAA  
PELFQGGKKYDGPEVDVWSLGVILYTLVSGSLPFDGQNLKELRERVLRGKYRI  
PFYMSTDCENLLKKFLVLNPQKRASLETIMKDRWMNVGYEDNELKPYKEPP  
LETDP RRIGEIMINMGYSRKDIEDSLVQNKYDDITATYLLLGRRSNELESSES  
SGSSLSLRQLQMTHRQNSEM NANS SQSPSHGGSKVQRSVSGSNSKTRRSSFGD  
NKTPSSKN SGVPSSASYTKRSSQGVDSASKDNAISGGSRSKGPSSGGSTPTSST  
SAASSMPQGESPKIPAASSPGKAAIPKKPQSKSGTVGVTRRNTFGYGDNKG  
AIERTNK TQTPTPSSNNSDFRSNIPSTPASQASDDRPAARPKGHQKSASTSHA  
VRDLGLPHAEPASGADPLRQTTTSSSQKSSAIPASPMATRQFPRSTPARSTFH  
AGQVRDRRATTNAYNGPGGLPTHQTQDTSAMAAHNRLSFFNKITSKFSRRYV

## A. Appendix

PGQELEPNRSMNEKDVGSGGGGGMGGVGLGGGASDQVKPRSLRFTWSMKT  
TSSMDPNEMMREIRKVLDDANNCDYEQREKFLLLCVHGDPTDLSLVQWEMEV  
CKLPRLSLNGVRFRKRISGTSIGFKNIASKIANELKL\*

### *PduPar3*

- DNA sequence

5'-GGGGAAGTTCCGACATTATTCATTTGGACTTGTTGTGATGCTCACCTG  
AGGATAGCTGGCGGTCGTTTATGAGGCTGCAGGAGCCGTAATTTTCGAA  
AATGAAGTCTTCGGAAGATAAGGAAGACACGTAGATGAATTTAGCGTAA  
TTTGGTGAGCCAATAACTATCTGGAAGTGATTTTACCAAGGAACAATGC  
ACCTGAAGAAAGTTACAACTTGGCCACCTGCCTTCTCACAACCTGTGGC  
GTTTGCAGCTCGTCTCAAATAAAAGTGGGTCGCTGATAAACGTTGACTG  
GTGGATTAATGTGCTTTACCTGTTGTGGTTATGATCATGTGGATCA**AT**  
**GTTTACTATATACGGACTTATTTTGGCGTTTCGTGAAGAAATCTGTC**  
AGATAGTCGTCATGAAAGTGACAGTTTGTTCGGGGCCACTCGCGTTGT  
TGTGCCTTGTGGAAATGGGGATTTACCAATCAGCGAACTCATTGACATG  
GCCATCACTCGGTACAAGAAGGCTTCTGGAAAGGCCTTGGATTACTGGG  
TGACTGTGCATACTTTGAAGTCTCAGTCAGATGGAGGAATTCTTGACCC  
TGATGACCTGCTCACTGATGTTGCTGATGACAGAGAACAGTTAATCGCA  
GAATATGAAGAACAAGATGCCCCCTGGTGCCACACAACGGAGGGGACG  
GGACAAGCGCCAGTTCTGTGGGGACGGCGAGTCCTGATATGTTCCACGC  
TCCAGAAATCAACAACCAACAACACAACCTCAACAACAACAAGCCCT  
ACGCTCCGTCCAGCTACGATGTTGTCATCACCCAGAATGACTTGAACAAT  
GTTTCCTCTCGGTTAATTGTTAGAAAGAGGAAGCGAACCTGCTTTGATCA  
ACATTGGAATTGAAAAAGAAAACGAAAATCCTCAGTTATCTTTGAAAAA  
CAGCAACAAACGATGGTCAGCTATTTCTTTGGTGACAATGGGAGGATA  
CCAAAGCAAGAGGATGCCGATGATGAGGAAAGTGATGAGGAAGGAGGA  
TTGTACCCGCCTCAGCAGCGGACGGGAGGCAATGGTCAGGAGAAGGACA  
AAGAGGTGCGGAGTGCCCTTACGAGGTTTGCAAGAGACTCTGCTCGCCA  
GTCATTGGCCAGCACCAACTCAGCCATGTACAGGTGGCTGGAGGCACAG  
GAGAGGACCGAGGAGAGAGCCATTGAGATGCAGGTGAGCAGAAAAGAG  
CCATTAGGAGGATCGGGAAAAGCGGAGGATGAAAGTGAGGAGGAAGAT  
GAACAAAGCAAAGAGACAATGTCGACTTTAGAGACAAAGCTGAAATTA

*A.6. Identified gene sequences and the cloning information*

TAACCCTGAAAAATACTGGTGGGGCACTAGGAATTCATGTAGTGCCTGA  
ATATGATGAGAAAGGAAGGGAGTTAGGCTTAGTAGTTCAAGGGGTAGAA  
GCTGGCGGACGTATTTTCGAGAGACGGCAGACTCAAAGTCAAGGATCAAA  
TTATTGAGATCAATGGAACAAGCTTAGTTGGAGTGGATTTCTGAAGGC  
ACAAGAAATTTTCAAACAAGCTCTTCAAACGGAAGAGATTCGTATGAGG  
GTGGTGAAAGCCGACCCTGAAGACTCTGACAATTCAGCTCCCGAAAAAC  
TGCCGTCTCCTGCCAAAAATAAACCTGATGATTTGGACTTATCACAAATA  
CCTGGTTCTCCCGGTTTGAATTCTCCCCAAAGGCCGGAGGGGGCTGAAT  
CTCCTGGTAAGAGAGCCCCCTCCCGTCCCTGTGAGAAATCCCAGCACGGC  
ATTATCCAGTGGTGCTTCATCTCCTACCAGGTCTGCCCTAATCCAACCCA  
CCAACACTCGCAGTATAGGCGAGATCATCACCATTGAACTTCATAAAGG  
CAATGAGGGTCTTGGCTTCAGTGTTACCACAAGAGACAACATGCCAGGC  
TCAGAAATCCCAGTCTACGTCAAGACGATACAGAACCGTGGCCCTGCTA  
TCAAGGATGGTCGCCTCAAGTCTTGGGACAGATTGCTAGAGGTGAATGG  
CATTCAAATGACTGGCAAGACCCAAACGGAGGCTGTAAGGGTGCTGAGG  
GAGATCCCAATTGGAACCTGATGCCGTCTGAAAATTTCTCGGCAAACGA  
CAGTCACTAAACCGAAATTCACAATGCCGAGAGAATTGCCTCCTGGCTC  
TTCTTCTCCTTCATCCACAACAACCTGTCTCACTACAGCCAACAGACAAAG  
CTGCCGAGGAGCTGACCACCCTCGCCCCTAACGCCACCAAGGAGGTCCA  
CTGCTTCAACATTCTCCTCAACGACTCAGGCTCGGCCGGATTGGGAGTC  
AGCGTCAAGGGCAAGACAACCACCAACCCAGAAGGAATCACAGACCTCG  
GAATTTTCATTAAGTCAGTCATAAGCGGTGGAGCTGCTCATCGGGATGA  
GCGCTTGCGAGTGAACGACCAGCTTGTGGAGGTCAACAACCAGCTTCTC  
GTTGGCAAGTCCAACACGGAGGCCATGGAGACCTTGAGGAACGCCATGC  
AGAGGGAGAGTCCCGTTCCAGGTCACATCAAATTGGTTGTCGCTCGGAG  
AAAGGCCTTACCCGCTCCTGACGAGGCAGACCAACCTTATGTAGACTCT  
AACGAGGTGCGGATAAGTGCCACTGACAATGTGGACGGTGGGGATAAGT  
GGGATGAGGAGGGTTTCAACAACCTCCACTCCACTTTCAAGAGTGATGA  
CAATACCCAATCTAACACTGCTCTTACTACCGCTCCTAAGCCCTTGCTTG  
ACAGAATCACAAACGTCACCACAACGCCCTCCCCACGCAGTAACAAAGCC  
AGCAACATGCAGTCCCCCACCATTACGCTAACCGAGCTGAACTGTACT  
AATAGAGGGAGAGAATAACCAGGTCCAGATGCGTCAGACAGACAAACAC  
AAGCCGCGACCAGCTTCGACTCTAGGGTTCCTGCAGAAGGCTCCAGATG

## A. Appendix

GCAGCACTAAGCTCTCAAGGAGTTCTGAGAATCTTGCCCAAGAAATCGA  
GTGGGATGCTGAGTCTAATATGTCCACAGACGTTGATCCCCAAATAATA  
TTTTCAAGGGAAGGATTTGGGCGACAGAGTATGTCTGAAAAACGCAAGG  
GTCACCTCGATCCAAAGTCTACGGAACTCTACCAAAAAATCAAAGTAA  
CAAAGCTCATGGAAATCAGTACTTATCAGCCACTTGGGAACGCAGGCGT  
TCAGCATCTTATAAAGAGCCAGCAGAGAAGAAGGATGAAGTTGTGGGAC  
CTGCCCTGGGACTGACTAAATCGAGCTCCTTAGAAAGTCTTCAGACTGC  
AATTCAGATTGCAGAGGAGGAAGACGGTGAAGTCACTTCCGCCTTTAAG  
TCTCCAACCCGGTCGATGGTCAGAGGACGCGGATGTAACGAGAGTTTCC  
GAGCTGCAGTTGATAGATCTTACGAAGGCGCAAATGACGCCGAGGCTAT  
GGAGACCTTGGAGGAGGAGAGCAGCGAGACTGGATCCTTTGGCCGCGGC  
CCTGGGGGTGGGTCAGTGCGGTCTTCACACTCTGGCAGTGAGCTGGACG  
ACAAGCGAAAGAAGGCTGGCTCCAAGTCAAAGAAAGACAAAGGATTGTT  
CAAATTTTTTCAAGTTTGGGAAGCAGAACAAAAGGGACGGATCTGAACT  
GGTCCTTCCGAGATCAAAGCTGCTGATGTTGACTTTGCCAAACTCAAAC  
AAGAAGATATTCTAAATACACGCCTAAGACTGAAGAGACTGATAGCAA  
AATCCAGGAACAATTTTCGAGAGCTCCAAGCACAAAGTCCTGGAGCAGCAG  
AACTGCACGACATGCAGGTGGCGGAGATACAACGACAGAACGAGAAGC  
AACGCTACCTGGAGGCGCAGATGAGAGCGAGGTCTCCTTATGGGGCTGC  
CCCTCCCGTGCCCCAGGAACCTCCTCCAGTTACCAAGCAACCTCTCCCT  
CTCGGACACGTCAATCAACTCAAGCGGAGAGACTGCAGAATCTAAGAGC  
GCATCATCAACGTATCCATCAGGAAAGGCAAGGACGCTACCCTAATGAA  
GATGTGGAGGAGCAGTACGAACGGCATCTGTTGCAACTGGAGAGACAGC  
GGCAGATGGCAGCACAGAGAGCTTCAGCATCGACTGTTCCCCCTGGTGG  
AGAGTTTCAACTTCCTCCTCGTCGGCCTCAAGATCGCAATTACAGCGGG  
CCTCAGAGCAGACAAGGATACGCTGACCCCGAACGATACAGTCATTACC  
AGAATCTGGGAGAAATCCAGGCTCAGCTACAGAAACATGCTCACTACCA  
GCAAATGTACAAGCAGCAAGCGGGACAACCCCCCTCTAGGTCGATGGTC  
GATCAGCAACGACAGCTGGTTGACTCCTCTCGGCACCTGGTTGATCAGC  
AGCAGCAAAGAGCTCTGGCTGAACAAAGACGTTTACTGGCCGAGCACCA  
GCAGAGGCAAATAAATGACCATCCACCACAAAGGGAGCTATCCTCGCAG  
AGGGAATTACACCCTCAAAGGGAAGTGCCCCCTCAACGAGAACTGCCCT  
CTCAACGAGAACTGCCCCCGCAAAGAGAACTGCCCCCACAAAGAAACCC

#### A.6. Identified gene sequences and the cloning information

TCAGTATATGCACCCGCAACAGATGCACGCCCAGCAGATCAGGCAGGGA  
GGTTACATGGTCCCTCAGCATCACCAACGCCCCCTCCACCACCCTCCCCA  
CTCGGGGGTCTTCCACGGCCACTCTGGGTCAGACCCGGCCAGGCATTAC  
GGACTAACAGAGACTAGAAGTGGGGGATTGCCCCATTATTACTCTCAGC  
CTGACACAAGATACCTCCACCCCAGCCTCCAACCTCGCAGTATCACACCG  
GGTGCCTCATCGTCCACCAGGGGGAGATCGCCTTCCCCTGGCACCACCA  
GAGCACGCTCTCATACCCCCATCAACCAGGTGGCGTACCTGTCCCAACAC  
ACCGCTGCCAAGTCTCATTCTAGTGCCTTACTGCCCCCTTCCACTAACGG  
TGGTCACCAGAAACGCTCTTACTCCACAGACTATGCCGAGTATGATGAC  
CCTCATTCGCGCTACCGGGACCCAGGGTTCAATTCCTTGCCCCGGAGAC  
CCAGGGAGAGAGCGTCCAGTGAGATCATAT**TCGGGTCTTGCCCAAGTA**  
**TGA**AGTTTTCCATTGTTAATATATCACACGTCCAAAAATGAAGTTAAT  
ATATTTTGTTAGCTGTTGTCTTTCTGTTTATGTTAGGTAAACATGAATTT  
TACGAGTTGTAGTAATAGATACTACTAATGTTTTTTAGAAAAC TGCTGTT  
AAATTCTATTCCATCCATATATATTCTTCACTATTTCACTCTCTTCATGA  
AGTTTGCTCCAGCTTTAAATTTTAACCATGTTAAATCTTTGTACTAGTTA  
GTACTTGATTTTAAGTGGGACATAATTTTTTACTCTGTTAACATTGTACGT  
TTAATGGAACTTATCTTTTTATTGTTAAATGTTGAGTGAAAAAGACTGT  
ACAGTAATTGTAGATCATGTCACAAGTTACTCAGAATCAATGAATCTGT  
ATTTACACGAACAAATGTTCAAATTTTATGACAAATTTGGTGCTTTTAGC  
GAGTAGGGTGAGAAATTGAGAACAAGGTAAC TGTTAGTATTAGCACAAA  
CTAAGTTTTTGGTATTCTTCCAGTATTCATCATGAATTGAACAATAAGTGT  
TTAGAAGAATTTTTTTGAAGAAATTCAGACAATCTATTCTCATTGATTTG  
AAAAAGTTAAGTGAAAAACTATTGAATTATCTAAATTAAGGAAATCTTG  
ATGCCTTTCTGAAACTCAATTTACTTGGTCACAGTAATATTACAGAATAA  
TCATTCATGTAAAATCATACTAAAATGATAGAAACACTTGATCACGACGA  
GATGTTTTTATTTGTGATTCTAGTCCCAATGATTCTGTTTTAATCGTTCAT  
AATTAACATGTATTAACATGTAATATGTTAGATAATTAAGAGTAGTAAT  
ATAGTTACTAAACTATCGTAGCGGAAACCAACAAAATGCTCACATCATTC  
ATTCTGCATGTATTAAGGAGTTAATTGTACATTGTCTTTGTAGCATGA  
AGTACAGAAAGACACACTGTGATGTCCTCTGATGCCCTCCACAACAAAT  
GTACTTATTTTGTAATAAAGGCTTTAC-3'

- Protein sequence

## A. Appendix

MFTIYGLILAFREEICQIVVMKVTVCFGATR VVVPCGNGDLPIS ELIDMAITRY  
KKASGKALDYWVTVHTLKSQSDGGILDPDDL TDVADDREQLIAEYEEQDA  
PLVPHNGGDGTSASSVGTASPD MFHAPEINNQQHNLNNNNKPYAPSSYDVVI  
TQNDLNNVSSRLIVRRGSEP ALINIGIEKENENPQLSLKNSNKRWSAISLVDNG  
RIPKQEDADDEESDEEGGLYPPQQRTGGNGQEKDKEVRS AFTRFARDSARQ  
SLASTNSAMYRWLEAQERTEERA IEMQVSRKEPLGGSGKA EDESEEEDEQSK  
ENNVDFRDKAEIITLKN TG GALGIHV VPEYDEK GRELGLVVQGV EAGGRISR  
DGRLKVKDQIIEINGTSLVGVD FLKAQE IFKQALQTEE IRMRVVKADPEDSDN  
SAPEKLPSPAKNKPDDL DLSQIPGSPGLNSPQRPEGAESP GKRAPPVVRNPS  
TALSSGASSPTRSALI QPTNTRSIGE IITIELHKGNEGLGFSVTTRDNMPGSEIP  
VYVKTIQNRGPAIKDGRLKSWDR LLEVNGIQMTGKTQTEA VRVLREIPIGTD  
AVLKISRQTTVTKPKFTMPREL PPGSSSPSTTTVSLQPTDKAAEELTTLAPN  
ATKEVHCFNILLNDSGSAG LGVSVKGKTTTNPEGITDLGIFIKSVISGGA AHRD  
ERLRVNDQLVEVNNQLLVGKS NTEAMETLRNAMQRESPVPGHIKLVVARRK  
ALPAPDEADQPYVDSNEVRISATDNVDGGDKWDEEGFNNLHSTFKSDDNTQ  
SNTALTTAPKPLLDRITNVTTTPSPRSNKASNMQSP TIHANRAETVLIEGENY  
QVQMRQTDKHKPRPASTLGFLQKAPDGSTKLSRSEN LAQEIEWDAESNMST  
DVDPQIIFSREGFGRQSMSEKRKGHLDPKSTELYQKIKLNKAHGNQYLSATW  
ERRRSASYKEPAEKKDEVVGPALGLTKSSSLESLQT AIQIAEEEDGEVTS AFKS  
PTRSMVRGRGCNESFRAAVDRSYEGANDAEAMETLEEESSETGSFGRGPGG  
GSVRSSHSGSELDDKRKKAGSKSKKDKGLFKFFKFGKQNK RDGSETGPSEIK  
AADVDFAKLKQEDIPKYTPKTEETDSKIQEQFRELQAQVLEQQKLHDMQVA  
EIQRQNEKQRYLEAQMRRASPYGAAPPVPQEPPPSYQATSPSRTRQSTQAER  
LQNLRAHHQRIHQERQGRYPNEDVEEQYERHLLQLERQRQMAAQRASASTV  
PPGGEFQLPPRRPQDRNYSGPQSRQGYADPERYSHYQNLGEIQAQLQKHAH  
YQQMYKQQAGQPPSRSMVDQQRQLVDSSRHLVDQQQQRALAEQRLLAEH  
QQRQINDHPPQRELSSQRELHPQREVPPQRELPSQRELPPQRELPPQRNPQY  
MHPQQMHAQQIRQGGYMVPQHHQRPLHHPHSGVFGHSGSDPARHYGLT  
ETRSGGLPHYYSQPDTRYLHPSLQPRSITPGASSSTRGRSPSPGTTRARSHTPI  
NQVAYLSQHTAAKSHSSALLPPSTNGGHQKRSYSTDYAEYDDPHSGYRDPGF  
NSLPRRPRERASSEIISGPAQV\*

#### A.6. Identified gene sequences and the cloning information

##### ***PduPar4***

- DNA sequence

5'-AATAACAATGGGTTGACACCCTCGGCATTGGCACCTAG**A TGGCTGC**  
**TGCAGTTGACATTACA**ATGGAAGTGGACACAGACTTCCTTGATGGAT  
CTATTCCTTCCCAAATTTCTCTGATGGTGCTGAGGCCATTGACTTTCTT  
GGGGACCCATTTTTTCCACCGAGTCGACTCTGACCAAATCGTTTATGCAC  
CAAGAAGAAAAAGGGCAAAGCTCATTGGCAAGTATGTCATGGGTGATTG  
CCTTGGAGAGGGATCATATGGAAAAGTCAAGGAGTGTCTTGACTCAGAG  
ACACTGTGCAGAAAGGCTGTCAAGATACTTCAGAAGAAAAAACTGCGAA  
AAATACCCAACGGTGAAGCGAATGTCAAAAGAGAGATTTCGTCTGCTAAA  
ACGACTGTGCCATAAAAAATGTTATCCAGTTATTTGATGTGTTATACAAC  
GATGAGAAACAGAAAAATGTATTTGATTATGGAATATTGTATGATTGGTT  
TGCATGAGATGTTGGAAAATGCCCCAGGAAAGAAATTGCCGATCTGGCA  
AGCACACAACACTACTTCTGCCAATTAATCGAAGGCCTGGAGTATCTTCATA  
GCCAAAGTATCATTACAAAGGATATCAAGCCTGGGAATTTGTTACTTAC  
CACTGGGAATACCCTCAAAATCACTGATTTGGGTGTCGCTGAGATGGTA  
GATCCTTTCTCTATGGACGACTCCTGCCAGACTAGTCAAGGTACGCCCCG  
CCTTCCAGCCGCCGGAGATAGCAAACGGAGATGACGTCTTTCCAGGCTT  
CAAAGTGGACATCTGGTCCTCTGGGGTCACTCTATATAATATCACCACA  
GGACAGTATCCATTTGAGGGTGATAACATATACAAGCTTTTTTGAAAAAA  
TAGGAAGAGGCGGCTTTACCATTCCAGATGAACTAGATGACTCTTTGAA  
AGATCTGATTCAAGGAATGATGGCTCATAATCCTGCAGATAGAATTGCA  
ATTCAACAAATTAGAGATCATACATGGTTCAGGAAAAGACCAGGTGCGAA  
CGTTTGAACACGTAGTACCCCCACCGCTATTGGATGGCACCGATAAACT  
CCGGAATATGTCAGTTTTTGCCGTACTTAGAGTCACTGCACAGATGCACG  
ACGCCCAGTCAGGAAGAGGAGGAGGATGAGTTGTCTTCAAGTTTGCAAC  
CTGTCAATCCTTCTCAACCACCAGCTGCAGCCTCAGCGTCTGGTGGCACC  
CCAGAAGTCCCTGCTGAAAGCGAGAAGCCAAAAAAGAAGCGAATCATTA  
ACGTGCGTAAATTGACAAT**AAACGCGTGCAAGCAGTCC T**GATCTCA  
TCACGTTTCACTCCCGGTCTGCATTATCTTTGTGTGCTGAACTGTTTTAC  
GGAACGTCAAAAATCAAGTCGTGCGGAGTATGTGATATTGTGTAAATTT  
GTTAGGGAATTATTTAATTTTAATAGTCAGCCAATGTTTTTTATGAATAA



## A. Appendix

ACTAAAGAGTGTGTTTTTATGACTAATGAA-3'

- Protein sequence

MAAAVDITMEVDTDFLDGSIPFPNFSDGAEIDFLGDPFFHRVDSQIVYAPR  
RKRAKLIGKYVMGDCLGEGSYGKVKECLDSETLCRKAVKILQKKKLRKIPNG  
EANVKREIRLLKRLCHKNVQLFDVLYNDEKQKMYLIMEYCMIGLHEMLENA  
PGKKLPWIWQAHNYFCQLIEGLEYLHSQSIHKDIKPGNLLLTTGNTLKITDLGV  
AEMVDPFMSDDSCQTSQGTAFQPPPEIANGDDVFPGFKVDIWSSGVTLYNIT  
TGQYPFEGDNIYKLFKIGRGGFTIPDELDDSLKDLIQGMMAHNPADRIAIQQ  
IRDHTWFRKRPGRTFEHVVPPLLDGTDKLRNMSVLPYLESLHRCTTPSQEE  
EDELSSSLQPVNPSQPPAAASASGGTPEVPAESEKPKKKRIINVRKLTINACK  
QS\*

### *PduPar6*

- DNA sequence

5'-TGAAAAGAGACAGTTTATCGGCTCCAATGTGGAATTTACCTGGATTTA  
ACCGGTGACCAAGCCCTGGAGGAGGGCACAAAGTCATCCACGA**ATGTCT**  
**ATGAACGGGAAATCTGGCCA**AGTACTGGCCAACAGAGTCATTGAAGT  
CAAGAGCAAGTTTGATGCTGAATACAGAAGGTTTTCAATCAACAAGGCG  
AAAATCCTTCGATATGAGGAGTTTTACCAACTCTTACAAGACCTGCACA  
GATTAAAAGACATTCCATTTATTGTGTGTTACACGGACCCCAAAGATGG  
GGATTTATTACCAATCAACAATGGGGACAACACTACATGCTCGCAATCAAC  
ACCACGCCAAGTATATTGCGGCTCACTGTGCAGAGAAAAGGCGAGAGTA  
TATTCGAAGTCAACGGCTATGGAACGTTGGGGCGACCGAAGAAGAACCC  
CATTACTAAATTTATGGCTAGCGAGCAACCGATTAAACCAAAAATACCA  
ATTAGCATGCCAGAGGACTTTAGGCGAGTGTTCGGCCATTATTGACGTGG  
ATATTATTCCCGAGACACAACGGAGAGTTAAGCTGATGAAGAACGGTAG  
TGATAAACCCCTCGGATTTTATATCAGGGATGGTACGAGCGTACGTGTG  
ACCCCTCACGGATTGGAGAAGGTACCGGGGGTGTTTCATATCGCGATTAG  
TGCCGGGAGGACTGGCGGAGAGCACGGGGTTAGTAGCCGTCAACGACGA  
GGTTTTGGAGGTAAACGGCATCGAGGTTGCTGGTAAGACTCTCGATCAA  
GTGACTGACATGATGGTGGCTAACAGCTCCAATCTAATCATCACGGTGA

## A.6. Identified gene sequences and the cloning information

AACCTGTGAACCAGCGGAACAACATCGCTCAAAAGAGCAGCAACGCCAG  
CAGTACTAACTCGATGCGGCAGAGTGTGATTTTCGGGGTCATCGCAACAG  
AGTTCGACTCACTCGTACGACTCGGACGAGATCCATGACTACGAGGAAG  
ACGAGGATGAAGTCAAAGACCATCTCCAGAAAGATCACTTGATGAAGAA  
ATCGAGCTCCTCTTCCTCTAATCCTCATCACAAAGATACCACATCCCTCT  
CTTCCATGAACAGCAATTCCCAAAAAGACTCGCCAAAATCTGAAGCGAA  
CGATTCCGCATTATCCGCTTCCCCCTCAACGTCACAGTCGGCCCAAGATA  
**AAGACAGCCCCATGGCCATGTTA TAG**CTAGGCCTGACTGTGCTGCT  
CGCTCTGGCTATAGCCTATATCAACGGATTCTAATGTGCGAAAGATATGT  
GCGAGATATCATCTCAGATATGGGATGCGAGATACGCGATAGTGTCTTA  
AACATGTGATGTGTATTCT-3'

- Protein sequence

MSMNGKSGQVLANRVIEVKSKFDAEYRRFSINKAKILRYEEFYQLLQDLHRL  
KDIPFIVCYTDPKDGDLLPINNGDNYMLAINTTPSILRLTVQRKGESIFEVNGY  
GTLGRPKNPITKFMASEQPIKPKIPISMPEDFRRVSAIIDVDIIPETQRRVKL  
MKNQSDKPLGFYIRDGTSVRVTPHGLEKVPGVFISRLVPGGLAESTGLVAVN  
DEVLEVNGIEVAGKTLQVTDMMVANSSNLIITVKPVNQRRNIAQKSSNASST  
NSMRQSVISGSSQSSSTHSYDSDEIHDYEEDEDEVKDHLQKDHLMKKSSSSSSN  
PHHKDTTSLSSMNSNSQKDSPKSEANDSALSASPSTSQSAQDKDSPMAML\*

### A.6.3. Non-muscle-myosin related proteins

#### Non-muscle-myosin heavy chain, *PduNmm*

- DNA sequence

5'-**ATGGCGGCCACGAGAGGAGG**CAACGAGTTGCAAGCCCTTCGGCC  
CAAAGTTAACCGGGAAATGATCAACGACCCGAGCCAACAAGCAGCATGG  
GCAGCCAAAAGACTCGTCTGGGTTCCCCACGAGAACCAGGGATTCGTAG  
CATCAAGTATTCGCGAAGAAAGAGGCGACGAAGTCTTGGTCGAATTGAT  
AGATTCAGGAAAGCATGTGCTTATCAATAAAGACGATATCCAAAAAATG  
AACCCTCCACGGTTCGACAAAGTTGAAGATATGGCAGAATTGACATGCT  
TAAACGAAGCCTCCGTCTTGCATAACTTAAAGGAGAGATACTATTCTGG

## A. Appendix

GTTGATATACACATACTCAGGATTGTTTTGTGTGGTAGTTAACCCTTAC  
CAGAGGCTACCAATTTTACACTGAGGAGGTGATTGAACAGTACAAAGGAA  
AAAAGCGACATGATGTACCCCCTCATGTCTTTGCCATCGCCGACACTGCT  
TACAGGAGCATGTTGCAAGATCGAGAAGACCAGACAATTCTATGCACAG  
GAGAATCAGGAGCAGGAAAAACAGAAAATACAAAAAAGGTCATCCAGTA  
CCTGGCCTACGTAGCAGCATCCCTCAGGTCCCAGAAACAGTCAACTTCCC  
AGGTCTCTCCAATCTGCAGCAAGATGAAGATAGAATTAGATGGGGAGA  
ATTAGAACAACAGTTACTTCAGGCTAACCCAATTCTTGAAGCTTTCGGAA  
ACGCCAAGACCGTCAAGAATGACAACTCCTCACGTTTTTGGCAAATTCATC  
AGGATCAATTTTCGATTCATCTGGTTTTCATCTCTGGGGCTAACATCGAGA  
CATATCTATTGGAGAAATCGAGGTCAGTGCGTCAAGCGCCCAACGAGAG  
GGCCTTCCACATATTTTACCAGATGCTTGGATCGTGTACGGACTCAGAA  
AGAAAGGACTTTTTTGCTGGAAGACATCAAGAACTACCGCTACTTGTCTC  
ACGGGCAGGTGCCATGTGGGACGCAGGACGACAAGGAGCTGTACCGGCA  
GCTGATCGAGGCTATGGAGATCATGAGCTTCAATACCGAGGAGGTTGCA  
GCTGTTTCAACAAGATTGTTTTCGGCCGTCTTGCTTTTTGGGCAACATGCAAT  
TCAGGCAAGAGAGAACTCCGACCAGGCGACCCTCCCCGACAACACAGT  
TGCCCCAAAAGACATGCCATTTACTTGGCCTTCCTGTAACTGAAATGACCA  
GAGCTTTCCTGAAACCAAGAATCAAAGTTGGCAGAGATTTTCGTACACAA  
GGCACAACTAAGGAACAGGTTGAGTTTGCAGTAGAAGCAATCAGCAAG  
GCCGTCTACGAGCGCCTCTTCAAATGGCTGGTTCGCTCGTATCAACAAGT  
CTTTGGACCGCACCAAGCGCCAGGGGGCCTCCTTCATTGGCATCCTCGA  
TATCGCTGGTTTTCGAGATCTTCCTGATGAACTCGTTTTGAGCAGCTCTGC  
ATCAACTACACCAACGAGAAGTTGCAGCAGCTCTTCAACCACACCATGTT  
CATCCTGGAGCAGGAGGAGTACCAGAGGGAGGGCATTGAATGGACCTTC  
ATTGATTTTCGGA CTCGACCTCCAGCCCACCATCGACCTCCTCGAGAAGCC  
TCTTGGTATCTTTGCCCTTGTGGACGAGGAGTGTTGGTTCCCCAAGGCG  
ACCGACAAGACTTTGGTGGAGAAGTTGAACGCCCAACACAGCACCACCC  
CCAAGTTCCAGAAACCTGCTTTCAGGGAGAAGGCCCATTTTCAGTCTCAT  
CCACTACGCCGGCAAGGTTGACTACTCGTGCGACCAGTGGCTCCTGAAG  
AACATGGATCCCCTGAACGAGAACGTGGTCTCGCTGCTCCAGGCCTCTT  
CTGACGAGTTTGTGCGAAACATCTGGAAGGATGCTGAGATAGTTGGAAT  
GGGAGCTGCCACAGCCAACGAGACTTCATTTGGAGCTAGGACTCGCAAG

*A.6. Identified gene sequences and the cloning information*

GGAATGTTCCGGACGGTCGGCCAGTTGTACAAGGAGCAGCTGAGTCGCT  
TGATGTCCACCCTCAACAACAGCAATCCCAACTTCGTCAGATGTATCATT  
CCTAACCACGAGAAGAAGACTGGCAAGATTGACGCAGCCCTGGTGCTGG  
ACCAGTTGAGGTGCAATGGTGTACTGGAAGGTATCAGGATCTGCCGACA  
AGGTTTCCCCAACAGAATTCTCTTCCAAGAGTTCAGACAACGATACGAA  
CTGCTCACTCCAAATGTCATCCCCCGCGGCTTCATGGACGGCAAGAAGG  
CCTGCGAAAACATGATCAGAGCCCTGGAACCTGGACCACAACCTGTACAG  
GATTGGCCAGAGCAAGATCTTCTTCAGGGCGGGAGTGCTGGCCCATCTT  
GAGGAGGAACGTGACTTGAAGCTCACCGACATCATCGTTAGGTTCCAGG  
CGTTCGCTCGTGGTTCCCTGGCAAGAAGGAATTACCAGAAGAGGCAGCA  
ACAGCTGAACGCCATCAGGATCATCCAGAGGAACTGCGCGGCCTACTTG  
AAGCTGCGCAACTGGCAGTGGTGGCGCCTCTTCACCAAGGTCAAGCCGC  
TGTTGCATTTTCGTGGACAACGAGGAGAAGTTTAAAGCCAAGGAGGAGGA  
GCTGAAGAAGATAGCCGACAAGTTTGACAAACAGGTCCAAGAAGTCCAG  
GAACTGGAGAAACGACACACCGAGCTGCTAGATGAGAAAAACGTTTTAA  
TGGAACAACCTTCAGGCCGAGTCAGAATTGTGTGCCGAGGCTGAAGAGTC  
GCGAGCGCGTTTTGTTCGGCTCGGAAGCAGGAGTTGGAGGAGGTTCTTGCT  
GAGATGGAGACGAGGATGGCTGAGGAGGAGGAACGAGCCCAAGTATTC  
GTGTCTGAGCGGAAGAACTACAGACAAATATACAGGACTTAGAGGAAC  
AGCTAGAGTCCGAAGAACAAGCCAGACAGAACTGCAGTTAGAGAAAGT  
ATCCACAGATGCCAAACTTAAAAAGCTGGAGGAGGACCTTGCTGTATTT  
GAAGATACTAATGCTAAGTTGACGAAGGAGAAGAACCAGATGGAGGAGA  
GATTGCAAGACATCCAATCAAACGTAGTCGACTCGGAGGAGAAAGTCAA  
ACAGCTTAATAAACTGAGAAATAAACACGACGCTATTATCAAGGACTTG  
GAAGAGAGGTTAAGACGTGAACAACAGCTCAGACAAGAATTAGAAAAAA  
TAAAACGCCGGTTGGAGACGGAAGTACAGATGTAAAAGAACAGCTGTC  
AGAAAAGTGTGTGCAGTTAGAAGAGTTACAAGCACAGCTCAACAAGCGG  
GAGGAGGAGGTGCAGGCTGCGCTCAACAGGGTGGAAGAAGAGGTTGCA  
GTTAAGGTTACATTCCAGAAACAGATCCGAGAGATGGAAAGTCAGTTAC  
AGGAGATCAACGAGGATTTGGACGCCGAGAAAGAAGCCAGAAATAAAGC  
AGAGAAGCAAAAGAGAGACTTAGGGGAGGAGTTGGAGGCACTCAAGTCT  
GAACTGGAGGATTCACAAGACACGACAGCGGCCGTCCAAGAGTTGCGGA  
ACAAGAGAGAGCACGAGGTAGCCATCTTGAAAAACAACCTGGAGGAAGA

*A. Appendix*

TGTGCGCAACCACGAGGAACAAGTGCGGGAATTCCGATCCAAGCACACC  
GTACAACTGGAAGAGATGAACGAACAGCTCGATCAAGCCAAGCGGTCTA  
AAGCAGCTCTGGACAAGATGAAGCAGACGTTAGAATCTGAAAACGTTGA  
CATGGCGAATGAAATCAAACAGCTGACGGCCTCCAAACAGGAATCAGAA  
AGGAAGCGGAAGCAACTGGAAACGTCCGTGCAGGAAGCCAACATCAAAT  
ACATCGAGGTGGAGAGGAATCGCAGCGACCTCATCGAGAAAGTGCAGAA  
GTTGCAGACTGAAGTGGAAGCGTCCACGTCGTCGTTTGAGGATGCGGAT  
GCCAAGGCGGCTGTGATGAACAAGCAGGTGACGTCACTAGAAGCCCAAT  
TAGCAGACGCCCAGGAGTTGCTACAGGAGGAGACCAAACAGAAGTTGGC  
TTGTTCAGTCTAGATTGCGGCAGTTGGAAGAGCAGTGCGATGTCCTCCAG  
GAGCAGATGGAAGACACGGAGGAAGCAAAGAAGACCTACGAGACGAAGC  
TAGCTCATGCCCTTGCTCAGGTTGTGGAAGCAAAGAAGAAGCAAGAGGA  
GGAGAAGGGACAGATAGAAGTGGTGGAGGAGACCAAGAAGAAGATGTC  
ACGCGACATGGACGGCCTGCAGGCCAGAATACAGCAGATGGAAGCAGAC  
AACGACCGACTGGGCAAGAGCAAGAAGAAGGTCCAGTCTGAACTGGACG  
ACCTCAACGTGGAGCTGGACAACCTACCGCTCTGGCCTCTCCGCCATGGA  
GAAGAAGCAGAAGAAATTCGACCAGAACCTTGCCGAGGAGAAAGCCATT  
TCAGAAAGACTTGCAATGGAGAGAGACAGCGCCGAGAGAGAGAGCAGAG  
AGAAGGAGACCAAGATCCTGGGTTTGTCTCGGGAATTGGAAGAGTTGCA  
AGACAGGTTGGAAGAAGTGGAGAGGACGAAAGTGACGCAGCAGAGAGA  
ACTGGAAGACCTCATGTCCTCCAAGGATGACGTCGGCAAAAGTGTCCAC  
GAACTTGAGAAGGCCAAGAGACAGTTGGAAGGACAAGTGGAGGAGCAG  
AGAACGCAGATCGAGGAATTGGAGGACGAACTGCAGGCCACGGAGGATG  
CCAAGTTGCGGCTGGAGGTGAACATGCAGGCCTTGAAGGCCCAGTTTGA  
GCGGGAAGTGCAGGGCAGAGATGAAGCAAGTGAAGACAAGAAGAAGGC  
GCTCGTCCGCCAACTGAGGGGAGATAGAAGCAGAATTGGAGGAGGAGAG  
GAAACAGCGTACGGCAGCTATTGGAGCCAGGAAGAAGTTGGAGGGAGAC  
CTGAAAGACATGGAAGGACAGGTTGACACGGCTTCCAAACTGAAGGAAG  
ACGCTGTGAGGCAGCTGAGAAAACCTTCAGGGCACACTCAAGGAGTTCCA  
GAGGGAGACTGAGGACGCCCTCAATGCCAAGGACGAGGCGTTTCGCGGCA  
GCCAAGGAGAACGAGAAGAAGGTGAAGAACCTGGAGGCGGACTTGGCTC  
ACATGCAGGAGGACCTGGCCGCCTCGGAGAGAGCGAGGAAAGCCGTGGA  
GTCAGAGAGAGACGAGTTGTCTCGGAGGAGGTGACGAGTGGTGCTAGTAA

#### A.6. Identified gene sequences and the cloning information

CAAGAACTCCCTGGTGGAGGAGAAGAGAAGGTTGGAGGGACGCATTGGC  
CAGCTGGAGGAGGAGCTGGAGGAGGAGACGAGCAACTTGGAGATCATG  
GCTGACAAGGCTCGCAAGAACGGTCTGCAGGTTGAACAGCTGACGACAG  
AATTGGCAGCTGAGCGATCCAACACGCAGAAGCTTGAGAATGGTCGGTT  
GTTGCTGGAAAGACAGAACAAGGACTTGAAGTCGAAGCTGGCCGAGTTG  
GAGGCGCAGATGAAGACTCGCTCCAAGGCCACGATCCAGTCGCTGGAGA  
GCAAGATCGGCAACCTGGAGGAGCAGCTGGACGTGGAGGGCAAGGAGA  
GACAGAACCTGGCCAAGATGAACAGACGTCTGGAGAAGAAGATGAAGGA  
CTTGGTCATGCAGGCCGAGGACGAACGCAGACATGCCGACCAGTACAAG  
GATCAGGTTGAGAAGCAGAGCGGCCGCATGAAGGCCTTGAAGAGGCAGT  
TGGACGAGGCGGAGGAGGAGTGCACGAGACTGAACGCTCAGAAACGCAA  
GGTCCAACGAGATCTAGACGAACAGATTGAGCAGACGGAAGTCGTGCAG  
AGAGAGAACGACCAGCTTAAGAACAAGCTCAGAGCAGGCGGAGACAAAT  
TAAGTTCCAAGTCACGCACTGGTCGCACCAGTTACTTGCTGGGCCGTAG  
CAGCATGATGCCTCCTTCGCCCCGCAAGTGACGACGGCTCTAACGAAGAA  
ACCCCAATGACCATGACGACACCCAGTGA-3'

- Protein sequence

MAATRGGNELQALRPKVNREMINDPSSQQAAWAAKRLVWVPHENQGFVASS  
IREERGDEVLVELIDSGKHVLINKDDIQKMNPFRFDKVEDMAELTCLNEASVL  
HNLKERYYSGLIYTYSGLFCVVVNPHYQRLPIYTEEVIEQYKGKKRHDVPPHV  
FAIADTAYRSMQLDREDQTICTGESGAGKTENTKKVIQYLAYVAASLRSQK  
QSTSQVLSNLQQDEDRIRWGELEQQLQANPILEAFGNAKTVKNDNSSRFGK  
FIRINFDSSGFISGANIETYLLEKSRSVRQAPNERAFHIFYQMLGSCTDSERKDF  
LLEDIKNYRYLSHGQVPCGTQDDKELYRQLIEAMEIMSFNTEEVAAVHKIVSA  
VLLLGNMQFRQERNSDQATLPDNTVAQKTCHLLGLPVTEMTRAFLKPRIKV  
GRDFVTKAQTKEQVEFAVEAISKAVYERLKFVWLVARINKSLDRTRKQGFASFI  
GILDIAGFEIFLMNSFEQLCINYTNEKLQQLFNHTMFILEQEEYQREGIEWTFI  
DFGLDLQPTIDLLEKPLGIFALVDEECWFPKATDKTLVEKLNAQHSTHPKFQ  
KPAFREKAHFSLIHYAGKVDYSCDQWLLKNMDPLNENVVSLQASSDEFVRN  
IWKDAEIVGMGAATANETSFGARTRKGMFRTVGQLYKEQLSRLMSTLNNSN  
PNFVRCIIPNHEKKTGKIDAALVLDQLRCNGVLEGIRICRQGFPNRILFQEFRQ  
RYELLTPNVIPRGFMDGKKACENMIRALELDHNLRYRIGQSKIFFRAGVLAHLE

## A. Appendix

EERDLKLTDIIVRFQAFARGSLARRNYQKRQQQLNAIRIIQRNCAAYLKLRNW  
QWWRLFTKVKPLLHFVDNEEKFKAKEEELKKIADKFDKQVQEVQELEKRH  
TELLDEKNVLMEQLQAESELCAEAESRARLSARKQELEEVLAEEMETRMAGE  
EERAQVVFVSERKKLQTNIQDLEEQLSEEEQARQKLQLEKVSTDAKLKKLEED  
LAVFEDTNAKLTKENQMEERLQDIQSNVVDSEEKVKQLNKLNRNKHDAIHKD  
LEERLRREQQLRQELEKIKRRLETELADVKEQLSEKCVQLEELQAQLNKREE  
EVQAALNRVEEEVAVKVTFQKQIREMESQLQEINEDLDAEKEARNKAQKQK  
RDLGEELEALKSELEDSQDTTAAVQELRNKREHEVAILKKQLEEDVRNHEEQ  
VREFRSKHTVQLEEMNEQLDQAKRSKAALDKMKQTLESENVDMANEIKQLT  
ASKQESERKRKQLETSVQEANIKYIEVERNRSDLIEKVQKLQTEVEASTSSFED  
ADAKAAVMNKQVTSLEAQLADAQELLQEETKQKLACQSRLRQLEEQCDVLQ  
EQMEDTEEAKKTYETKLAHALAQVVEAKKKQEEEEKGQIEVVEETKKKMSR  
DMDGLQARIQQMEADNDRLGKSKKKVQSELDDLNVELDNYSRGLSAMEKKQ  
KKFDQNLAEEKAISERLAMERDSAERESREKETKILGLSRELEELQDRLEEVE  
RTKVTTQQRELEDLMSSKDDVGKSVHELEKAKRQLEGQVEEQRTQIEELEDEL  
QATEDAKLRLEVNMQALKAQFEREVQGRDEASEDKKKALVRQLREIEAELE  
EERKQRTAAIGARKKLEGDLKDMEGQVDTASKLKEDAVRQLRKLQGTLEKEF  
QRETEDALNAKDEAFAAAKENEKKVKNLEADLAHMQEDLAASERARKAVES  
ERDELSEEVTSGLSNKNSLVEEKRRLEGRIGQLEEELEEEETSNLEIMADKARK  
NGLQVEQLTTTELAAERSNTQKLENGRLLLERQNKDLKSKLAELEAQMKTTSK  
ATIQSLESKIGNLEEQLDVEGKERQNLAKMNRRLKMKMDLVMQAEDERRH  
ADQYKDQVEKQSGRMKALKRQLDEAEEECTRLNAQKRKVQRDLDEQIEQT  
EVLVQRENDQLKNKLRRAGGDKLSSKSRTGRTSYLLGRSSMMPPSPASDDGSNE  
ETPNDDHDDTQ\*

### Non-muscle-myosin essential light chain 1, *PduElc1*

- DNA sequence

5'-**ATGGCTGCCTTCAACGAAGAT**CAGATCGTGGAGTTCCAGGAAGCC  
TTCACCATCTTTGATCAGAAAGGTGATGGCAAGATCCAAGTATCCCAGA  
TCGGGGAGGTGCTGCGGGGCACTCGGTCAGAACCCCACTGAGGCTGACGT  
GAAGAAGCTGTCCCACCAGCACCGTCCAGATGAGAGAATTAGCTTTGAG  
GTGTTCCCTGCCAATCATGCAAACCATCTCCCGCCAACGTCCTGTTGATAC  
TGCCGACGACTTTATTGAGGGACTCCGCCACTTTGACAAGGATGGCAAT

#### A.6. Identified gene sequences and the cloning information

GGCTACATCTCTTCTGCTGAACTCCGACATCTCATGACACATTTGGGAG  
AGAAGCTGACTGATGAGGAGGTGGAGCAGCTGTTGGCCGGCCAAGAGG  
ACTCCCAGGGCAACATCAACTATGAGGAGTTTGTTC**GCCTGGTCCTCA  
GTGCTTAG-3'**

- Protein sequence

MAAFNEDQIVEFQEAFITFDQKGDGKIQVSQIGEVLRALGQNPTEADVKKLS  
HQHRPDERISFEVFLPIMQTISRQRPVDTADDFIEGLRHFDKDGNGYISSAELR  
HLMTHLGEKLTDEEVEQLLAGQEDSQGNINYEEFVRLVLSA\*

#### Non-muscle-myosin essential light chain 2, *PduElc2*

- DNA sequence

5'-**ATGTCTAGCCTCTCAGAAGATCAAATTT**CAGAATACCAGGAGACC  
TTCTCCTTGTTGACAACAAGGGCGATGGTAAGATCTTCGCTCACCAGTT  
GGGAGAGGTCCCTCCGGGCCATGGGTCAGAACCCACCGAGGCAGAGGTC  
AGGAAGTGCGGCTACCAGAACGATCTAGACACGAGAATCAGTTTTGAGA  
TGTTCCCTTCCCATTTCTCCAGACGGTCAGCAAGAACAGAGACCACCCACG  
GCTGACGACTTCGTCGAGGGATTCCGAGTATTCGACAAAGATCAAAACG  
GCACGATCAGCAGCGCCGAGTTGAGGCATCTGTTGACTAGTTTGGGTGA  
ACGTTTGACGGACGAAGAAGTCGAACAACCTCTTGCAAGGACAGGAGGAC  
GCCCAGGGAAATATTAACCTATGAAGACTTT**TGTCAAGAACGTGATGGT  
TGGTTGA-3'**

- Protein sequence

MSSLSEDQISEYQETFSLFDNKGDKIFAHQLGEVLRAMGQNPTEAEVRKCG  
YQNDLDTRISFEMFLPILQTVSKNRDHPTADDFVEGFRVFDKDQNGTISSAEL  
RHLLTSLGERLTDEEVEQLLQGQEDAQGNINYEDFVKNVMVG\*

#### Non-muscle-myosin regulatory light chain 1, *PduRlc1*

- DNA sequence



## A. Appendix

5'-**ATGTCGAGTCGAAAAGCCAAGAAGACAGTAAAGAAGAGGGCCCA**  
GAGGGCTACCTCAAATGTCTTTGCTATGTTTCGACCAAGCACAAATCCAG  
GAGTTCAAAGAAGCATTCAACATGATCGACCAGAACAGAGATGGCTTTA  
TCGACAAGGAGGATTTGCATGACATGCTTGCTTCTTTAGGCCAAAGACCC  
CACAGACCAGTACTTGGAGGCCATGATGGCCGAGGCCCCCTGGTCCCATC  
AACTTCACAATGTTCCCTTACCATGTTTGGAGAAAAACAAAACGGGCACAG  
ACCCCGAAGATGTCATCAAAAATGCCTTCGCTTGTTTTGATGAAGAAAA  
CAAAGGTTACATCCACGAAGACAAGCTTCGAGAACTTCTGACAACAATG  
GGGGATCGGTTTACTGATGAAGATGTTGATGAGATGTACAGAGAGGCTC  
CTATCAGCAAAAATGGCTATTTTCGATTATGTGGAATTCACCCGTATTCT  
GAAGCATGGCAAGAAGGACAAGGATGACGAC**TAG-3'**

- Protein sequence

MSSRKTAGRRATTKKRAQRATSNVFAMFDQAQIAEFKEAFNMIDQNRDGFV  
EKEDLHDMLASLGKNPTDDYLDGMMNEAPGPINFMTFLTLFGERLQGTDPE  
DVIKNAFGCFDEENMGVLPEDRLRELLTTMGDRFTDEDVDEMYREAPIKNG  
LFDYLEFTRILKHGAKDKDEQ\*

### Non-muscle-myosin regulatory light chain 2, *PduRlc2*

- DNA sequence

5'-**ATGTCTTCAAAAATCGAAAAAGAAACATCGGCAAAGACTCCACAG**  
ACACACGTCAAATGTCTTCTCCATGTTCAACCAAGACCAGATTCAAGAGT  
TCAAGGAGGCTTTCAACATGATAGATCAAAACAGAGACGGTTTTATCGA  
CAGAGATGATTTGATTGAGATCTTCACTTCTCTCGGCAAGAACCCCACT  
GACGATTTGATGATCCAGATGTTGAGGGAAGCCCCCGGCCCAATCAATT  
TCACGATGTTCTTGACGTTATTCGGAGAGAACTCAATGGCACCGATCC  
AGAAGATGTGATAAGGAATGCGTTTCGCGTGTTTTGATATGATCGGCGGA  
GGTGAACCTTGCAGAAGGCTACCTCCGTGAAATCATGACAACAATGGGAG  
ACAGGTGGACGCACGACATGGTAGATGAGCTCTTGTATGGAGTGCCCAT  
GAAAGAGGGGAAAATTTGATTACATCGAATTCACCCGAGTTCTCAAACAC  
GGGGCGAAGGAGAAAGATGAGAAGAACGAGGGAATGCCACAAGGTGCG  
CCACAAGGTGCGCCTATGCTGCCACCT**ATGCCACCAATGCAGCGATA**  
**G-3'**

## A.6. Identified gene sequences and the cloning information

- Protein sequence

MSSKSKKKHRQRLHRHTSNVFSMFNQDQIQEFKEAFNMIDQNRDGFIDRDDL  
IEIFTSLGKNPTDDLMIQMLREAPGPINFMTFLTLFGEKLNGLTDPEDVIRNAF  
ACFDMIGGGELAEGYLREIMTTMGDRWTHDMVDELLYGVP MKEGKFDYIE  
FTRVLKHGAKEKDEKNEGMPQGAPQGAPMLPPMPPMQR\*

### A.6.4. Actin binding protein

#### *PduMeosin*

- DNA sequence

5'-**ATGCCTAAGCCTGTCAATGTCCGCGTCACCACCATGGACGCCGAG**  
CTGGAGTTTGCCATCCAGCCGAGCACAACCTGGCAAACAGCTCTTCGATC  
AGGTGGTTAAGACCATCGGTCTCCGAGAAATTTGGTTCTTCGGTTTACA  
GTACACAGACAGCAAGGGACTGTCCACGTGGCTAAAGCTCAATAAAAAG  
GTCTTGAATCAAGATGTCCGCAAAGAAACACCCCTCCAGTTCAAGTTCA  
GAGCCAAGTTTTATCCAGAAGATGTCTCGGAGGAGCTCATCCAGGAGGT  
CACGCAGCGCATGTTCTTCTTACAAGTGAAAGAGGGAATCTTGAATGAT  
GAAATCTACTGCCCTCCGGAGACGTCCGTGCTCTTGCGCTCCTACGCTG  
TCCAGGCCAAATACGGAGACTACAACCCAGACGTCCACCAATCAGGCGT  
CCTCCACAACGACAACTCCTACCTCAGAGAGTTCTTGATCAGCATAAGA  
TGACCAAAGAACAATGGGAGGAGAGAATTGTCAACTGGTGGGCAGAACAA  
CAAAGGCATGCTCAGGGAAGATTCAATGATGGAGTATCTGAAAATTGCC  
CAGGATTTAGAAATGTACGGAGTGAATTACTTTGAAATTAAGAACAAGA  
AGGGAACAGACCTCTGGCTAGGAGTAGACGCTTTAGGTCTTAATATTTA  
TGAAAAAGAAGACAGACTGACACCCAAAATAGGCTTCCCATGGAGTGAA  
ATCCGAAATATTTCTTTCAATGACAAGAAATTCACAATCAAGCCAATTGA  
CAAGAAAGCACCTGACTTTATCTTCTTCGCACCAAGATTGAGAATTAACA  
AGAGAATCCTGGCTTTATGTATGGGCAATCACGAGCTTTACATGAGACG  
GCGTAAGCCTGACACCATTGAGGTCCAACAAATGAAAGCTCAAGCCAGA  
GAGGACAGGCTCGCCAAACAGGCAGAACGTGCACAACTGCAGAAGGAGA  
AACAAATGAGGGAGGAGGCTGAACGGGCAAGAAAGGAATTGGAAGACA  
GAATTAAGAAATACGAAAATGATATGGAATCCACAAAAAAGAACTTGA

## A. Appendix

AAAATCAAGAGAGATCACATTAGATTTAGAAAAGAAAATGAACGAAGCC  
GAACGGGAAAGAATAGAATTGGAAGAAGCCCCAAAGGAAAGCAAACGAAT  
TGAGAGTAGCAGCCGAAGCCGCCCGCCAGATGGAGAGAGAAGAGAGGGA  
ACGTATGGAGAGAGAGGGCTGCGGAGGCCCGAGGCTGAAGCCGAAGCTCGT  
GCTCTTGCCGCTCGGGAGAGAGAAGAGGAGGCCCGACGATTGCAAGAAG  
AGCTGGAAGCCACAAGAATGAAGATGGAGACGAAAGAAAAAGAATTGGA  
GGAGGCTCTTGCCAAGCCCGCTCCCCCGTCCAGAACAATGTTGTTGCT  
CATCTGCGGGAGACCGAAGAAGACGAGGGCGAGGATAGGAACGAATAC  
GAAAGCGTGGAACCCAGCGTTCCATCTCTAACTACTCCGAGGATTACT  
ACAACCTCGACCACCCAAGATAACGGCACCGTCGGAAGTGATGACTATTT  
TGAGAGAGCTGAGCTCTCAATAGCTGAGAACGAGAACCTGCCCAGACCT  
GAGGAGGAACGTATCACCCAGGCCGAGAAGAATAAGAGAATGCAGGAAC  
AGTTAAAGACGCTGGGAGCGGAACTTGCAGCTGCCAAGGATAAGACCCA  
GTTGACCAAGAACGACCATCTTCACAGCCAGAACGTGGCTCAGGGCCGA  
GACAAGTACAAGACCTTGAAACAGATCCGACAAGGAAACACCAAGCAGC  
GAGTAGACATGTTTCGAGGCCATG TAA-3'

- Protein sequence

MPKPVNVRVTTMDAELEFAIQPSTTGKQLFDQVVKTIGLREIWFFGLQYTDS  
KGLSTWLKLNKKVLNQDVRKETPLQFKFRAKFYPEDVSEELIQEVTQRMFFL  
QVKEGILNDEIYCPPETSVLLASYAVQAKYGDYNPDVHQSGVLHNDKLLPQR  
VLDQHKMTKEQWEERIVNWWAEHKGMLREDSMMEYLNKIAQDLEMYGVNY  
FEIKNKKGTDLWLGVDALGLNIYEKEDRLTPKIGFPWSEIRNISFNDKKFTIK  
PIDKKAPDFIFFAPRLRINKRILALCMGNHELYMRRRKPDITIEVQQMKAQAR  
EDRLAKQAERAQLQKEKQMREEAERARKELEDRIKKYENDMESHKKELEKS  
REITLDLEKKMNEAERERIELEEAQRKANELRVAAEAARQMEREERERMER  
EAAEAQAEAEARALAAEREREEEARLQEELEATRMKMETKEKELEALAKP  
APPVQNNVVAHLRETEEDEGEDRNEYESVETQRSISNYSEDYNNSTTQDNGT  
VGSDDYFERAELSIAENENLPRPEERITQAEKNKRMQEQLKTLGAELAAAK  
DKTQLTKNDHLHSQNVAAQGRDKYKTLKQIRQGNTKQRVDMFEAM\*

### A.6.5. gDNA fragment and guide RNA sequences for CRISPR-Cas9 transgenesis

The 3kb gDNA fragment including the last exon of *Pdunmm*

5'-GAGCTGGTTGCTCTGCCTTGGAAATGCCGTTGCATGTGTTTGTCT  
CTTGGAGTTTTTAATCATCTTCTGCTAATTCAAATGTTGAAGTCCTTCCAG  
AGCAGGATCTCGTATGAATCTAATCTCTGCCTTGCTACTAACGTTGTTTG  
AACCTTCCGAATGGGCCTTGTTCTTCAATGTGATCATTGGAATGTGTAT  
GTGTATGTTGGATTGTAAACTGATTCACTGCCAAGTACTAATCCTGAT  
GAATGTGTGAGATCATTGCGATGAAGGGGATTTGAAATGAATCTTGTTT  
CTCCCTTGCGTTTGACGTGTGTTTTTGACTGATGTCTCTTATTCTTGTC  
TGTTTCATGTATCTCGTCCTTGTTGTTTTTCGTGATGTATTTAAATATCTTG  
TTGCATTTCTGTTATTGATTGAGATAAGGCTGTAATTAGCAAAAACGTG  
GCATGAGAGTATTCTACATTAAGGTGTTGTGTTGTAATCTTTCAGAAGC  
AAACCAACTAGTAAAGACAGGTCGGTATCTGTTATGCATGCCGAATGAC  
TGTTTGTTTTTAAGTTTTTGATCATTTTGTTTTTTATTCTGTTTTTCATTTT  
TTTGCCCCATCAAATCCTGCCTAAATAGTTTCCTTGTCCTCAATTTTTG  
GTATTACTAAATTTCTGATTCTTGATGATGCAGATTCAAATTTATGTAG  
TTTGATATAATTCTGATTATTTTATTTTATTTCAAGCTAGACCTTGCGCT  
ATGAAATATTTCTTAACACCAAATTCTGTATTATTTATATGAATTAGATT  
ACAAGTACAACCGACAACAGTTGAACAGCATTTGAACATGAACTTCATT  
GAACACGTTTATGTTCACTTCAATGAGATTCTTGTTTCTTTCACCATAAA  
CCTATTCCTCCCCTCCCCTCAAATTGAAGCCTTCATTTGCATGAACTTGC  
AACTAATTAAGCACTTGTTGTTCTACTAATGCACTCCCTGTTGACATCGG  
TTGAACTGGAACCTGACAGGGTTCCACAGATCCAGGAATACAGGAA  
AAACCTGTGAAAATGGTATAGAAAATTCACCCATGAAAATTTGATGTTA  
ACCCATGAAAAATCGATGAAAATCCCGTGAAATTTTTCTTCTTGAAAATCT  
GTGGGAACCCTGTACGTGAATAATTTTGCTGTAATTAAAGCAGCACTAC  
CCACTTTGACACTGCAGCCACCTGTTCAACTATAAGAACTAGTTCTGTC  
ATCTCCAGTGACAATACGATGTAACAATAAGAAATATGAATCTCCCCATT  
CCCCTGTCCACAGAGGTTGCTGCAGTCGCACCACAGAAGCCTGGTTCAC  
TGATCTACGTCCTCGCATTTTGTTGGATTGACCTGCAGCCATTGAACTCTG  
TGGGCAGGGGTCTCTTTTGGTAGCCATCAATTTGAATTCATTGTAGAGA

## A. Appendix

ATAACAATTATGGAATATTTTGTGAGCTGGCATTGTGTTTTAAAGTTAAC  
TTAATATGCAGACATATGTATGGTCTGAATATACATAATAAGTATTTGTA  
TTTAATGAAAATATCTTGTTATTCTC**AGGTACGCACTGGTTCGCAAC**  
**AGTTACTTGCTGGGCCGTAGCAGCATGATGCCTCCTTCGCCCCGCAAGTG**  
**ACGACGGCTCTAACGAAGAAACCCCAATGACCATGACGACACCCAGTG**  
**AACAGCCCACAAGCGCCCCCTAGTGGAATCGCTCGCCACCGACCAACCCGT**  
**GCTGCTACCTGGTTGTAGACGGCCGCTTCAGTCTCCCAGGCTTACTGGA**  
**GGGACTTGAGATTCAAGTTCCCGACACCCGCTTAAGTGA**  
GAGACACTCTGCTTTCATTTATATATTGTAATTAGTTAACGGTTAAGGG  
GAAAATTAAGTATTTGAGTATATTACATGGCATATAAAATATTATTTCA  
GTTTTGTTTTGAAGAATGCCTTTATTTTCATGTGATATGAAAAAGCAAC  
TTCCAAGAATGTACAAAGTATATAGCTGACTCCCTGGTCTCCTGCATCTA  
ACATTATCGTTTTGCCTTTTGTATTCCCTAACTGCATTTAGAACGATACGC  
AATGTCAGTGAATGATTCACATAACTACAAAAGTGCACCAGGGAGTAAA  
ATGATTAAATATTTGCAAATTCTTGACCGCTGGCGAATGTTTGTTTCGCA  
TGCAGCAGATATTTTCTTACATGCCAAATTTTTCTGCAAAAGCTGAGCCA  
GATGCACTGCTAAATTGACTAATGCAGTGCACCTCCTATAGCTCAAGTTG  
TGCTACTATGTAGCAATGTATTAATATATAGCTATATATTATTTGAGAT  
GTGTAACCCATTGTGAATGCCAAGAGAGTCTAACAAAGTCTTTTAACTT  
ATAAGCAATTGAAAATGGAAAAAAGATAAGAAGGGTCTCTCTTTGACCT  
GCTTTGTTGCGCTCAACTGCTAATCCTAGGTAGACAGCACTCTGACAGC  
ACGCCACTGCGCACTCCTGCAGCATATTATTGCACGCTGACACCATAGTT  
ATTATTTGTAG**TTACAGCCAGCTGCTAACGATTA**AATAAGCTTGTGA  
GCGTAGTCTTGTTAATTGATATCTATTGCTAGGAATTTACATTGATTTAT  
ATTCTATTATGTATACACTTATGCATTAATTCAAATTAAGTCTACTCTATAA  
TGCTGTATCTGTACATGTATCTCATTGTATGAAACAAATCTTAAAAATT  
AGGGGAAGGAAATGGCAAGAGAATATTTTCCTATTTGACCCCAGATGTG  
ATAACTTGAAGAGTAATCTTGTTGTTATGCTTTGTATTCTGATCCAAAGT  
CTGAAATTGTGTGCACAACAAAACGATACATATTGCAAACACACAACAA  
ATCCGAGTACTTATAACTTAATCTTCCAGGACAGTGGTCTTGAGGCTTG  
CATCTACTCGCCACGCGCTTGGTACTTGCTTGCCTGAAGGCGCTGCCAC  
CGCAATCGTTCAATCATGACCTTCATGAGGAGACCCCTTCATGAGTATGG  
CTTTAATTTAAGCGTGTTCTGTTCCCTGCAGCTCTACGCTGTTTCATTTG

A.6. Identified gene sequences and the cloning information

AGTGATTTCCCTGTTCAAAAATTGTGATGTTTCATTCCAAAATGGCCTCCT  
TTGGGGTGGCCATCTTACCCATTCTTTGAGCTGGTTTGCCAGATGACG  
ATTGTTGAAGTCC-3'

**Guide RNA for *Pdunmm* transgenesis with CRISPR-Cas9 knock-in system\***

- **Cr9:** 5'-GGCGCTTGTGGGCTGTTTAC-3' (rev)
- **Cr15:** 5'-ATTCCACTAGGGGCGCTTGT-3' (rev)
- **Cr19:** 5'-GCGCTTGTGGGCTGTTCACT-3' (rev)
- **Cr26:** 5'-CTGTTCACTGGGTGTCGTCA-3' (rev)
- **Cr28:** 5'-GGTGTCGTCATGGTCATTGG-3' (rev)

\*All the guide RNAs are reverse complimentary sequences targeting the end codon of *Pdunmm*

## A.7. *P. dumerilii* immunofluorescence protocol

- Day 1 – Sample preparation

1. Wash 2x the embryos in filtered natural seawater (F-NSW).
2. Permeabilization: Protease K treatment (0.005%) in F-NSW for 37 sec.
3. Fix in ice cold (4 °C) Zamboni's fixative at room temperature.

Fixation duration	Embryonic stage
20 min	0-24 hpf
25 min	24-48 hpf
30 min	48-72 hpf
50 min	3-5 dpf
1 hr 30 min	5-14 dpf

4. Wash 5 x 10 min in PTw and store at 4 °C for up to 2 weeks.

- Day 2 – Primary antibody incubation

5. Recover the specimen from 4 °C to room temperature for 30 min.
6. Permeabilization: Protease K treatment (0.005%) in PTw.

Treatment duration	Embryonic stage
***	0-24 hpf
30 sec	24-48 hpf
40 sec	48-72 hpf
55 sec	3-5 dpf
1 min 20 sec	5-14 dpf

\*\*\* for this stage: Milli-Q H<sub>2</sub>O treatment for 15 min at room temperature.

7. Post-fixation in Zamboni's fixative at room temperature for 20 min (0-72 hpf) or 40 min (72 hpf-14 dpf).
8. Wash 5 x 10 min in PTw.
9. Blocking for 1 hr at room temperature in 5% sheep serum/PTw. Incubate the primary antibody in 2.5% sheep serum/PTw for pre-absorption.

#### A.7. *P. dumerilii* immunofluorescence protocol

10. Incubate the sample in the pre-absorbed primary antibody solution for 1 hr with agitation at room temperature, then at 4 °C with agitation for an overnight.

- Day 3 – Secondary antibody incubation

11. Wash 5 x 15 min in PTw.
12. Pre-absorb the secondary antibody in 2.5% sheep serum/PTw for 1 hr. DAPI 1:200 and Phalloidin 1:250 can be added into the secondary antibody solution if necessary.
13. Incubate the sample for 1 hr at room temperature then an overnight at 4 °C in the pre-absorbed secondary antibody in 2.5% sheep serum/PTw.

- Day 4 – Mounting and imaging

14. Wash 5 x 15 min in PTw.
15. Mount the sample in PTw and imaging or,
16. Equilibrate the sample in glycerol/PTw with the following order for 10 min each,
  - 20% glycerol/PTw
  - 40% glycerol/PTw
  - 50% glycerol/PTw
  - 70% glycerol/PTw
  - 80% glycerol with 6g/L DABCO (1,4-diazabicyclo[2.2.2]octane)
17. Store at 4 °C for imaging.

#### Reagents and solutions

Zamboni's fixative (20mL)	
Chemical	Amount
Na <sub>2</sub> HPO <sub>4</sub> 0.2M	12.74mL
NaH <sub>2</sub> PO <sub>4</sub> 0.2M	3.59mL
Picric acid 1.3%	0.545mL
PFA 16%	3.125mL



## A. Appendix

- Modified from the first published description by Stefanini et al. (1967).

10x Phosphate buffer saline (PBS, for *P. dumerilii* sample)

Chemical	Amount
NaCl	70g
Na <sub>2</sub> HPO <sub>4</sub> ·2H <sub>2</sub> O	62.4g
KH <sub>2</sub> PO <sub>4</sub>	3.4g
ddH <sub>2</sub> O	till 1L

- Titrate the solution to pH7.4.
- Sterile by autoclave.
- PTw: 1x PBS with 0.1% Tween-20.

## **A.8. Preparation of the TOP10 competent cell for electroporation**

- Day 1

1. Make the LB/streptomycin plate.
2. Take one vial of TOP10 competent cell and plate it.
3. Culture at 37°C for an overnight.

- Day 2

4. Pick one colony and grow it in 5mL LB/streptomycin broth for an overnight at 37°C with agitation.
5. Pre-cool the following instruments
  - 5.1. Pipette boy and the 10mL plastic pipette.
  - 5.2. Two 1L bottles for ultracentrifugation.
  - 5.3. Tips and pipettes.
  - 5.4. 1.5mL tubes (~100x).
  - 5.5. 2L 10% glycerol/ddH<sub>2</sub>O.
  - 5.6. 2L ddH<sub>2</sub>O.

- Day 3

6. Pre-cool the centrifuge.
7. Add 500 µL of the overnight culture (from step 4) to 1L LB/streptomycin broth (1:500).
8. Shake (160-180 rpm) for ~4 hr to reach O.D.<sub>600</sub>=0.6-1.0
9. Work in the cold room on-ice.
10. Put the broth on-ice in the cold room for 30 min, mix every 10 min to cool down the culture.
11. Collect them into the 1L bottle for ultracentrifugation.
  - 11.1. 3000 rcf, 10 min, 2°C.
  - 11.2. Discard the supernatant. Add 1L ddH<sub>2</sub>O and resuspend the pellet gently.
  - 11.3. 3000 rcf, 10 min, 2°C.

## A. Appendix

- 11.4. Discard the supernatant. Add 500mL of 10% glycerol/ddH<sub>2</sub>O and resuspend the pellet gently.
- 11.5. 3000 rcf, 10 min, 2 °C.
- 11.6. Discard the supernatant. Add 500mL 10% glycerol/ddH<sub>2</sub>O and resuspend the pellet gently.
- 11.7. 3000 rcf, 10 min, 2 °C.
- 11.8. Discard the supernatant. Add 1mL 10% glycerol/ddH<sub>2</sub>O and resuspend the pellet gently.
12. Take 10 µL of the cell-containing solution and make a 100x dilution (add 990 µL of ddH<sub>2</sub>O). Measure the O.D.600 (try to reach 3.75). Don't forget the blank is water.
13. Dilute the cell suspension to a concentration of  $2 \times 10^{10}$  to  $3 \times 10^{10}$  cell/mL (1.0 of O.D.600=approx.  $2.5 \times 10^8$  cell/mL) with ice-cold 10% glycerol/ddH<sub>2</sub>O.
  - 13.1. Note: The desired concentration is  $2.5 \times 10^{11}$  cell/mL, giving  $1 \times 10^{10}$  cells per 40 µL (one vial). This corresponds to an O.D.600 (after 100x dilution) of ~3.75. It is difficult to reach this value, but it is still important to know the concentration of cells to calculate the transformation efficiency.
14. Aliquot the competent cells into 1.5mL pre-cooled Eppendorf tubes, 40 µL each. Liquid-nitrogen flash freeze right after aliquot.
15. Store at -80 °C.
  - Day 4
16. Test the competency.
  - 16.1. Note: According to Thermo Fisher Scientific user manual, "TOP10 *E. coli* are provided at a transformation efficiency of  $1 \times 10^9$  cfu/µg supercoiled DNA and are ideal for high-efficiency cloning and plasmid propagation."

## A.9. Gene cloning

- Plasmid (vector)

### 1. Linearize plasmids with two restriction enzymes (RE).

#### 1.1. Recipe.

DNA	X $\mu$ L (1 $\mu$ g)	X $\mu$ L (2-5 $\mu$ g)	X $\mu$ L (5-10 $\mu$ g)
RE1-HF (NEB)	0.5 $\mu$ L	1 $\mu$ L	2 $\mu$ L
RE2-HF (NEB)	0.5 $\mu$ L	1 $\mu$ L	2 $\mu$ L
CutSmartBuffer (10x, NEB)	2 $\mu$ L	5 $\mu$ L	8 $\mu$ L
ddH <sub>2</sub> O	Up to 17 $\mu$ L	Up to 43 $\mu$ L	Up to 68 $\mu$ L
Total	20 $\mu$ L	50 $\mu$ L	80 $\mu$ L
Incubation time	1 hr	2 hr	4 hr

#### 1.2. Incubation temperature follows the instruction of each RE.

### 2. Dephosphorylate plasmid

#### 2.1. Recipe.

Antarctic phosphatase (NEB) (5 unit/ $\mu$ L)	1.2 $\mu$ L
Buffer (10x, NEB)	6 $\mu$ L
linearized DNA	in RE buffer or in ddH <sub>2</sub> O
ddH <sub>2</sub> O	up to 53 $\mu$ L
Total	60 $\mu$ L

#### 2.2. Incubation

## A. Appendix

5' overhang	20 min at 37 °C
Blunt end	20 min at 37 °C
3' overhang	60 min at 37 °C

### 2.3. Inactivation

Inactivate for 5 min at 70 °C.

3. Electrophoresis to separate the DNA by size and cut the linearized plasmid and purify the DNA using the Promega gel and PCR clean-up kit (Wizard SV Gel and PCR Clean-Up System, Cat. No. A9282). Elute the DNA with 30  $\mu$ L of ddH<sub>2</sub>O and measure the concentration. Store the DNA at  $-20^{\circ}\text{C}$ .

- Gene fragment (insert)

4. Amplify the gene fragment by PCR with Phusion polymerase. Note: Set the annealing temperature  $3^{\circ}\text{C}$  higher than the  $T_m$  of the primers and assume the elongation rate as 30 sec/kb for setting the PCR machine.

#### 4.1. Recipe.

Buffer HF (5X)	10 $\mu$ L
dNTPs (10mM)	1 $\mu$ L
Forward primer (10 $\mu$ M)	1 $\mu$ L
Reverse primer (10 $\mu$ M)	1 $\mu$ L
Phusion DNA polymerase	0.5 $\mu$ L
ddH <sub>2</sub> O	Till 50 $\mu$ L

#### 4.2. PCR condition

98 °C	30 sec	
98 °C	10 sec	35 cycles
T <sub>m</sub> + 3 °C	20 sec	
72 °C	30 sec/kb	
72 °C	10 min	
4 °C	—	

4.3. Gel electrophoresis with 5 µL of the PCR product to investigate if the desired fragment is shown and use the rest for purification.

## 5. Digestion of PCR fragment

### 5.1. Recipe.

DNA	1 µg
RE1-HF (NEB)	0.5 µL
RE2-HF (NEB)	0.5 µL
CutSmartBuffer (10x, NEB)	2 µL
ddH <sub>2</sub> O	Till 20 µL

### 5.2. Reaction and purification

Digest at 37 °C (or the temperature indicated for each RE) for 2-4 hr. And Purify the digested DNA with Promega gel and PCR clean-up kit and elute the product in 30 µL of ddH<sub>2</sub>O.

## 6. Phosphorylate the PCR fragment

### 6.1. Recipe.

## A. Appendix

T4 PNK (10 unit/ $\mu$ L)	1 $\mu$ L
T4 PNK buffer (10x)	7 $\mu$ L
20mM dATP	7 $\mu$ L
DNA	All from step 5
ddH <sub>2</sub> O	Till 70 $\mu$ L

### 6.2. Reaction (Use PCR machine)

Heat up the DNA and the buffer for 10 min at 70 °C (for the 5' overhang). Put them on ice and add dATP and T4 PNK enzyme. Incubate 30 min at 37 °C. Then terminate the reaction for 20 min at 65 °C.

### 6.3. Purification and storage

Purify with Promega gel and PCR clean-up kit and resuspend the product in 30  $\mu$ L ddH<sub>2</sub>O. Measure the DNA concentration and store it at  $-20^{\circ}\text{C}$ .

- Ligation of the vector and the insert

## 7. Ligation of the vector and the insert

Try molar ratio of 1:3 or 1:6 (vector:insert). Prepare one ligation sample with digested plasmid without the DNA fragment as a negative control. This will tell how much background colonies are in the system.

### 7.1. Recipe.

## A.9. Gene cloning

Reagent	2-fragment ligation	3-fragment ligation
Vector	50-100 µg	100-150 µg
Ligase buffer (10x)	1 µL	1.5 µL
dATP (20mM)	0.5 µL	0.75 µL
T4 DNA Ligase	0.5 µL	1.5 µL
Insert 1	1:3-1:6 molar ratio to vector	1:2 molar ratio to vector
Insert 2	—	1:2 molar ratio to vector
ddH <sub>2</sub> O	Till 10 µL	Till 15 µL

7.2. Incubate 1 hr at room temperature or overnight at 4 °C.

## 8. Dialysis

8.1. Put the dialysis membrane (Cat. No. VVLP04700, MilliporeSigma HVLP02500 Durapore PVDF Membrane Filter, Hydrophilic Plain White, 0.45 µm, Millipore) on the water, glassy side facing the air.

8.2. Put the ligated DNA on the membrane.

8.3. Incubate for 1 hr at room temperature.

8.4. Collect the sample in the new tubes.

## 9. Transformation

9.1. Put the TOP10 competent cells on ice. There is 40 µL in each tube.

9.2. Add ice-cold 10% glycerol and aliquot the solution into the pre-cooled tubes to reach 50 µL/transformation. (Each competent cell stock can be used for up to 10 transformations.)

9.3. Add all of the dialyzed ligation solution (10 µL, pre-cooled), place on ice for 10-30 min.

9.4. Place the LB plates to 37 °C for at least 1 hr.

9.5. Place the competent cells and ligation product in the pre-cooled cuvettes.

9.6. Electroporation.



## A. Appendix

- 9.7. Add 1mL of BL medium, then transfer it to a new tube. Incubate for 20-60 min at 37°C with agitation.
- 9.8. Spin down the cells with 5000 rpm, 2 min.
- 9.9. Discard 700 µL of the medium, and resuspend the cells.
- 9.10. Plate either 100, 200, or 10 µL.
- 9.11. Incubate for 8-20 hr at 37°C until the colonies are visible.
10. Pick the colonies and grow each of them in 5mL LB/antibiotics broth at 37°C for 16 hr.
11. Proofread the colonies with restriction enzyme digestion or by PCR.
12. Purify the plasmid from the selected colony by QIAprep Spin Miniprep Kit (Cat. No. 27106, QIAGEN) or prepare a larger culture for HiSpeed Plasmid Midi Kit (Cat. No. 12643, QIAGEN) or QIAGEN Plasmid Maxi Kit (Cat. No. 12163, QIAGEN) and store the plasmid at −20°C.

- TA cloning (Cloning of the gDNA fragments)

The PCR, transformation, and purification steps follow the protocol above. The modified procedures are described below.

1. Insert: Add dA after PCR

- 1.1. Recipe.

Purified PCR product	up to 43.8 µL
dATP (10mM)	1 µL
PCR buffer (10x, MPI-CBG)	5 µL
Taq DNA polymerase (5 unit/µL, MPI-CBG)	0.2 µL
ddH <sub>2</sub> O	Till 50 µL

- 1.2. Incubate at 72°C for 20 min, then store at −20°C.

## 2. Ligation

### 2.1. Recipe.

pCR2.1 TOPO vector	0.25 $\mu$ L
Salt (0.25x, for electroporation-based transformation)	0.25 $\mu$ L
Insert (from step 1)	1 $\mu$ L

2.2. Incubate at room temperature for 1 hr or at 4 °C for an overnight.

2.3. Add 8.5  $\mu$ L of ddH<sub>2</sub>O after ligation and use it for dialysis and transformation.

## A.10. Protein expression and purification from bacteria

- Day 1 – Transformation of the expression strain (T7 promoter with built-in pRARE plasmid)
  1. Mix 0.5-1  $\mu$ L of the expression plasmid and 100  $\mu$ L of the competent cells.
  2. Incubate on ice for 15-30 min.
  3. Heat transform the cells at 42 °C for 45 sec.
  4. Add 1mL of LB or SOC media.
  5. Incubate at 37 °C for 1 hr.
  6. Plate 1000x or 100x diluted cells on the LB plates with appropriate antibiotics.
  7. Shake for an overnight at 37 °C.
- Day 2 – Pre-culture
  8. Inoculate separately 2 or 3 colonies in 2ml of LB + Kanamycin (Km, 50  $\mu$ g/mL) + Chloramphenicol (Cm, 17  $\mu$ g/mL).
  9. Shake for an overnight at 37 °C. The pre-culture can be stored at 4 °C for 1-2 weeks.
- Day 3 – Induction of protein expression
  10. Dilute the pre-culture by 500x or 1000x in TB media + Km (90  $\mu$ g/mL) + Cm (17  $\mu$ g/mL). Shake at 37 °C until O.D.600 reaches 0.4-0.5. Usually it takes about 4 hr.
  11. Shift the culture to 18 °C and shake for another hour.
  12. Add IPTG to the final concentration of 0.2mM.
  13. Shake for an overnight at 18 °C.
- Day 4 – Protein purification (solutions are listed below)

#### *A.10. Protein expression and purification from bacteria*

14. Collect the cells by centrifugation at 5000 rpm for 5 min.
15. Resuspend the cell pellet in lysis buffer (50ml for the cells of a 1L culture), add DTT (Cat. No. 97061-338, VWR) to 1mM, 0.1% protease inhibitors cocktail (Bimek), and 0.1% benzonase (MPI-CBG, Germany).
16. Lyse cells by Emulsiflex C-5, Avestin homogenizer.
17. Ultracentrifugation of the lysate at 16000 rpm for 30 min.
18. Pre-equilibrate the HisTrap column (Cat. No. 17524801, GE Healthcare) with lysis buffer + 1mM DTT.
19. Filter supernatant through 0.45  $\mu$ m filter (Cat. No. SLHAM33SS, Sigma-Aldrich).
20. Load supernatant on HisTrap column.
21. Wash column with 10 column volumes (CV) of lysis buffer + 1mM DTT, 5 CV of high salt buffer + 1mM DTT, then 5 CV of lysis buffer + 1mM DTT.
22. Elute the sample with elution buffer.
23. Dialyze the sample against the protein buffer for an overnight.
24. Size exclusive chromatography (Cat. No. 28989335, HiLoad superdex 200 16/60, GE Healthcare) if necessary.
25. Measure the concentration and store the protein at  $-80^{\circ}\text{C}$ .
  - Lysis buffer: 2x PBS, 20 mM imidazole (Cat. No. 97064-890, VWR)
  - High salt buffer: 6x PBS
  - Elution buffer: 2x PBS, 250 mM imidazole
  - Protein buffer: 20mM Hepes (Cat. No. 97061-822, VWR), pH7.5, 150mM KCl



Part VI.

Bibliography



# Bibliography

- Abe, M., & Kuroda, R. (2019). The development of CRISPR for a mollusc establishes the formin *Lsdia1* as the long-sought gene for snail dextral/sinistral coiling. *Development*, *146*(9), dev175976.
- Ackermann, C., Dorresteyn, A., & Fischer, A. (2005). Clonal domains in postlarval *Platynereis dumerilii* (Annelida: Polychaeta). *Journal of Morphology*, *266*(3), 258–280.
- Adoutte, A., Balavoine, G., Lartillot, N., & de Rosa, R. (1999). Animal evolution. The end of the intermediate taxa? *Trends in Genetics*, *15*(3), 104–108.
- Aguinaldo, A. M. A., Turbeville, J. M., Linford, L. S., Rivera, M. C., Garey, J. R., Raff, R. A., & Lake, J. A. (1997). Evidence for a clade of nematodes, arthropods and other moulting animals. *Nature*, *387*(6632), 489–493.
- Alvarado, J., Sheinman, M., Sharma, A., MacKintosh, F. C., & Koenderink, G. H. (2013). Molecular motors robustly drive active gels to a critically connected state. *Nature Physics*, *9*(9), 591–597.
- Amat, F., Höckendorf, B., Wan, Y., Lemon, W. C., McDole, K., & Keller, P. J. (2015). Efficient processing and analysis of large-scale light-sheet microscopy data. *Nature Protocols*, *10*(11), 1679–1696.
- Amat, F., Lemon, W., Mossing, D. P., McDole, K., Wan, Y., Branson, K., ... Keller, P. J. (2014). Fast, accurate reconstruction of cell lineages from large-scale fluorescence microscopy data. *Nature Methods*, *11*(9), 951–958.
- Andreatta, G., Broyart, C., Borghgraef, C., Vadiwala, K., Kozin, V., Polo, A., ... Raible, F. (2019). Corazonin signaling integrates energy homeostasis and lunar phase to regulate aspects of growth and sexual maturation in *Platynereis*. *Proceedings of the National Academy of Sciences of the United States of America*, *8*, 201910262.
- Arata, Y., Lee, J. Y., Goldstein, B., & Sawa, H. (2000). Extracellular control of PAR protein localization during asymmetric cell division in the *C. elegans* embryo. *Development*, *137*(19), 3337–3345.



## BIBLIOGRAPHY

- Arboleda, E., Zurl, M., Waldherr, M., & Tessmar-Raible, K. (2019). Differential impacts of the head on *Platynereis dumerilii* peripheral circadian rhythms. *Frontiers in Physiology*, *10*, 900.
- Arendt, D., Tessmar, K., de Campos-Baptista, M. M., Dorresteyn, A., & Wittbrodt, J. (2002). Development of pigment-cup eyes in the polychaete *Platynereis dumerilii* and evolutionary conservation of larval eyes in Bilateria. *Development*, *129*(5), 1143–1154.
- Arendt, D., Tessmar-Raible, K., Snyman, H., Dorresteyn, A. W., & Wittbrodt, J. (2004). Ciliary photoreceptors with a vertebrate-type opsin in an invertebrate brain. *Science*, *306*(5697), 869–871.
- Arthur, W. (2002). The emerging conceptual framework of evolutionary developmental biology. *Nature*, *415*(6873), 757–764.
- Autenrieth, T. J., Frank, S. C., & Greiner, A. M. (2016). Actomyosin contractility and RhoGTPases affect cell-polarity and directional migration during haptotaxis. *Integrative Biology*, *8*(10), 1067–1078.
- Ayers, T., Tsukamoto, H., Gühmann, M., Veedin R, V. B., & Tessmar-Raible, K. (2018). A Go-type opsin mediates the shadow reflex in the annelid *Platynereis dumerilii*. *BMC Biology*, *16*(1), 41–49.
- Backfisch, B., Kozin, V. V., Kirchmaier, S., Tessmar-Raible, K., & Raible, F. (2014). Tools for gene-regulatory analyses in the marine annelid *Platynereis dumerilii*. *PloS One*, *9*(4), e93076.
- Backfisch, B., Rajan, V. B. V., Fischer, R. M., Lohs, C., Arboleda, E., Tessmar-Raible, K., & Raible, F. (2013). Stable transgenesis in the marine annelid *Platynereis dumerilii* sheds new light on photoreceptor evolution. *Proceedings of the National Academy of Sciences*, *110*(1), 193–198.
- Bannister, S., Antonova, O., Polo, A., Lohs, C., Hallay, N., Valinciute, A., ... Tessmar-Raible, K. (2014). TALENs mediate efficient and heritable mutation of endogenous genes in the marine annelid *Platynereis dumerilii*. *Genetics*, *197*(1), 77–89.
- Bartolini, F., & Gundersen, G. G. (2010). Formins and microtubules. *Biochimica et Biophysica Acta*, *1803*(2), 164–173.
- Bayraktar, J., Zygmunt, D., & Carthew, R. W. (2006). Par-1 kinase establishes cell polarity and functions in Notch signaling in the *Drosophila* embryo. *Journal of Cell Science*, *119*(Pt 4), 711–721.

- Beach, J. R., Shao, L., Remmert, K., Li, D., Betzig, E., & Hammer III, J. A. (2014). Nonmuscle Myosin II Isoforms Coassemble in Living Cells. *Current Biology*, *24*(10), 1160–1166.
- Beausang, J. F., Schroeder, H. W., Nelson, P. C., & Goldman, Y. E. (2008). Twirling of actin by myosins II and V observed via polarized TIRF in a modified gliding assay. *Biophysical Journal*, *95*(12), 5820–5831.
- Bement, W. M., Leda, M., Moe, A. M., Kita, A. M., Larson, M. E., Golding, A. E., ... von Dassow, G. (2015). Activator-inhibitor coupling between Rho signalling and actin assembly makes the cell cortex an excitable medium. *Nature Cell Biology*, *17*(11), 1471–1483.
- Billington, N., Beach, J. R., Heissler, S. M., Remmert, K., Guzik-Lendrum, S., Nagy, A., ... Sellers, J. R. (2015). Myosin 18A coassembles with nonmuscle myosin 2 to form mixed bipolar filaments. *Current Biology*, *25*(7), 942–948.
- Biro, M., Romeo, Y., Kroschwald, S., Bovellan, M., Boden, A., Tcherkezian, J., ... Paluch, E. K. (2013). Cell cortex composition and homeostasis resolved by integrating proteomics and quantitative imaging. *Cytoskeleton*, *70*(11), 741–754.
- Blajeski, A. L., Phan, V. A., Kottke, T. J., & Kaufmann, S. H. (2002). G(1) and G(2) cell-cycle arrest following microtubule depolymerization in human breast cancer cells. *The Journal of Clinical Investigation*, *110*(1), 91–99.
- Bönisch, C., Temme, C., Moritz, B., & Wahle, E. (2007). Degradation of hsp70 and other mRNAs in *Drosophila* via the 5' 3' pathway and its regulation by heat shock. *Journal of Biological Chemistry*, *282*(30), 21818–21828.
- Boyer, B. C., & Jonathan, Q. H. (1998). Evolutionary modifications of the spiralian developmental program. *Integrative and Comparative Biology*, *38*(4), 621–633.
- Brun-Usan, M., Marín-Riera, M., Grande, C., Truchado-Garcia, M., & Salazar-Ciudad, I. (2017). A set of simple cell processes is sufficient to model spiral cleavage. *Development*, *144*(1), 54–62.
- Campanale, J. P., Sun, T. Y., & Montell, D. J. (2017). Development and dynamics of cell polarity at a glance. *Journal of Cell Science*, *130*(7), 1201–1207.
- Carvalho, K., Tsai, F. C., Lees, E., Voituriez, R., Koenderink, G. H., & Sykes, C. (2013). Cell-sized liposomes reveal how actomyosin cortical tension drives shape change. *Proceedings of the National Academy of Sciences*, *110*(41), 16456–16461.
- Cheffings, T. H., Burroughs, N. J., & Balasubramanian, M. K. (2016). Actomyosin ring formation and tension generation in eukaryotic cytokinesis. *Current Biology*, *26*(15), R719–R737.

## BIBLIOGRAPHY

- Chen, G., Hou, Z., Gulbranson, D. R., & Thomson, J. A. (2010). Actin-myosin contractility is responsible for the reduced viability of dissociated human embryonic stem cells. *Cell Stem Cell*, 7(2), 240–248.
- Chhetri, R. K., Amat, F., Wan, Y., Höckendorf, B., Lemon, W. C., & Keller, P. J. (2015). Whole-animal functional and developmental imaging with isotropic spatial resolution. *Nature Methods*, 12(12), 1171–1178.
- Child, C. M. (1900). The early development of Arenicola and Sternaspis. *Archiv für Entwicklungsmechanik der Organismen*, 9(4), 587–723.
- Chou, H. C., Acevedo-Luna, N., Kuhlman, J. A., & Schneider, S. Q. (2018). PdmBase: A transcriptome database and research tool for *Platynereis dumerilii* and early development of other metazoans. *BMC Genomics*, 19(1), 618–11.
- Chou, H. C., Pruitt, M. M., Bastin, B. R., & Schneider, S. Q. (2016). A transcriptional blueprint for a spiral-cleaving embryo. *BMC Genomics*, 17(1), 552.
- Chugh, P., & Paluch, E. K. (2018). The actin cortex at a glance. *Journal of Cell Science*, 131(14), jcs186254.
- Chun, J. T., Vasilev, F., Limatola, N., & Santella, L. (2018). Fertilization in starfish and sea urchin: Roles of actin. *Results and Problems in Cell Differentiation*, 65(Suppl 1).
- Coluccio, L. M. (2007). *Myosins* (Vol. 7). Springer Science & Business Media.
- Combs, C. A. (2010). Fluorescence microscopy: A concise guide to current imaging methods. *Current Protocols in Neuroscience*, Chapter 2(1), Unit2.1–Unit2.1.14.
- Conklin, E. G. (1897). The embryology of crepidula, a contribution to the cell lineage and early development of some marine gasteropods. *Journal of Morphology*, 13(1), 1–226.
- Conrad, G. W., Schantz, A. R., & Patron, R. R. (1990). Mechanisms of Polar Lobe Formation in Fertilized Eggs of Molluscs *Crepidula fornicata*. *Annals of the New York Academy of Sciences*, 582(1), 273–294.
- Conzelmann, M., Williams, E. A., Krug, K., Franz-Wachtel, M., Macek, B., & Jékely, G. (2013). The neuropeptide complement of the marine annelid *Platynereis dumerilii*. *BMC Genomics*, 14(1), 906–915.
- Costello, D. P. (1945). Experimental studies of germinal localization in nereis. I. The development of isolated blastomeres. *Journal of Experimental Zoology*, 100(1), 19–66.

- Costello, D. P., & Henley, C. (1976). Spiralian development: A perspective. *American Zoologist*, 16, 277–291.
- Coué, M., Brenner, S. L., Spector, I., & Korn, E. D. (1987). Inhibition of actin polymerization by latrunculin A. *FEBS Letters*, 213(2), 316–318.
- Cowan, C. R., & Hyman, A. A. (2007). Acto-myosin reorganization and PAR polarity in *C. elegans*. *Development*, 134(6), 1035–1043.
- Craig, R., & Woodhead, J. L. (2006). Structure and function of myosin filaments. *Current Opinion in Structural Biology*, 16(2), 204–212.
- D’Avino, P. P. (2009). How to scaffold the contractile ring for a safe cytokinesis – lessons from Anillin-related proteins. *Journal of Cell Science*, 122(Pt 8), 1071–1079.
- Davison, A., McDowell, G. S., Holden, J. M., Johnson, H. F., Koutsovoulos, G. D., Liu, M. M., ... Blaxter, M. L. (2016). Formin is associated with left-right asymmetry in the pond snail and the frog. *Current Biology*, 26(5), 654–660.
- Dekraker, C., Boucher, E., & Mandato, C. A. (2018). Regulation and assembly of actomyosin contractile rings in cytokinesis and cell repair. *Anatomical Record*, 301(12), 2051–2066.
- Demilly, A., Steinmetz, P., Gazave, E., Marchand, L., & Vervoort, M. (2013). Involvement of the Wnt/ $\beta$ -catenin pathway in neurectoderm architecture in *Platynereis dumerilii*. *Nature Communications*, 4(1), 1915.
- Denes, A. S., Jékely, G., Steinmetz, P. R. H., Raible, F., Snyman, H., Prud’homme, B., ... Arendt, D. (2007). Molecular architecture of annelid nerve cord supports common origin of nervous system centralization in bilateria. *Cell*, 129(2), 277–288.
- de Rosa, R., Prud’homme, B., & Balavoine, G. (2005). Caudal and even-skipped in the annelid *Platynereis dumerilii* and the ancestry of posterior growth. *Evolution & Development*, 7(6), 574–587.
- Dill, K. K., Thamm, K., & Seaver, E. C. (2007). Characterization of twist and snail gene expression during mesoderm and nervous system development in the polychaete annelid *Capitella* sp. I. *Development Genes and Evolution*, 217(6), 435–447.
- Doe, C. Q., & Bowerman, B. (2001). Asymmetric cell division: Fly neuroblast meets worm zygote. *Current Opinion in Cell Biology*, 13(1), 68–75.
- Dorresteyn, A. W. C., O’Grady, B., Fischer, A., Porchet-Henneré, E., & Boilly-Marer, Y. (1993). Molecular specification of cell lines in the embryo of *Platynereis* (Annelida). *Roux’s Archives of Developmental Biology: The Official Organ of the EDBO*, 202(5), 260–269.

## BIBLIOGRAPHY

- Dorresteijs, A. W. C., & Westheide, W. (2013). *Reproductive strategies and developmental patterns in annelids*. Springer Science & Business Media.
- Dray, N., Tessmar-Raible, K., Le Gouar, M., Vibert, L., Christodoulou, F., Schipany, K., ... Balavoine, G. (2010). Hedgehog signaling regulates segment formation in the annelid *Platynereis*. *Science*, *329*(5989), 339–342.
- DuBuc, T. Q., Dattoli, A. A., Babonis, L. S., Salinas-Saavedra, M., Röttinger, E., Martindale, M. Q., & Postma, M. (2014). In vivo imaging of *Nematostella vectensis* embryogenesis and late development using fluorescent probes. *BMC Cell Biology*, *15*(1), 44.
- Dunn, C. W., Hejnol, A., Matus, D. Q., Pang, K., Browne, W. E., Smith, S. A., ... Giribet, G. (2008). Broad phylogenomic sampling improves resolution of the animal tree of life. *Nature*, *452*(7188), 745–749.
- Egger, M. D., & Petrăn, M. (1967). New reflected-light microscope for viewing unstained brain and ganglion cells. *Science*, *157*(3786), 305–307.
- Ennomani, H., Letort, G., Guérin, C., Martiel, J. L., Cao, W., Nédélec, F., ... Blanchoin, L. (2016). Architecture and connectivity govern actin network contractility. *Current Biology*, *26*(5), 616–626.
- Ettinger, A., & Wittmann, T. (2014). Fluorescence live cell imaging. *Methods in Cell Biology*, *123*, 77–94.
- Evangelista, M., Zigmond, S., & Boone, C. (2003). Formins: Signaling effectors for assembly and polarization of actin filaments. *Journal of Cell Science*, *116*(Pt 13), 2603–2611.
- Even-Ram, S., Doyle, A. D., Conti, M. A., Matsumoto, K., Adelstein, R. S., & Yamada, K. M. (2007). Myosin IIA regulates cell motility and actomyosin–microtubule crosstalk. *Nature Cell Biology*, *9*(3), 299–309.
- Fededa, J. P., & Gerlich, D. W. (2012). Molecular control of animal cell cytokinesis. *Nature Cell Biology*, *14*(5), 440–447.
- Fehon, R. G., McClatchey, A. I., & Bretscher, A. (2010). Organizing the cell cortex: The role of ERM proteins. *Nature Reviews Molecular Cell Biology*, *11*(4), 276–287.
- Fischer, A., & Dorresteijs, A. (2004). The polychaete *Platynereis dumerilii* (Annelida): A laboratory animal with spiralian cleavage, lifelong segment proliferation and a mixed benthic/pelagic life cycle. *BioEssays: News and Reviews in Molecular, Cellular and Developmental Biology*, *26*(3), 314–325.

## BIBLIOGRAPHY

- Fischer, A. H., Henrich, T., & Arendt, D. (2010). The normal development of *Platynereis dumerilii* (Nereididae, Annelida). *Frontiers in Zoology*, 7(1), 31–39.
- Fraschini, R. (2017). Factors that control mitotic spindle dynamics. *Advances in Experimental Medicine and Biology*, 925(4), 89–101.
- Freeman, G., & Lundelius, J. W. (1982). The developmental genetics of dextrality and sinistrality in the gastropod *Lymnaea peregra*. *Wilhelm Roux's Archives of Developmental Biology*, 191(2), 69–83.
- Freeman, G., & Lundelius, J. W. (1992). Evolutionary implications of the mode of D quadrant specification in coelomates with spiral cleavage. *Journal of Evolutionary Biology*, 5(2), 205–247.
- Gallaud, E., Pham, T., & Cabernard, C. (2017). *Drosophila melanogaster* neuroblasts: A model for asymmetric stem cell divisions. *Results and Problems in Cell Differentiation*, 61(1489), 183–210.
- Galli, M., & van den Heuvel, S. (2008). Determination of the cleavage plane in early *C. elegans* embryos. *Annual Review of Genetics*, 42(1), 389–411.
- Gazave, E., Béhague, J., Laplane, L., Guillou, A., Préau, L., Demilly, A., . . . Vervoort, M. (2013). Posterior elongation in the annelid *Platynereis dumerilii* involves stem cells molecularly related to primordial germ cells. *Developmental Biology*, 382(1), 246–267.
- Gilbert, S. F. (2000). *An introduction to early developmental processes*. Sinauer Associates.
- Girouard, M., Pool, M., Alchini, R., Rambaldi, I., & Fournier, A. E. (2016). RhoA proteolysis regulates the actin cytoskeleton in response to oxidative stress. *PloS One*, 11(12), e0168641.
- Girstmair, J., & Telford, M. J. (2019). Reinvestigating the early embryogenesis in the flatworm *Maritigrella crozieri* highlights the unique spiral cleavage program found in polyclad flatworms. *EvoDevo*, 10(1), 12.
- Goldstein, B. (1995). Cell contacts orient some cell division axes in the *Caenorhabditis elegans* embryo. *The Journal of Cell Biology*, 129(4), 1071–1080.
- Goode, B. L., & Eck, M. J. (2007). Mechanism and function of formins in the control of actin assembly. *Annual Review of Biochemistry*, 76(1), 593–627.
- Gorfinkiel, N., Sánchez, L., & Guerrero, I. (1999). *Drosophila terminalia* as an appendage-like structure. *Mechanisms of Development*, 86(1-2), 113–123.



## BIBLIOGRAPHY

- Gotta, M., & Ahringer, J. (2001). Axis determination in *C. elegans*: Initiating and transducing polarity. *Current Opinion in Genetics & Development*, 11(4), 367–373.
- Goulding, M. Q. (2009). Cell lineage of the *Ilyanassa* embryo: Evolutionary acceleration of regional differentiation during early development. *PloS One*, 4(5), e5506.
- Goulding, M. Q., & Lambert, J. D. (2016). Mollusc models I. The snail *Ilyanassa*. *Current Opinion in Genetics & Development*, 39, 168–174.
- Grande, C., & Patel, N. H. (2009). Nodal signalling is involved in left-right asymmetry in snails. *Nature*, 457(7232), 1007–1011.
- Green, S., & Batterman, R. (2017). Biology meets physics: Reductionism and multi-scale modeling of morphogenesis. *Studies in History and Philosophy of Science Part C: Studies in History and Philosophy of Biological and Biomedical Sciences*, 61, 20–34.
- Grimmel, J., Dorresteyn, A. W. C., & Fröbuis, A. C. (2016). Formation of body appendages during caudal regeneration in *Platynereis dumerilii*: Adaptation of conserved molecular toolsets. *EvoDevo*, 7(1), 10–14.
- Guralnick, R. P., & Lindberg, D. R. (2001). Reconnecting cell and animal lineages: What do cell lineages tell us about the evolution and development of Spiralia? *Evolution*, 55(8), 1501–1519.
- Häcker, U., Kaufmann, E., Hartmann, C., Jürgens, G., Knochel, W., & Jäckle, H. (1995). The *Drosophila* fork head domain protein crocodile is required for the establishment of head structures. *The EMBO Journal*, 14(21), 5306–5317.
- Hahn, W. (1998). *Symmetry as a developmental principle in nature and art*. World Scientific.
- Halanych, K. M., Bacheller, J. D., Aguinaldo, A. M., Liva, S. M., Hillis, D. M., & Lake, J. A. (1995). Evidence from 18S ribosomal DNA that the lophophorates are protostome animals. *Science*, 267(5204), 1641–1643.
- Hall, A. (1998). Rho GTPases and the actin cytoskeleton. *Science*, 279(5350), 509–514.
- Handberg-Thorsager, M., Gutierrez-Mazariegos, J., Arold, S. T., Nadendla, E. K., Bertucci, P. Y., Germain, P., ... Schubert, M. (2018). The ancestral retinoic acid receptor was a low-affinity sensor triggering neuronal differentiation. *Science Advances*, 4(2), eaao1261.

## BIBLIOGRAPHY

- Handberg-Thorsager, M., Ulman, V., Tomançak, P., Arendt, D., & Schubert, M. (2019). A behavioral assay to study effects of retinoid pharmacology on nervous system development in a marine annelid. *Methods in Molecular Biology*, 2019(Chapter 14), 193–207.
- Hauenschild, C., & Fischer, A. (1969). *Platynereis dumerilii: Mikroskopische Anatomie, Fortpflanzung, Entwicklung* (Vol. 10b). Grosses Zoologisches Praktikum.
- Hejnol, A. (2010). A twist in time – the evolution of spiral cleavage in the light of animal phylogeny. *Integrative and Comparative Biology*, 50(5), 695–706.
- Henry, J. Q., Hejnol, A., , Perry, K. J., & Martindale, M. Q. (2007). Homology of ciliary bands in spiralian trochophores. *Integrative and Comparative Biology*, 47(6), 865–871.
- Henry, J. Q., & Jonathan, Q. (2015). Spiralian model systems. *The International Journal of Developmental Biology*, 58(6-7-8), 389–401.
- Henry, J. Q., & Martindale, M. Q. (1987). The organizing role of the D quadrant as revealed through the phenomenon of twinning in the polychaete *Chaetopterus variopedatus*. *Roux's Archives of Developmental Biology: The Official Organ of the EDBO*, 196(8), 499–510.
- Henry, J. Q., & Martindale, M. Q. (1999). Conservation and innovation in spiralian development. *Hydrobiologia*, 402(0), 255–265.
- Henry, J. Q., & Perry, K. J. (2008). MAPK activation and the specification of the D quadrant in the gastropod mollusc, *Crepidula fornicata*. *Developmental Biology*, 313(1), 181–195.
- Henry, J. Q., Perry, K. J., & Martindale, M. Q. (2006). Cell specification and the role of the polar lobe in the gastropod mollusc *Crepidula fornicata*. *Developmental Biology*, 297(2), 295–307.
- Hernandez, O. M., Jones, M., Guzman, G., & Szczesna-Cordary, D. (2007). Myosin essential light chain in health and disease. *American Journal of Physiology. Heart and Circulatory Physiology*, 292(4), H1643–H1654.
- Hertzler, P. L., & Clark, W. H. (1992). Cleavage and gastrulation in the shrimp *Sicyonia ingentis*: Invagination is accompanied by oriented cell division. *Development*, 116(1), 127–140.
- Hetrick, B., Han, M. S., Helgeson, L. A., & Nolen, B. J. (2013). Small molecules CK-666 and CK-869 inhibit actin-related protein 2/3 complex by blocking an activating conformational change. *Chemistry & Biology*, 20(5), 701–712.



## BIBLIOGRAPHY

- Hoege, C., & Hyman, A. A. (2013). Principles of PAR polarity in *Caenorhabditis elegans* embryos. *Nature Reviews Molecular Cell Biology*, 14(5), 315–322.
- Hofmann, D. K. (1975). Prostomial regeneration in the polychaete *Platynereis dumerilii* (Audouin et Milne-Edwards) (Annelida). *Wilhelm Roux's Archives of Developmental Biology*, 177(4), 309–322.
- Holmes, K. C. (2008). Myosin structure. In *Myosins* (pp. 35–54). Springer, Dordrecht.
- Homem, C. C. F., & Knoblich, J. A. (2012). *Drosophila* neuroblasts: A model for stem cell biology. *Development*, 139(23), 4297–4310.
- Howard, J., & Garzon-Coral, C. (2017). Physical limits on the precision of mitotic spindle positioning by microtubule pushing forces: Mechanics of mitotic spindle positioning. *BioEssays: News and Reviews in Molecular, Cellular and Developmental Biology*, 39(11), 1700122.
- Hu, J., Cheng, S., Wang, H., Li, X., Liu, S., Wu, M., . . . Wang, X. (2019). Distinct roles of two myosins in *C. elegans* spermatid differentiation. *PLOS Biology*, 17(4), e3000211.
- Hudson, C., Kawai, N., Negishi, T., & Yasuo, H. (2013).  $\beta$ -catenin-driven binary fate specification segregates germ layers in ascidian embryos. *Current Biology*, 23(6), 491–495.
- Huisken, J., Swoger, J., Del Bene, F., Wittbrodt, J., & Stelzer, E. H. K. (2004). Optical sectioning deep inside live embryos by selective plane illumination microscopy. *Science*, 305(5686), 1007–1009.
- Hutterer, A., Betschinger, J., Petronczki, M., & Knoblich, J. A. (2004). Sequential roles of Cdc42, Par-6, aPKC, and Lgl in the establishment of epithelial polarity during *Drosophila* embryogenesis. *Developmental Cell*, 6(6), 845–854.
- Icha, J., Weber, M., Waters, J. C., & Norden, C. (2017). Phototoxicity in live fluorescence microscopy, and how to avoid it. *BioEssays: News and Reviews in Molecular, Cellular and Developmental Biology*, 39(8), 1700003.
- Iglesias, M., Gomez-Skarmeta, J. L., Saló, E., & Adell, T. (2008). Silencing of *Smed- $\beta$ catenin1* generates radial-like hypercephalized planarians. *Development*, 135(7), 1215–1221.
- Imai, K. S., Hino, K., Yagi, K., Satoh, N., & Satou, Y. (2004). Gene expression profiles of transcription factors and signaling molecules in the ascidian embryo: Towards a comprehensive understanding of gene networks. *Development*, 131(16), 4047–4058.

- Imai, K. S., Takada, N., Satoh, N., & Satou, Y. (2000). (beta)-catenin mediates the specification of endoderm cells in ascidian embryos. *Development*, 127(14), 3009–3020.
- Inaki, M., Liu, J., & Matsuno, K. (2016). Cell chirality: Its origin and roles in left-right asymmetric development. *Philosophical Transactions of the Royal Society of London. Series B, Biological Sciences*, 371(1710), 20150403.
- Inaki, M., Sasamura, T., & Matsuno, K. (2018). Cell chirality drives left-right asymmetric morphogenesis. *Frontiers in Cell and Developmental Biology*, 6, 34.
- Ishizaki, T., Uehata, M., Tamechika, I., Keel, J., Nonomura, K., Maekawa, M., & Narumiya, S. (2000). Pharmacological properties of Y-27632, a specific inhibitor of Rho-associated kinases. *Molecular Pharmacology*, 57(5), 976–983.
- Isogai, T., van der Kammen, R., & Innocenti, M. (2015). SMIFH2 has effects on Formins and p53 that perturb the cell cytoskeleton. *Scientific Reports*, 5(1), 1–15.
- Iwase, K., Tanaka, M., Hirose, K., Uyeda, T. Q. P., & Honda, H. (2017). Acceleration of the sliding movement of actin filaments with the use of a non-motile mutant myosin in in vitro motility assays driven by skeletal muscle heavy meromyosin. *PloS One*, 12(7), e0181171.
- Jacobsohn, S. (1999). Characterization of novel F-actin envelopes surrounding nuclei during cleavage of a polychaete worm. *The International Journal of Developmental Biology*, 43(1), 19–26.
- Janssen, A. F. J., Tas, R. P., van Bergeijk, P., Oost, R., Hoogenraad, C. C., & Kapitein, L. C. (2017). Myosin-V induces cargo immobilization and clustering at the axon initial segment. *Frontiers in Cellular Neuroscience*, 11, 260.
- Jeffery, W. R. (1992). Axis determination in sea urchin embryos: From confusion to evolution. *Trends in Genetics*, 8(7), 223–225.
- Jékely, G., & Arendt, D. (2007). *Cellular resolution expression profiling using confocal detection of NBT/BCIP precipitate by reflection microscopy* (Tech. Rep.). Developmental Biology Unit, European Molecular Biology Laboratory, Heidelberg, Germany. jekely@embl.de.
- Joo, E. E., & Yamada, K. M. (2016). Post-polymerization crosstalk between the actin cytoskeleton and microtubule network. *BioArchitecture*, 6(3), 53–59.
- Jossin, Y., Lee, M., Klezovitch, O., Kon, E., Cossard, A., Lien, W. H., ... Vasioukhin, V. (2017). Llg1 connects cell polarity with cell-cell adhesion in embryonic neural stem cells. *Developmental Cell*, 41(5), 481–495.e5.

## BIBLIOGRAPHY

- Kamijo, K., Ohara, N., Abe, M., Uchimura, T., Hosoya, H., Lee, J. S., & Miki, T. (2006). Dissecting the role of Rho-mediated signaling in contractile ring formation. *Molecular Biology of the Cell*, 17(1), 43–55.
- Kasioulis, I., & Storey, K. G. (2018). Cell biological mechanisms regulating chick neurogenesis. *The International Journal of Developmental Biology*, 62(1-2-3), 167–175.
- Kasza, K. E., & Zallen, J. A. (2011). Dynamics and regulation of contractile actin-myosin networks in morphogenesis. *Current Opinion in Cell Biology*, 23(1), 30–38.
- Kato, T., Watanabe, N., Morishima, Y., Fujita, A., Ishizaki, T., & Narumiya, S. (2001). Localization of a mammalian homolog of diaphanous, mDia1, to the mitotic spindle in HeLa cells. *Journal of Cell Science*, 114(Pt 4), 775–784.
- Keller, P. J., Pampaloni, F., Lattanzi, G., & Stelzer, E. H. K. (2008). Three-dimensional microtubule behavior in *Xenopus* egg extracts reveals four dynamic states and state-dependent elastic properties. *Biophysical Journal*, 95(3), 1474–1486.
- Keller, P. J., Schmidt, A. D., Wittbrodt, J., & Stelzer, E. H. K. (2008). Reconstruction of zebrafish early embryonic development by scanned light sheet microscopy. *Science*, 322(5904), 1065–1069.
- Keller, P. J., Schmidt, A. D., Wittbrodt, J., & Stelzer, E. H. K. (2011). Digital scanned laser light-sheet fluorescence microscopy (DSLM) of zebrafish and *Drosophila* embryonic development. *Cold Spring Harbor Protocols*, 2011(10), 1235–1243.
- Kitamura, K., & Shimizu, T. (2000). Analyses of segment-specific expression of alkaline phosphatase activity in the mesoderm of the oligochaete annelid tubifex: implications for specification of segmental identity. *Developmental Biology*, 219(2), 214–223.
- Kitanishi-Yumura, T., & Fukui, Y. (1989). Actomyosin organization during cytokinesis: Reversible translocation and differential redistribution in *Dictyostelium*. *Cell motility and the cytoskeleton*, 12(2), 78–89.
- Kline-Smith, S. L., & Walczak, C. E. (2004). Mitotic spindle assembly and chromosome segregation: Refocusing on microtubule dynamics. *Molecular Cell*, 15(3), 317–327.
- Koop, D., Richards, G. S., Wanninger, A., Gunter, H. M., & Degnan, B. M. (2007). The role of MAPK signaling in patterning and establishing axial symmetry in the gastropod *Haliotis asinina*. *Developmental Biology*, 311(1), 200–212.

- Krendel, M., Gloushankova, N. A., Bonder, E. M., Feder, H. H., Vasiliev, J. M., & Gelfand, I. M. (1999). Myosin-dependent contractile activity of the actin cytoskeleton modulates the spatial organization of cell-cell contacts in cultured epitheliocytes. *Proceedings of the National Academy of Sciences*, 96(17), 9666–9670.
- Kron, S. J., & Spudich, J. A. (1986). Fluorescent actin filaments move on myosin fixed to a glass surface. *Proceedings of the National Academy of Sciences*, 83(17), 6272–6276.
- Kuroda, R. (2014). How a single gene twists a snail. *Integrative and Comparative Biology*, 54(4), 677–687.
- Kuroda, R. (2015). A twisting story: How a single gene twists a snail? Mechanogenetics. *Quarterly Reviews of Biophysics*, 48(4), 445–452.
- Kuroda, R., Endo, B., Abe, M., & Shimizu, M. (2009). Chiral blastomere arrangement dictates zygotic left-right asymmetry pathway in snails. *Nature*, 462(7274), 790–794.
- Kuroda, R., Fujikura, K., Abe, M., Hosoiri, Y., Asakawa, S., Shimizu, M., ... Takahashi, H. (2016). Diaphanous gene mutation affects spiral cleavage and chirality in snails. *Scientific Reports*, 6(1), 34809.
- Labbé, J. C., Maddox, P. S., Salmon, E. D., & Goldstein, B. (2003). PAR proteins regulate microtubule dynamics at the cell cortex in *C. elegans*. *Current Biology*, 13(9), 707–714.
- Laissue, P. P., Alghamdi, R. A., Tomancak, P., Reynaud, E. G., & Shroff, H. (2017). Assessing phototoxicity in live fluorescence imaging. *Nature Methods*, 14(7), 657–661.
- Lambert, J. D. (2008). Mesoderm in spiralian: The organizer and the 4d cell. *Journal of Experimental Zoology. Part B, Molecular and Developmental Evolution*, 310(1), 15–23.
- Lambert, J. D. (2010). Developmental patterns in spiralian embryos. *Current Biology*, 20(2), R72–R77.
- Lambert, J. D., & Nagy, L. M. (2001). MAPK signaling by the D quadrant embryonic organizer of the mollusc *Ilyanassa obsoleta*. *Development*, 128(1), 45–56.
- Lambert, J. D., & Nagy, L. M. (2003). The MAPK cascade in equally cleaving spiralian embryos. *Developmental Biology*, 263(2), 231–241.
- Lang, C. F., & Munro, E. (2017). The PAR proteins: From molecular circuits to dynamic self-stabilizing cell polarity. *Development*, 144(19), 3405–3416.

## BIBLIOGRAPHY

- Larabell, C. A., Torres, M., Rowning, B. A., Yost, C., Miller, J. R., Wu, M., ... Moon, R. T. (1997). Establishment of the dorso-ventral axis in *Xenopus* embryos is presaged by early asymmetries in  $\beta$ -catenin that are modulated by the Wnt signaling pathway. *The Journal of Cell Biology*, 136(5), 1123–1136.
- Laumer, C. E., Bekkouche, N., Kerbl, A., Goetz, F., Neves, R. C., Sørensen, M. V., ... Worsaae, K. (2015). Spiralian phylogeny informs the evolution of microscopic lineages. *Current Biology*, 25(15), 2000–2006.
- Laumer, C. E., Fernández, R., Lemer, S., Combosch, D., Kocot, K. M., Riesgo, A., ... Giribet, G. (2019). Revisiting metazoan phylogeny with genomic sampling of all phyla. *Proceedings of the Royal Society B: Biological Sciences*, 286(1906), 20190831.
- Lauri, A., Bertucci, P., & Arendt, D. (2016). Neurotrophin, p75, and Trk signaling module in the developing nervous system of the marine annelid *Platynereis dumerilii*. *BioMed Research International*, 2016(5), 1–12.
- Lawrence, P. A., & Levine, M. (2006). Mosaic and regulative development: Two faces of one coin. *Current Biology*, 16(7), R236–R239.
- Lecuit, T., & Lenne, P. F. (2007). Cell surface mechanics and the control of cell shape, tissue patterns and morphogenesis. *Nature Reviews Molecular Cell Biology*, 8(8), 633–644.
- Levayer, R., & Lecuit, T. (2012). Biomechanical regulation of contractility: Spatial control and dynamics. *Trends in Cell Biology*, 22(2), 61–81.
- Levin, M. (2005). Left–right asymmetry in embryonic development: A comprehensive review. *Mechanisms of Development*, 122(1), 3–25.
- Li, Z., Bhat, N., Manali, D., Wang, D., Hong, N., Yi, M., ... Hong, Y. (2011). Medaka cleavage embryos are capable of generating ES-like cell cultures. *International Journal of Biological Sciences*, 7(4), 418–425.
- Lichtman, J. W., & Conchello, J. A. (2005). Fluorescence microscopy. *Nature Methods*, 2(12), 910–919.
- Lien, W. H., & Fuchs, E. (2014). Wnt some lose some: Transcriptional governance of stem cells by Wnt/ $\beta$ -catenin signaling. *Genes & Development*, 28(14), 1517–1532.
- Lillie, F. R. (1895). The embryology of the unionidae. A study in cell-lineage. *Journal of Morphology*, 10(1), 1–100.
- Lin, R., Hill, R. J., & Priess, J. R. (1998). POP-1 and anterior–posterior fate decisions in *C. elegans* embryos. *Cell*, 92(2), 229–239.

- Litschko, C., Brühmann, S., Csiszár, A., Stephan, T., Dimchev, V., Damiano-Guercio, J., ... Faix, J. (2019). Functional integrity of the contractile actin cortex is safeguarded by multiple Diaphanous-related formins. *Proceedings of the National Academy of Sciences of the United States of America*, 116(9), 3594–3603.
- Liu, Y., Hancock, M., Workman, A., Doster, A., Jones, C., & Longnecker, R. M. (2016).  $\beta$ -Catenin, a transcription factor activated by canonical Wnt signaling, is expressed in sensory neurons of calves latently infected with bovine herpesvirus 1. *Journal of Virology*, 90(6), 3148–3159.
- Logvinova, D. S., & Levitsky, D. I. (2018). Essential light chains of myosin and their role in functioning of the Myosin motor. *Biochemistry. Biokhimiia*, 83(8), 944–960.
- Lu, M. S., & Johnston, C. A. (2013). Molecular pathways regulating mitotic spindle orientation in animal cells. *Development*, 140(9), 1843–1856.
- Lukinavičius, G., Reymond, L., D’Este, E., Masharina, A., Göttfert, F., Ta, H., ... Johnsson, K. (2014). Fluorogenic probes for live-cell imaging of the cytoskeleton. *Nature Methods*, 11(7), 731–733.
- Lyons, D. C., & Henry, J. Q. (2015). Ins and outs of Spiralian gastrulation. *The International Journal of Developmental Biology*, 58(6-7-8), 413–428.
- Lyons, D. C., Perry, K. J., & Henry, J. Q. (2017). Morphogenesis along the animal-vegetal axis: Fates of primary quartet micromere daughters in the gastropod *Crepidula fornicata*. *BMC Evolutionary Biology*, 17(1), 1–13.
- Ma, Y. Z., & Taylor, E. W. (1994). The mechanism of actomyosin and microtubule-kinesin systems. In *Biomechanics of active movement and division of cells* (pp. 525–531). Springer, Berlin, Heidelberg.
- MacDonald, B. T., Tamai, K., & He, X. (2009). Wnt/ $\beta$ -catenin signaling: Components, mechanisms, and diseases. *Developmental Cell*, 17(1), 9–26.
- Maddox, A. S., & Burridge, K. (2003). RhoA is required for cortical retraction and rigidity during mitotic cell rounding. *The Journal of Cell Biology*, 160(2), 255–265.
- Maître, J., Turlier, H., Illukkumbura, R., Eismann, B., Niwayama, R., Nédélec, F., & Hiiragi, T. (2016). Asymmetric division of contractile domains couples cell positioning and fate specification. *Nature*, 536(7616), 344–348.
- Maliga, Z., Junqueira, M., Toyoda, Y., Ettinger, A., Mora-Bermúdez, F., Klemm, R. W., ... Hyman, A. A. (2013). A genomic toolkit to investigate kinesin and myosin motor function in cells. *Nature Cell Biology*, 15(3), 325–334.



## BIBLIOGRAPHY

- Mangione, M. C., & Gould, K. L. (2019). Molecular form and function of the cytokinetic ring. *Journal of Cell Science*, 132(12), jcs226928.
- Marlow, H., Tosches, M. A., Tomer, R., Steinmetz, P. R., Lauri, A., Larsson, T., & Arendt, D. (2014). Larval body patterning and apical organs are conserved in animal evolution. *BMC Biology*, 12(1), 1–17.
- Martin, B. L., & Kimelman, D. (2009). Wnt signaling and the evolution of embryonic posterior development. *Current Biology*, 19(5), R215–R219.
- Martín-Durán, J. M., Vellutini, B. C., & Hejnal, A. (2016). Embryonic chirality and the evolution of spiralian left-right asymmetries. *Philosophical Transactions of the Royal Society of London. Series B, Biological Sciences*, 371(1710), 20150411.
- Matzke, R., Jacobson, K., & Radmacher, M. (2001). Direct, high-resolution measurement of furrow stiffening during division of adherent cells. *Nature Cell Biology*, 3(6), 607–610.
- Mazet, F., Amemiya, C. T., & Shimeld, S. M. (2006). An ancient Fox gene cluster in bilaterian animals. *Current Biology*, 16(9), R314–R316.
- McCarthy, E. K., & Goldstein, B. (2006). Asymmetric spindle positioning. *Current Opinion in Cell Biology*, 18(1), 79–85.
- Melak, M., Plessner, M., & Grosse, R. (2017). Actin visualization at a glance. *Journal of Cell Science*, 130(3), 525–530.
- Merkel, J., Wollesen, T., Lieb, B., & Wanninger, A. (2012). Spiral cleavage and early embryology of a loxosomatid entoproct and the usefulness of spiralian apical cross patterns for phylogenetic inferences. *BMC Developmental Biology*, 12(1), 1–11.
- Meshcheriakov, V. N. (1978). Orientation of the cleavage spindles in pulmonate mollusks. I. The role of the form of the blastomeres in 2d cleavage spindle orientation. *Ontogenez*, 9(6), 558–566.
- Minc, N., & Piel, M. (2012). Predicting division plane position and orientation. *Trends in Cell Biology*, 22(4), 193–200.
- Morris, V. B., Dixon, K. E., & Cowan, R. (1989). *The topology of cleavage patterns with examples from embryos of Nereis, Styela and Xenopus* (Vol. 325) (No. 1225). Royal Society.
- Munjal, A., & Lecuit, T. (2014). Actomyosin networks and tissue morphogenesis. *Development*, 141(9), 1789–1793.

- Munro, E., Nance, J., & Priess, J. R. (2004). Cortical flows powered by asymmetrical contraction transport PAR proteins to establish and maintain anterior-posterior polarity in the early *C. elegans* embryo. *Developmental Cell*, 7(3), 413–424.
- Münster, S., Jain, A., Mietke, A., Pavlopoulos, A., Grill, S. W., & Tomancak, P. (2019). Attachment of the blastoderm to the vitelline envelope affects gastrulation of insects. *Nature*, 568(7752), 395–399.
- Murphy, C. T., Rock, R. S., & Spudich, J. A. (2001). A myosin II mutation uncouples ATPase activity from motility and shortens step size. *Nature Cell Biology*, 3(3), 311–315.
- Murrell, M., Oakes, P. W., Lenz, M., & Gardel, M. L. (2015). Forcing cells into shape: The mechanics of actomyosin contractility. *Nature Reviews Molecular Cell Biology*, 16(8), 486–498.
- Naganathan, S. R., Fürthauer, S., Nishikawa, M., Jülicher, F., & Grill, S. W. (2014). Active torque generation by the actomyosin cell cortex drives left-right symmetry breaking. *eLife*, 3, e04165.
- Nakama, A. B., Chou, H. C., & Schneider, S. Q. (2017). The asymmetric cell division machinery in the spiral-cleaving egg and embryo of the marine annelid *Platynereis dumerilii*. *BMC Developmental Biology*, 17(1), 16–22.
- Nakamoto, A., Nagy, L. M., & Shimizu, T. (2011). Secondary embryonic axis formation by transplantation of D quadrant micromeres in an oligochaete annelid. *Development*, 138(2), 283–290.
- Nance, J. (2005). PAR proteins and the establishment of cell polarity during *C. elegans* development. *BioEssays: News and Reviews in Molecular, Cellular and Developmental Biology*, 27(2), 126–135.
- Nance, J., & Zallen, J. A. (2011). Elaborating polarity: PAR proteins and the cytoskeleton. *Development*, 138(5), 799–809.
- Narumiya, S., Ishizaki, T., & Ufhata, M. (2000). Use and properties of ROCK-specific inhibitor Y-27632. *Methods in Enzymology*, 325, 273–284.
- Nederbragt, A. J., Lespinet, O., Van Wageningen, S., Van Loon, A. E., Adoutte, A., & Dictus, W. J. A. G. (2002). A lophotrochozoan twist gene is expressed in the ectomesoderm of the gastropod mollusk *Patella vulgata*. *Evolution & Development*, 4(5), 334–343.
- Negishi, T., & Yasuo, H. (2015). Distinct modes of mitotic spindle orientation align cells in the dorsal midline of ascidian embryos. *Developmental Biology*, 408(1), 66–78.



## BIBLIOGRAPHY

- Niwayama, R., Shinohara, K., & Kimura, A. (2011). Hydrodynamic property of the cytoplasm is sufficient to mediate cytoplasmic streaming in the *Caenorhabditis elegans* embryo. *Proceedings of the National Academy of Sciences of the United States of America*, 108(29), 11900–11905.
- Nolen, B. J., Tomasevic, N., Russell, A., Pierce, D. W., Jia, Z., McCormick, C. D., ... Pollard, T. D. (2009). Characterization of two classes of small molecule inhibitors of Arp2/3 complex. *Nature*, 460(7258), 1031–1034.
- Orsulic, S., & Peifer, M. (1996). An in vivo structure-function study of armadillo, the beta-catenin homologue, reveals both separate and overlapping regions of the protein required for cell adhesion and for wingless signaling. *The Journal of Cell Biology*, 134(5), 1283–1300.
- Özpolat, B. D., Handberg-Thorsager, M., & M, V. (2017). Cell lineage and cell cycling analyses of the 4d micromere using live imaging in the marine annelid *Platynereis dumerilii*. *eLife*, 6, e30463.
- Padrick, S. B., Doolittle, L. K., Brautigam, C. A., King, D. S., & Rosen, M. K. (2011). Arp2/3 complex is bound and activated by two WASP proteins. *Proceedings of the National Academy of Sciences of the United States of America*, 108(33), E472–E279.
- Palazzo, A. F., Cook, T. A., Alberts, A. S., & Gundersen, G. G. (2001). mDia mediates Rho-regulated formation and orientation of stable microtubules. *Nature Cell Biology*, 3(8), 723–729.
- Pantazis, P., & Supatto, W. (2014). Advances in whole-embryo imaging: A quantitative transition is underway. *Nature Reviews Molecular Cell Biology*, 15(5), 327–339.
- Parry, L., & Caron, J. B. (2019). *Canadia spinosa* and the early evolution of the annelid nervous system. *Science Advances*, 5(9), eaax5858.
- Passamanek, Y. J., Hejnol, A., & Martindale, M. Q. (2015). Mesodermal gene expression during the embryonic and larval development of the articulate brachiopod *Terebratalia transversa*. *EvoDevo*, 6(1), 1–21.
- Pease, J. C., & Tirnauer, J. S. (2011). Mitotic spindle misorientation in cancer – out of alignment and into the fire. *Journal of Cell Science*, 124(Pt 7), 1007–1016.
- Pellegrin, S., & Mellor, H. (2007). Actin stress fibres. *Journal of Cell Science*, 120(Pt 20), 3491–3499.
- Pennerstorfer, M., & Scholtz, G. (2012). Early cleavage in *Phoronis muelleri* (Phoronida) displays spiral features. *Evolution & Development*, 14(6), 484–500.

- Pérez Sánchez, C., Casas-Tintó, S., Sánchez, L., Rey-Campos, J., & Granadino, B. (2002). DmFoxF, a novel *Drosophila* fork head factor expressed in visceral mesoderm. *Mechanisms of Development*, 111(1-2), 163–166.
- Perry, K. J., & Henry, J. Q. (2015). CRISPR/Cas9-mediated genome modification in the mollusc, *Crepidula fornicata*. *Genesis*, 53(2), 237–244.
- Perry, K. J., Lyons, D. C., Garcia, M. T., Fischer, A. H. L., Helfrich, L. W., Johansson, K. B., ... Henry, J. Q. (2015). Deployment of regulatory genes during gastrulation and germ layer specification in a model spiralian mollusc *Crepidula*. *Developmental Dynamics*, 244(10), 1215–1248.
- Petersen, C. P., & Reddien, P. W. (2008). Smed- $\beta$ catenin-1 is required for anteroposterior blastema polarity in Planarian regeneration. *Science*, 319(5861), 327–330.
- Pfeifer, K., Dorresteijn, A. W. C., & Fröbuis, A. C. (2012). Activation of Hox genes during caudal regeneration of the polychaete annelid *Platynereis dumerilii*. *Development Genes and Evolution*, 222(3), 165–179.
- Pfeifer, K., Schaub, C., Domsch, K., Dorresteijn, A., & Wolfstetter, G. (2014). Maternal inheritance of twist and analysis of MAPK activation in embryos of the polychaete annelid *Platynereis dumerilii*. *PloS One*, 9(5), e96702.
- Pfeifer, K., Schaub, C., Wolfstetter, G., & Dorresteijn, A. (2013). Identification and characterization of a *twist* ortholog in the polychaete annelid *Platynereis dumerilii* reveals mesodermal expression of *Pdu-twist*. *Development Genes and Evolution*, 223(5), 319–328.
- Pfeiffer, B. D., Truman, J. W., & Rubin, G. M. (2012). Using translational enhancers to increase transgene expression in *Drosophila*. *Proceedings of the National Academy of Sciences*, 109(17), 6626–6631.
- Pierre, A., Sallé, J., Wühr, M., & Minc, N. (2016). Generic theoretical models to predict division patterns of cleaving embryos. *Developmental Cell*, 39(6), 667–682.
- Pimpale, L., Middelkoop, T. C., Mietke, A., & Grill, S. W. (2019). Cell lineage-dependent chiral actomyosin flows drive cellular rearrangements in early development. *bioRxiv*.
- Pitrone, P. G., Schindelin, J., Stuyvenberg, L., Preibisch, S., Weber, M., Eliceiri, K. W., ... Tomancak, P. (2013). OpenSPIM: An open-access light-sheet microscopy platform. *Nature Methods*, 10(7), 598–599.

## BIBLIOGRAPHY

- Pohl, C. (2011). Left-right patterning in the *C. elegans* embryo: Unique mechanisms and common principles. *Communicative & Integrative Biology*, 4(1), 34–40.
- Prehoda, K. E. (2009). Polarization of *Drosophila* neuroblasts during asymmetric division. *Cold Spring Harbor Perspectives in Biology*, 1(2), a001388–a001388.
- Preibisch, S., Amat, F., Stamatakis, E., Sarov, M., Singer, R. H., Myers, E., & Tomancak, P. (2014). Efficient Bayesian-based multiview deconvolution. *Nature Methods*, 11(6), 645–648.
- Preibisch, S., Saalfeld, S., Schindelin, J., & Tomancak, P. (2010). Software for bead-based registration of selective plane illumination microscopy data. *Nature Methods*, 7(6), 418–419.
- Prud'homme, B., de Rosa, R., Arendt, D., Julien, J., Pajaziti, R., Dorresteyn, A. W. C., ... Balavoine, G. (2003). Arthropod-like expression patterns of engrailed and wingless in the annelid *Platynereis dumerilii* suggest a role in segment formation. *Current Biology*, 13(21), 1876–1881.
- Raible, F., & Tessmar-Raible, K. (2014). *Platynereis dumerilii*. *Current Biology*, 24(15), R676–R677.
- Raman, R., Pinto, C. S., & Sonawane, M. (2018). Polarized organization of the cytoskeleton: Regulation by cell polarity proteins. *Journal of Molecular Biology*, 430(19), 3565–3584.
- Raven, C. P. (1951). On the structure of cyclopic, synophthalmic and anophthalmic embryos, obtained by the action of lithium in *Limnaea stagnalis*. *Archives Néerlandaises de Zoologie*, 8(1), 323–352.
- Rebscher, N. (2014). Establishing the germline in spiralian embryos. *The International Journal of Developmental Biology*, 58(6-8), 403–411.
- Render, J. (1989). Development of *Ilyanassa obsoleta* embryos after equal distribution of polar lobe material at first cleavage. *Developmental Biology*, 132(1), 241–250.
- Reynolds, A., & Hülsmann, N. (2008). Ernst Haeckel's discovery of *Magosphaera planula*: A vestige of metazoan origins? *History and Philosophy of the Life Sciences*, 30, 339–386.
- Riedl, J., Crevenna, A. H., Kessenbrock, K., Yu, J. H., Neukirchen, D., Bista, M., ... Wedlich-Soldner, R. (2008). Lifeact: A versatile marker to visualize F-actin. *Nature Methods*, 5(7), 605–607.
- Riedl, R. J. (1969). Gnathostomulida from America. *Science*, 163(3866), 445–452.

- Rizvi, S. A., Neidt, E. M., Cui, J., Feiger, Z., Skau, C. T., Gardel, M. L., ... Kovar, D. R. (2009). Identification and characterization of a small molecule inhibitor of Formin-mediated actin assembly. *Chemistry & Biology*, 16(11), 1158–1168.
- Robinson, R. C., Turbedsky, K., Kaiser, D. A., Marchand, J. B., Higgs, H. N., Choe, S., & Pollard, T. D. (2001). Crystal structure of Arp2/3 complex. *Science*, 294(5547), 1679–1684.
- Rocheleau, C. E., Yasuda, J., Shin, T. H., Lin, R., Sawa, H., Okano, H., ... Mello, C. C. (1999). WRM-1 activates the LIT-1 protein kinase to transduce anterior/posterior polarity signals in *C. elegans*. *Cell*, 97(6), 717–726.
- Rodriguez, J., Peglion, F., Martin, J., Hubatsch, L., Reich, J., Hirani, N., ... Goehring, N. W. (2017). aPKC cycles between functionally distinct PAR protein assemblies to drive cell polarity. *Developmental Cell*, 42(4), 400–415.
- Rogulja, D., Rauskolb, C., & Irvine, K. D. (2008). Morphogen control of wing growth through the Fat signaling pathway. *Developmental Cell*, 15(2), 309–321.
- Roh-Johnson, M., Shemer, G., Higgins, C. D., McClellan, J. H., Werts, A. D., Tulu, U. S., ... Goldstein, B. (2012). Triggering a cell shape change by exploiting preexisting actomyosin contractions. *Science*, 335(6073), 1232–1235.
- Rose, L., & Gönczy, P. (2014). Polarity establishment, asymmetric division and segregation of fate determinants in early *C. elegans* embryos. *WormBook: The Online Review of C. elegans Biology*, 1–43.
- Saha, S., Nagy, T. L., & Weiner, O. D. (2018). Joining forces: Crosstalk between biochemical signalling and physical forces orchestrates cellular polarity and dynamics. *Philosophical Transactions of the Royal Society of London. Series B, Biological sciences*, 373(1747), 20170145.
- Salbreux, G., Charra, G., & Paluch, E. (2012). Actin cortex mechanics and cellular morphogenesis. *Trends in Cell Biology*, 22(10), 536–545.
- Salinas-Saavedra, M., & Martindale, M. Q. (2019). Par protein localization during the early development of *mnemiopsis leidyi* suggests different modes of epithelial organization in metazoa. *bioRxiv*.
- Salinas-Saavedra, M., Rock, A. Q., & Martindale, M. Q. (2018). Germ layer-specific regulation of cell polarity and adhesion gives insight into the evolution of mesoderm. *eLife*, 7, 1438.
- Sandersius, S. A., & Newman, T. J. (2008). Modeling cell rheology with the subcellular element model. *Physical Biology*, 5(1), 015002.

## BIBLIOGRAPHY

- Sase, I., Miyata, H., Ishiwata, S., & Kinoshita, K. (1997). Axial rotation of sliding actin filaments revealed by single-fluorophore imaging. *Proceedings of the National Academy of Sciences*, 94(11), 5646–5650.
- Sawa, H., & Korswagen, H. C. (2013). Wnt signaling in *C. elegans*. *WormBook: The Online Review of C. elegans Biology*, 1–30.
- Schenk, S., Bannister, S. C., Sedlazeck, F. J., Anrather, D., Minh, B. Q., Bileck, A., ... Tessmar-Raible, K. (2019). Combined transcriptome and proteome profiling reveals specific molecular brain signatures for sex, maturation and circalunar clock phase. *eLife*, 8, 161.
- Schermelleh, L., Heintzmann, R., & Leonhardt, H. (2010). A guide to super-resolution fluorescence microscopy. *The Journal of Cell Biology*, 190(2), 165–175.
- Schmied, C., Steinbach, P., Pietzsch, T., Preibisch, S., & Tomancak, P. (2016). An automated workflow for parallel processing of large multiview SPIM recordings. *Bioinformatics*, 32(7), 1112–1114.
- Schneider, S., Steinbeisser, H., Warga, R. M., & Hausen, P. (1996).  $\beta$ -catenin translocation into nuclei demarcates the dorsalizing centers in frog and fish embryos. *Mechanisms of Development*, 57(2), 191–198.
- Schneider, S. Q., & Bowerman, B. (2007).  $\beta$ -catenin asymmetries after all animal/vegetal- oriented cell divisions in *Platynereis dumerilii* embryos mediate binary cell-fate specification. *Developmental Cell*, 13(1), 73–86.
- Sedzinski, J., Biro, M., Oswald, A., Tinevez, J., Salbreux, G., & Paluch, E. (2011). Polar actomyosin contractility destabilizes the position of the cytokinetic furrow. *Nature*, 476(7361), 462–466.
- Shahidi, R., Williams, E. A., Conzelmann, M., Asadulina, A., Verasztó, C., Jasek, S., ... Jékely, G. (2015). A serial multiplex immunogold labeling method for identifying peptidergic neurons in connectomes. *eLife*, 4, 193.
- Shibasaki, Y., Shimizu, M., & Kuroda, R. (2004). Body handedness is directed by genetically determined cytoskeletal dynamics in the early embryo. *Current Biology*, 14(16), 1462–1467.
- Shimada, A., Nyitrai, M., Vetter, I. R., Kühlmann, D., Bugyi, B., Narumiya, S., ... Wittinghofer, A. (2004). The core FH2 domain of diaphanous-related formins is an elongated actin binding protein that inhibits polymerization. *Molecular Cell*, 13(4), 511–522.

- Shimeld, S. M., Boyle, M. J., Brunet, T., Luke, G. N., & Seaver, E. C. (2010). Clustered Fox genes in lophotrochozoans and the evolution of the bilaterian Fox gene cluster. *Developmental Biology*, 340(2), 234–248.
- Shrivastava, R., Rai, A., Salapaka, M., & Sivaramakrishnan, S. (2019). Stiffness of cargo-motor linkage tunes Myosin VI motility and response to Load. *Biochemistry*, 58(47), 4721–4725.
- Shu, S., Liu, X., & Korn, E. D. (2005). Blebbistatin and blebbistatin-inactivated myosin II inhibit myosin II-independent processes in Dictyostelium. *Proceedings of the National Academy of Sciences*, 102(5), 1472–1477.
- Sit, S., & Manser, E. (2011). Rho GTPases and their role in organizing the actin cytoskeleton. *Journal of Cell Science*, 124(Pt 5), 679–683.
- Smith, P., Azzam, M., & Hinck, L. (2017). Extracellular regulation of the mitotic spindle and fate determinants driving asymmetric cell division. *Results and Problems in Cell Differentiation*, 61(9), 351–373.
- Spiering, D., & Hodgson, L. (2011). Dynamics of the Rho-family small GTPases in actin regulation and motility. *Cell Adhesion & Migration*, 5(2), 170–180.
- Spira, F., Cuylen-Haering, S., Mehta, S., Samwer, M., Reversat, A., Verma, A., ... Gerlich, D. W. (2017). Cytokinesis in vertebrate cells initiates by contraction of an equatorial actomyosin network composed of randomly oriented filaments. *eLife*, 6, 983.
- Stefanini, M., De Martino, C., & Zamboni, L. (1967). Fixation of ejaculated spermatozoa for electron microscopy. *Nature*, 216(5111), 173–174.
- Stegmaier, J., Amat, F., Lemon, W. C., McDole, K., Wan, Y., Teodoro, G., ... Keller, P. J. (2016). Real-time three-dimensional cell segmentation in large-scale microscopy data of developing embryos. *Developmental Cell*, 36(2), 225–240.
- Steinhart, Z., & Angers, S. (2018). Wnt signaling in development and tissue homeostasis. *Development*, 145(11), dev146589.
- Steinmetz, P. R. H., Kostyuchenko, R. P., Fischer, A., & Arendt, D. (2011). The segmental pattern of otx, gbx, and Hox genes in the annelid *Platynereis dumerilii*. *Evolution & Development*, 13(1), 72–79.
- Stewart, M. P., Helenius, J., Toyoda, Y., Ramanathan, S. P., Muller, D. J., & Hyman, A. A. (2011). Hydrostatic pressure and the actomyosin cortex drive mitotic cell rounding. *Nature*, 469(7329), 226–230.



## BIBLIOGRAPHY

- Sun, T. Q., Lu, B., Feng, J. J., Reinhard, C., Jan, Y. N., Fantl, W. J., & Williams, L. T. (2001). PAR-1 is a Dishevelled-associated kinase and a positive regulator of Wnt signalling. *Nature Cell Biology*, 3(7), 628–636.
- Takahashi, H., & Shimizu, T. (1997). Role of intercellular contacts in generating an asymmetric mitotic apparatus in the Tubifex embryo. *Development, Growth & Differentiation*, 39(3), 351–362.
- Takaoka, K., & Hamada, H. (2012). Cell fate decisions and axis determination in the early mouse embryo. *Development*, 139(1), 3–14.
- Takeya, R., & Sumimoto, H. (2003). Fhos, a mammalian formin, directly binds to F-actin via a region N-terminal to the FH1 domain and forms a homotypic complex via the FH2 domain to promote actin fiber formation. *Journal of Cell Science*, 116(Pt 22), 4567–4575.
- Taubman, M. B., Grant, J. W., & Nadal-Ginard, B. (1987). Cloning and characterization of mammalian myosin regulatory light chain (RLC) cDNA: The RLC gene is expressed in smooth, sarcomeric, and nonmuscle tissues. *The Journal of Cell Biology*, 104(6), 1505–1513.
- Taylor, E. W. (1965). The mechanism of colchicine inhibition of mitosis. I. Kinetics of inhibition and the binding of H3-colchicine. *The Journal of Cell Biology*, 25(1), SUPPL:145–160.
- Telford, M. J., & Littlewood, D. T. J. (2009). *Animal evolution: Genomes, fossils and trees*. Oxford Scholarship Online.
- Tessmar-Raible, K., & Arendt, D. (2003). Emerging systems: Between vertebrates and arthropods, the Lophotrochozoa. *Current Opinion in Genetics & Development*, 13(4), 331–340.
- Thaëron, C., Avaron, F., Casane, D., Borday, V., Thisse, B., Thisse, C., ... Laurenti, P. (2000). Zebrafish *evx1* is dynamically expressed during embryogenesis in subsets of interneurons, posterior gut and urogenital system. *Mechanisms of Development*, 99(1-2), 167–172.
- Theka, I., Sottile, F., Cammisa, M., Bonnin, S., Sanchez-Delgado, M., Di Vicino, U., ... Cosma, M. P. (2019). Wnt/ $\beta$ -catenin signaling pathway safeguards epigenetic stability and homeostasis of mouse embryonic stem cells. *Scientific Reports*, 9(1), 1–18.
- Théry, M., & Bornens, M. (2006). Cell shape and cell division. *Current Opinion in Cell Biology*, 18(6), 648–657.

## BIBLIOGRAPHY

- Thorn, K. (2016). A quick guide to light microscopy in cell biology. *Molecular Biology of the Cell*, 27(2), 219–222.
- Tojkander, S., Gateva, G., & Lappalainen, P. (2012). Actin stress fibers – assembly, dynamics and biological roles. *Journal of Cell Science*, 125(Pt 8), 1855–1864.
- Toledano, H., & Jones, D. L. (2008). Mechanisms regulating stem cell polarity and the specification of asymmetric divisions. *StemBook*.
- Tomer, R., Denes, A. S., Tessmar-Raible, K., & Arendt, D. (2010). Profiling by image registration reveals common origin of annelid mushroom bodies and vertebrate pallium. *Cell*, 142(5), 800–809.
- Tomer, R., Khairy, K., Amat, F., & Keller, P. J. (2012, June). Quantitative high-speed imaging of entire developing embryos with simultaneous multiview light-sheet microscopy. *Nature methods*, 9(7), 755–763.
- Tosches, M. A., Bucher, D., Vopalensky, P., & Arendt, D. (2014). Melatonin signaling controls circadian swimming behavior in marine zooplankton. *Cell*, 159(1), 46–57.
- Uetz, P., Fumagalli, S., James, D., & Zeller, R. (1996). Molecular interaction between limb deformity proteins (formins) and Src family kinases. *Journal of Biological Chemistry*, 271(52), 33525–33530.
- Unsain, N., Stefani, F. D., & Cáceres, A. (2018). The Actin/Spectrin membrane-associated periodic skeleton in neurons. *Frontiers in Synaptic Neuroscience*, 10, 10.
- Valentine, J. W. (1997). Cleavage patterns and the topology of the metazoan tree of life. *Proceedings of the National Academy of Sciences*, 94(15), 8001–8005.
- van den Biggelaar, J. A. M., & Haszprunar, G. (1996). Cleavage patterns and mesentoblast formation in the gastropoda: An evolutionary perspective. *Evolution*, 50(4), 1520–1540.
- Vellutini, B. C., & Hejnol, A. (2016). Expression of segment polarity genes in brachiopods supports a non-segmental ancestral role of engrailed for bilaterians. *Scientific Reports*, 6, 23287.
- Vellutini, B. C., Martín-Durán, J. M., & Hejnol, A. (2017). Cleavage modification did not alter blastomere fates during bryozoan evolution. *BMC Biology*, 15(1), 33–28.
- Venkei, Z. G., & Yamashita, Y. M. (2018). Emerging mechanisms of asymmetric stem cell division. *The Journal of Cell Biology*, 217(11), 3785–3795.



## BIBLIOGRAPHY

- Vergara, H. M., Bertucci, P. Y., Hantz, P., Tosches, M. A., Achim, K., Vopalensky, P., & Arendt, D. (2017). Whole-organism cellular gene-expression atlas reveals conserved cell types in the ventral nerve cord of *Platynereis dumerilii*. *Proceedings of the National Academy of Sciences*, *114*(23), 5878–5885.
- Vicente-Manzanares, M., Ma, X., Adelstein, R. S., & Horwitz, A. R. (2009). Non-muscle myosin II takes centre stage in cell adhesion and migration. *Nature Reviews Molecular Cell Biology*, *10*(11), 778–790.
- Vopalensky, P., Tosches, M. A., Achim, K., Handberg-Thorsager, M., & Arendt, D. (2019). From spiral cleavage to bilateral symmetry: The developmental cell lineage of the annelid brain. *BMC Biology*, *17*(1), 81–19.
- Wang, Y., Xu, Y., Liu, Q., Zhang, Y., Gao, Z., Yin, M., ... Kou, J. (2017). Myosin IIA-related actomyosin contractility mediates oxidative stress-induced neuronal apoptosis. *Frontiers in Molecular Neuroscience*, *10*, 75.
- Webb, T. A., Kowalski, W. J., & Fluck, R. A. (1995). Microtubule-based movements during ooplasmic segregation in the medaka fish egg (*Oryzias latipes*). *The Biological Bulletin*, *188*(2), 146–156.
- Wedlich-Soldner, R., Altschuler, S., Wu, L., & Li, R. (2003). Spontaneous cell polarization through actomyosin-based delivery of the Cdc42 GTPase. *Science*, *299*(5610), 1231–1235.
- Wegner, A. M., Nebhan, C. A., Hu, L., Majumdar, D., Meier, K. M., Weaver, A. M., & Webb, D. J. (2008). N-wasp and the arp2/3 complex are critical regulators of actin in the development of dendritic spines and synapses. *Journal of Biological Chemistry*, *283*(23), 15912–15920.
- Welch, M. D., DePace, A. H., Verma, S., Iwamatsu, A., & Mitchison, T. J. (1997). The human Arp2/3 complex is composed of evolutionarily conserved subunits and is localized to cellular regions of dynamic actin filament assembly. *The Journal of Cell Biology*, *138*(2), 375–384.
- Willert, C. E., & Gharib, M. (1991). Digital particle image velocimetry. *Experiments in Fluids*, *10*(4), 181–193.
- Williams, E. A., Conzelmann, M., & Jékely, G. (2015). Myoinhibitory peptide regulates feeding in the marine annelid *Platynereis*. *Frontiers in Zoology*, *12*(1), 1–16.
- Williams, E. A., & Jékely, G. (2016). Towards a systems-level understanding of development in the marine annelid *Platynereis dumerilii*. *Current Opinion in Genetics & Development*, *39*, 175–181.

- Wilson, A. K., Pollenz, R. S., Chisholm, R. L., & de Lanerolle, P. (1992). The role of myosin I and II in cell motility. *Cancer Metastasis Reviews*, 11(1), 79–91.
- Wilson, E. B. (1892). The cell-lineage of Nereis. A contribution to the cytogeny of the annelid body. *Journal of Morphology*, 6(3), 361–480.
- Wolff, C., Tinevez, J., Pietzsch, T., Stamataki, E., Harich, B., Guignard, L., ... Pavlopoulos, A. (2018). Multi-view light-sheet imaging and tracking with the MaMuT software reveals the cell lineage of a direct developing arthropod limb. *eLife*, 7, 375.
- Wotton, K. R., Jiménez-Guri, E., & Jaeger, J. (2015). Maternal co-ordinate gene regulation and axis polarity in the scuttle fly *Megaselia abdita*. *PLOS Genetics*, 11(3), e1005042.
- Yamamoto, K., & Kimura, A. (2017). An asymmetric attraction model for the diversity and robustness of cell arrangement in nematodes. *Development*, 144(23), 4437–4449.
- Yu, F., Kuo, C. T., & Jan, Y. N. (2006). Drosophila neuroblast asymmetric cell division: Recent advances and implications for stem cell biology. *Neuron*, 51(1), 13–20.
- Yu, H., Chakravorty, S., Song, W., & Ferenczi, M. A. (2016). Phosphorylation of the regulatory light chain of myosin in striated muscle: Methodological perspectives. *European Biophysics Journal*, 45(8), 779–805.
- Yu, H., Ma, L., Yang, Y., & Cui, Q. (2007). Mechanochemical coupling in the myosin motor domain. I. Insights from equilibrium active-site simulations. *PLoS Computational Biology*, 3(2), e21.
- Zaffran, S., Küchler, A., Lee, H. H., & Frasch, M. (2001). binou (FoxF), a central component in a regulatory network controlling visceral mesoderm development and midgut morphogenesis in Drosophila. *Genes & Development*, 15(21), 2900–2915.
- Zantke, J., Bannister, S., Rajan, V. B. V., Raible, F., & Tessmar-Raible, K. (2014). Genetic and genomic tools for the marine annelid *Platynereis dumerilii*. *Genetics*, 197(1), 19–31.
- Zantke, J., Ishikawa-Fujiwara, T., Arboleda, E., Lohs, C., Schipany, K., Hallay, N., ... Tessmar-Raible, K. (2013). Circadian and circalunar clock interactions in a marine annelid. *Cell Reports*, 5(1), 99–113.
- Zdravkovic, T., Nazor, K. L., Larocque, N., Gormley, M., Donne, M., Hunkapillar, N., ... Fisher, S. J. (2015). Human stem cells from single blastomeres reveal pathways of embryonic or trophoblast fate specification. *Development*, 142(23), 4010–4025.